A Study of the Beam Physics in the CLIC Drive Beam Decelerator

Erik Adli
Department of Physics
University of Oslo
Norway

Dissertation presented for the degree of
Philosophiae Doctor (PhD) in Physics

October 2009

Series of dissertations submitted to the
Faculty of Mathematics and Natural Sciences, University of Oslo
No. 899

ISSN 1501-7710

Cover: Inger Sandved Anfinsen.
Printed in Norway: AiT e-dit AS, Oslo, 2009.

Produced in co-operation with Unipub AS.
The thesis is produced by Unipub AS merely in connection with the
thesis defence. Kindly direct all inquiries regarding the thesis to the copyright
holder or the unit which grants the doctorate.

Unipub AS is owned by
The University Foundation for Student Life (SiO)

Preface and Acknowledgements

When I was a CERN Fellow working on the ATLAS superconducting magnet system, Professor Steinar Stapnes suggested that I study a subject called accelerator physics for my PhD; an advice I considered, debated and eventually followed. This choice launched me into the exiting world of linear colliders, where I soon found myself involved with all aspects of the energy extraction needed to propel the particles in the CLIC collider. Now, four years after the choice to dive into accelerators, I am happy to say that I am confident it was a good one.

The story started some years earlier. I grew up in the small city of Steinkjer, and continued by doing my master thesis in the nearby city of Trondheim. Although the university was very good, this choice could not be said to be neither particularly adventurous nor ambitious. Interest for the outside world, combined with a fair amount of serendipity, lead me to the European Space Agency's research centre in the Netherlands. I arrived there with an open mind, but without any real master plan or ambition. What happened was that I formed friendship with a number of young persons from all over Europe. What struck me after some time was that most of my friends at ESA were so full of projects, plans, ideas, even on grand international scales - and they just went for it. They all inspired me. In particular I must mention Enrico Chesta, Lisa Kaltenegger and Andre Schiele as scientific catalysts. I felt though that the web of opportunity had started to tighten, and I needed a fresh base to unfold my new inspiration. At CERN I found the almost infinite land of discovery I was looking for, and I decided to go for it.

I would like to thank everyone who have supported my road towards this thesis. My supervisor Steinar Stapnes started the process, acquired funding in record time and contacted the CLIC project, where Daniel Schulte agreed to be my scientific supervisor. I did not know Daniel beforehand, but it turned our that I was in luck again; his knowledge of accelerator physics and the CLIC project turned out to be an inexhaustible source for a fresh PhD student, and he never hesitated to share both knowledge and ideas with me (even when he had claimed in advance he was extremely busy, I found our conversations lasting far into the lunch hour). I wish to thank both my supervisors for their excellent and continuous support during the entire thesis work. In addition, I wish to thank Igor Syratchev who very quickly after my arrival started initiating me to the murky depths of radio-frequency systems, despite that he to begin with found himself staring annoyingly at a wall of ignorance. Speaking about my formation process, I must also emphasise the effect of the several accelerator schools and seminar I have attended in Europe and the US. I consider these schools invaluable to my learning process in the field of accelerator physics. The professional inspiration I received during these gathering enlarged my enthusiasm for the field, and I would like in particular to highlight Professor Alex Chao's lectures during the USPAS in Houston, 2007. I would wish for everyone to experience similar learning experiences. Many thanks goes as well to numerous colleagues in the CLIC project who provided valuable input from

their fields of expertise, including Hans Braun, Rogelio Tomás, Frank Tecker, Anne Dabrowski, Carsten Welsch, Steffen Döbert, Roberto Corsini, Simona Bettoni, Barbara Dalena, Thibaut Lefèvre, Walter Wünsch, Günther Geschonke, Alexandre Samoshkin, Erk Jensen, Marco Battaglia and many more. Particular thanks to Andrea Latina for excellent PLACET support, and for doing the "stroke of genius" of merging PLACET with Octave, and Jean Bernard Jeanneret for always having time for stimulating beam dynamic discussions. For the Two-beam Test Stand operations, the co-operation with Roger Ruber and Volker Ziemann from Uppsala University has been vital. I acknowledge my colleagues in the Oslo experimental particle physics group for cake and valuable support during the final preparations of the dissertation. Finally, I acknowledge Kari Adli for thorough English proof-reading during the writing and Stian Mong for final proof-reading.

Despite the support on the professional side, it was not easy to enter a completely new field as a student, starting from scratch, after several years of successful experience in other fields. My integrating into "the other side" of CERN, the beams department, was eased by my fellow PhD students and Fellows whom I had met at the CERN Accelerator School; Peder Eliasson, Andrea Latina, Elena Benedetto, Javier Resta López, and later Sandra Aumon, Roderick Bruce, Riccardo de Maria, Sandro Bonacini, Matteo Magistris and many more - thank you for making the accelerator physics research at CERN such a young and vibrating environment. I wish in particular to thank my office mates during three tough years, Javier Barranco and Seyd Hamed Shaker, for their patience and ability to tolerate my presence in good as well as evil days, and for all the philosophical discussions we had. I direct warm thoughts as well to the number of very nice persons I was fortunate to meet through the international seminars and conferences I have attended, rending my professional travel assignments special experiences, again showing the good spirit within the community.

In order to perform continuously during a long PhD it is invaluable to have support outside the working environment as well. I wish to thank all my friends in Geneva for supporting fully my work, and providing oases when needed. Especially thanks to the HHH-coupling, Henna, Hege and Henning (an observable production of a HHHH-coupling might be within reach!). During my years of expatriation I have been fortunate to have a stable base in Norway, with family and friends luckily residing close to my home university in Oslo and whenever I have returned to Norway after longer or shorter stays abroad I have always been warmly welcomed. My parents, Arne, Kristine, Andreas and Aksel, Lobben, Kopland and my friends have always been there, as if I never left, something which I have greatly appreciated.

I dedicate this thesis to my parents. To my mother, because of her never ending support for me, for my endeavours and my choices, and for always providing a haven. And to my father, who left us the very moment I started this thesis, but who parted with the firm knowledge that my future had taken a promising direction.

Erik Adli, October 1, 2009

Abstract

CLIC is a study for a Multi-TeV e^+e^- linear collider, in which the rf power for the main linacs is extracted from 100 ampere electron drive beams, by the use of specially designed power extraction structures. Up to 90% of the beam energy is extracted from the drive beams along one kilometer long decelerator sectors, rendering the beam transport challenging.

We have identified two major challenges for robust beam transport: the significant transverse wakes in the power extraction structures, and the large energy spread induced by the power extraction process. By beam dynamics studies we have qualified power extraction structure designs, leading to the present CLIC baseline structure in which the transverse wakes are sufficiently mitigated. We have further shown that the beam energy spread induced by the deceleration implies that standard 1-to-1 correction might not ensure satisfactory drive beam transport. As alternative, we propose a decelerator orbit correction scheme based on dispersion-free steering and exploiting the structure beam loading. By simulation the proposed scheme shows excellent performance, assuming sufficient beam position monitor resolution. We have performed successful demonstrations of similar orbit correction schemes in the linac of the CLIC Test Facility 3. The results of the beam dynamics studies have lead to specifications for decelerator instrumentation and magnets, described in detail in this work.

The first prototype of the baseline power extraction structure has been tested with beam in the Two-beam Test Stand in the CLIC Experiment Area, where a field recirculator has been installed to boost power production. We have derived formulae for rf power production and voltage, including a simple model describing power extraction with recirculation. The model has been applied to the first Two-beam Test Stand experimental result. We compare the measured rf power, phase and energy loss with reconstructed signals based on beam intensity measurements, and a good agreement between the measurements and the reconstruction is shown.

Contents

List of Figures

List of Tables

1. Introduction

This thesis concerns accelerator physics research related to the international efforts towards the design and construction of a linear electron-positron collider for high-energy particle physics. Specifically, we have studied the beam physics in the decelerator (energy-extractor) of the Compact Linear Collider, CLIC. We introduce the subject by a presentation of particle physics, aimed at the non-expert, followed by a brief description of the methods used in high-energy particle physics, and an introduction to CLIC, also in a non-technical language. At the end of this introductory chapter an outline of the thesis is presented.

1.1 Particle physics

Particle physics is the study of the smallest, most fundamental constituents of nature. Physics seeks to describe nature by laws that are uniform in both space and time, and particle physics is an essential part of the effort to explain the early stages of the universe and the properties of today's universe. The link between particle physics and cosmology together with astrophysics is therefore very strong. The development of the great theories of *quantum mechanics* and the *special theory of relativity* in the first half of the 20th century provides the pillars needed to describe the fundamental particles and the interactions between them.

Systems of atomic dimensions are not well described by the laws of classical mechanics and electrodynamics. Quantum mechanics provides a description of such small-scale systems, based on a framework where systems consist of superposition of possible states. When measuring a system observable, there is a certain *probability* of measuring the value corresponding to a given possible state. Quantum mechanics implies thus a non-deterministic description of nature. Since its conception in the late 1920s and up to today, excellent agreement between the predictions of quantum mechanics and experiments has been shown.

The special theory of relativity is based on the invariance of the laws of physics with respect to any inertial frame, and the constancy of the speed of light. This theory has shown excellent agreement with experiments as well. A profound implication of the theory is the equivalence of energy and mass, expressed through Einstein's equation

$$E = mc^2 \tag{1.1}$$

which shows that energy, E, can be exchanged with mass, m, by an exchange-ratio equal to the square of the speed of light, c.

In particle physics, a very fruitful approach to describe fundamental particles has proven to be *relativistic quantum-field theory*, a theory combining quantum mechanics and the special theory of relativity. In quantum-field theory, particles as well as forces are represented as the quanta of fields, and the theory allows for particles to be created and annihilated. As illustration, Figure 1.1 shows two examples of processes described by the quantum-field description of the electromagnetic force; quantum electrodynamics. In the diagrams, time flows from the left to the right. Figure 1.1(a) shows electron-electron scattering; two electrons experiencing a mutual repulsive force, mediated by the force carrier particle, a photon. Figure 1.1(b) shows pair-production in vicinity of a nucleus; a massless photon is converted into a massive electron and positron (anti-electron) pair. The latter process illustrates the implications of both quantum mechanics and relativity; quantum-field theory does not predict exactly *when* the pair-production will take place, only the probability for it to take place. When the process does take place, energy is converted into mass, in accordance with Eq. (1.1).

In the second half of the 20th century a consistent framework based on quantum-field theory, describing the fundamental particles and their interactions, the *Standard Model of Particle Physics*, has been developed. Excellent agreement has been found between the predictions of the Standard Model and experiments. However, there are many unanswered questions about the theory which can only be sought answered by further experiments. We will come back to the Standard Model of Particle Physics in Chapter 2.

Every time particle physics experiments have accessed a higher energy scale, new particles or phenomena have been discovered. The experimental discoveries may have provided confirmation of existing theories, e.g. the discovery of the mediators of the weak interaction at CERN in 1983, discussed below, or they may have provided stimulus for new theory development, e.g. the first evidence for neutrino mass with Super-Kamiokande in 1998, well described in reference [1].

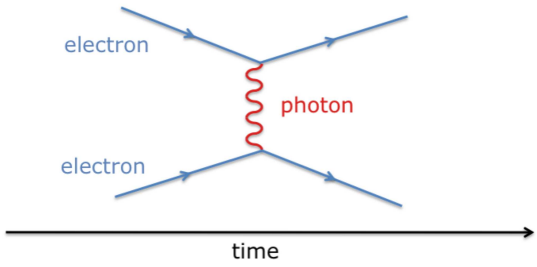

(a) Electron-electron scattering

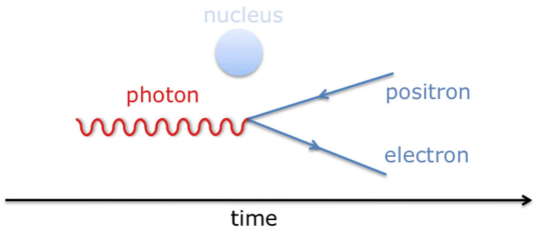

(b) Electron-positron pair production

Figure 1.1: Example of particle physics processes described by the Standard Model. (a) Electron-electron scattering where the scattering force is mediated by a force-carrier photon. (b) Pair-production, in vicinity of a nucleus, where a massless photon is converted into an electron-positron pair.

In high-energy particle physics, particles interactions occurring at high energies are studied. Using particle accelerators it is possible to generate intense beams of particles at high energies, colliding either with fixed targets, or with particles moving in the opposite direction. Using particle detectors surrounding the regions of collisions, one can detect the products of the collisions and analyse the physics processes occurring at the moment of collision.

1.2 CERN - the European laboratory for particle physics

CERN, originally standing for "Conseil Européen pour la Recherche Nucléaire", is the European laboratory for particle physics. The laboratory was founded in 1954, partly as an effort to revive and reunite European science after the Second World War. CERN has today 20 member states, including Norway, and serves as an international particle accelerator laboratory for the high-energy particle and nuclear physics community worldwide.

The main role of the laboratory is to provide large scale experimental infrastructure for high-energy particle physics; more specifically particle accelerators and detectors, as well as IT-infrastructure. In CERN-based projects, design and construction of particle detectors, as well as data-analysis, have typically been performed by large collaborations of universities and institutes, including CERN. Design and construction of particle accelerators have traditionally been more exclusively the domain of CERN. This is, however, about to change with the next generation of particle colliders considered, which will be designed and constructed by large international collaborations.

To illustrate how large-scale high-energy particle physics experiments are performed, we use as example the CERN-situated 27 km Large Hadron Collider ring (LHC). The purpose of the LHC project is to collide protons against each other, at very high energies, and analyse the outcome. The proton-proton collision energy will be 14 TeV. One TeV is equal to the kinetic energy a particle with unit charge gains by being accelerated by an electric voltage of 1000 billion volt, and particle physics processes at this energy scale have never been explored in collider experiments before. Figure 1.2 shows the region in which CERN and the LHC are located, on both sides of the Franco-Swiss border close to Geneva, Switzerland. The track of the underground LHC ring is indicated in white.

Particle accelerators

Particle accelerators, circular as well as linear, use electric fields to accelerate charged particles. The fields are typically oscillating at radio-frequency (rf), and are synchronised with the particle motion in order to provide net acceleration. The average electric field seen by the particles in an accelerating structure (the *accelerating gradient*), can reach

several million volts per meter. Furthermore, electric or magnetic fields are used to steer and focus the particle beams. At high energies, magnetic forces become relatively stronger, so for high-energy accelerators typically magnetic fields are used for steering and focusing.

Before collisions in the LHC, bunches of protons are accelerated to high energies using a chain of accelerators, as shown in Figure 1.3(a). Linear accelerators are used to accelerate the particles up to an energy of 50 MeV. A set of ring accelerators (synchrotrons) brings the energy up to 450 GeV before injecting the bunches into the LHC, both in clock-wise and counter-clockwise directions. When the LHC has been filled with proton bunches, the machine will provide the final acceleration up to 7 TeV per proton. Protons in the two directions will travel in separate beam pipes for most of the trajectory, but the pipes join close to four interaction regions, allowing for bunches to collide. When the particles

Figure 1.2: Aerial photo of the region in which CERN and the LHC are located. The trajectory of the underground LHC proton-proton collider is indicated by the large white ring. The CERN main site (Meyrin, Switzerland) is located just above the wine fields in the bottom middle of the picture. The Jura mountains and the Lake Geneva is seen to the left and to the right respectively. Picture copyright CERN.

have reached full energy, magnets are used to bring the particle beams into collision at the interaction regions. The interaction regions are surrounded by the particle detectors of the LHC experiments ATLAS, ALICE, CMS and LHCb, their location indicated on Figure 1.3(a).

The interaction region

Figure 1.3(b) shows how the proton beams are squeezed and steered into collision in the ATLAS interaction region. Out of the 100 billions particles in each LHC proton bunch, about 20 pairs of protons, on average, will come close enough to generate hard collisions of interests. In these processes, described by standard model physics, or eventually new physics, new particles may be produced. The particles produced are typically unstable and they quickly decay (transform) into new particles.

Particle detectors

The particles created in the collision, and their decay products, will travel away from the collision point in all directions. Around the interaction region, layers of particle detectors are installed in order to identify and measure properties of particles passing through. From these measurements, the processes occurring in the interaction region are sought reconstructed. Figure 1.3(c) illustrates the layers of a generic particle detector surrounding the interaction point, showing how different particle types are interacting with the different layers of the detector. Both LHC general purpose experiments, ATLAS and CMS, have detector layers very similar to Figure 1.3(c) surrounding the interaction regions.

Information technology

Some of the physics processes of interest occur very infrequently, and it is therefore of importance to collide particles at the highest possible rate. In LHC, bunches will collide in the interaction regions with an average frequency of 32 MHz. Even though detector trigger mechanisms select in real-time but a tiny fraction of the collisions for further analysis, the resulting amount of data to be stored is estimated to reach many petabytes per year (one petabyte is one million gigabytes). Therefore GRID-based solutions for sharing of storage space and processor power across the world have been developed for the LHC experiments. Figure 1.3(d) depicts the overall structure of the LHC-grid. Collision data from the LHC experiments will be transferred from CERN (the Tier-0 centre) to 11 main hubs world-wide (the Tier-1 centres), which will store most of the data. Much of the data-analysis will be performed at the regional (Tier-2) centres, accessible for physicists participating in the experiments.

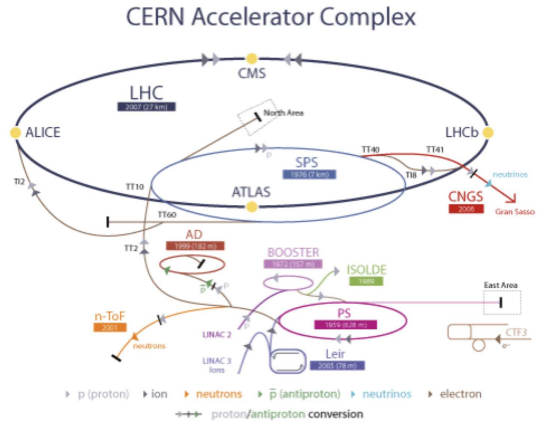

(a) The CERN accelerator complex

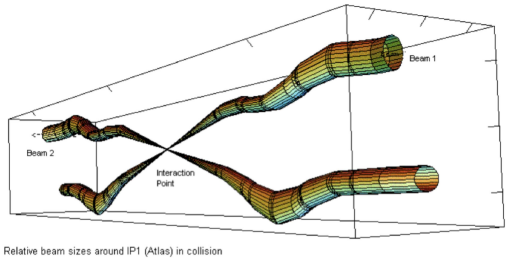

(b) Proton beams colliding in ATLAS

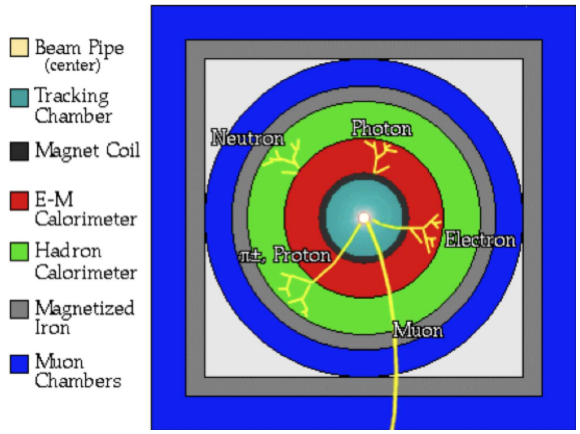

(c) Detector layers

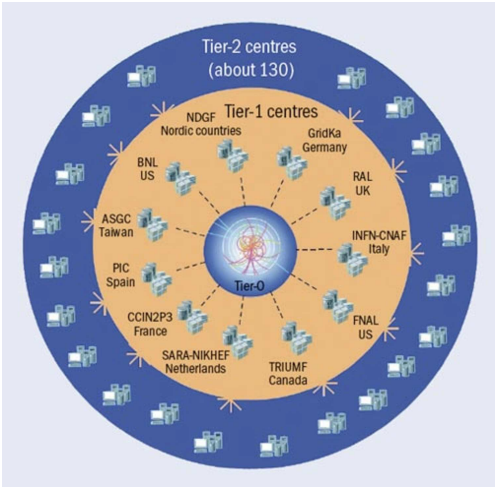

(d) GRID

Figure 1.3: The ingredients of high-energy particle physics collider experiments, with the LHC as example: (a) The CERN accelerator complex, including the accelerator chain leading to the LHC. The protons to be collided in the LHC are first accelerated in the linear accelerator LINAC 2, then further accelerated in a series of ring accelerators, before receiving the final boost in the LHC. (b) At four interaction regions the beams are squeezed down to a very small size, and steered into collision by magnets. Only a tiny fraction of the protons collide close enough to produce new particles. Most protons pass through an interaction region unaffected, but will continue to circulate in order to aim for collision at the next interaction region. (c) Typical layers of a particle detector. Each layer has a specific function, allowing the different particle species produced in the collisions, and their decay products, to be identified and measured. Low energy particles are strongly bent by magnetic fields provided by the detector, while high energy particles travel in almost straight lines (in the figure the colliding beams travel into and out of the paper). (d) The GRID organisation of the data expected from the LHC. Tier-1 centres around the world store the bulk of the data. Much of the data-analysis are performed using the data-power of the many regional Tier-2 centres. Picture (a) and (b) copyright CERN.

1.3 Hadron colliders versus lepton colliders

Particles species are classified into *hadrons*, which are composite particles constituted of quarks, confined by the strong interaction, and *leptons* which are modelled as fundamental, point-like particles. For example, the proton is constituted of quarks and is a hadron, while the electron is considered to be a fundamental particle, a lepton.

The fraction of the momentum carried by the constituents of the hadrons at a given time is continuously fluctuating, quantified statistically by parton density functions, and the collision energy will vary from collision to collision. A hadron collider like the LHC will therefore effectively scan the energy range up to a few TeV for new particles and physical phenomena. However, hadron collisions are not well suited to do precision physics, needed to measure to a good level of accuracy important model parameters. Lepton colliders are better suited, because colliding fundamental particles instead of hadrons, produces much smaller amount of background particles (which impede data-analysis) and because the initial state of the colliding particles is well know. Historically, colliders for high-energy particle physics have therefore varied between hadron and lepton colliders, where the results of the two often are complementary.

A famous example of the mutual achievements of hadron and lepton colliders is found in the history of CERN; in 1983 the 7 km long proton anti-proton collider S$p\bar{p}$S discovered experimentally the particles that mediate the weak interaction, the $W^{\pm}$and Z^0 bosons, exactly as predicted by the Standard Model many years earlier. The fascination story of the hunt for these particles is told in reference [2], in a language accessible to the general public. Refs. [3, 4] are scientific papers reporting the discoveries, leading to the Nobel price in physics already the following year. A few years later, the 27 km long electron-positron collider, LEP, was used to produce a very large number of Z^0 bosons by tuning the collision energy to the value corresponding to the Z^0 resonance peak (in the order of 1000 Z^0's could be produced per hour this way). Experimentally it has been found that there exist several generations of fundamental particles, where each particle generation shares the same characteristics, except mass and stability (for example, two heavier, but unstable, variations of the electron have been discovered; the muon in 1937 and the tau in the 1970s). By comparing measurements of the decay width of the Z^0 at LEP, with the Standard Model predictions, one found strong indications that there exist only three generations of matter in nature.

With the exception of the 2-mile Stanford Linear Collider, all particle colliders operated up to today have been single or double ring colliders [5]. For example, LEP collided electrons towards positrons in the same tunnel now used for the LHC, in the period 1989-2000. However, as will be shown quantitatively in Chapter 2, synchrotron radiation loss imposes limits to the energy that light particles can reach in rings. Linear colliders are therefore considered the better option for lepton collisions at high energy. Particle physics experiments in linear colliders are performed very similarly to what was presented for the LHC; after acceleration to high energies by radio-frequency fields pumped into two very long linear accelerators, electron and positron bunches will collide in the centre of the machine, surrounded by particle detectors. Figure 1.4 shows the

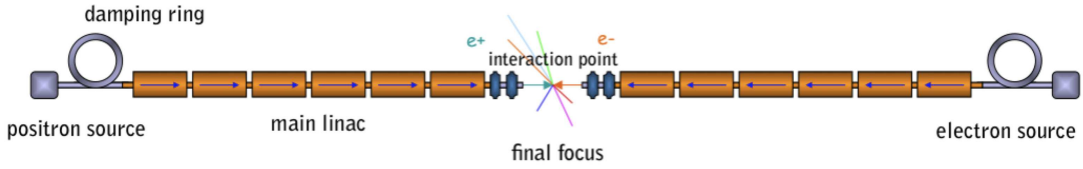

Figure 1.4: A basic linear collider. Electrons and positrons generated by the sources are accelerated to high energy in two very long linear accelerators, and collide with each other at the interaction point. Picture courtesy of the CLIC study.

layout of a basic linear collider.

In order to complement the LHC results and do precision measurements on physics at TeV-scale energies, there is general agreement in the international particle physics community that the next collider should be *a linear electron-positron collider*. At present there are two design studies for linear electron-positron colliders on-going, one being the International Linear Collider study [6] and the other the Compact Linear Collider study, which is the focus of this thesis.

1.4 The Compact Linear Collider

The Compact Linear Collider, CLIC [7], is a study for a Multi-TeV linear collider. The study began at CERN in the mid-80s as a limited effort [8] and is today an international collaboration, with CERN and 32 universities and institutes from three continents participating in the research [9], including the University of Oslo, Norway. The baseline design is for a collision energy of 3 TeV, and CLIC is today the only study accommodating high luminosity e^+e^- collisions above 1 TeV. The site length of the CLIC machine is estimated to 48 km, whereof the main linacs total length is 42 km.

The CLIC study, reaching towards Multi-TeV energies, has developed a novel linear collider concept altogether, based on *two-beam acceleration*. Here the rf power for the main linac accelerating structures is not provided by pulsed klystrons, as is conventional, but by high-current low energy *drive beams*, running in parallel with the main beams. In this scheme, all the energy required for the main beam acceleration is stored in drive beams generated by a relatively small, centrally located drive beam complex. The drive beams are then transferred into *decelerators* running in parallel with the main linacs, where almost 90% of the beam energy will be extracted, converted into rf fields and subsequently transferred into the accelerating structures. Figure 1.5 shows the principle of the two-beam scheme. It is a simple and elegant way to provide rf power. However, in the history of accelerators no similar projects have been performed, and the feasibility of the two-beam scheme is still to be proven. This thesis is concerned with the very heart of the two-beam scheme; the drive beam energy-extraction and rf power production.

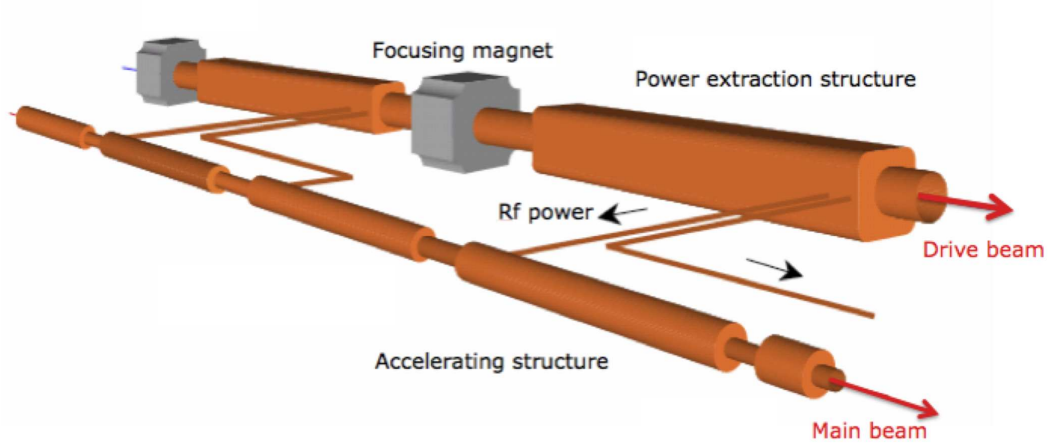

Figure 1.5: CLIC power extraction and transfer principle. Energy in form of rf power is extracted from drive beams by means of special power extraction structures (PETS). The extracted power is coupled out of the PETS and subsequently transferred into the accelerating structures, providing power for the main beams. Picture courtesy of the CLIC study.

The CLIC study is supported by the European strategy for particle physics [10] and represents a considerable effort within the particle physics community, with significant investments from both CERN and the collaborating partners. As example, CERN provides man-power in the order of 50 full-time equivalents per year, plus comprehensive experimental test facilities for CLIC. The current milestone for the CLIC collaboration is to provide a Conceptual Design Report, including a discussion on the feasibility of CLIC, by the end of 2010.

1.5 Outline of the thesis

In Chapter 2 of the thesis we discuss the particle physics motivation for constructing a future linear collider, and we see how the physics requirements dictate the general design of such a collider. In Chapter 3 the CLIC machine is described in more detail, with emphasise on the two-beam scheme. Comparison with the International Linear collider study is also touched upon, in order to illustrate the advantages and disadvantages of the CLIC scheme.

Chapters 4 and 5 constitute the main part of the thesis, containing the author's new contributions. The most important results have been presented at five different international conferences and workshops during the thesis period, and the corresponding publications are included in Appendix B. An important part of the CLIC study is to arrive at a conceptual design for a CLIC machine, and two component hardware specifications, included in Appendix C, have resulted from the thesis work. The text in Chapters 4 and 5 aims at presenting the necessary background and framework needed to arrive at the conclusions of the publications. The publications and specifications will

be referred to at the appropriate locations in the chapters.

In Chapter 4 we step into the core of the two-beam acceleration scheme and focus on the power-extraction process itself. We develop the framework necessary to understand the physics of the power extraction, and we present the results of the first experimental tests of the CLIC 12 GHz power extraction structure with beam, in the *Two-beam Test Stand* experimental set-up.

In Chapter 5 we broaden the perspective and investigate the beam dynamics of the CLIC energy-extractor, the *decelerator*, where each sector will have more than 1400 power extraction structures installed. The beam dynamics is, as will be discussed, driven by the effects of these structures.

In Chapter 6 we glance towards the future, describing the first prototype for the CLIC decelerator, the *Test Beam Line*, and the experiments planned for the coming few years.

2. From Physics Requirements to a Linear Collider

In this chapter we discuss a few characteristic of the Standard Model, and based on this we give examples of the particle physics motivation for a future lepton collider. We furthermore illustrate how the particle physics requirements suggest the main functionality and features of such a collider.

2.1 The Standard Model of Particle Physics

The Standard Model of Particle Physics [11–13] is a quantum-field theory which describes the properties and interaction of point-like fundamental particles, presented in Figure 2.1, which represents the observed matter and forces in nature. It can be expressed in compact form as the Lagrangian density [14]

$$\mathcal{L}_{\mathrm{SM}}(x) = \mathcal{L}_f(x) + \mathcal{L}_G(x) + \mathcal{L}_\phi(x) + \mathcal{L}_{f\phi}(x), \tag{2.1}$$

where $\mathcal{L}_f$ is the fermion sector, $\mathcal{L}_G$ the gauge sector, $\mathcal{L}_\phi$ the Higgs sector and $\mathcal{L}_{f\phi}$ the mass-generating sector. All terms are functions of the space-time coordinates $x^\mu = [t, x, y, z]$, spanning all of time and space. We will here do no attempt to describe the Standard Model in full; we will only briefly discuss the significance of each term in Eq. (2.1) and highlight some features used to introduce the particle physics motivation for a future collider.

The fermion sector, $\mathcal{L}_f(x)$, describes fermion fields, representing *matter and anti-matter particles*; charged leptons (the three electron generations), neutral leptons (the three neutrino generations) and quarks (the three generations of quark pairs).

The Standard Model requires the fermion fields to be invariant with respect to local phase transformations. This invariance property is called *gauge-invariance,* by analogy with the gauge-invariance properties of classical electromagnetic fields. Requiring gauge-invariance of the matter fields leads to the introduction of gauge fields, coupled to the fermion fields. The gauge sector, $\mathcal{L}_G(x)$, describes these gauge fields, representing *force carrier particles*; the photon, mediator of the electromagnetic force acting on particles with electric charge; the $W^\pm$ and Z^0 bosons, mediators of the weak force acting on particles with weak charge (leptons and quarks); and the gluons, mediators of the strong

force acting on particles with colour charge (quarks and gluons). At high energies ($\gtrsim$ 100 GeV) the photon and the $W^{\pm}$ and Z^0 bosons become indistinghuisable, and the electromagnetic and the weak force are unified. $\mathcal{L}_f(x)$ contains interaction terms describing the *coupling* between the fermion fields and the gauge fields. $\mathcal{L}_G(x)$ contains interaction terms describing the coupling of gauge fields to themselves. The gauge sector self-interaction terms arise from the principle of gauge invariance.

The requirement of local gauge invariance thus dictates the form of the particle interactions in the Standard Model. The validity of this approach is the decades of experimental results showing excellent agreement [15] between the Standard Model predictions and corresponding physics processes observed in nature, for example in high-energy particle colliders.

2.1.1 The Higgs mechanism

Nature tells us that some particles are massless while most particles have masses, where the magnitude of particle masses varies by many orders of magnitude. This observation, combined with the requirement of local gauge invariance, have lead to the introduction of the so-called Higgs mechanism, in which most particles acquire mass through interaction

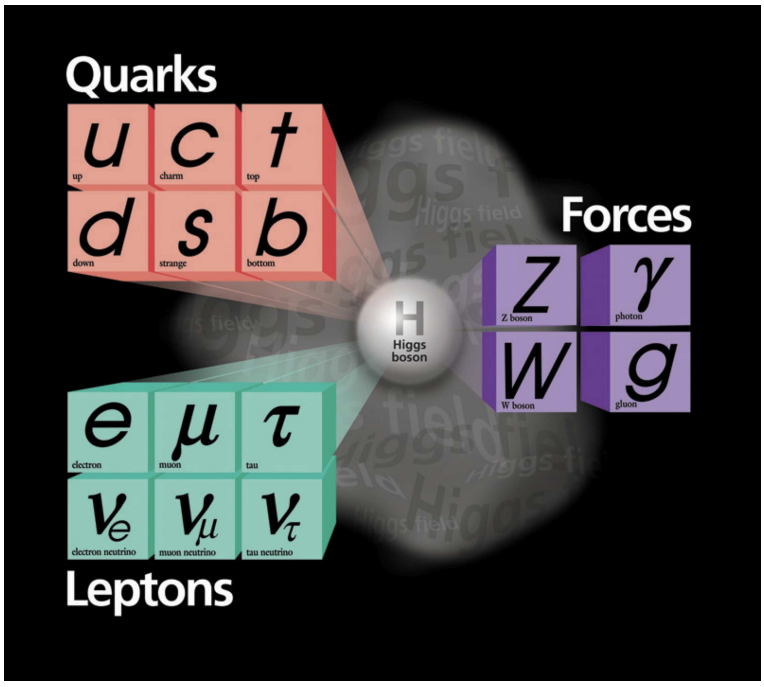

Figure 2.1: Nature's fundamental building blocks, according to the Standard Model of Particle Physics. The matter particles (fermions) comprise leptons and quarks, and the force carrier particles (bosons) comprise the photon, the gluons, and the $W^{\pm}$ and Z^0 bosons. The mass-generation mechanism of the Standard Model predicts the existence of a hitherto unobserved particle; the Higgs boson. Picture courtesy of Fermilab.

with a Higgs field, permeating all of space. The Higgs mechanism affects the electro-weak part of the Standard Model, where interactions are governed by the massless photon and the massive $W^{\pm}$ and Z^0 bosons.

The Higgs mechanism achieves asymmetry in the gauge boson masses by the concept of spontaneous symmetry breaking, where the vacuum is assumed a non-zero expectation value, v, and a Higgs field, η, represents real fluctuations about v. The mechanism predicts that the $W^{\pm}$ and Z^0 bosons acquire masses according to [14]

$$m_W = \frac{1}{2}gv \tag{2.2}$$

and

$$m_Z = \frac{m_W}{\cos\theta_W}, \tag{2.3}$$

where g is the coupling constant of the electro-weak force and θ_W the weak mixing angle, quantifying the mixing between the electromagnetic and the weak force. The photon, on the other hand, remains massless after the symmetry breaking.

The potential of the Higgs field assumed by the Standard Model Higgs mechanism [14] is

$$V(\eta) = \lambda v\eta^3 + \frac{1}{4}\lambda\eta^4, \tag{2.4}$$

where λ is a free parameter in the model. As indicated by Eq. (2.2), the vacuum expectation value, v, can be estimated from experimentally measured quantities to [15]

$$v = 246 \text{ GeV}.$$

It can further be shown [14] that the mass of the quantum of the Higgs field, the Higgs particle, is given by

$$m_H = \sqrt{2\lambda v^2} \tag{2.5}$$

implying that the value of the Higgs mass cannot be directly predicted from known measurement data, due to the dependence on λ. In Eq. (2.1) the Higgs sector, $\mathcal{L}_\phi(x)$, describes the Higgs field and the coupling of the Higgs field to the $W^{\pm}$ and Z^0 bosons.

The Higgs mechanism does directly generate masses for the $W^{\pm}$and Z^0 boson, while in order for the fermions to acquire mass, Yukawa couplings [14] to the Higgs field are added to the Standard Model, yielding fermion masses, m_f, given by

$$m_f = g_{Hff}\frac{v}{\sqrt{2}}, \tag{2.6}$$

where g_{Hff} are free coupling constants. In Eq. (2.1) the fermion mass-generating sector, $\mathcal{L}_{f\phi}(x)$, describes the Yukawa couplings. The Higgs mechanism thus introduces the possibility for fermions to acquire masses, but it does not give any answer to why their masses take on seemingly arbitrary values.

Nevertheless, the Higgs mechanism is considered to be the most elegant way to introduce mass terms, and the mechanism is an integral part of the framework of the Standard

Model. As discussed in the introduction, the masses of the the Z^0 and the $W^{\pm}$ bosons have been measured to excellent agreement with the theoretical predictions. Furthermore, the existence of a Higgs particle is integral to the renormalizability [14] of the Standard Model. However, the Higgs particle remains the only particle in the Standard Model that has not been observed experimentally. Until an eventual discovery of a Higgs particle and measurements of its properties, the mechanisms of the electro-weak symmetry breaking and mass generation will remain unproven theories.

2.2 Examples of Higgs physics at a future lepton collider

We will motivate the need for a future lepton collider by looking to Standard Model Higgs physics, with the understanding that this represents only a small fraction of potential physics processes to be studied at a future collider. LHC physics result will precede any electron-positron collider by many years, and if there exists a Higgs particle as described by the Standard Model, the LHC detectors ATLAS and CMS are designed so that such a particle should be discovered with a high confidence level (5σ), in a relatively early phase (30 fb^{-1}) of LHC operation, see e.g. [16]. It is further reported in [16] that after 300 fb^{-1}, a mass estimate precise to about 0.1% is expected for a Standard Model Higgs. However, if the LHC discovers and measures the mass of a Higgs-like particle, there are a number of precision tests to be performed before one can really be sure that the particle found is a Higgs boson as predicted by theory.

A few cases where future lepton colliders are expected to perform better than LHC will be highlighted, emphasising the *collision centre of mass energy,* $\sqrt{s} = E_{\mathrm{CMS}}$*,* and the *integrated luminosity,* $\int \mathcal{L}dt$*,* needed for such performance. The centre of mass energy equals the maximum energy available for particle production; $\sqrt{s}$ must at least equal the sum of the mass of the particles to be produced. The integrated luminosity quantifies here the amount of collisions needed to perform a given collider physics investigation, and will be given in units of inverse attobarn and inverse femtobarn, ab^{-1} and fb^{-1} (a process with a cross-section of 1 fb is expected once in data amounting to 1 fb^{-1}).

The following paragraphs, based on literature survey, illustrate some of the Standard Model Higgs physics that can be performed at a future electron-positron collider. The literature on the subject is extensive, and the most important sources used here have been the reviews found in [6, 17] which focus on the energy range $\sqrt{s}$ = 200-1000 GeV and [18, 19] which focus on the Multi-TeV energy range. Ref. [20] discusses specifically the interplay between the LHC and the ILC, emphasising their complementarity.

Higgs production

A requirement for e^+e^- Higgs precision measurements is copious Higgs particle production. Dominant processes for Higgs production in e^+e^- colliders are Higgs-strahlung,

$e^+e^- \to Z^* \to Z^0H$; an s-channel process with cross-section $\sigma_s \propto 1/s$, and vector boson fusion, $e^+e^- \to W^*W^* \to \bar{\nu}_e\nu_e H$, and for large $\sqrt{s}$ also $e^+e^- \to Z^*Z^* \to e^+e^-H$; t-channel processes with cross-section $\sigma_t \propto \log(s/m_H^2)$ [6]. The Higgs-strahlung and WW-fusion cross-sections are approximately equal at $\sqrt{s} = 500$ GeV, and fusion dominates at higher energy [6]. Figure 2.2(a) shows the Feynman diagram for the three processes, and Figure 2.2(b) shows the Higgs-production cross-section for different $\sqrt{s}$. For example would 1 ab^{-1} of data yield about 500'000 Higgs events at $\sqrt{s} = 3$ TeV and about 100'000 events at $\sqrt{s} = 500$ GeV, assuming a light Higgs.

Higgs Yukawa and gauge boson couplings

In the Standard Model, the Higgs mechanism is responsible for all fundamental particle masses, and a clear prediction, following from Eq. (2.6), is that each fermion couples to the Higgs field proportionally to their mass

$$\frac{m_{f_1}}{m_{f_2}} = \frac{g_{Hf_1f_1}}{g_{Hf_2f_2}}.$$

Measurements of the coupling strengths g_{Hff} must be checked for quarks and leptons. For charged leptons the relatively small muon Yukawa coupling, $g_{H\mu\mu}$, is the most challenging to measure. However, according to [19] this coupling can be measured with an accuracy of up to about 4% assuming an $\sqrt{s} = 3$ TeV and an integrated luminosity of 3 ab^{-1}, for a Higgs mass around 120 GeV. Furthermore, the ratio $g_{H\mu\mu}/g_{H\tau\tau}$ can be verified to within 5-8%, thus verifying the lepton coupling universality to good pre-

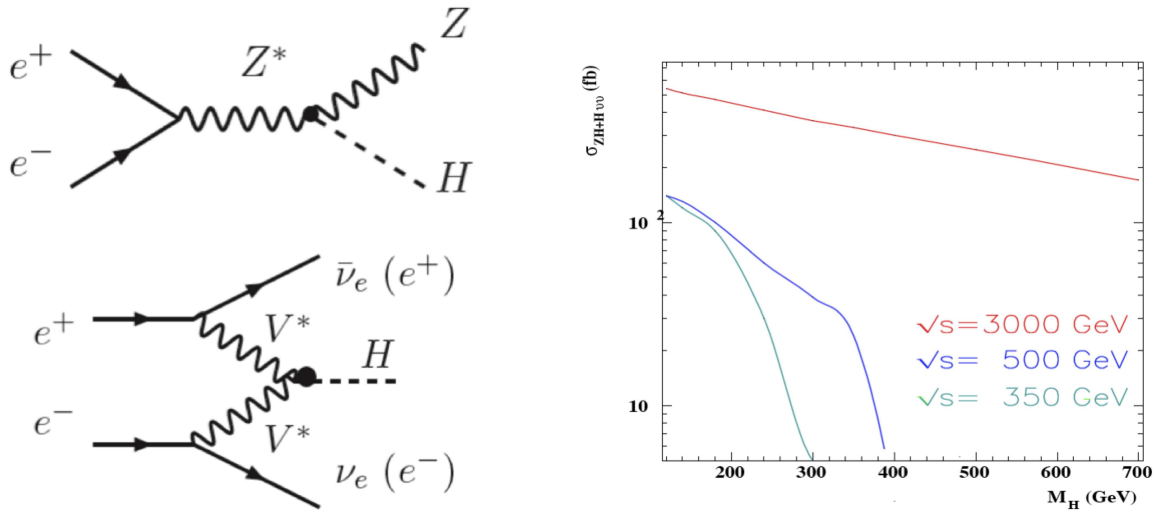

(a) Higgs production processes

(b) Higgs production cross-sections

Figure 2.2: Higgs production in an e^+e^- collider. (a) The dominant production processes are Higgs-strahlung and vector boson fusion. Picture courtesy of ILC [6]. (b) Higgs production cross-section in an e^+e^- collider for different $\sqrt{s}$. Picture courtesy of the CLIC study [18].

cision. In comparison, the $g_{H\mu\mu}$ measurement is considered very difficult both at the LHC and at a sub-TeV e^+e^- collider. Measurements of the Yukawa quark couplings for the lightest quarks are also considered very difficult, even at high luminosity Multi-TeV colliders. In contrast, the Higgs coupling to the massive gauge bosons, g_{HZZ} and g_{HWW}, can be measured relatively easily, independently of the Higgs decay channel as seen from Figure 2.2(a). According to [6], an accuracy of less than 3% can be achieved assuming a $\sqrt{s} = 500$ GeV and an integrated luminosity of 500 fb^{-1} (m_H= 120 GeV assumed for the g_{HWW} estimate).

Higgs spin

The Higgs boson as predicted by the Standard Model is a spin-0 scalar particle; the only scalar particle among the Standard Model fundamental particles. It is therefore of high importance to measure the spin of Higgs boson candidates. An e^+e^--collider can with relative ease perform Higgs spin measurements. For example, [21] indicates that with an energy scan in the $\sqrt{s} = 200$ GeV to $\sqrt{s} = 250$ GeV range, a spin-0 scenario can be distinguished from spin-1 and spin-2 scenarios for an integrated luminosity of only 20 fb^{-1}, based on the spin-dependence of the cross-section $e^+e^- \to ZH \to l^+l^-+$ 2 jets. This measurement is illustrated in Figure 2.3(a), reproduced from [21].

Probing the Higgs potential

The Standard Model predicts a Higgs potential of the form of Eq. (2.4), where the trilinear Higgs self-coupling constant, $g_{HHH} \propto v\lambda$, contains the same parameters as the Higgs mass, Eq. (2.5). A measurement of the trilinear coupling g_{HHH} will therefore provide an independent estimate of the λ parameter with respect to the value deduced from Higgs mass measurements, and will thus provide a direct verification of the form of the Higgs potential. This measurement is therefore considered highly important to fully establish the electro-weak symmetry breaking mechanism. However, triple-Higgs processes have several orders of magnitude lower cross-section than the processes in Figure 2.2(a), rendering the measurement challenging. For $m_H = 120$ GeV, [18] estimates an accuracy of about 8% for the g_{HHH} measurement, assuming $\sqrt{s} = 3$ TeV and an integrated luminosity of 5 ab^{-1}. In comparison, Ref. [6] reports an estimated accuracy of 22% for $\sqrt{s} = 500$ GeV, assuming 1 ab^{-1}. In contrast, measurement of the Higgs self-coupling is considered very difficult at the LHC at the predicted luminosity values, according to e.g. [6]. This measurement is illustrated in Figure 2.3(b), showing how precision measurements of the Higgs trilinear coupling can be used to constrain the possible scenarios for the Higgs scalar potential.

Other physics

The previous examples, related to the Standard Model Higgs sector, illustrate the type of precision physics that could be performed with a linear collider. Refs. [6, 17–19] present

a wealth of other scenarios including potential to complete an eventual super-symmetric particle spectrum and probing extra space-time dimensions. In many scenarios only a Multi-TeV collision centre of mass energy yield the full physics potential. Investigations with $\sqrt{s}$ in the Multi-TeV range often need to be accompanied by integrated luminosity of order ab^{-1} (due, in part, to the $1/s$ cross-section dependence of s-channel processes). Finally, it should be noted that as the required integrated luminosity for a physics investigation depends on the process, LHC results should not only point to the energy scale for a future lepton collider, but also help indicate the luminosity requirements.

2.3 Characteristics of a future lepton collider

In this section we will study how the physics requirements of TeV range collision energy and ab^{-1} range integrated luminosity will influence the design of a future lepton collider.

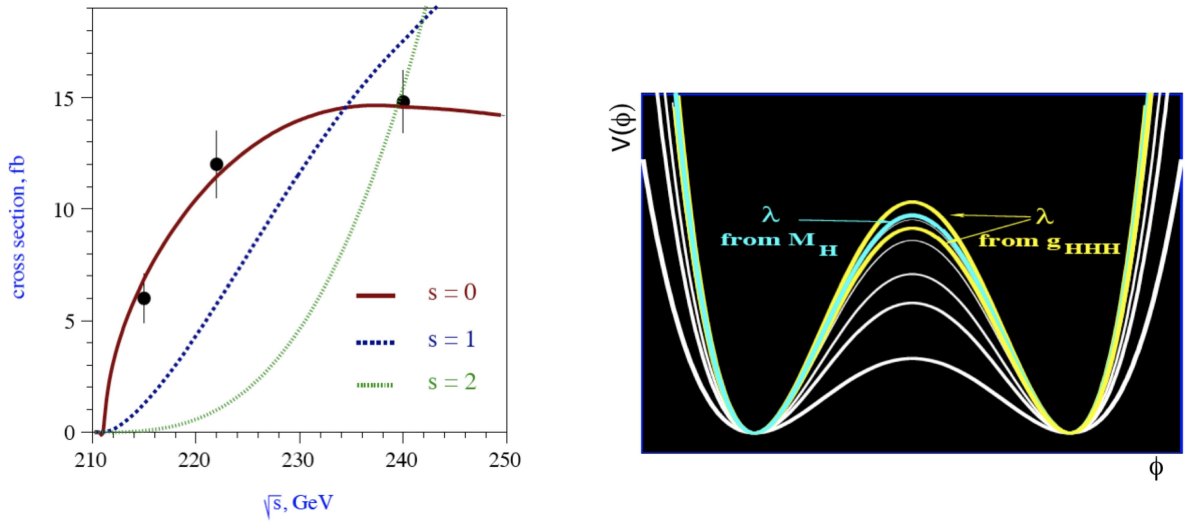

(a) Higgs spin measurement by energy scan

(b) Precision measurement of the Higgs potential

Figure 2.3: Examples of linear e^+e^- collider Higgs physics. (a) Measurements of the Higgs spin by the method of energy scan. Because the centre of mass energy, $\sqrt{s}$, will be adjustable in a linear e^+e^- collider, this measurement can be performed with relative ease in such a machine. Plot courtesy of M. T. Dova [21]. (b) Precision measurements of the Higgs trilinear coupling at a 3 TeV electron-positron collider, constraining the possible scenarios for the Higgs scalar potential. The scalar potential assumed by the Standard Model corresponds to the green line, while alternative scenarios correspond to the white lines. Plot courtesy of M. Battaglia.

2.3.1 From rings to linear colliders

The highest energy lepton collider to date was the CERN LEP ring, with a peak collision energy of $\sqrt{s}_{\mathrm{LEP}} = 209$ GeV [22]. In LEP the peak collision energy was limited by the synchrotron radiation energy loss. Due to synchrotron radiation, a particle travelling in circular motion will, in the ultra-relativistic approximation, lose energy at an average rate of [23]

$$P = \frac{e^2 c}{6\pi\varepsilon_0} \frac{1}{(m_0 c^2)^4} \frac{E^4}{R^2}, \tag{2.7}$$

where e is the electron charge, c the speed of light, ε_0 the permittivity of free space, m_0 the particle rest mass, E the particle kinetic energy and R the radius of the circular motion. The corresponding energy loss per revolution is

$$\Delta U = \oint P dt = \frac{e^2}{3\varepsilon_0} \frac{1}{(m_0 c^2)^4} \frac{E^4}{R}. \tag{2.8}$$

At LEP peak energy, the particle energy loss per turn reached more than $\Delta U = 3$ GeV [22]. The radio-frequency accelerating system (rf) needs to replace the lost energy, and LEP needed several upgrades before achieving $\sqrt{s}_{\mathrm{LEP}} = 209$ GeV, including upgrade to superconducting rf with the accelerating gradient increasing gradually [22].

The implications of Eqs. (2.7) and (2.8) for future electron-positron colliders are best summarised in terms of cost. For ring colliders the major cost factors are the tunnel and magnets cost, scaling linearly with the ring radius, $C_{\mathrm{infra}} \propto R$, as well as the rf power cost, scaling according to Eq. (2.8), $C_{\mathrm{RF}} \propto E^4/R$. The total optimised cost, $C_{\mathrm{ring}} \sim C_{\mathrm{infra}} + C_{\mathrm{RF}}$, is found for a given energy by requiring

$$\frac{\partial C_{\mathrm{ring}}}{\partial R} = \frac{\partial}{\partial R}(R + \frac{E^4}{R}) = 0 \Rightarrow R \propto E^2,$$

implying that cost scales for ring colliders as

$$C_{\mathrm{ring}} \propto E^2. \tag{2.9}$$

As example, [24] discusses an electron-positron collider in a ring of 233 km circumference. Assuming a synchrotron radiation loss of 100 MW, [24] concludes that the collision energy is limited to about $\sqrt{s} = 370$ GeV, if luminosity of at least $\mathcal{L} = 1 \times 10^{34}$ cm^{-2}s^{-1} is required.

On the other hand, if the acceleration is done linearly the synchrotron radiation loss is negligible with respect to the energy gain due to acceleration [23]. For a given linac accelerating gradient, the energy reach will to first order be proportional to the linac length and cost

$$C_{\mathrm{linear}} \propto E. \tag{2.10}$$

For TeV-scale energies, the cost scaling factors point towards linear machines for a future electron-positron collider, and the bulk of the world-wide R&D effort for future lepton colliders has been in this direction, e.g. [6, 7, 17, 25]. A linear collider, however, has two disadvantages with respect to a ring collider that needs to be addressed:

1. In a linear collider each accelerating element can be used only once, while in a ring the accelerating elements provide fresh voltage every turn.
2. In a linear collider the particle bunches must be dumped after collision, while in a ring the bunches can collide every turn until they are exhausted.

The first point makes it challenging to reach very high energies, the second point makes it challenging to reach very high luminosity; we will now investigate these two issues further.

It should here be noted that due to the factor $1/(m_0c^2)^4$ in Eq. (2.8), the synchrotron radiation loss in ring colliders can be strongly suppressed by colliding heavier particles than electrons. In principle TeV lepton collisions can therefore also be achieved by colliding muons in a ring, and on-going studies are investigating this possibility [26].

2.3.2 Accelerating gradient constraints in a linear collider

Each structure or cavity will accelerate particles only once. For a given $\sqrt{s}$, the accelerating gradient, G, will thus dictate the collider length.

Electron accelerating structures have been routinely operated at gradients of up to a few tens of MV/m. For example, the structure used for the Stanford Linear Collider (SLC) operated at G=17 MV/m [27]. If we want colliding beams with $\sqrt{s} = 1.0$ TeV, and assume two linear accelerators (linacs) where a fill factor F=75% of the total length is filled with SLC-type structures, the length of the linacs would need to be

$$L_{\text{linacs}} = \frac{\sqrt{s}}{eGF} = 78 \text{ km}.$$

Clearly, it is of interest to push the gradient to higher values in order to reach reasonable linac lengths for TeV-scale linear colliders. During the last decades there have been two lines of development for high gradient electron linacs; superconducting cavities and room-temperature structures.

Superconducting rf cavities

Superconducting rf cavities (SC cavities) made from Niobium are now in service in several projects world wide. The main advantage of SC cavities are very low wall losses, which for linear colliders implies several distinct advantages. As will be discussed further on, power consumption is a key parameter in linear collider design. SC cavities allow for standing-wave operation, which again allows for relatively long beam pulses without excessive power loss. Furthermore, the shape, size and operating frequency of the cavities can be chosen without worrying about increased wall power loss.

The critical magnetic field for superconductivity, however, limits the gradient in SC cavities to about 50 MV/m [28]. The TESLA collaboration [17], started in 1992, performed extensive research to improve gradient and cost per MeV of superconducting rf

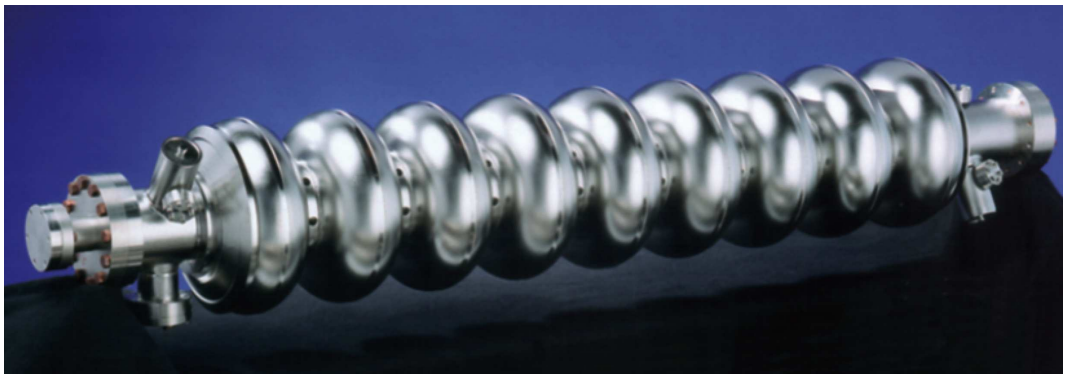

Figure 2.4: International Linear Collider TESLA type superconducting cavity. The 1.3 GHz cavity consists of nine coupled cells, made from Niobium. Current research efforts aims at reaching gradient of 35 MV/m with a production yield of 50%. Picture courtesy of ILC [6].

cavities. Superconducting technology was adopted for the International Linear Collider study [6] following the International Technology Recommendation Panel (ITRP) decision in 2004 [29]. The ILC target is an average operational gradient of 31.5 MV/m [6] in the TESLA type 9-cell cavities, shown in Figure 2.4. Current research efforts [30] include demonstrating production of 9-cell cavities where at least 50% of the cavities achieve a gradient of 35 MV/m at Q-factors of at least 10^{10} (referred to as a *yield* of 50%), as well as improving the understanding of the observed limitations to the gradient [30].

Normal conducting rf structures

Normal conducting structures have no defined hard limitation on the accelerating gradient in the structure. However, structures filled with an intense rf field corresponding to a high accelerating gradient, experience several physical phenomena shown to limit the gradient. Electron field emission becomes significant at high surface fields, and is believed to be the cause of a runaway condition in the cavity leading to *breakdown* of the rf field [31]. Rf breakdown leads to change of the accelerating field in the structure, and the breakdown rate must therefore be contained to very small values. In addition rf breakdown may, in the worst case, damage the structure walls thus decreasing its efficiency. The exact mechanisms leading to rf breakdown in a structure are not fully understood, and therefore the limits on the surface fields due to breakdown are not fully clear.

Another limiting phenomenon is the surface heating due to the rf magnetic fields and corresponding induced wall currents [31]. The surface heating, and correspondingly the peak surface magnetic fields, must be kept within acceptable limits.

Within the NLC/GLC studies [25], research in high gradient normal conducting rf structures were performed until the ITRP decision [29]. For NLC/GLC, the design criterion of unloaded gradient of 65 MV/m, at breakdown rate below 0.1 per hour for a 400 ns pulse, was successfully demonstrated [32]. The CLIC study as well has adopted normal

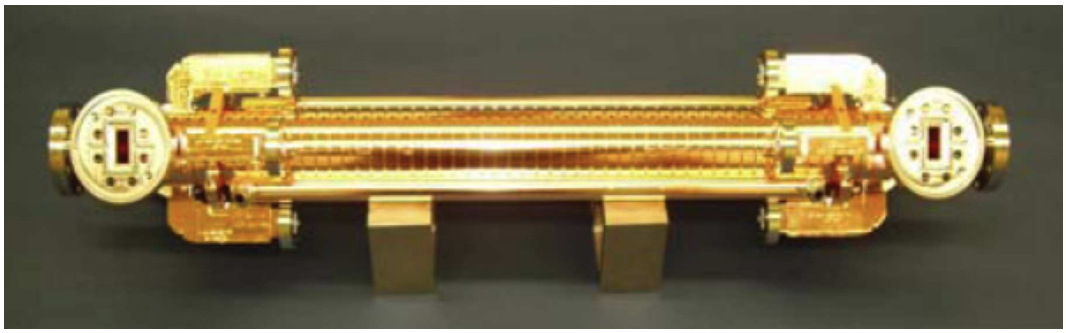

Figure 2.5: The 11.4 GHz NLC/GLC type normal conducting structure. The design criterion of 65 MV/m gradient and breakdown rate below 0.1 per hour for a 400 ns pulse, was successfully demonstrated for this structure. Picture courtesy of S. Döbert [32].

conducting structures, profiting from the advantages of the two-beam scheme, explained in Chapter 3.

2.3.3 Luminosity constraints in a linear collider

The luminosity of a particle collider, $\mathcal{L}$, is defined as the proportional constant relating the rate of events for a given process, R, to the process cross-section, σ,

$$R = \mathcal{L}\sigma$$

and is normally given in units of $\mathrm{cm}^{-2}\mathrm{s}^{-1}$. The integrated luminosity requirements originating from the particle physics studies [6, 17–19] relate to the collider luminosity as

$$\int \mathcal{L}dt \ [\mathrm{fb}^{-1}] = \mathcal{L} \ [\mathrm{cm}^{-2}\mathrm{s}^{-1}] \times T \ [\mathrm{s}] \times 10^{-39},$$

where $\mathcal{L}$ is the luminosity during the time period T. For example, if one would want to collect one ab^{-1} of data after operating at peak luminosity during one "Snowmass year", corresponding to 1×10^7 s, a peak collider luminosity of $\mathcal{L} = 1 \times 10^{35}$ $\mathrm{cm}^{-2}s^{-1}$ would be needed. In comparison, the Large Hadron Collider has a luminosity goal of $\mathcal{L}_{\mathrm{LHC}} \approx 1 \times 10^{34}$ $\mathrm{cm}^{-2}\mathrm{s}^{-1}$, profiting, however, from a a very high average bunch crossing rate (32 MHz) and a high charge per bunch (100 billions of protons) [33].

In general, collider luminosity for bunched beams can be expressed as [23]

$$\mathcal{L} = f_{\mathrm{bunch}} \frac{N^2}{4\pi\sigma_x\sigma_y}, \tag{2.11}$$

where N is the number of particles in each bunch, f_{bunch} the average bunch crossing rate and σ_x and σ_y the transverse beam sizes. Gaussian transverse beam distributions are assumed in Eq. (2.11). The bunch crossing rate for linear colliders is equal to the pulse repetition rate, f_{rep}, times the number of bunches fired per pulse, N_b, $f_{\mathrm{bunch}} = f_{\mathrm{rep}}N_b$.

In linear colliders the beams are after collision dumped in dedicated post-collision lines. At the repetition rate, two beam pulses of total energy $E_{\text{beam}} = NN_bE_{\text{CMS}}$ must therefore be produced. For linear collider design considerations it is fruitful to re-express Eq. (2.11) in terms of the average power of the colliding beams (*beam power)*, $P_{\text{beam}} \equiv E_{\text{beam}}f_{\text{rep}}$. Furthermore, we introduce the total power efficiency η from the total wall-plug AC power, P_{machine}, to the beam, $P_{\text{beam}} = \eta P_{\text{machine}}$. The luminosity in linear colliders is furthermore increased by a factor denoted H_D, usually in the range 1-2 depending on the collider parameters, due to extra beam-beam focusing effects at the interaction point. Eq. (2.11) can then be re-written as

$$\frac{\mathcal{L}}{P_{\text{machine}}} = \frac{N\eta}{4\pi\sigma_x\sigma_y E_{\text{CMS}}} H_D. \tag{2.12}$$

The *ratio of luminosity to total power* is one of the key figures of merit for linear collider design. The parameters, however, are chosen very differently than for a ring collider. For example, linear collider bunch collision with beam parameters corresponding to LHC nominal operation [33] would require a beam power of $P_{\text{beam}} \approx 32$ MHz $\times$ 1 $\times$ 10^{11} $\times$ 1 TeV $\approx$ 1 TW - a prohibitively high power consumption. If we, on the other hand, require the same luminosity as LHC with more moderate beam power of say P_{beam} = 10 MW, the remaining factors in Eq. (2.12) must be increased by a total factor of $N\eta/\sigma_x\sigma_y \sim 10^5$ to compensate.

To achieve this increase, linear colliders require very small transverse beam sizes at the interaction point. However, when very small bunches come close together, the electromagnetic interaction between the bunches becomes intense. The corresponding bending of the particle trajectories leads to the emission of synchrotron radiation, in this context named *beamstrahlung*. The beamstrahlung leads to a luminosity *spectrum*, where the total luminosity is produced over a range of energies, $\mathcal{L} = \mathcal{L}(E)$, and the quantity to be maximised now becomes luminosity in the high-energy range of the spectrum [34] (for some physics processes the total luminosity will still be of interest, though [18]). This leads to constraints on the ratio N/σ_x; if σ_x is reduced, the luminosity is increased, but at the same time the spectrum degrades more due to beamstrahlung. [34] concludes that for luminosity optimisation it is required that

$$N/\sigma_x \propto 1/\sqrt{\sigma_z},$$

where σ_z is the bunch length at the collision point. Also the beam-delivery system and the damping rings (see next section) constraints σ_x from below [34]. Because of the limitations on σ_x, the vertical beam size has to be pushed to very small values, yielding a *flat* beam, $\sigma_x \gg \sigma_y$. The transverse beam size, in a given plane, is in general given by [23]

$$\sigma = \sqrt{\epsilon\beta},$$

where the *beam emittance*, ϵ, is a measure of the transverse phase-space, and the *beta function,* β, a measure of how well focused the beam is.

The very simplified discussion in this section indicates thus that in order to maximise $\mathcal{L}/P_{\text{machine}}$, Eq. (2.12), both ϵ_y and β_y must take on very small values, and the machine

efficiency η must be very good. We will discuss luminosity optimisation and parameters values further when we in the next chapter present the CLIC machine, where indeed η, ϵ_y and β_y are highly optimised. Before discussing the specific CLIC design choices, we conclude the chapter by summarising the basic functionality of a linear collider.

2.3.4 Functionality of a linear collider

In brief terms, the functionality of a basic linear collider, illustrated in Figure 1.4, is to generate pulses of opposite charge, accelerate them to the desired energy at very high accelerating gradients, and steer them into collision at the interaction point. We have seen that the transverse beam sizes, especially the vertical, must be very small at collision to ensure sufficient collision luminosity. This is ensured first by exploitation of synchrotron radiation damping [23] in dedicated damping rings. When electron or positron beams circulate in rings, synchrotron radiation damps transverse oscillations, and the transverse beam emittances can therefore be shrunk to very small values. The transverse emittances must furthermore be preserved very well from the damping rings to the interaction point, including in the long main linacs. Potential sources of emittance growth [35] include machine imperfections, radiation effects, wake fields, electron cloud [36] and ion effects [37]. The very strong focusing of the beam into the interaction point is performed by the final focus, which primary purpose is to act as an optical telescope turned around. Because of the non-zero beam energy spread, however, the final focus lattice is more complex, including non-linear magnets to correct for chromatic effects. A future linear collider must push the limits of today's technology for all parts of the collider, in order to achieve the requirements set by particle physics.

3. Two-Beam Acceleration and CLIC

In this chapter we first discuss the major design choices of CLIC, then the CLIC two-beam scheme is presented, with emphasis on the power efficiency. The advantages and disadvantages of the design are briefly discussed, and finally the future steps for CLIC are outlined.

3.1 Design choices for a Multi-TeV collider

The CLIC baseline design is for a centre of mass energy of $\sqrt{s} = 3$ TeV [38]. The luminosity target, based on physics analyses reported in e.g. [18, 19], is a luminosity within 1% of the centre of mass energy of $\mathcal{L}_{1\%} = 2.0 \times 10^{34}$ cm^{-2}s^{-1} corresponding to a total luminosity of $\mathcal{L} = 6.0 \times 10^{34}$ cm^{-2}s^{-1} [38]. We will see how these requirements have lead CLIC to adopt a two-beam acceleration scheme.

3.1.1 Reaching high accelerating gradient

Today's gradient limit for superconducting cavities would imply a 150 km long machine for a $\sqrt{s} = 3$ TeV collider, and is not considered a viable option. The CLIC accelerating technology of choice is therefore normal conducting structures.

Empirical scaling laws based on decades of accelerating structure design experience have shown that the breakdown limit increases with the resonant frequency of the structures, as indicated by e.g. the Kilpatrick rule-of-thumb [39]. It has been found [38], however, that the achievable gradient dependence on frequency is less clear for high frequencies, and in the frequency range between 12 GHz and 30 GHz negligible correlation between achievable gradient and frequency has been found. Previous versions of the CLIC structures operated at 30 GHz fundamental mode frequency [40]. During the recent few years, however, a new CLIC accelerating structure and main linac parameter set has been derived using a novel approach based on a methodical optimisation procedure, described in the following.

The structures must adhere to a breakdown rate in the order of 10^{-7} breakdowns per

pulse per structure, in order to limit luminosity loss due to rf breakdown to about 1% [41] (it is assumed that if breakdown occurs during a pulse, the pulse is lost for luminosity purposes). Accelerating structure design parameters affect the rf properties of the structure but also the beam dynamics of the main linac, and thus ultimately the collider luminosity. The complex interplay between the parameters has lead to an integrated CLIC main linac optimisation procedure [42, 43], taking into account a number of rf constraints enforcing the breakdown rate (limitations on surface field, pulsed surface heating, power and pulse length) as well as beam dynamics constraints (limitations on emittance growth and beam-beam effects). The optimisation criterion takes into consideration the ratio of collider luminosity to input main linac power, as well as the total collider cost, including investment and exploitation.

The optimisation procedure resulted in a choice of 12 GHz structures with an accelerating gradient of 100 MV/m (including the effect of beam loading) [38]. It is important to note that the gradient is not an input to the optimisation, but an outcome, yielding low cost and a good luminosity to power ratio. The frequency of 12 GHz was close to the optimum; moreover, 12 GHz X-band frequency was chosen also due to closeness to the NLC frequency of 11.4 GHz, allowing to profit from NLC experience (the frequency must be an integer multiple of 3 GHz in order to test structures with beam in CTF3). The parameter optimisation resulted as well in a very short CLIC main beam pulse of 156 ns [38].

Compared to the NLC structures with unloaded gradient of 65 MV/m [32], the CLIC structures with loaded gradient of 100 MV/m profit from reduced aperture to rf wavelength ratio (lower surface electric field for the same gradient) and the possibility to allow for very short main beam pulses, due to the availability of highly compressed rf power due to the two-beam scheme (cf. Section 3.1.3). The CLIC structures profit as well from improved damping due to damping wave-guides for each slot, with dielectric damping material in the wave-guides in order to sufficiently damp higher-order wake field modes. The improved damping allows for relatively shorter bunch spacing and larger average pulse intensity during the short pulses, resulting in good rf to beam efficiency.

The CLIC 12 GHz baseline structure

By 2008 a baseline design for the CLIC 12 GHz structure was established [44]. The CLIC baseline is a travelling-wave structure with linearly varying iris radius and wave-guide damping. An earlier version named T18, similar to the baseline design, has been tested successfully at an unloaded gradient above 100 MV/m, with a break down rate in the range of 10^{-7} at the CLIC pulse length [45]. The T18 is depicted in Figure 3.1(a). This structure, however, is not equipped with damping wave-guides. For illustration a disc with damping wave-guides is shown in Figure 3.1(b). To demonstrate the feasibility of the CLIC structure, high-gradient tests of structures with damping wave-guides are required, such tests are foreseen for the second half of 2009.

The gradient of 100 MV/m, combined with a fill factor of 79% and 10% energy margin

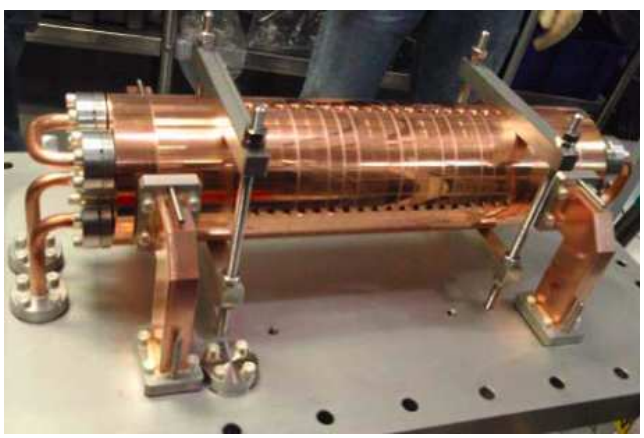

(a) The T18 structure

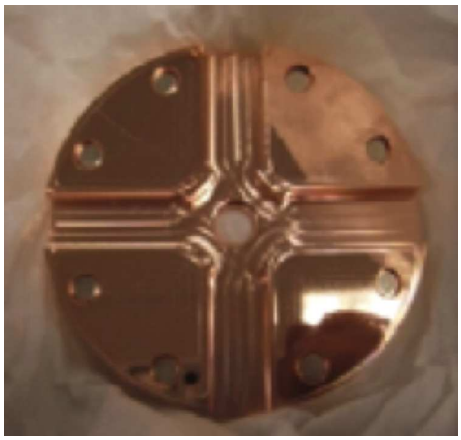

(b) Disc equipped with wave-guides

Figure 3.1: (a) The CLIC 12 GHz T18 accelerating structure mounted for testing. (b) A disc equipped with damping wave-guides. Pictures courtesy of the CLIC study [45].

needed for robust operation [38], implies a CLIC main linac length of 21 km, considered to be within the limit of feasibility.

3.1.2 Reaching high luminosity

As discussed in Chapter 2, a good wall-plug to main beam power efficiency η is desirable and a very small vertical beam size σ_y is necessary in order to reach the CLIC design luminosity of several $10^{34}\text{cm}^{-2}\text{s}^{-1}$.

Vertical beam size

In the CLIC baseline design an ultra-small vertical beam size of

$$\sigma_y = \sqrt{\epsilon_y^* \beta_y^*} \approx 1 \text{ nm}$$

is foreseen [38] at the interaction point (IP), corresponding to the width of a water molecule. In order to achieve this, both the emittance at the IP, ϵ_y^*, and the beta function at the IP, β_y^*, must be highly optimised.

The target output normalised vertical emittance [23] for the CLIC damping rings is $\epsilon_{\text{Ny}} \leq 5$ nm. The target value is smaller than what has been obtained in any existing storage or damping ring, but deemed feasible assuming adequate machine alignment precision [46], and the estimated performance is reported to $\epsilon_{\text{Ny}} = 4$ nm [47]. In CLIC the damping cannot be performed with a single ring, because of the high repetition rate of 50 Hz and too large incoming transverse emittances, and two damping rings per colliding beam are therefore required. CLIC requires a maximum emittance growth factor of four from the exit of the damping rings, during the transport to the main

linac, through the 21 km main linac and to the end of the 2.8 km long beam-delivery system.

The CLIC final focus lattice of the beam-delivery system must generate a focal point at the IP corresponding to a beta function of $\beta_y^* = 0.07$ mm; six orders of magnitude lower than the main linac β. A particular challenge related to the small σ_y is the need for extremely stable quadrupole final doublet magnets [48]. The design and optimisation of the CLIC beam-delivery system are described in e.g. [49].

Wall-plug to main beam efficiency

In simple terms, two major sources of efficiency loss for a pulsed operation high-gradient rf linac are

1. Limited efficiency from the accelerating structure input power to the beam power, η_{rf}
2. Limited efficiency in the klystrons and the klystron modulators, $\eta_{\mathrm{klystron}} = \eta_{\mathrm{modulator}} \times \eta_{\mathrm{tube}}$

As example, the International Linear Collider L-band klystrons have an efficiency of $\eta_{\mathrm{klystron,ILC}} = 0.83 \times 0.65 = 0.54$ [6]. Furthermore, the design choice of superconducting cavities allows for a good $\eta_{\mathrm{rf,ILC}}$ (still limited to about 2/3, due to long fill-time). However, the power consumption of the cryogenic systems is significant, and the total collider wall-plug to main beam efficiency for ILC is estimated to $\eta_{\mathrm{ILC}} = 9\%$ [6]. For a viable CLIC design it is of importance that the efficiency of the CLIC machine is of the same order.

By adopting X-band frequency for the CLIC main linacs, the challenge of efficient X-band rf power production in short pulses, must be addressed. Klystron efficiency tends to decrease with frequency, and equipping 42 km of underground main linacs with high-power X-band klystrons is considered to be very costly and maintenance intensive since a very large number of klystrons would be needed. Furthermore, due to the short CLIC pulse length of 156 ns flat-top, the rf klystron pulse would need to be highly compressed. Techniques for rf pulse compression are available, but at the cost of large efficiency loss [50].

Instead of using X-band klystrons, CLIC has adopted a novel approach for X-band rf power generation: *two-beam acceleration*.

3.1.3 Two-beam acceleration

The concept of two-beam acceleration was proposed in 1982 [51] and adopted for the CLIC scheme a few years later [8]. Ref. [52] describes in detail the history and evolution of the two-beam scheme in CLIC; we will here highlight the main features of today's implementation, with focus on the power efficiency.

The CLIC two-beam scheme consists of producing rf power for the main beams to be

collided, by extracting energy from electron drive beams running in parallel with the main beams. The drive beams will be of much higher current (beam intensity) and much lower energy than the main beams, and can therefore be generated by a relatively short drive beam accelerator. The principle is analogous to a *transformer*; the low voltage seen by the high current drive beam is converted into high voltage seen by the low current main beam.

The CLIC power extraction and transfer principle is illustrated schematically in Figure 1.5. Figure 3.2 illustrates the relevant components of a CLIC 12 GHz two-beam module. The drive beam energy is extracted by sending the beam through special copper power extraction and transfer structures (PETS) where part of the electron beam field is captured by the geometry of the structure. The captured field will resonate at the fundamental mode resonant frequency of the structure, the same frequency as for the fundamental mode of the accelerating structure (12 GHz). The rf field will travel out of the structure with a high group velocity. At the PETS end the field will be coupled out, transferred via waveguides to the accelerating structures (located no more than about a meter away from the PETS, see Figure 3.2) and coupled in, exactly as if the power had been generated by a klystron. Both the drive beam and the main beam must be monitored to a high degree of precision using beam position monitors, and kept stable and focused with the help of magnetic lenses (quadrupole magnets).

There are a number of considerations on how to best form a drive beam for a two-beam accelerator scheme. For example, it is not trivial to produce very high current beams, furthermore, the amount of energy extracted must be as high as possible, while at the same time keeping the drive beam stable. The overall efficiency from wall-plug power to main beam power must be optimized. We will in the next section present the design choices adopted for the CLIC two-beam scheme.

3.2 Overview of the CLIC two-beam scheme

Figure 3.3 presents a functional sketch of the entire CLIC 12 GHz machine. In the bottom half of the picture we recognise the sub-systems corresponding to a generic linear collider, sketched in Figure 1.4. The top half of Figure 3.3 illustrates the drive beam complex which will act as the rf power source for the main beams.

The drive beam parameter choices are the result of a continuous optimisation effort, on-going since the start of the CLIC project, and we will not attempt here to justify all choices. A detailed description of the drive beam complex, however with outdated parameters, can be found in [52]. We will here explain the main CLIC power efficiency factors, and cite values from from the last major CLIC parameter revision [38]. It should be noted that because the CLIC 12 GHz design is not finalised, some of the efficiency numbers quoted, and therefore also the overall efficiency, should be considered as estimates subject to change.

The power production requirements originate from the main beam and main linac pa-

rameters (which again originate from the collision energy and luminosity required by particle physics). We therefore start the discussion of the drive beam complex with the sub-system closest to the main linac; the *decelerator*, in which the actual energy extraction and rf power production take place.

3.2.1 Drive beam deceleration

As discussed in [52], using a single drive beam pulse (continuously decelerated along the linac length) to provide power to each main beam pulse, would require short pulses of very high energy and current. Such pulses would be very challenging to create, accelerate and manipulate. Instead, for CLIC, $N_S = 24$ decelerator sectors per linac are envisaged, as shown in Figure 3.3. In each sector a different drive beam train is decelerated from the initial energy to a minimum value. The length of each drive beam train must correspond

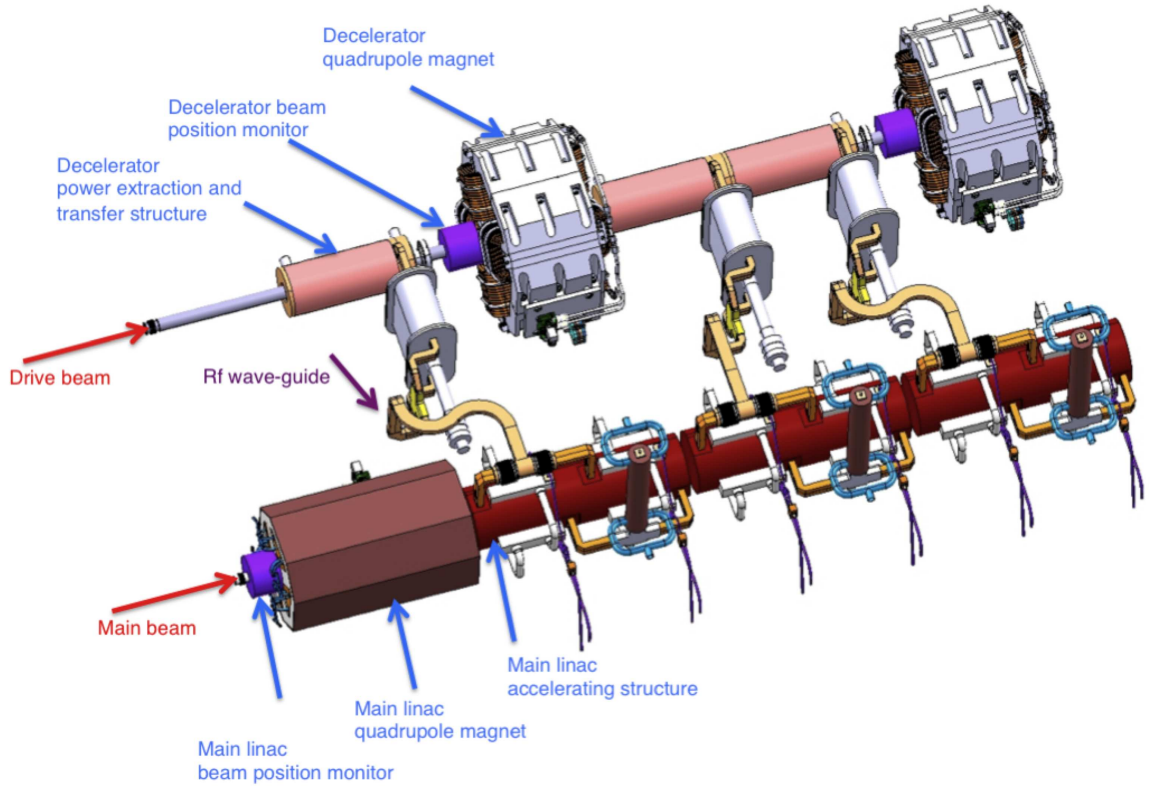

Figure 3.2: View of a CLIC 12 GHz two-beam module highlighting the CLIC power extraction and transfer principle. One module contains up to four power extraction and transfer structures (PETS), where each PETS feeds two accelerating structures (here three PETS and six accelerating structures are shown). Rf waveguides transfer the rf power generated from the PETS into the accelerating structures. Quadrupole magnets are used for strong focusing of both beams. Picture courtesy of the CLIC study.

to the pulse length of the main beam pulse plus the accelerating structure fill time and rise time [38], yielding a train length of $t_{\text{train}} = 243$ ns. The drive beam energy before deceleration, E_0, is upwards limited by synchrotron radiation effects; for CLIC 12 GHz, E_0 is set to 2.4 GeV.

The minimum energy of particles in the drive beam after deceleration, E_{min}, depends on the number of and the characteristics of the PETS, and can be adjusted by changing the decelerator design. The maximum energy extracted from the drive beam particles after deceleration is denoted

$$\eta_{\text{extr}} \equiv \frac{E_0 - E_{\text{min}}}{E_0}. \tag{3.1}$$

In [38] the extraction efficiency is set to $\eta_{\text{extr}} = 90\%$ as a compromise between efficiency and beam stability, yielding a minimum drive beam energy of $E_{\text{min}} = E_0(1 - \eta_{\text{extr}}) = 0.24$ GeV.

The drive beam current must provide enough power to fulfil the main beam power

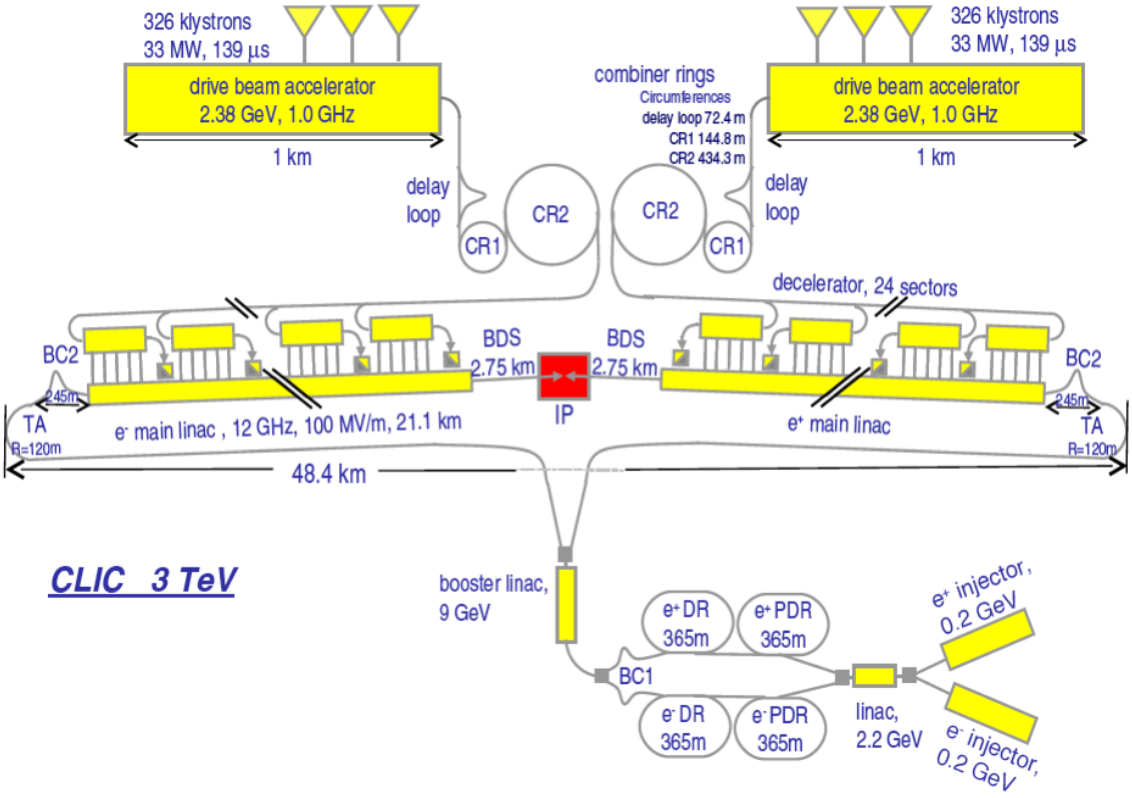

Figure 3.3: Functional sketch of the Compact Linear Collider, CLIC. The lower half of the figure, including the main linacs, incorporates the parts needed in a conventional linear collider (cf. Figure 1.4). The upper half shows the CLIC drive beam complex, where the drive beam is generated, as well as the decelerators where a large amount of energy is extracted from the drive beams and converted into rf power used to accelerated the main beams. The drawing is not to scale. Picture courtesy of the CLIC study [38].

requirement of $P_{\mathrm{MB}} = 14$ MW [38], after all efficiency factors from drive beam power to the main beam power have been taken into account. From the drive beam to the rf power produced in the PETS there is a total efficiency

$$\eta_{\mathrm{DB}} = \eta_{\mathrm{extr}} \times \eta_{\mathrm{dist}} \times \ \eta_{\Omega,\mathrm{PETS}} \times \eta_{\mathrm{ramp}} \times F(\lambda) = 0.77, \tag{3.2}$$

where $F(\lambda)$ is the charge distribution form factor, η_{dist} efficiency loss due to single-bunch effects, $\eta_{\Omega,\mathrm{PETS}}$ efficiency loss due to PETS ohmic losses and η_{ramp} efficiency loss due the drive beam charge ramp required for accelerating structure beam-loading compensation [53]. $F(\lambda)$, η_{dist} and $\eta_{\Omega,\mathrm{PETS}}$ will be discussed further in Chapter 4 and 5 of this thesis. The losses from the PETS rf output to the accelerating structure rf input are given by

$$\eta_{\mathrm{TR}} = 0.94$$

and finally, the efficiency from the input rf to the main beam is estimated to

$$\eta_{\mathrm{rf}} = 0.28.$$

To comply with the main beam power requirement the average drive beam power must be

$$P_{\mathrm{DB}} = \frac{P_{\mathrm{MB}}}{\eta_{\mathrm{DB}} \times \eta_{\mathrm{TR}} \times \eta_{\mathrm{rf}}} = 70 \text{ MW}.$$

To find the decelerator train average current we write

$$P_{\mathrm{DB}} = E_0/e \times f_{\mathrm{rep}} \times t_{\mathrm{train}} \times I_{\mathrm{dec}} \times N_S$$

yielding

$$I_{\mathrm{dec}} = \frac{70 \text{ MW}}{2.4 \text{ GeV}/e \times 50 \text{ Hz} \times 243 \text{ ns} \times 24} = 101 \text{ A}.$$

We note that even though the split of the decelerator into sectors reduces the current by a factor $N_S = 24$, the required drive beam current remains very large. The drive beam bunch frequency is defined to f_{bunch}= 12 GHz, corresponding to the fundamental mode of the power extraction and transfer structures.

To ensure uniform rf power production it is important that the drive beam is transported through the decelerator with very small beam losses. This issue will be studied further in Chapter 5.

3.2.2 Drive beam pulse compression by frequency multiplication

The very intense drive beam will be generated by *frequency multiplication,* where the bunches of a 0.5 GHz 4.2 ampere electron beam will be interleaved to yield a factor N_S = 24 increase in both frequency and average current. The rationale is that a 0.5 GHz 4.2 ampere beam is much more readily generated and accelerated by an electron linac than a 12 GHz 101 ampere beam.

The frequency multiplication will be performed using one *delay loop* and two *combiner rings*, as shown in Figure 3.4. The delay loop will combine incoming bunches spaced with 0.5 GHz by a factor two by the following scheme: the drive beam accelerator will have a frequency of 1 GHz and accelerate two drive beam half-train, where one half-train occupies every odd rf bucket and the other half-train every even rf bucket. This *phase-coding* is made feasible by a phase-switch in the sub-harmonic buncher in the injector [7]. After the drive beam linac, a 0.5 GHz rf-deflector will kick the first half of the train into the delay loop, while not affecting the second half. The delay loop length is such that the two half-pulse interleave, generating a train of 8.2 A and 1 GHz bunch frequency with half the initial train length.

The two combiner rings use rf deflectors in a similar manner to interleave upstream trains with trains already inside the rings [7]. Now the bunch frequency and the intensity increase as new trains are interleaved, while the train length remains the same. The first combiner ring increases the bunch frequency by a factor three and the second ring by a factor four. The net result is the 101 ampere 12 GHz trains required by the decelerator. The initial and final time structure of the drive beam train are shown in Figure 3.4.

The bunch trains will be transported in long transport lines with big beam pipe aper-

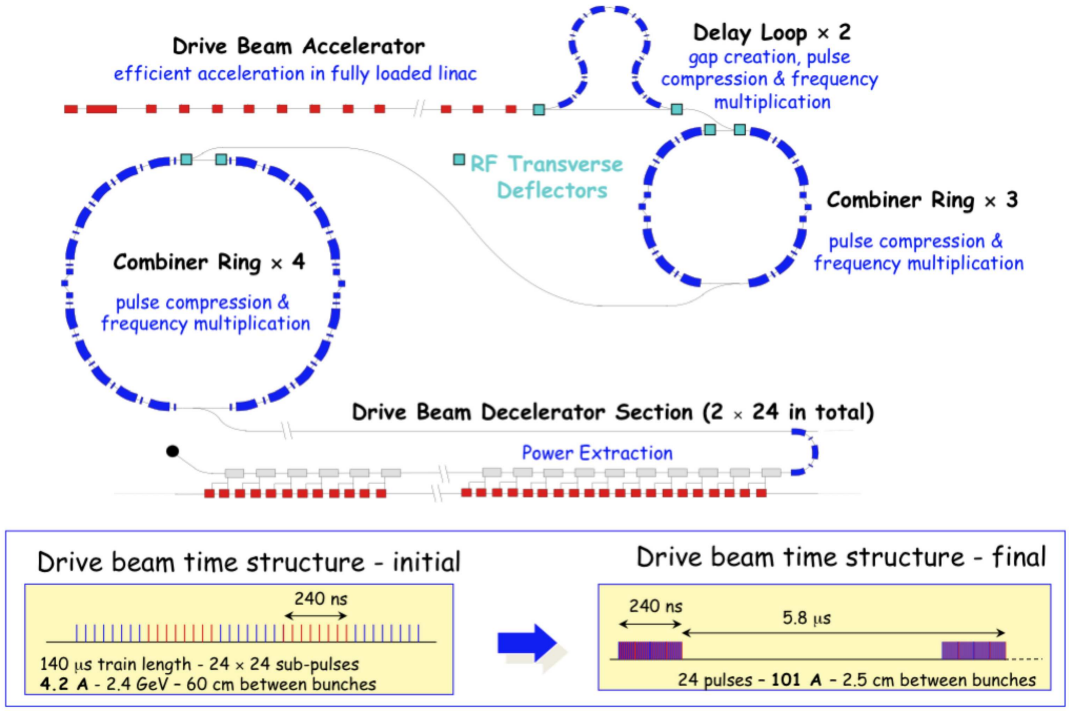

Figure 3.4: Functional sketch of the pulse compression and frequency multiplication for the CLIC drive beam (not to scale). The delay loop and the two combiner rings will increase the bunch frequency and the beam intensity of the beam from the linac by a total factor of $N_S = 24$. Picture courtesy of the CLIC study.

tures [54] and kicked into each decelerator sector after turn. To ensure uniform rf power production it is important that the pulse compression and transportation of the drive beam pulses are achieved with very small beam losses. The current estimate of the efficiency from the drive beam accelerator to the entrance of the decelerator is [38]

$$\eta_{\mathrm{PC}} = 1.$$

This efficiency figure, however, is subject to further studies, including precise estimates of energy loss due to synchrotron radiation and wake field effects. It is expected, however, that the efficiency η_{PC} will remain very good, and therefore not influence significantly the overall CLIC efficiency [55].

3.2.3 Drive beam acceleration

The 4.2 ampere 0.5 GHz drive beam will be generated by an electron linac operating at L-band frequency. In order to maximise the wall-plug to rf efficiency, the drive beam linac is designed so that the beam will extract all of the rf power coupled into the structure, except what is lost in the walls. Furthermore, a choice of short structures yields relatively small wall losses. This *fully loaded* operation with short structures is estimated to give a very high drive beam accelerator rf to beam power efficiency of [38]

$$\eta_{\mathrm{DB,rf}} = 0.93.$$

The klystron efficiency of the drive beam accelerator, from klystron modulator power input, to rf input to structure, is estimated to [38]

$$\eta_{\mathrm{klystron}} = 0.57,$$

a figure comparable to the ILC L-band efficiency of $\eta_{\mathrm{klystron,ILC}} = 0.54$ [6].

3.2.4 Overall CLIC power efficiency

We summarise the overall efficiency of the CLIC scheme, going from the start to the end of the power chain, using the efficiencies calculated in the previous sections. A more detailed calculation is presented in [38]. The power input to the drive beam klystron modulator is converted into drive beam accelerator rf with an efficiency of η_{klystron}. The drive beam rf-to-beam efficiency is $\eta_{\mathrm{DB,rf}}$. The pulse compression and transport to the decelerator are performed with an efficiency η_{PC}. The decelerator rf power extraction efficiency is given by η_{DB}. The losses in the transfer from the PETS output to the main linac structure input are given by η_{TR}. The main beam rf-to-beam efficiency is η_{rf}. The overall efficiency of the CLIC machine from the drive beam modulator power input to main beam is thus

$$\eta_{\mathrm{beam}} = \eta_{\mathrm{klystron}} \times \eta_{\mathrm{DB,rf}} \times \eta_{\mathrm{PC}} \times \eta_{\mathrm{DB}} \times \eta_{\mathrm{TR}} \times \eta_{\mathrm{rf}} = 10.7\%, \tag{3.3}$$

which for the main beam power requirement of $P_{\mathrm{MB}} = 14$ MW per beam implies that a power of

$$P_{\mathrm{beams}} = 2P_{\mathrm{MB}}/\eta_{\mathrm{beam}} = 263 \text{ MW}$$

is needed to produce the main beams.

To calculate the overall efficiency of the machine, power estimates of infrastructure and other subsystems must be taken into account, for CLIC estimated to $P_{\mathrm{infra}} = 129$ MW [38]. The estimation of the overall wall-plug power consumption for a CLIC 12 GHz machine is thus

$$P_{\mathrm{CLIC}} = P_{\mathrm{beams}} + P_{\mathrm{infra}} = 392 \text{ MW},$$

yielding an efficiency of the CLIC machine, from wall-plug to main beam power, of

$$\eta_{\mathrm{CLIC}} = \frac{2P_{\mathrm{MB}}}{P_{\mathrm{CLIC}}} = 7.2\%.$$

3.3 Advantages and disadvantages of CLIC

The design choices of the CLIC scheme, presented in this chapter, have a number of advantages, but also disadvantages. A natural design for comparison is that of the International Linear Collider, ILC [6]. First, because it is the only other linear collider study on-going, and second, because the main linac technologies adopted are diametrically different for the two machines; normal conducting drive beam fed X-band accelerating structures for CLIC, versus superconducting klystron fed L-band accelerating cavities for ILC. We will here do a brief point-by-point comparison of collider performance issues arising from the design differences. Ref. [29] presents a more detailed comparison between the super conducting and normal conducting technologies developed for TESLA/ILC and NLC/GLC respectively. It should be noted, however, that not all points in [29] are equally applicable to CLIC.

Collision energy and site length

ILC and CLIC are optimised for different collision energies. The ILC baseline design provides for $\sqrt{s} = 500$ GeV (31 km site length) with possibilities for an upgrade to $\sqrt{s} = 1$ TeV ($\sim$ 53 km site length), while the CLIC baseline design provides for $\sqrt{s} = 3$ TeV (48 km site length) with possibilities to start with a machine with $\sqrt{s} = 500$ GeV (13 km site length).

Power efficiency

Comparing the ILC overall efficiency of 9% [6] with the CLIC total efficiency of 7.2%, we see that although normal conducting main linac structures are used, the CLIC overall

efficiency is only marginally smaller. This can be explained by the estimated high efficiency of the drive beam acceleration, compression and deceleration, as well as optimised main linac rf to beam efficiency.

Frequency and cavity aperture

To reach the specified gradient, CLIC operates at X-band frequency (12 GHz), while ILC operates at L-band frequency (1.3 GHz). The lower operating frequency and subsequently larger structure apertures at L-band lead to smaller transverse wake fields. Sufficient mitigation of transverse wakes is therefore considered to be a challenge for CLIC, while much less so for the ILC. For example, the CLIC main linac will be operated using BNS damping [56], while this is not considered necessary in the ILC.

Alignment and tolerances

To preserve the ultra-low emittances needed in both ILC and CLIC, the component misalignments must be kept within specified tolerances. This is particularly important in the very long main linacs. In ILC the main linacs will be cooled down to 2 K, and the alignment tolerances are relatively relaxed. For example, the assumed component offsets with respect to the modules, in the ILC main linacs, are 300 μm [6]. For CLIC the alignment tolerances are generally tighter. For example, the CLIC main linac pre-alignment tolerances are in the order of 10 μm. In order to reach these very tight tolerances a novel system, based on active pre-alignment, is being developed for CLIC [57].

Pulse length and bunch spacing

The CLIC main linac and accelerating structure optimisation [43] yields very short pulses of 156 ns with very short bunch-spacing of 0.5 ns. This makes intra-beam feedback extremely challenging, and poses as well challenges for detector design; in particular, single bunch-crossings can probably not be resolved. Because of the superconducting cavities, ILC can allow for long pulses without loss of efficiency. The ILC bunch spacing is 370 ns; a factor two longer than the length of the entire CLIC main beam pulse. The large bunch spacing in ILC furthermore mitigates multi-bunch wake field effects, and lowers the risk of harmful electron cloud and ion effects.

Challenges related to the CLIC two-beam scheme

The CLIC two-beam scheme requires that rf power is generated in a stable manner, timely and uniformly along the decelerator sectors. Very small loss levels are therefore required along the whole of the drive beam chain, including acceleration, beam pulse compression and deceleration. Furthermore, the main beam must be synchronised with the rf power generated by the drive beam to a precision of about 15 fs (0.1° at

12 GHz) [38]. In order to achieve this target, feed-back and/or feed-forward systems are very likely needed, requiring phase-monitoring with the same order of precision. Experiments reporting beam timing measurements with precision within 10 fs are found in [58].

Technology readiness

All feasibility issues for the ILC are considered solved, and with the completion of the Reference Design Report [6], the ILC study has now entered the technical design phase. The main remaining challenge seems to be reaching the superconducting cavity gradient yield [30]. The feasibility of CLIC, on the other hand, is still to be proven. The goal is that major issues will be addressed with the Conceptual Design Report, discussed in the next section.

Cost

The ILC Reference Design Report cost estimate is 6.6 Billion US $ (2007 values) [6] for the 500 GeV machine (detectors not included). The CLIC cost estimate is still under evaluation. There is, however, general agreement that with higher collision energy, the relative cost of the CLIC scheme with respect to the ILC scheme decreases. The main reason for this scaling is the CLIC drive beam complex; the complex represents a fixed cost needed also at low collision energies, while once constructed the extension of CLIC to higher energies can be done straight-forwardly by adding new sectors. To power the new sectors, the drive beam complex simply needs to generate a longer drive beam pulse.

3.4 The road to CLIC

The present main goal of the CLIC study is to prove the feasibility of all aspects of CLIC. A list of the most critical issues have been defined by the CLIC Steering Committee. A summary of the critical issues, reported by the CLIC project to the 4th CLIC Advisory Committee [59], is presented in Table 3.1. The feasibility of the critical issues will be shown by a combination of theory studies, simulation studies and experimental demonstrations. The items to which this thesis has made contributions are emphasised with bold font.

3.4.1 CLIC Test Facility 3

The CLIC Test Facility 3 (CTF3) [60], presented in Figure 3.5, is built to test key concepts of the CLIC drive beam generation and two-beam acceleration scheme.

Table 3.1: CLIC feasibility issues

Item	Description
C1	Operation of high-gradient accelerator structures
C2	**Operation of high-power power extraction and transfer structures**
C3	Two-beam acceleration and operation in prototype CLIC module
C4	Drive beam generation and combination
C5	**Drive beam energy extraction and power production**
C6	Generation and preservation of low emittances
C7	**Component alignment and stabilisation**
C8	Operation and machine protection
C9	Experimental conditions in the detector

The CTF3 150 MeV electron drive beam linac operates with Slotted Iris Constant Aperture structures [61]. The slots continue into wave-guides with SiC dielectric material to provide strong damping of the dipole modes. After the linac a magnetic chicane is installed to provide for bunch lengthening before the delay loop and combiner rings, in order to minimise coherent synchrotron radiation effects [62]. After the chicane, the beam may be combined by a factor two in the 42 m circumference delay loop, and up to a factor five in the 84 m circumference combiner ring (alternatively the delay loop can be bypassed, and the combiner ring can be used for making only a half-turn, allowing for the use of uncombined beams). The delay loop and the combiner ring must be isochronous in order to preserve the longitudinal structure of the bunches [60]. In the CLIC Experimental Area (CLEX), shown in Figure 3.6, demonstrations of two-beam acceleration and drive beam deceleration will be performed in the *Two-beam Test Stand* (discussed further in Chapter 4 of this thesis) and the *Test Beam Line* (discussed further in Chapter 6 of this thesis), respectively.

A number of important CLIC concepts have already been demonstrated in CTF3. The full-beam loading operation of the linac has been demonstrated [63] and the linac is now routinely operating at full beam loading, with a stable beam, indicating that the dipole mode damping works as foreseen. Bunch-length control and measurement have been performed [64]. A factor two combination with the delay loop using phase-coding and a factor four combination with the combiner ring have been demonstrated [65]. However, simultaneous use of the delay loop and the combination ring, is still to be demonstrated at the time of writing, as well as most of the experiments foreseen in CLEX.

Even though CTF3 will address many of the critical issues for CLIC, the value of the demonstration will to some extent be limited by the large difference between key parameters in CTF3 and the CLIC machine. Most notably: the drive beam energy is a factor 16 smaller in CTF3, the drive beam current is a factor 3.5 smaller in CTF3, the drive beam pulse length is a factor 100 smaller in CTF3. As consequence of the low drive beam energy, the energy fraction extracted in CTF3 will be smaller than the $\eta_{\text{extr}} = 90\%$ defined for the CLIC decelerator. Between the limited scale of CTF3 and a CLIC

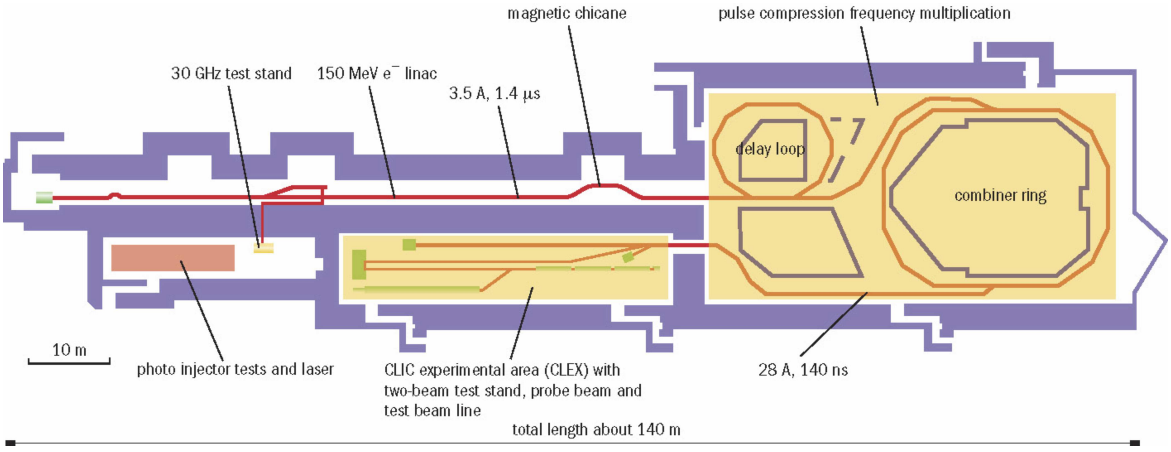

Figure 3.5: The CLIC Test Facility 3 (CTF3) included a 150 MeV electron linac, a delay loop and a combiner ring to perform drive beam frequency multiplication, as well as an experimental area (CLEX). Picture courtesy of the CLIC study.

machine used for particle physics, it is considered that a smaller prototype would be useful.

3.4.2 Conceptual Design Report

A major milestone for the CLIC study is the publication of the CLIC Conceptual Design Report (CDR), currently foreseen to be completed by the end of 2010. Perhaps most importantly, in the CDR the feasibility issues for CLIC, item C1-C9 in Table 3.1, should be reported on.

In addition the CDR should present the scientific case for CLIC, a conceptual design of the machine, an estimate of the overall performance and the related component requirements, proof that all components and their interplay are conceptually understood,

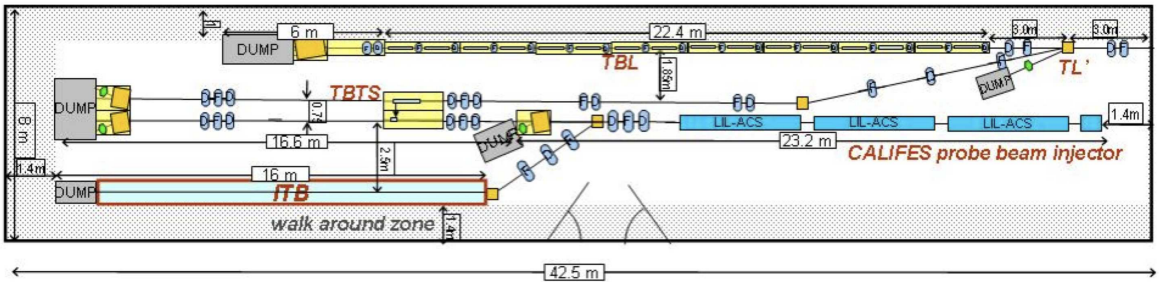

Figure 3.6: The CLIC Experimental Area (CLEX), where experiments of drive beam deceleration, rf power production and two-beam acceleration will take place. The CTF3 drive beam enters CLEX from the upper right beam line. The locations of the Two-beam Test Stand (TBTS) and the Test Beam Line (TBL) are indicated. Picture courtesy of the CLIC study.

evolution path to a Technical Design Report and a cost estimate.

3.4.3 CLIC 500 GeV and beyond

The separation of the decelerator and main linac into sectors makes it straightforward to build the CLIC machine in stages. The first stage would include the full drive beam complex, a shortened version of the beam delivery system, and the sectors closest to the interaction point. A typical energy level for the first machine built for particle physics is considered to be 500 GeV (but will depend on the physics needs identified by the LHC). In parallel with the CLIC 3 TeV baseline design, parameter optimisation for a CLIC 500 GeV machine has also been performed. CLIC 500 GeV parameters are found in [66]; nominal key parameters are collision energy of 500 GeV at a peak luminosity of 2.3×10^{34} $\mathrm{cm}^{-2}\mathrm{s}^{-1}$, a total length of 13 km and an overall power consumption of 129 MW. Ideally a 500 GeV machine can enter operation while the next sectors of the machine are being tunnelled and built (at some point the beam-delivery system would be extended by converting the adjacent sectors). This shows one of the major advantages of CLIC: the machine will provide a highly upgradable straight path towards future research in particle physics.

4. The Power Extraction and Transfer Structure

The rf power required for the CLIC main linac accelerating structures will be generated by a 101 ampere drive beam travelling through a number of power extraction and transfer structures (PETS) [67]. When the drive beam passes through the PETS it generates an electromagnetic field due to the impedance, oscillating with the fundamental mode frequency of $f_{\mathrm{rf}} = 12$ GHz and travelling with a group velocity $\beta_g c$ of about half the velocity of light. This rf field is coupled out and transferred to the main linac accelerating structures where it is used for accelerating the main beam.

The first tests of the 12 GHz PETS with beam took place in November and December 2008, in the specially designed Two-beam Test Stand (TBTS) [68] in the CLIC experimental area (CLEX). The prototype PETS constructed for tests in CLEX corresponds to a one meter version of the PETS designed for CLIC (which has length of 21 cm). The prototype is longer in order to produce nominal CLIC PETS power from the CLEX nominal beam intensity of 28 A (compared to 101 A in CLIC). A photo of the one meter prototype PETS after final assembly is presented in Figure 4.1. The PETS in the TBTS is equipped with a field recirculator, which couples part of the rf power produced back into the PETS, in order to further increase the power production from a limited current.

This chapter discusses the PETS power production as well as the effect *of* one PETS *on* the drive beam, the latter providing vital input for the decelerator beam dynamics studies. In comparison, Chapter 5 discusses the effect of multiple PETS on the drive beam in the decelerator lattice. Furthermore, the theory of PETS operation with field recirculation is discussed in this chapter. We aim at developing a simplified system model in which the physics of the PETS and the recirculation can be explained in a transparent way, using closed-form mathematical expressions. Finally, the test results of the 2008 run are analysed using the model developed, and agreement between the model and the measurements is quantified. These test results also provide the first benchmarking of the theory and simulation studies on which the CLIC decelerator studies are based.

The most important results in this chapter have been presented in two papers included in Appendix B. The first paper [67], presented at the 22nd IEEE Particle Accelerator Conference (PAC 2007, Albuquerque, USA) summarises the design of the 12 GHz CLIC power extraction and transfer structure. The second paper [69], presented at the 19th

European Workshop on Beam Diagnostics and Instrumentation for Particle Accelerators (DIPAC 2009, Basel, Switzerland), summarises the results from the first beam tests of this structure.

4.1 Basic concepts

A charged particle interacts electromagnetically with its surroundings, due to the geometry and the finite conductivity of the surroundings. The electromagnetic fields originating from the interactions might interact with other particles in the vicinity. For arbitrary particle motion, analytical calculations of the forces acting on the particles would be intractable, even for very simple geometries and small number of particles. For relativistic particle beams, however, the calculations of electromagnetic interactions can often be simplified.

In high-energy electron accelerators particles travel very close to the speed of the light. Assuming the particle speed to be equal to the speed of light (ultra-relativistic) is therefore for many purposes a good approximation when working with electrons. Due to causality, the electromagnetic field generated by the particle will then trail the source particle, and therefore only affect trailing particles. In this case the field is called a *wake*

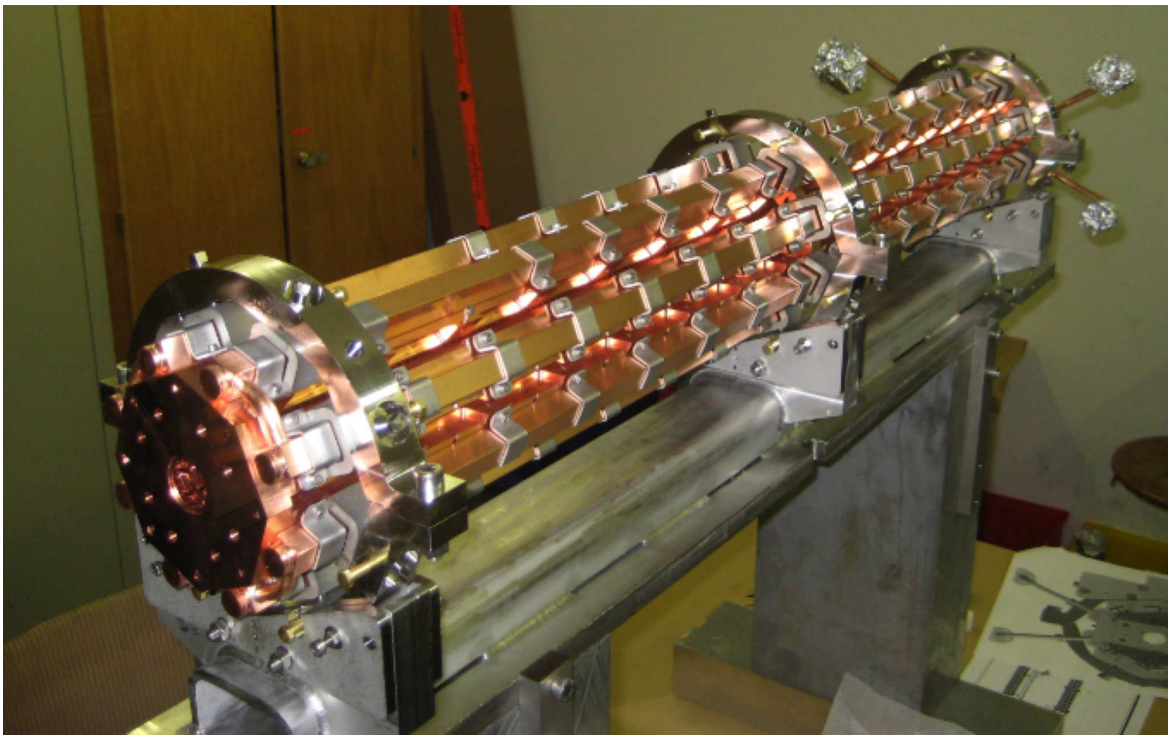

Figure 4.1: The one meter prototype 12 GHz power extraction and transfer structure, in its final assembly before installation and test in the Two-beam Test-Stand in the CLIC Experimental Area at CERN.

field. For illustrational purposes Figure 4.2 shows the electromagnetic field trailing a highly relativistic Gaussian electron-bunch passing through an iris with thickness three times the bunch RMS length, simulated with the Azimuthal Beam Cavity Interaction (ABCI) computer code [70]. By passing through the iris the bunch has lost a fraction of its energy to the wake field.

In the ultra-relativistic approximation, particles travel along the machine with a fixed distance with respect to each other. The forces experienced by a witness particle, due to the wake field generated by a given source particle, can therefore be evaluated in the frame moving with the source particle, simplifying calculations. We will measure the beam motion along the machine using an axis denoted s, fixed in the laboratory frame. The particle to particle (and bunch to bunch) distances will be measured along an axis denoted z, moving with the beam, with values given in the laboratory frame. When plotting values along the beam we will in this work put time on the ordinate axis, where $t = z/c$. This way the plots relate immediately to typical beam diagnostics observables and requirements. Our definition of coordinates is illustrated in Figure 4.3.

In a *travelling-wave structure* [71] for particle beams, a high amplitude electromagnetic field can be set up where one of the travelling wave modes has a phase velocity that matches the particle velocity (for high-energy electrons equal to c). The phase-velocity is matched e.g. by suitable periodicity of the structure irises. Characteristics of ac-

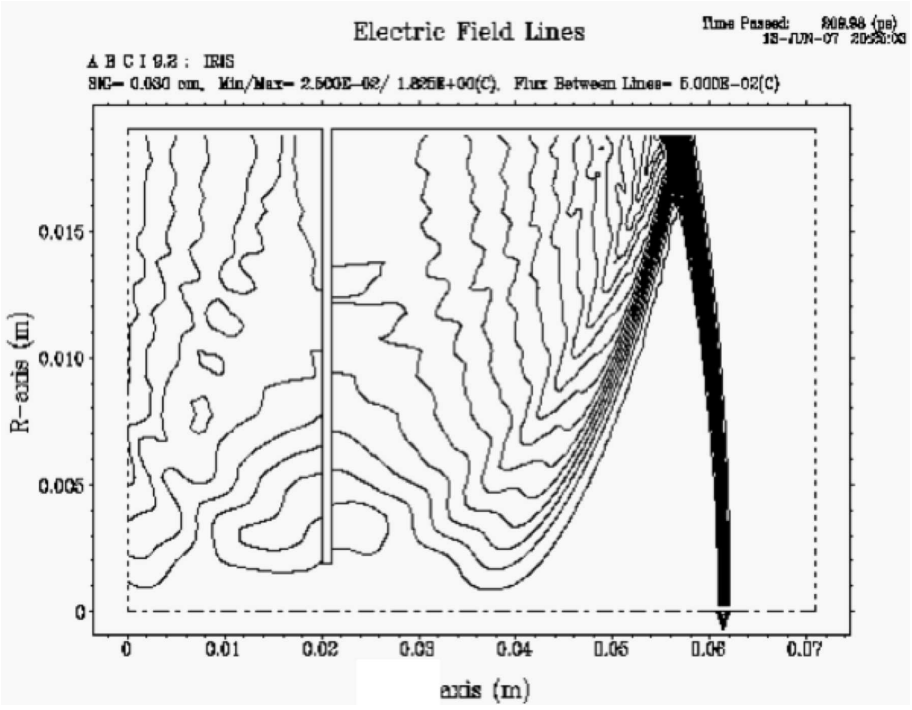

Figure 4.2: The electromagnetic field trailing a highly relativistic Gaussian electron-bunch passing through an iris with thickness three times the bunch RMS length (upper half of the plane shown only). By passing through the iris the bunch has lost a fraction of its energy to this field.

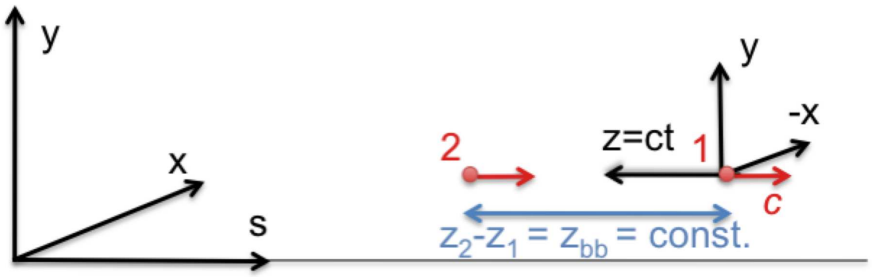

Figure 4.3: Two coordinate systems are used to describe the particle motion. Electron bunches (in red, indicated by "1" and "2") move along the s-axis of the machine with the speed of light c. The distance between bunches is fixed, and is measured in the laboratory frame along the z-axis of a frame moving synchronously with the beam. The distance between two subsequent bunches is denoted z_{bb}. Transverse displacements from the ideal beam are along axes denoted by x and y. The direction of the z-axis is chosen as to correspond to the convention of the CLIC beam physics simulation code, PLACET. In plots in this work, time, where $t = z/c$, is normally used on the ordinate axis.

celerating structures for high-energy electron linacs in general are discussed thoroughly in [71], and we here summarise the key parameters needed for our studies.

4.1.1 Structure parameters

For a travelling-wave structures the following quantities can be defined for a given mode [71], assuming the linac-Ω convention[1]:

1) The shunt-impedance per unit length

$$R' = \frac{(\text{travelling-wave longitudinal electric field})^2}{\text{ohmic losses per unit length}} = \frac{E^2}{\mathscr{P}'} \tag{4.1}$$

2) The quality factor

$$Q = \frac{\text{stored field energy per unit length}}{\text{ohmic losses per unit length per radian of rf oscillations}} = \frac{\mathscr{E}'}{\mathscr{P}'}\omega_{\text{rf}} \tag{4.2}$$

where ω_{rf} is the fundamental mode angular frequency, $2\pi \times f_{\text{rf}}$. In general we will denote quantities per unit length by a prime ('). In [71], the concept of wake functions and impedances are introduced as well. The wake function describes the potential seen by a particle trailing a unit charge at a fixed distance, while the impedance is the Fourier transform of the wake function. The concepts of wake fields and impedances are further developed, using a fully Maxwellian approach, in [72]. The mode longitudinal loss factor per unit length is defined as the energy a point-charge, q, loses to the impedance, per unit

[1]The circuit-Ω/m convention, in which the shunt-impedance equals the resistance of the equivalent LRC-circuit, is also in frequent use in the accelerator community. The relation between the two conventions is R'/Q [Linac-Ω/m] $= 2R'/Q$ [Circuit-Ω/m]. In this work we consistently use linac-Ω.

length, normalised to the charge squared. Furthermore, for a structure with a sharply peaked (high Q) fundamental mode, the impedance of this mode is proportional to the ratio (R'/Q) [72]. For a mode with low group velocity the loss factor can be calculated as [71] $k'_{|v_g \to 0} \equiv \mathscr{E}'/q^2 = \frac{1}{4}(R'/Q)\omega_{rf}$. The energy lost to the mode impedance is converted into a wake field trailing the charge.

4.1.2 Particularities of the PETS

The CLIC power extraction and transfer structure is basically a constant impedance travelling wave-structure, where the required rf power is generated by *deceleration* of electron bunches moving through the structure, as will be explained in detail below. The PETS is not fundamentally different from a travelling wave *accelerating* structure, but it is characterised by a fundamental mode group velocity of almost half the speed of light, and some of its characteristics are not covered by [71, 72]. For the analysis of the first CLIC PETS tests with beam and also as a starting point for the beam dynamics work it is important to have a clear picture of the PETS dynamics. We will therefore develop formulae for the PETS, starting from basic structure parameters. The expressions developed are only valid when the structure length is much longer than the bunch spacing, as will become clear as we proceed.

4.2 PETS power extraction and energy loss

We are here interested in expressions for the PETS fundamental mode field, voltage and output power. As basic assumption, the trailing wake field of a particle is modelled as a "field sausage" with sharply cut edges, travelling with the group velocity of the field [73]. We assume that the field is coupled instantaneously out of the PETS, thus not taking into account bandwidth considerations. We further assume PETS nominal operating conditions where bunch-trains are uniform, with bunch spacing equal to the fundamental mode frequency and zero phase slip (these conditions correspond to the baseline for the decelerator beam dynamics studies in Chapter 5). These simplifications allow the expressions for field, power and voltage to take a simple form. The expression can then readily be further developed, e.g. in the case of field recirculation, as discussed in Section 4.4. In contrast, [71] contains some more general expressions, e.g. for beam loading for a bunch train with a fixed phase slip per bunch, limited however, to the case of low group velocity.

A charge passing through the PETS excites preferentially the fundamental mode, and the mode wake field will travel along the PETS with a group velocity $v_g < c$. When the particle has reached the PETS output at distance L_{PETS}, the field will have travelled a distance $v_g L/c \equiv \beta_g L$. This is illustrated in Figure 4.4.

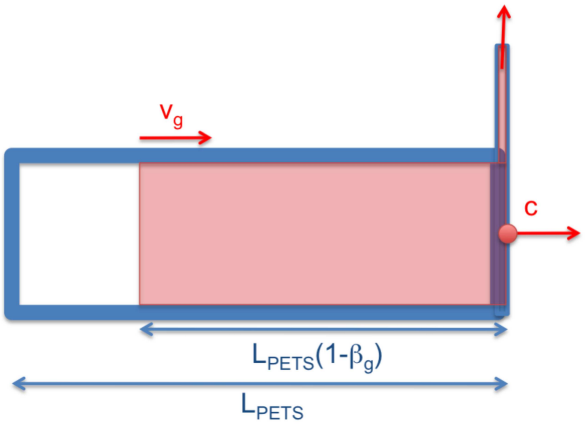

Figure 4.4: The PETS field from a single charge. The fundamental mode wake field will travel along the PETS with a group velocity v_g. When the charge has reached the PETS end, the field has travelled a distance $\beta_g L$ into the PETS. For illustrational purposes a group velocity of $v_g \approx 0.25c$ has been used for this drawing.

4.2.1 PETS longitudinal loss factor and wake function

For structures with high group velocity the energy in the field will be concentrated in a fraction $(1-\beta_g)$ of the structure length, as illustrated in Figure 4.4, implying that the loss factor per unit length defined in [71] must be scaled by a field compression factor $1/(1-\beta_g)$ [74]. The PETS loss factor per unit length should thus be expressed as

$$k' = \frac{1}{4}(R'/Q)\omega_{\mathrm{rf}}\frac{1}{1-\beta_g}.$$

The loss factor should in principle be extended with a damping term due to finite mode Q-values [71]. In this work we will for notation simplicity take ohmic losses into account by incorporating an ohmic loss reduction factor in the field expressions, $\eta_{\Omega,\mathrm{PETS}}$. $\eta_{\Omega,\mathrm{PETS}}$ quantifies the reduction of the field at the PETS end due to ohmic losses (no losses implies $\eta_{\Omega,\mathrm{PETS}} = 1$), and is a function of the structure length, the mode group velocity and the mode Q (for the PETS fundamental mode $Q \approx$7200 [75]). For the CLIC PETS of 0.21 m length, $\eta_{\Omega,\mathrm{PETS}}$ is higher than 99%.

The average force of the wake field per unit length on a witness particle, trailing a point-like source particle generating the wake field, normalised to the charge of both particles, is defined as the longitudinal wake function per unit length $W_0'(z)$. The wake function depends on the distance z between the two particles, and for a sharply peaked mode it is given by [72]

$$W_0'(z) = 2k'\cos(\frac{\omega_{\mathrm{rf}}}{c}z) = \frac{1}{2}(R'/Q)\omega_{\mathrm{rf}}\cos(\frac{\omega_{\mathrm{rf}}}{c}z)\frac{1}{1-\beta_g}, \tag{4.3}$$

where the field-compression factor again must be included. The wake function amplitude is two times the loss factor, because the driving charge sees only half of the field it

generates, while a trailing charge will see the full field (cf. the fundamental theorem of beam loading [72]).

Because the field travels out of the PETS due to the group velocity, the wake function per unit length is only to be applied after a particle catches up with the leading source field. The catch-up distance, $d_{\mathrm{catch-up}}$, is calculated e.g. by noticing from Figure 4.4 that a trailing particle will catch up with the field of a particle a distance z ahead, after a time $t_{\mathrm{catch-up}} = d_{\mathrm{catch-up}}/c$. The field travels a distance $(d_{\mathrm{catch-up}} - z\beta_g)$ in the same time, $t_{\mathrm{catch-up}} = (d_{\mathrm{catch-up}} - z\beta_g)/v_g$, yielding

$$d_{\mathrm{catch-up}}(z) = z\frac{\beta_g}{1-\beta_g}. \tag{4.4}$$

The wake field will therefore only be felt over an effective length

$$L_{\mathrm{effective}}(z) = L_{\mathrm{PETS}} - d_{\mathrm{catch-up}}. \tag{4.5}$$

We could include the factor $L_{\mathrm{effective}}$ in Eq. (4.3) and continue the development using the effective integrated wake function. We believe, however, that the discussions in this chapter become more clear working with Eq. (4.3) as it stands, and Eqs. (4.4) and (4.5) will therefore not be applied explicitly.

The actual parameters of the PETS longitudinal modes have been calculated [75] using the electromagnetic solvers HFSS [76] and GdfidL [77, 78].

4.2.2 PETS fundamental mode field

We consider here only the dominant, sharply peaked 12.0 GHz fundamental mode. The amplitude of the longitudinal electric field trailing a point-like source bunch (plb) with charge q_b is equivalent to the mode wake function per unit length, multiplied by the source charge, and multiplied by the ohmic loss reduction factor $\eta_{\Omega,\mathrm{PETS}}$. We will from now on write *"the field"* for the fundamental mode longitudinal field amplitude. We have assumed that the bunch frequency equals the fundamental mode frequency,

$$f_{\mathrm{bunch}} = f_{\mathrm{rf}}.$$

At the location of trailing bunches having caught up with the wake, the field is then

$$E_{\mathrm{plb}} = q_b W_0'(0) = \frac{1}{2} q_b (R'/Q)\omega_{\mathrm{rf}} \frac{1}{1-\beta_g}\,\eta_{\Omega,\mathrm{PETS}}.$$

For a bunch with finite length, if the bunch length is much shorter than the distance between bunches (which is true for the CLIC drive beam), the effective field originating from a bunch is found by summation over the normalised longitudinal bunch charge distribution $\lambda(z)$,

$$E_{\mathrm{bunch}} = q_b \int_{-\infty}^{\infty} dz' \lambda(z') W_0'(z') \equiv E_{\mathrm{plb}} F(\lambda), \tag{4.6}$$

which defines the charge distribution form factor (a symmetric bunch is assumed here for simplicity),

$$F(\lambda) \equiv \int_{-\infty}^{\infty} dz' \lambda(z') \cos(\frac{\omega_{\rm rf}}{c} z'). \tag{4.7}$$

For a Gaussian bunch the form factor evaluates to $F(\lambda(\sigma_z)) = \exp(-\frac{1}{2}(\sigma_z \omega_{\rm rf}/c)^2)$, where σ_z is the bunch rms length. The effective field trailing a bunch is thus reduced by a factor $F(\lambda)$. The form factor enters directly in the efficiency calculations for the CLIC machine, as can be seen from Eq. (3.2). In addition to the explicit form factor in Eq. (3.2), there is a second, implicit form factor in $\eta_{\rm extr}$. The implicit form factor does not contribute to machine efficiency loss, however, since $\eta_{\rm extr}$ is an input parameter for machine design, cf. discussion above Eq. (3.2).

The rf field will reach steady state when a trailing bunch catches up with the end of the field of the first bunch at the PETS output, as illustrated in Figure 4.5. The fill-time, defined here as the time between first rf at the PETS output until a steady state condition is reached, is therefore given by the time it takes the field of a bunch to travel the distance $L_{\rm PETS}(1-\beta_g)$,

$$t_{\rm fill} \equiv \frac{L_{\rm PETS}}{v_g}(1-\beta_g), \tag{4.8}$$

and the corresponding number of trailing bunches before this condition is reached is

$$N_{\rm fill} \equiv t_{\rm fill} f_{\rm bunch} = \frac{L_{\rm PETS} f_{\rm bunch}}{v_g}(1-\beta_g). \tag{4.9}$$

At steady state conditions the field originating from $N_{\rm fill}$ bunches will be superpositioned towards the PETS end, as shown in Figure 4.5, and the total field at the PETS end can therefore be computed as

$$E_{\rm beam} = N_{\rm fill} E_{\rm bunch}, \tag{4.10}$$

which, using Eq. (4.6), can be written as

$$E_{\rm beam} = \frac{1}{2}(R'/Q)\omega_{\rm rf} \frac{L_{\rm PETS}}{v_g} I F(\lambda) \eta_{\Omega,\rm PETS}, \tag{4.11}$$

where we have introduced the average beam intensity $I = q_b f_{\rm bunch}$. We note that because $N_{\rm fill}$ in reality is a discrete quantity for a bunched beam, Eq. (4.11), which is linear in $L_{\rm PETS}$, will not be accurate for small $N_{\rm fill}$.

4.2.3 PETS output power

By applying Eqs. (4.1) and (4.2) at the PETS end, where the travelling wave field, E, is given by Eq. (4.11), $E = E_{\rm beam}$, we can express R'/Q as

$$(R'/Q)\omega_{\rm rf} = \frac{E_{\rm beam}^2}{\mathscr{E}'},$$

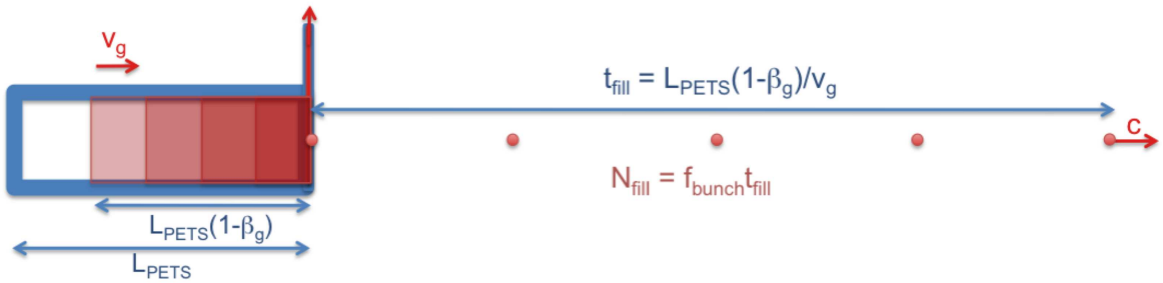

Figure 4.5: The PETS completely filled, after a time t_{fill}, with N_{fill} bunches contributing to the end field. The rf power is extracted at the PETS end (right side of the PETS in the figure). Fields of bunches trailing the bunch at the PETS end are not shown (they do not contribute to the field at the PETS end). For illustrational purposes parameters $L_{\text{PETS}} = 1$ m, group velocity $v_g \approx 0.25c$ and bunch frequency $f_{\text{bunch}} \approx 0.4$ GHz have been used for this drawing.

linking the travelling-wave field and the corresponding stored field energy per unit length. The field is coupled out and exits the PETS with the group velocity v_g. The PETS output power can be found by evaluating the energy flow out of the PETS, using that the energy flow velocity is equal to the group velocity [71]

$$P \equiv \frac{d\mathscr{E}}{dt} = \frac{d\mathscr{E}}{ds}\frac{ds}{dt} = \mathscr{E}' v_g = \frac{E_{\text{beam}}^2}{(R'/Q)\omega_{\text{rf}}} v_g, \tag{4.12}$$

yielding

$$P = \frac{1}{4}(R'/Q)\frac{\omega_{\text{rf}}}{v_g} L_{\text{PETS}}^2 I^2 F^2(\lambda)\eta_{\Omega,\text{PETS}}^2. \tag{4.13}$$

4.2.4 PETS mean and peak voltage

The voltage experienced by an electron in the PETS, in units of V, corresponds to the energy loss of the electron, in units of eV. For the beam dynamics studies in Chapters 5 and 6 it is of importance to know the maximum energy loss of the beam. We will therefore develop an expression for the PETS *peak voltage* (for symmetric bunch charge distributions and assuming negligible single-bunch effects, the peak voltage will be experienced in the middle of the bunches). We assume here that the energy change due to other modes than the fundamental is negligible.

The longitudinal field, seen by a synchronous witness particle, builds up step-wise as the fields from leading bunches are caught up with, as seen from Figure 4.5. For sufficiently large N_{fill} self-field corrections will be negligible, and we here calculate the peak integrated longitudinal field seen, the peak PETS voltage $\hat{U}$, by adding contributions from all leading bunches seen in the PETS. Each leading bunch seen will contribute by a factor

$$\Delta U_{\text{bunch}} = E_{\text{bunch}} L_{\text{PETS}}(1 - t_{\text{catch-up}}/t_{\text{fill}}),$$

where the catch-up time, $t_{\text{catch-up}}$, increases linearly with the distance from the witness bunch to the leading bunch. For large N_{fill} we can therefore estimate the voltage seen

after a time $t < t_{\text{fill}}$ as

$$\hat{U}(t) = E_{\text{bunch}} L_{\text{PETS}} f_{\text{bunch}} \int_0^t d\tau (1 - \frac{\tau}{t_{\text{fill}}}),$$

which after integration and using Eqs. (4.9) and (4.10) yields the following expression for the energy loss in the transient part of the beam

$$\hat{U}(t) = E_{\text{beam}} L_{\text{PETS}} (\frac{t}{t_{\text{fill}}} - \frac{1}{2}(\frac{t}{t_{\text{fill}}})^2), \qquad t < t_{\text{fill}}. \tag{4.14}$$

For the steady state part, reached at $t = t_{\text{fill}}$, the peak voltage becomes

$$\hat{U} = \frac{1}{2} E_{\text{beam}} L_{\text{PETS}}, \qquad t \geq t_{\text{fill}}. \tag{4.15}$$

Eventually, if one wants to estimate $\hat{U}$ from P, combining Eqs. (4.12) and (4.15) yields the following relation

$$\hat{U}^2 = \frac{1}{4} L_{\text{PETS}}^2 \frac{(R'/Q)\omega_{\text{rf}}}{v_g} P. \tag{4.16}$$

Another useful quantity is the *mean voltage* seen by a steady state particle bunch, $\langle U \rangle$. By writing the generated power as $P = \langle U \rangle I \eta_{\Omega,\text{PETS}}$ we get, using Eqs. (4.11), (4.13) and (4.15), the following relation

$$\langle U \rangle = \hat{U} F(\lambda). \tag{4.17}$$

Finally, we note that the amplification factor of resonant energy loss with respect to single bunch self-field energy loss, given by $U_{\text{self}} = \frac{1}{2} E_{\text{bunch}} L_{\text{PETS}}$, is found from Eqs. (4.11) and (4.15) as

$$A_{\text{resonance}} \equiv \hat{U}/U_{\text{self}} = N_{\text{fill}}.$$

4.2.5 Limitations of the expressions

We have taken into account the bunch charge distribution by scaling the field expressions with the form factor $F(\lambda)$, starting from Eq. (4.6). Within a single bunch, the field generated from the bunch itself is more complicated, due to causality. For the expressions Eqs. (4.11), (4.13) and (4.15) to be accurate, N_{fill} must be sufficiently large to render single-bunch effects insignificant. Furthermore, N_{fill} must be sufficiently large so that the discreteness of the field build-up, shown in Figure 4.5, can be ignored. The bunch must in addition be sufficiently long as to render the energy profile after extraction approximately symmetric; if it is not symmetric the tail of the bunch will experience a larger voltage than the head, implying a different peak voltage. The expressions developed above are therefore suggested to be used only for rough estimations. For precise calculations the particle tracking code PLACET [73] can be used. PLACET incorporates a PETS element which calculates the voltage for arbitrary N_{fill} and $\lambda(z)$, as well as a dedicated routine which calculates rf power and phase, also for arbitrary charge distributions. The expressions Eqs. (4.11), (4.13) and (4.15), however, are indeed good approximations for PETS operations in the CLIC Test Facility 3, discussed in the next sections and in Chapter 6.

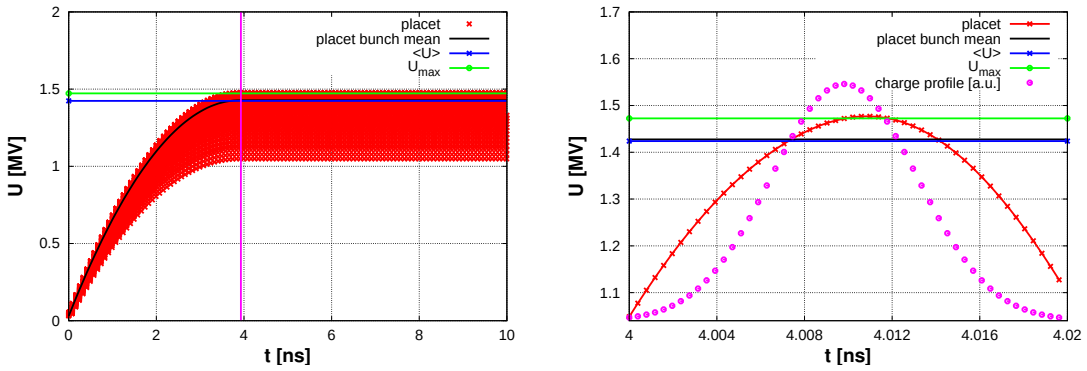

(a) Energy loss along beam (first 10 ns) (b) Energy loss inside a bunch (steady state)

Figure 4.6: Energy loss in a 1 meter long PETS for a 5 A 12 GHz bunch train with 1 mm rms Gaussian longitudinal charge profile. Simulated slice energy loss in red. Simulated bunch centroid energy loss in black. Calculated steady state mean energy loss in blue. Calculated steady state maximum energy loss in green. (a) The first 10 ns of a pulse. (b) Zoom on a single bunch in the steady state regime, starting after 3.9 ns. The Gaussian bunch charge profile is shown as well, in magenta (o), for clarity.

4.2.6 Example for a 1 meter long PETS

As an example we calculate field, power and voltage for the 1 meter long 12 GHz PETS designed for the CTF3 Two-beam Test Stand (discussed further in Section 4.5) with parameters as given in Table A.2. We assume a rectangular pulse with intensity of 5 A, bunch frequency $f_{\mathrm{bunch}} = 12$ GHz and pulse length 10 ns. We further assume zero phase slip, a Gaussian longitudinal charge profile with rms length of $\sigma_z = 1$ mm and no ohmic losses. Eqs. (4.11), (4.13), (4.15) and (4.17) yield for this example $P = 7.12$ MW, $E_{\mathrm{beam}} = 2.94$ MV/m, $\hat{U} = 1.47$ MV and $\langle U \rangle = 1.42$ MV. Furthermore, Eqs. (4.8) and (4.9) give a fill time of $t_{\mathrm{fill}} = 3.9$ ns and correspondingly $N_{\mathrm{fill}} = 47$ bunches.

For illustration, Figure 4.6 shows a PLACET simulation for the same set-up, showing the energy loss along a 10 ns long pulse. The energy loss in the transient part is given by Eq. (4.14), while after the fill time of $t_{\mathrm{fill}} = 3.9$ ns the energy loss is given by Eq. (4.15). The calculated values for mean and maximum energy loss are marked on the graph, as well as the simulated beam energy loss along the pulse. Eqs. (4.11), (4.13), (4.15) and (4.17) give accurate estimates better than 1% for this structure and beam, with respect to the PLACET simulation. The single-bunch wake effect is visible as an asymmetry in the energy loss profile in the right plot, and is responsible for part of the small discrepancy between the analytical estimates and the simulation.

4.3 PETS transverse wakes

The beam current can in general be decomposed in multipole moments of all orders. Each multipole moment will induce a wake potential of the same order [72]. While

the fundamental mode induced by the monopole moment is what provides the PETS rf power, the higher order modes induced by higher order beam moments lead to unwanted and potentially harmful effects.

For the decelerator beam dynamics studies, the transverse wake potential originating from the dipole moment of the beam has been studied extensively, by a procedure discussed below. In earlier work, radial dependence of the longitudinal field has been studied [79], but for the 12 GHz PETS no rf data have been available for such studies. Wake potentials resulting from quadrupole (or higher) moments have not been studied either in this work, however, by requiring all parts of the simulated beams to stay within half the aperture radius, see Section 5.2, their effects would be mitigated.

One of the main PETS design drivers is sufficient suppression of the dipole wake. In the current design, the dipole wake has been strongly suppressed by the use of longitudinal slots filled with lossy dielectric material, and the resulting dipole spectrum has been optimised to minimise the effect on the beam dynamics [67].

The structure rf simulation and design work were not part of the thesis work and we here only outline the procedure and results. We also discuss briefly how the wake is implemented in the beam dynamics simulation tools and discuss the impact of the dipole wake when the beam goes through a *single* PETS. The actual optimisation of the PETS dipole mode is part of the thesis work. The effect of the dipole wake combined with strong focusing in long beam lines is further discussed in Chapter 5, and the interplay between decelerator beam dynamics and PETS rf design, culminating in the present PETS dipole spectrum, is explained there.

4.3.1 Calculation of the dipole wake

The simulation code PLACET [73] represents the dipole wake as a finite set of discrete time-domain modes. Each mode is modelled as a damped sine with separate amplitude, $2k'_T$, frequency ω_T, Q-factor Q_T and group velocity β_T. For each dipole mode, the wake function per unit length can be written as [67]

$$W'_T(z) = 2k'_T \sin(\frac{\omega_T}{c}z) \exp(-\frac{1}{2}\frac{1}{Q(1-\beta_T)}\frac{\omega_T}{c}z), \tag{4.18}$$

where k'_T is the transverse kick factor, including the field-compression factor $1/(1-\beta_T)$ [74,80]. Analogous to the PETS longitudinal wake function, the transverse wake function is also experienced over an effective length given by Eqs. (4.4) and (4.5), where Eq. (4.4) is calculated using β_T.

The PETS dipole mode parameters are identified by the following procedure [67]: time-domain simulations performed with GdfidL [77] yield the dipole wake potential for a finite bunch length (1-2 mm was used), as well as an estimate of the impedance calculated by dividing the Fourier transform of the wake potential with the bunch spectrum. This impedance estimate is a good approximation up to frequencies of about $\sim$100 GHz, depending on the bunch length simulated [75]. A set of modes that best represents the

impedance estimated is then fitted, while keeping the total number of modes reasonably small. A final check is performed by convoluting the discrete mode wakes with the bunch used for GdfidL simulations and compare the result with the GdfidL wake potential calculation. It should be noted that even though the PLACET model and the formalism allow for high group-velocity also for the dipole modes, it is not obvious to separate the effect of the group velocity and the damping from the calculated GdfidL wake potential. It is expected, however, that the damping term (Q) will be dominant with respect to the catch-up effects (β_T) [75]. The PETS modes for the base line PETS have therefore been modelled as static modes with $\beta_T \to 0$, with the remaining parameters adjusted to best represent the GdfidL impedance.

The modes used to model the 12 GHz CLIC PETS for the beam dynamics simulations in this thesis are best illustrated by the corresponding impedance. The impedance is easily calculated as the sum of the Fourier-transform of each wake function [72], and is shown in Figure 4.7. Nine time-domain modes contribute to this impedance, and the parameters for each mode are specified in Table A.5. Figure 4.7 shows that both relatively broad band modes (low Q-factor and relatively high amplitude) and sharply peaked modes (high Q-factor and relatively low amplitude) have been taken into account in the representation of the PETS impedance.

Finally, it should be noted that unlike for other structures, the wake function in Eq. (4.18) holds for *both* multi-bunch effects and single-bunch effects, as discussed in [81]. The beam dynamics simulations performed with PLACET, discussed in Chapter 5, thus correctly take into account both multi-bunch and single-bunch effects by implementing the impedance spectrum in Figure 4.7.

4.3.2 The effect of the dipole wake on the beam

We here present some considerations of the effect a dipole mode of a *single* PETS has on the beam, assuming static transverse modes with $\beta_T \to 0$. In the next chapter the effect of the dipole wake of multiple PETS, combined with betatron motion, will be treated. The force acting on an electron inside the PETS, due to the dipole wake from a particle leading at a distance z, is found by scaling the wake function per unit length $W_T'(z)$ by the source charge, q_1, the unit charge e and the offset of the source particle with respect to the structure centre axis, y_1 [72]

$$F_{y,wake}(s,z) = eq_1 W_T'(z) y_1(s). \tag{4.19}$$

Assuming $v \approx c$, slowly-varying γ in the PETS and linear motion we can write Newton's second law as

$$F_y = \frac{d}{dt}(p_y) = \frac{d}{dt}(\gamma m_0 \dot{y}) \approx \gamma m_0 c^2 y'' = E_{tot} y'', \tag{4.20}$$

where $y' = \frac{dy}{ds}$ and E_{tot} is the total energy of the particle. From Eqs. (4.19) and (4.20) we get

$$y''(s,z) = \frac{y_1(s)}{E_{tot}} eq_1 W_T'(z). \tag{4.21}$$

The total kick a trailing particle receives, $\theta \equiv \Delta y'$, due the offset of the driving particle, $y_1(s)$, is found by integrating Eq. (4.21) over the PETS length

$$\theta(z) = \int_0^{L_{\mathrm{PETS}}} \frac{y_1(s)}{E_{tot}} e q_1 W_T'(z) ds. \tag{4.22}$$

4.3.3 Example for a 1 meter long PETS

We use again the example of a bunch train with $f_{\mathrm{bunch}} = 12$ GHz and an intensity of I = 5 A from Section 4.2.6 and we assume the CTF3 2008 PETS run energy of $E_{tot} = 127$ MeV [82]. The PETS tested in 2008 did not have damping material installed in the slots, and the dipole wake can for this case be approximated as a single mode with parameters $2k_T' \approx 8.3$ V/pC/m/mm, $Q \approx 5000$, $f_T \approx 15$ GHz and a group velocity $\beta \approx 0.7$, but bouncing forth and back inside the cavity [75]. In this example we consider the undamped mode to be static ($\beta_T \to 0$) for simplicity, which also corresponds to the worst case scenario in terms of kick amplitude. The kick per initial offset is then found

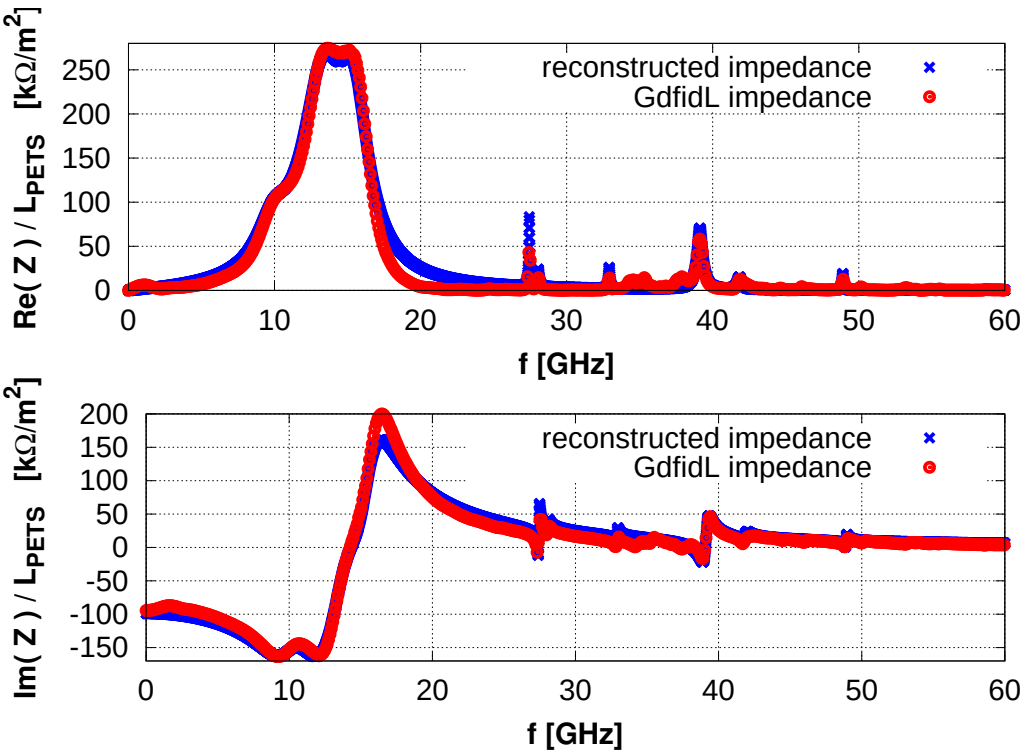

Figure 4.7: The PETS transverse dipole mode impedance. The GdfidL calculation is shown in red (o). The impedance fitted using a set of nine discrete time-domain modes is shown in blue (x). The remaining discrepancy between the curves comes from the limited number of modes used, plus that fact that the time-domain modes are modelled with zero group velocity, while the real modes have finite group velocity. For the decelerator beam dynamics studies, the time-domain modes (corresponding to the blue curve) are implemented in the tracking code PLACET.

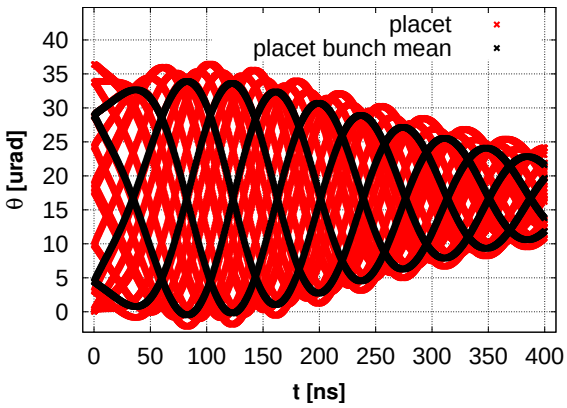

Figure 4.8: The kick along the pulse with an initial offset of 1 mm after passing through a 1 meter long PETS without damping material. The resulting kick applied to each of the bunch slices are shown in red, while the mean kick applied to each bunch is shown in black.

from Eq. (4.22). For the example parameters we estimate the maximum kick due to a leading bunch on a trailing bunch to

$$\theta/y_1 = 2e\frac{L_{\mathrm{PETS}}}{E_{tot}}\frac{I}{f_{\mathrm{bunch}}}k'_T = 27\ \mu\mathrm{rad/mm}.$$

Figure 4.8 shows PLACET simulations of the resulting kick along a pulse having passed through the 1 meter long undamped PETS. Before entering the PETS all the bunches in the pulse have zero angle and 1 mm offset with respect to the PETS centre. We have set the mode frequency of $f_T = 15.0$ GHz. However, the order of magnitude of the kicks does not depend strongly on the frequency as long as it is far from a multiple of the bunch frequency of 12 GHz.

In the PLACET simulations each bunch is sliced longitudinally. In red the resulting kick applied to each of the bunch slices are shown, while the mean kick applied to each bunch is shown in black. PLACET does take into account motion inside the PETS and in this scenario this effect is significant. PLACET also takes into account rf edge-focusing effects (which are here negligible with respect to the effect of the transverse wakes). We note that the final kick along the pulse is within the order of the estimated kick on the second bunch, $\theta \sim 27\ \mu$rad, as expected. The discrepancy with the analytical estimate is due to single-bunch effects and the motion inside the PETS.

4.4 Field recirculation

The PETS output power is limited by the current, as indicated by Eq. (4.13). By coupling a fraction of the output field back into the PETS, a relatively higher PETS output power (and higher beam energy loss) can be achieved for the same current. We say that the field is *recirculated*. We remind of our simplified use of the term *"the field"* for the fundamental mode longitudinal field amplitude.

For the first 12 GHz PETS beam tests in CLEX [82], the recirculation was performed using an external recirculation arm [83], as illustrated in Figure 4.9. Recirculation can also be performed by internal reflection, where a fraction of the beam generated field is reflected at the output coupler, travelling backwards in anti-phase with the beam generated field, and then being reflected back into the forward direction at the PETS input coupler. Since the backward wave will be out of phase with the beam generated field, the effect of the backward wave on the beam is to first order negligible. Recirculation is not part of the present CLIC baseline design, however, recirculation by internal reflection might be considered as an option for the CLIC project in the future [75].

We now develop analytical expressions for the PETS fundamental mode field, output power and voltage, including the effect of recirculation. These expressions will in the next section be used to analyse the first PETS beam tests. We assume that the fill-time of the PETS is much smaller than the recirculation round trip time. Other considerations concerning PETS operation with recirculation can be found in [84, 85].

4.4.1 Principle

In the cases of both external and internal recirculation, a fraction of the PETS field, g, is circulated back in parallel with the beam generated field, after a round trip time t_{circ}. g thus includes the total gain factor, consisting of the splitter ratio κ times the round-trip ohmic loss reduction factor $\eta_{\Omega,\mathrm{circ}}$,

$$g = \kappa\eta_{\Omega,\mathrm{circ}}.$$

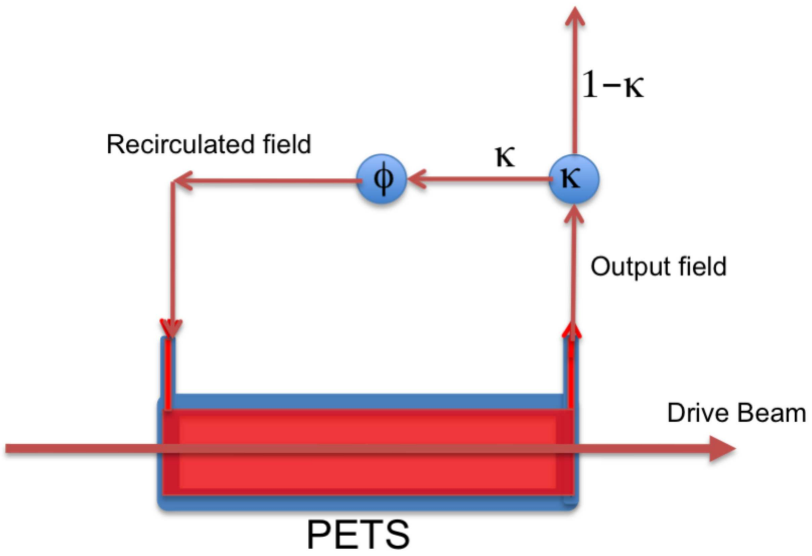

Figure 4.9: Principle of PETS operation with external recirculation of the field.

The recirculated field might be shifted in phase with respect to the beam generated phase, and we denote this phase-shift ϕ. The total multiplication factor for the recirculated field is then given by the phasor $ge^{i\phi}$. For $\phi \neq 0$ the total field at the PETS output will in general not be in phase with the beam generated field, and we will denote the total field phase with respect to the beam generated field phase by θ. We will use a tilde ($\sim$) to indicate that the field is given by the complex phasor

$$\tilde{E} = Ee^{i\theta}.$$

For clarity we will still write fields in phase with the beam generated field (which with our definitions is a real quantity) without the tilde.

If at time m the field at the PETS output is E_m, this field, multiplied by $ge^{i\phi}$, will one recirculation cycle later add to the field generated by the interaction of the beam with the PETS impedance, E_{beam}, yielding a total field of

$$\tilde{E}_{m+1} = \tilde{E}_m ge^{i\phi} + E_{\text{beam}}, \tag{4.23}$$

where E_{beam} was derived in Eq. (4.11).

4.4.2 PETS fundamental mode field with recirculation

For steady state conditions with constant beam intensity, I, we can find analytic expressions for the steady state amplitude and phase of the total PETS field. Using Eq. (4.23) the total field after M full recirculation cycles can be written

$$\tilde{E}_M = E_{\text{beam}} \sum_{m=0}^{M} ge^{i\phi} \equiv E_{\text{beam}} \left\{ \frac{1 - g^{M+1}\exp(i(M+1)\phi)}{1 - g\exp(i\phi)} \right\}. \tag{4.24}$$

The *steady state solution* $M \to \infty$ yields the field

$$\tilde{E}_{ss} = \frac{E_{\text{beam}}}{1 - g\exp(i\phi)} = \frac{E_{\text{beam}}}{\sqrt{1 - 2g\cos\phi + g^2}} \exp\left\{ \arctan\left(\frac{g\sin\phi}{1 - g\cos\phi}\right) \right\}, \tag{4.25}$$

and a steady state field phase

$$\theta_{ss} = \arctan\left\{ \frac{g\sin\phi}{1 - g\cos\phi} \right\}.$$

After the beam has passed the PETS the driving term, E_{beam}, in Eq. (4.23) will not be present anymore. Assuming that steady state has been reached, we see from Eq. (4.23) that the field will *decay* according to

$$\tilde{E}_P = \tilde{E}_{ss}(ge^{i\phi})^P, \tag{4.26}$$

where P is the number of full recirculation cycles after the beam has passed. For a *perfect recirculation phase* ($\phi = 0$) the steady state field, Eq. (4.25), reduces to

$$E_{ss,\phi=0} = \frac{E_{\text{beam}}}{1 - g}, \tag{4.27}$$

and zero relative steady state field phase.

4.4.3 PETS output power with recirculation

The PETS output power, including the effect of recirculation, is still related to the PETS output field by Eq. (4.12). In this chapter we are mainly concerned with the output power amplitude, which is found by squaring the absolute value of the field phasor, Eq. (4.24), yielding

$$P_M = \frac{\mathrm{Abs}(\tilde{E}_M)^2}{(R'/Q)\omega_{\mathrm{rf}}} v_g. \tag{4.28}$$

4.4.4 PETS voltage with recirculation

In the case of no recirculation the PETS peak voltage seen by the beam particles is given by Eq. (4.15)

$$\hat{U} = \frac{1}{2} E_{\mathrm{beam}} L_{\mathrm{PETS}},$$

where the factor $\frac{1}{2}$ entered because the beam generated field builds up stepwise in the PETS. With field recirculation, the circulated field enters the PETS and passes through it, only affected by ohmic losses (which we have included in the total gain factor g). This circulating field also contributes to the voltage, but without the factor $\frac{1}{2}$. Furthermore, a particle travelling through the PETS will only see the part of the field in phase with its motion, with our definitions corresponding to the real part of the field. Thus due to the recirculation, the energy loss increases by a term

$$\hat{U}_{circ,M} = \Re(\tilde{E}_{circ,M}) L_{\mathrm{PETS}},$$

where $\tilde{E}_{circ,M}$ is the total field circulated into the PETS after M full recirculation cycles

$$\tilde{E}_{circ,M} = E_{\mathrm{beam}} \sum_{m=1}^{M} g^m e^{im\phi}. \tag{4.29}$$

Note that the summation in Eq. (4.29) starts from one, unlike the summation for the total output field, $\tilde{E}_M$, in Eq. (4.24). Expressing the total energy loss in terms of the total output field we get

$$\hat{U}_M = \hat{U}_{circ,M} + \hat{U}_{\mathrm{beam}} = \left(\Re(\tilde{E}_M) - \frac{1}{2} E_{\mathrm{beam}} \right) L_{\mathrm{PETS}}, \tag{4.30}$$

while the mean beam energy loss is found by combining Eqs. (4.17) and (4.30)

$$\langle U_M \rangle = \left(\Re(\tilde{E}_M) - \frac{1}{2} E_{\mathrm{beam}} \right) L_{\mathrm{PETS}} F(\lambda). \tag{4.31}$$

The *steady state solution* $M \to \infty$ is found by substituting the real part of Eq. (4.25) into Eq. (4.31), yielding

$$\langle U_{ss} \rangle = \frac{1}{2} E_{\mathrm{beam}} L_{\mathrm{PETS}} F(\lambda) \left(\frac{2(1 - g\cos\phi)}{1 - 2g\cos\phi + g^2} - 1 \right), \tag{4.32}$$

which, for a *perfect recirculation phase* ($\phi = 0$), becomes

$$\langle U_{ss,\phi=0} \rangle = \frac{1}{2} E_{\text{beam}} L_{\text{PETS}} F(\lambda) \frac{1+g}{1-g}. \tag{4.33}$$

PETS voltage deduced from the output POWER

The energy loss can be calculated in an alternative and equivalent way, considering the PETS output power P. The power out of the PETS must equal the power circulated back into the PETS plus the power generated by the beam, $P_{\text{beam}} = P$, given by Eq. (4.13). The power circulated back into the PETS is by our definitions g^2 times the PETS output power one recirculation cycle earlier. The PETS output power after M full recirculation cycles can thus be expressed simply as

$$P_M = g^2 P_{M-1} + P_{\text{beam}}. \tag{4.34}$$

The power extracted from the beam can also be written as

$$P_{\text{beam}} = \langle U_M \rangle I \eta_{\Omega,\text{PETS}}. \tag{4.35}$$

Combining Eqs. (4.34) and (4.35) we can therefore express the mean voltage seen by the beam as

$$\langle U_M \rangle_{\text{POW}} = \frac{1}{I \eta_{\Omega,\text{PETS}}} (P_M - g^2 P_{M-1}), \tag{4.36}$$

which can indeed be shown to be equivalent to Eq. (4.31). This equivalence is shown in Appendix D.

4.4.5 Recirculation of the PETS dipole wake

It is expected from the PETS design that most of the energy of the transverse modes is stored in the slots [67] and will therefore neither be coupled out nor recirculated [75], and this issue is not pursued further here.

4.4.6 Example for a 1 meter long PETS

For illustration, Figure 4.10 shows the power, relative field phase and voltage for the same 1 meter PETS and 5 A beam as described in the example in Section 4.2.6, but now including the effect of recirculation, computed using Eq. (4.23). The power and energy loss without recirculation correspond to the first plateau in the plots. Examples for two different recirculation scenarios are shown: in scenario (a), presented in the left column of the figure, the recirculation settings are g=0.5 and $\phi = 0$ (a possible scenario for a CLIC machine with recirculation), in scenario (b), presented in the right column of the figure, the recirculation settings are g=0.75 and ϕ = -18° (the actual identified recirculator settings for the CTF3 PETS tests in 2008, as discussed further

in Section 4.5.3). The recirculation round-trip time is here set to $t_{\mathrm{circ}} = 26$ ns (also as identified for the CTF3 PETS tests [82]). The fill-time is assumed to be negligible with respect to the round-trip time.

With respect to the energy loss without recirculation, calculated in Section 4.2.6, the steady state energy loss for scenario (a) is increased by a factor 3 and for scenario (b) by a factor 3.2, in correspondence with Eqs. (4.32) and (4.33). With respect to the power production without recirculation, the power in scenario (a) is increased by a factor 4, and in scenario (b) by a factor 7.4, in correspondence with Eqs. (4.26), (4.27) and (4.28). In scenario (b) the total power is almost a factor two higher than in scenario (a), while the energy loss is only slightly higher. This occurs because in scenario (a) the recirculated field builds up quicker due to the larger g, while it is not completely in phase with the beam due to the non-zero recirculation phase ϕ, and therefore do not decelerate the beam as much (we remind that the power discussed here is the total power flowing out of the PETS, not only the power in phase).

Finally, we note the dip into negative voltage in Figure 4.10(f), due to the rotation of the field phasor by more than 90°. A sufficiently small charge entering the PETS in this time (after the mean pulse has passed) will thus be accelerated.

4.5 First 12 GHz PETS experiments with beam in the CTF3 TBTS

The first 12 GHz CLIC power extraction and transfer structure was first tested with beam in the Two-beam Test Stand (TBTS) [68] in the CLIC Test Facility 3 [60] in November and December 2008.

4.5.1 The Two-beam Test Stand

The Two-beam Test Stand (TBTS) is a unique and versatile facility devised to test key components of two-beam acceleration [68]. Worldwide it is the only facility where CLIC type power production (combining PETS and accelerating structures) can be tested with beam. The prototype PETS mounted in the TBTS is equipped with an external field recirculator [83], in order to more rapidly reach the power level specified for the CLIC PETS (135 MW [38]). The recirculator is equipped with a remotely controlled splitter for adjusting the percentage of the field being recirculated, and a remotely controlled phase-shifter for adjusting the phase of the recirculated field. The TBTS PETS with recirculator will be modelled using the expressions developed in Section 4.4, and the gain g and phase ϕ in Eqs. (4.23) to (4.36) can thus in principle be adjusted during operation. Within the individual pulses, however, g and ϕ remain constant in our formalism.

The thesis work included responsibility for the data acquisition and TBTS experiments co-ordination during the 2008 run as well as the analysis of the data logged during this run [69, 82, 86]. The work did not include design nor construction of the TBTS; the

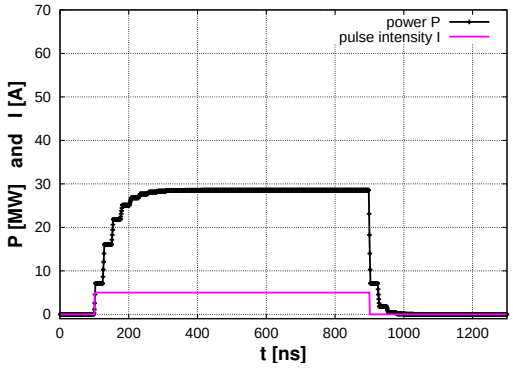

(a) Rf power, g=0.5 and ϕ=0°

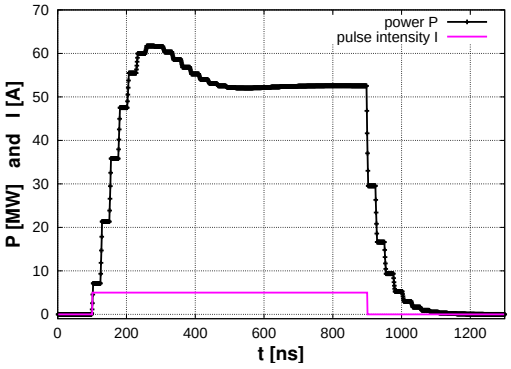

(b) Rf power, g=0.75 and ϕ=-18°

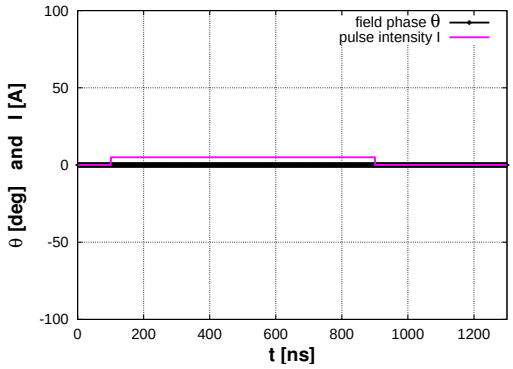

(c) Rf field phase, g=0.5 and ϕ=0°

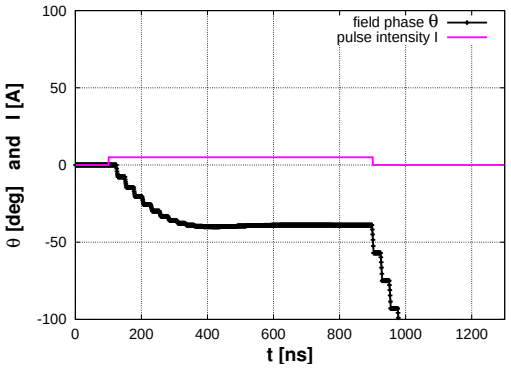

(d) Rf field phase, g=0.75 and ϕ=-18°

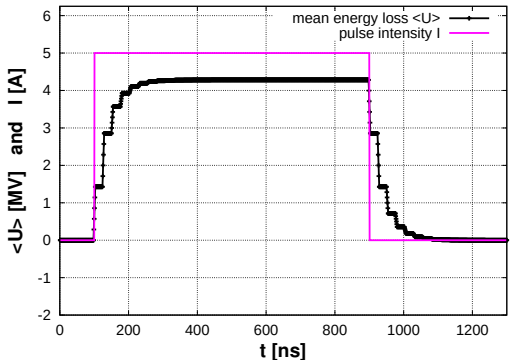

(e) Energy loss, g=0.5 and ϕ=0°

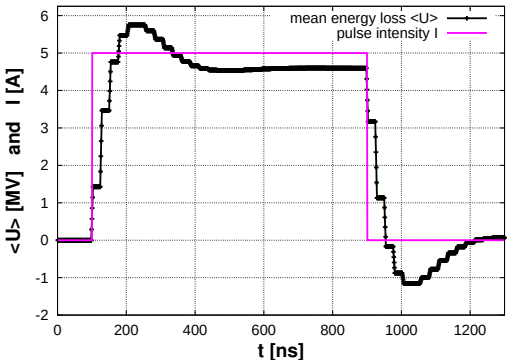

(f) Energy loss, g=0.75 and ϕ=-18°

Figure 4.10: Computed power, field phase and energy loss for a rectangular beam pulse passing through a 1 meter PETS with external recirculation. Left column, scenario (a) with recirculator settings g=0.5 and ϕ=0°. Right column, scenario (b) with recirculator settings g=0.75 and ϕ=-18°. The upper row shows computed PETS output rf power, the middle row shows the computed PETS output field phase and the lower row shows the computed voltage in the PETS. In all the plots the pulse intensity is shown in magenta for reference. The steady state power and mean voltage without recirculation is 7.1 MW and 1.4 MV respectively, as calculated in the example in Section 4.2.6. In scenario (a) the steady state power is a factor 4 higher and the steady state energy loss a factor 3 higher than without recirculation. In scenario (b) the steady state power is a factor 7.4 higher and the steady state mean energy loss a factor 3.2 higher than without recirculation.

TBTS was constructed by Uppsala University [87], funded by the Swedish Research Council and the Knut and Alice Wallenberg Foundation.

4.5.2 The TBTS 2008 run

The TBTS consists of two parallel beam lines; one for the drive beam with PETS and one for the probe beam with accelerating structures. In the 2008 run only the drive beam was operational and power extracted from the PETS was terminated in a load. The Two-beam Test Stand in its December 2008 configuration is presented in Figure 4.11.

The first beam arrived in the TBTS PETS on 14 November 2008, and the beam pulse intensity increased gradually from a couple of amperes to a maximum of about 5 amperes on 11 December 2008 (the last day of operation in 2008).

The 2008 run was part of the TBTS commissioning and there were still issues with data signal timing and calibration that needed to be taken into account in the data analysis. A particular problem during this run was that *due to mechanical problems neither the splitter nor the phase-shifter could be remotely adjusted during the run, and the settings of neither were known a priori*, which made it necessary to identify the recirculator parameters as part of the data analysis. In addition the CTF3 machine was not always running in a stable fashion, e.g. klystron failure occurred regularly, leading to smaller or larger perturbation of the klystron working point. Nevertheless, from the data logged during the run (beam and rf signals), it was possible to perform a thorough analysis and in particular to study the agreement between the logged data and the model approach outlined in this chapter.

A detailed analysis of the run is found in [82]. In [86] the analysis is further extended by correlating three different ways of estimating the beam energy loss.

The results of the first beam tests of the CLIC power extraction and transfer structure in the Two-beam Test Stand were summarised and presented at the 19th European Workshop on Beam Diagnostics and Instrumentation for Particle Accelerators, DIPAC'09 [69], paper included in the Appendix B. Key results originating from the analysis of the TBTS 2008 run were in addition included as part of three different oral presentations at the 23rd IEEE Particle Accelerator Conference, PAC'09 [65, 88, 89].

4.5.3 Summary of the experimental results

Extending Eq. (4.24) to arbitrary beam pulse intensities [82], keeping all other model parameters constant, the BPM intensity measurements can be used to reconstruct the expected PETS output field, PETS output power, P_{rec}, as well as the relative field phase with respect to the beam generated field, θ_{rec}. The reconstructed rf quantities are then compared with measured rf quantities, P_{meas} and θ_{meas}.

Similarly, the energy loss can be calculated from Eq. (4.31) for arbitrary pulse intensities,

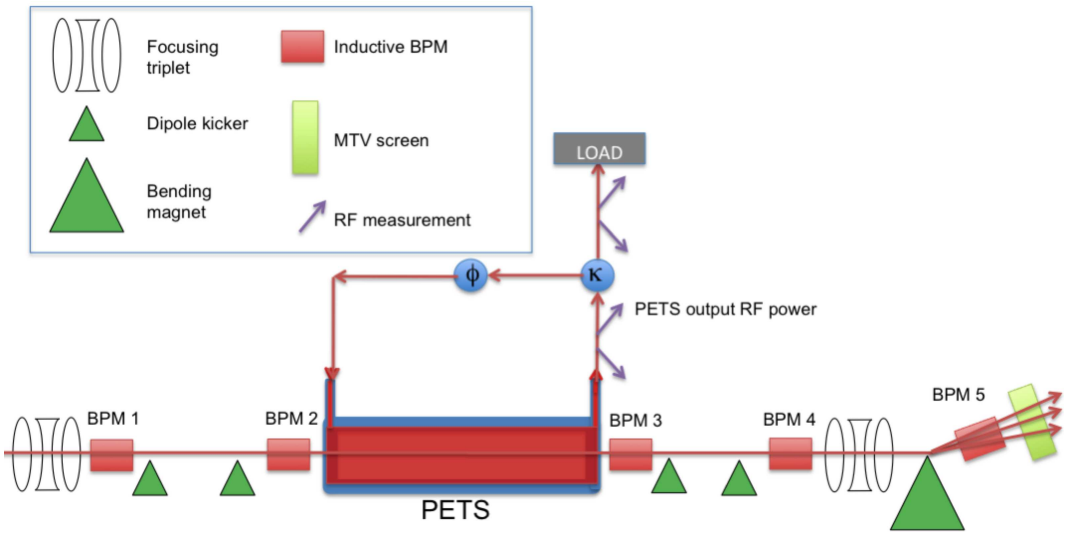

(a) Sketch of the Two-beam Test Stand - December 2008 configuration (not to scale)

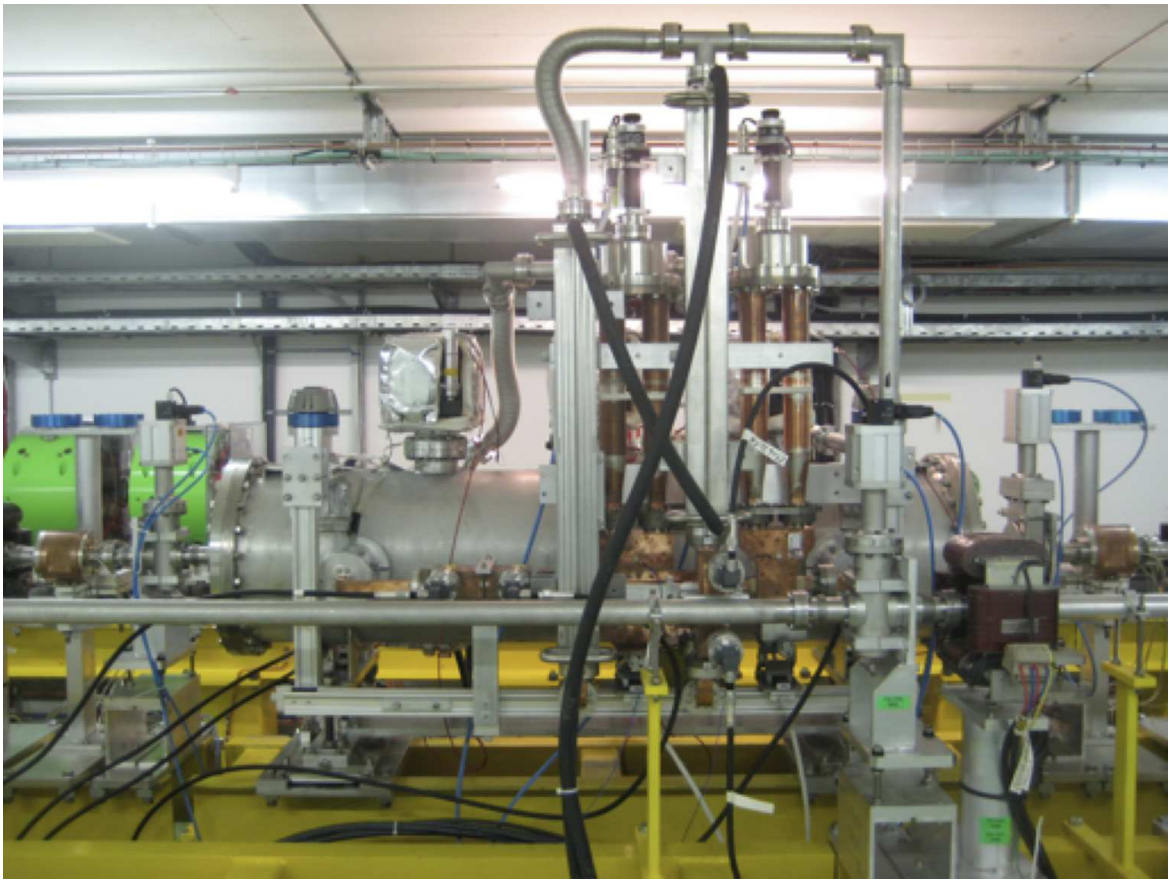

(b) TBTS PETS tank, field splitter and phase-shifter

Figure 4.11: The Two-beam Test Stand (TBTS). (a) Sketch of the TBTS elements considered for the experimental results reported in this thesis. (b) Photo of a Two-beam Test Stand PETS tank. The left-most copper structure in front of the tank is the field splitter while the right-most is the phase-shifter. One inductive BPM is seen on each side of the PETS tank. In the foreground the beam line for the TBTS probe beam is seen; at this point no accelerating structures were installed in this line.

using either the reconstructed power and the measured beam pulse intensity, U_{rec}, or the measured power combined with the measured pulse intensity U_{meas}. In addition the energy loss can be estimated independently from rf measurements using the BPM in the spectrometer line, U_H, with the technique outlined in [90]. The three estimation approaches can then be compared [86].

In order to identify the unknown recirculation parameters, a continuous series of 200 logged pulses was used. The series was extracted from a period where no significant shortening of the pulses was observed, since our model approach is only valid for nominal PETS operation. It was also mandatory to fit a constant factor, because the output power depends strongly on the bunch length (e.g. increasing the bunch rms length from 1 mm to 2 mm reduces the power production by 17%), and no drive beam bunch length measurements had been performed in the CLEX area at the time of writing. Measurements done some time before the TBTS run indicated a relatively long bunch in CTF3 before the combiner ring of order $\sim$ 1.5 mm to 2 mm [91], but these measurements are not necessary valid for the CLEX bunch length during the TBTS run. A three-parameter fit [82] gave as results $g = 0.75$, ϕ = -18° and $k = 0.78$ where k is the scaling factor needed to fit the reconstructed model assuming nominal PETS parameters and a form factor $F(\lambda) = 1$. The scaling factor, k, thus lumps deviations from the PETS nominal parameters, calibration errors as well as the unknown form factor. If the PETS power production would be as expected from Eq. (4.13), and perfect signal calibration is assumed, $k = 0.78$ would imply to a bunch length of 2.8 mm [82]. In other words, when or if all TBTS and PETS signals are fully understood and calibrated to high precision, the PETS power production would also provide a high precision bunch form-factor measurement.

We end this chapter by presenting measured and reconstructed PETS output power, field phase and energy loss for a few pulses, to show the agreement between the simple modelling approach presented in this chapter and the TBTS measurements. All model parameter stay the same for all pulses. We distinguish between pulses where the measured rf pulse length is comparable to the measured BPM intensity pulse length (nominal pulses) and pulses where the rf pulse length is considerably shorter than the BPM intensity pulse length (shortened pulses). The pulse shortening is believed to be due to rf breakdown [31] in the PETS or other parts of the rf network, as the beam tests were performed simultaneously with the rf conditioning of the PETS (no rf conditioning was performed prior to the beam tests). At this stage of the commissioning, the BPM signals did not allow for precise enough kick measurements to perform a detailed study of the dipole wake, however, significant kicks were identified for some shortened pulses [69]. More pulses and a more detailed discussion about the agreement model and measurements are found in [82] and [86].

Pulses showing no rf pulse shortening

Our constant parameter recirculation model used for fit and reconstruction showed reasonable agreement for logged pulses in the series, regardless of the beam intensity profile

(which varied quite a lot during the data logging [82]); the rms difference of the measured and reconstructed power pulses lies within 10% for 75% of the pulses in the series used for the fit. The rms difference between the three estimations of the beam energy loss lies within 20% for 75% of the pulses [86].

In Figures 4.12 and 4.13 we present four pulses with different power level and pulse shape in order to demonstrate to which degree our approach handles a variety of different BPM pulse intensity profiles. The reconstruction does not take into account the transient effects at the beginning of the pulse, and some discrepancies occur due to imperfections of the measured signals [82]. Apart from that, the physics of the PETS operation with recirculation seem to be reasonably well explained by the modelling approach developed in this chapter. Finally, it must also be noted that the most important conclusion of the first 12 GHz PETS with beam was the excellent performance of the PETS itself - a big step towards showing the feasibility of two-beam acceleration.

Pulses showing rf pulse shortening

For a number of pulses logged there is a clear shortening of the rf pulse length with respect to the BPM intensity pulse length. This is seen most readily by comparing the reconstructed rf power and the measured rf power.

In Figure 4.14 we present two shortened pulses to illustrate the observed pulse shortening during the TBTS run. The measured power and phases of these pulses show different behaviour; for the pulse numbered "4-1" the power descends monotonously to zero while for the pulse numbered "7-455" the measured power at some point increases slightly after having descended monotonously. The energy loss estimate based on the BPM spectrometer still gives information about the real energy loss, while the two other estimates are not valid for shortened pulses [86].

The different behaviour of the shortened pulses might indicate different locations of an eventual breakdown, but this is a subject for a study of its own. By extending the simple constant-parameter system model used here, by varying parameters along the pulse, or by introducing new parameters, it is clear that the agreement between the reconstructed and measured power, phase and energy loss can be improved. E.g. by varying several parameters along the pulse, [85] fits the reconstructed and measured power and phase well.

We believe, however, that it is an important point that PETS operation under nominal conditions apparently can be well described using simple constant-parameter models as developed in this chapter. Other physics, e.g. the occurrence of rf breakdown, can then be more easily studied as deviations from the constant-parameter model. By combining models of the physics of breakdown with varying parameter modelling, the TBTS may thus be a very powerful tool to study the physics of breakdown. Such work is outside the scope of this thesis and will be addressed in future TBTS sessions. However, the first PETS beam tests have demonstrated excellent capability of the Two-beam Test Stand as a test-bench for both breakdown studies as well as nominal PETS operation.

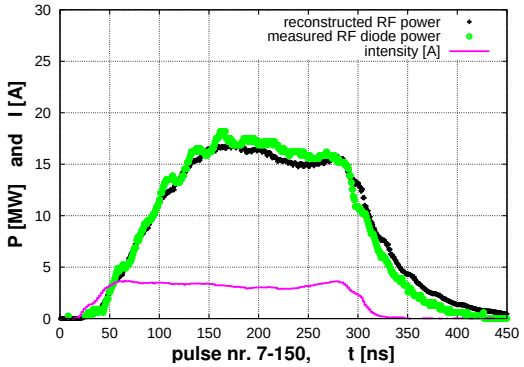

(a) Rf power, pulse nr. 7-150

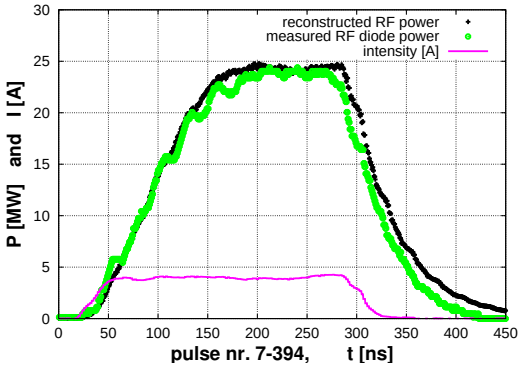

(b) Rf power, pulse nr. 7-394

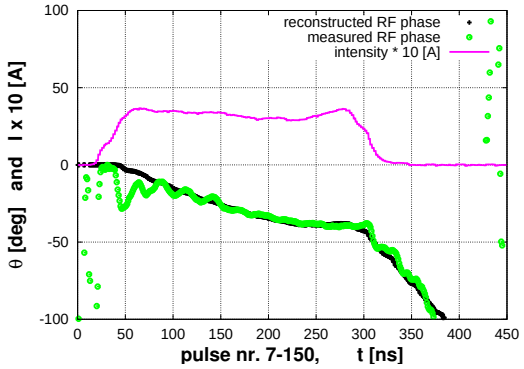

(c) Rf field phase, pulse nr. 7-150

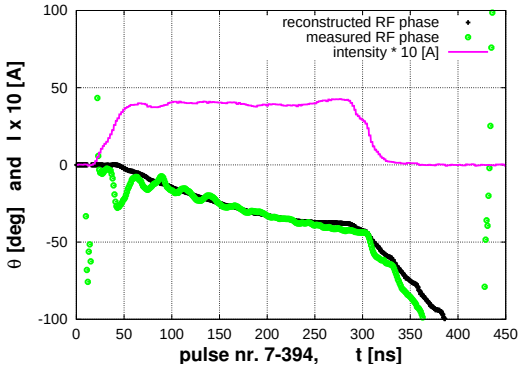

(d) Rf field phase, pulse nr. 7-394

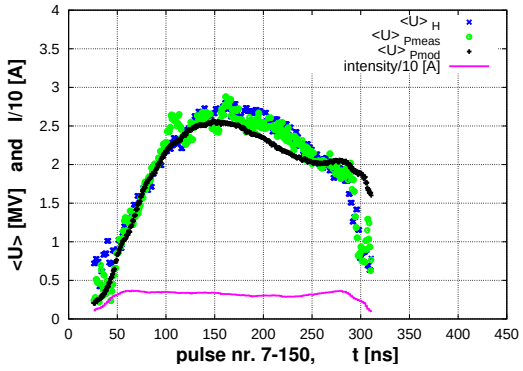

(e) Energy loss, pulse nr. 7-150

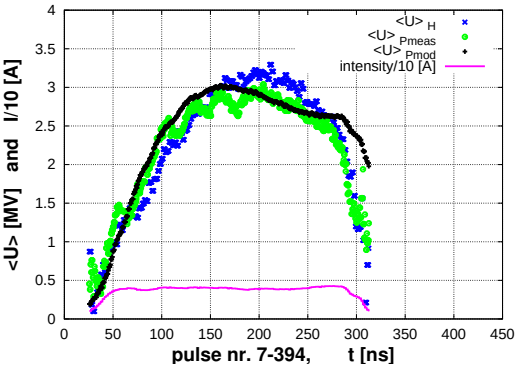

(f) Energy loss, pulse nr. 7-394

Figure 4.12: Reconstructed and measured rf and beam quantities for two pulses showing no rf shortening. Left column: a 17 MW pulse. Right column: a 25 MW pulse. The upper row shows reconstructed and measured PETS output rf power, the middle row shows reconstructed and measured PETS output field phase, the lower row shows the reconstructed and measured beam energy loss in the PETS. Reconstructed values are shown in black (+), measured values are shown in green (o). In the lower row, the energy loss estimated using the spectrometer dipole is shown in blue (x). In all the plots the pulse intensity is shown in magenta for reference.

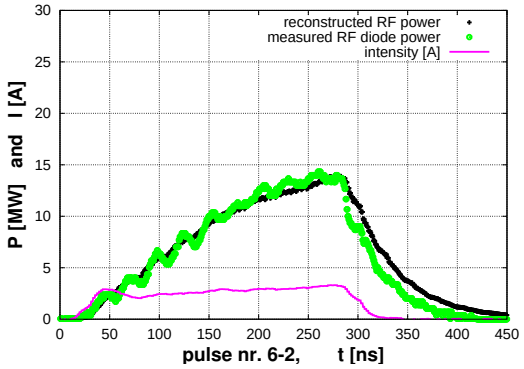

(a) Rf power, pulse nr. 6-2

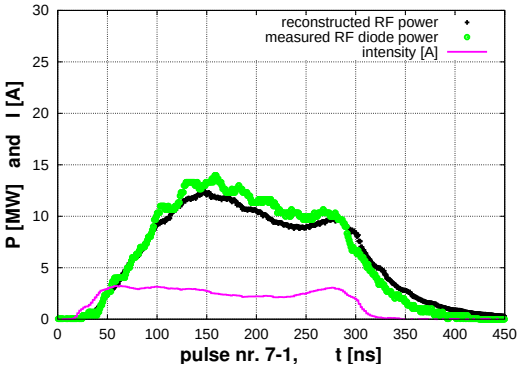

(b) Rf power, pulse nr. 7-1

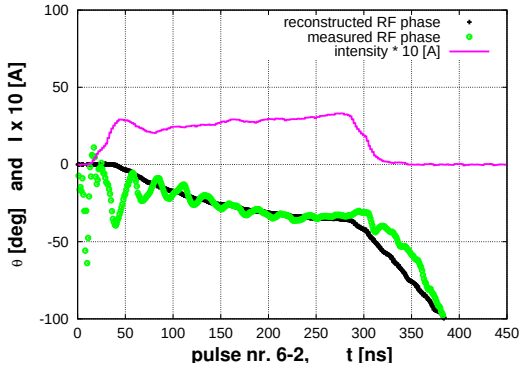

(c) Rf field phase, pulse nr. 6-2

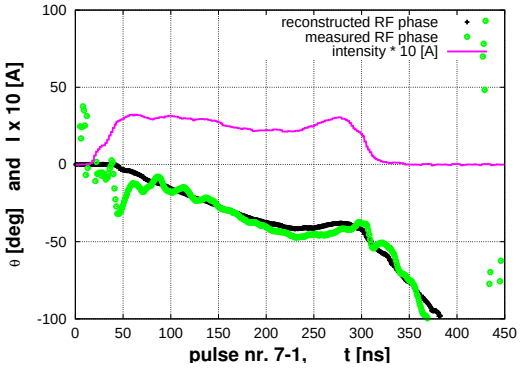

(d) Rf field phase, pulse nr. 7-1

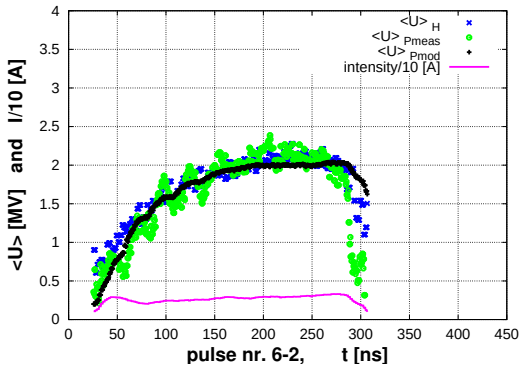

(e) Energy loss, pulse nr. 6-2

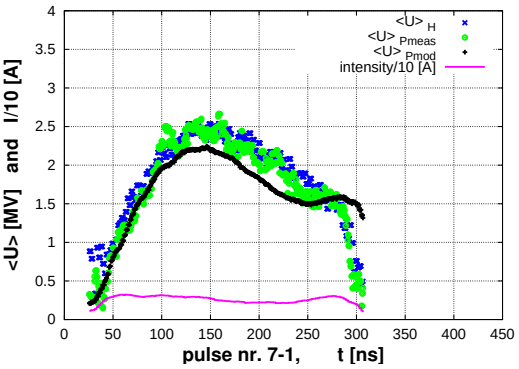

(f) Energy loss, pulse nr. 7-1

Figure 4.13: Reconstructed and measured rf and beam quantities for two pulses showing no rf shortening. Left column: a 14 MW pulse, with monotonous increase and decrease in the rf power. Right column: a 13 MW pulse with a notably different beam intensity profile. For both pulses the simple constant-parameter model gives a reasonable agreement between measurements and reconstruction. The upper row shows reconstructed and measured PETS output rf power, the middle row shows reconstructed and measured PETS output field phase, the lower row shows the reconstructed and measured beam energy loss in the PETS. Reconstructed values are shown in black (+), measured values are shown in green (o). In the lower row, the energy loss estimated using the spectrometer dipole is shown in blue (x). In all the plots the pulse intensity is shown in magenta for reference.

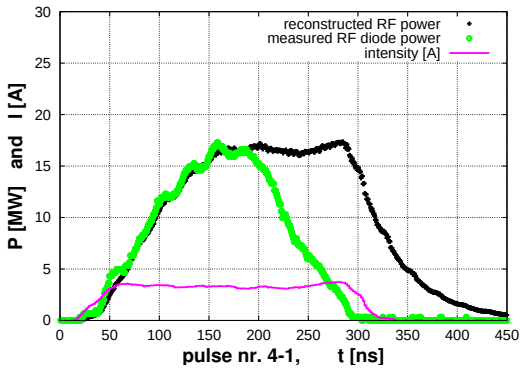

(a) Rf power, pulse nr. 4-1

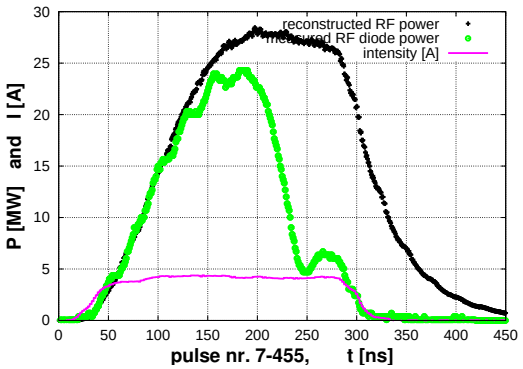

(b) Rf power, pulse nr. 4-455

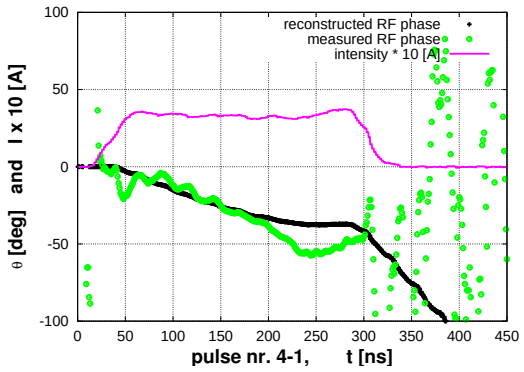

(c) Rf field phase, pulse nr. 4-1

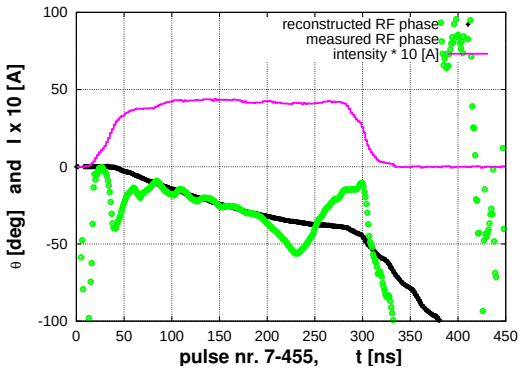

(d) Rf field phase, pulse nr. 4-455

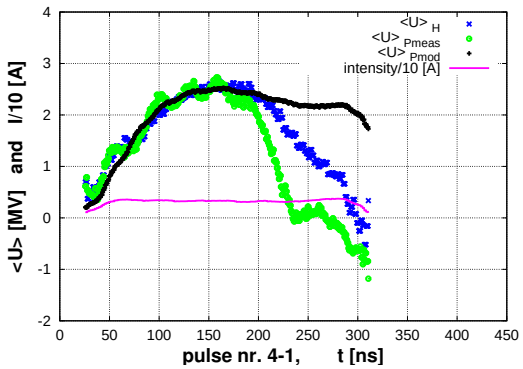

(e) Energy loss, pulse nr. 4-1

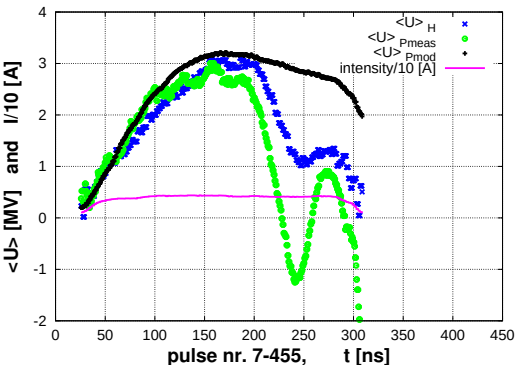

(f) Energy loss, pulse nr. 4-455

Figure 4.14: Reconstructed and measured rf and beam quantities for two shortened pulses. Left column: a shortened pulse with peak power of 17 MW where the measured power drops monotonously to zero. Right column: a 25 MW pulse where the measured power drops monotonously to recover slightly and rise again until it drops to zero. The upper row shows reconstructed and measured PETS output rf power, the middle row shows reconstructed and measured PETS output field phase, the lower row shows the reconstructed and measured beam energy loss in the PETS. Reconstructed values are shown in black (+), measured values are shown in green (o). In the lower row, the energy loss estimated using the spectrometer dipole is shown in blue (x). In all the plots the pulse intensity is shown in magenta for reference.

5. Decelerator Beam Dynamics

The sole purpose of the CLIC electron drive beam is to generate rf power for the accelerating structures. This power must be generated timely and uniformly along each decelerator sector, shown in Figure 3.3, and at the same time a high energy extraction efficiency must be achieved. Uniform and stable power production implies that the beam must be transported to the end with very small losses.

The PETS introduces a particularly large energy spread in the drive beam, and it is important to ensure transport of particles in the whole energy range in order to minimise losses. This implies that the dispersive effects have to be considered with special care. The PETS transverse wakes, introduced in Chapter 4, are another major challenge to minimal loss transport. These effects combined render the beam dynamics in the drive beam a novel challenge, and we will in this chapter outline how this challenge has been addressed in the framework of this thesis.

The most important results have been presented in four papers included in Appendix B. The first paper [81], presented at the 44th ICFA Workshop on X-Band rf Structure and Beam Dynamics (The Cockroft Institute, United Kingdom, 2008) summarises the key topics of the beam dynamics studies performed for the CLIC decelerator in the framework of this thesis. The second paper [92], presented at the 11th biennial European Particle Accelerator Conference (EPAC'08, Genova, Italy, 2008), investigates the need for advanced orbit correction for the CLIC decelerator, and proposes correction schemes, shown by simulation to perform satisfactory. The third paper [93], presented at the 11th biennial European Particle Accelerator Conference (EPAC'08, Genova, Italy, 2008), investigates a number of failure scenarios for the decelerator. The fourth paper [94], presented at the XXIV Linear Accelerator Conference (LINAC'08, Victoria, Canada, 2008) reports on correction experiments performed in the linac of the CLIC Test Facility 3, thus demonstrating on a real machine the algorithms studies of [92]. In addition, the beam dynamics studies have been a vital input to the 12 GHz PETS design leading to the paper [67], included in Appendix B. In this chapter we will take the occasion to elaborate on the underlying physical principles for the results in these papers and CLIC specifications.

The thesis work has also resulted in formal specifications input to the CLIC study, included in Appendix C, concerning two of the main components of the decelerator; a quadrupole specification [95] and a BPM specification [96]. The specifications illustrate the fact that a thorough understanding of the beam dynamics is necessary in order to

pin down clear specifications for hardware components.

The work in this chapter partially builds on and extends earlier decelerator studies, reported in [53, 79, 97–99].

5.1 Energy spread and focusing strategy

5.1.1 Pulse energy profile after deceleration

The beam dynamics in the CLIC drive beam decelerator is driven by the physics of the power extraction and transfer structure. The stability of the drive beam depends on how much energy the decelerator extracts in form of rf power. As baseline specification a fraction

$$\eta_{\text{extr}} = \frac{E_0 - E_{\text{min}}}{E_0} = 90\% \tag{5.1}$$

of the energy shall be extracted from the most decelerated particles, where E_0 is the drive beam energy at decelerator injection and E_{min} the minimum particle energy at the dump. In this work the value of η_{extr} is considered an input to the study from [38], where the choice of 90% originates from a compromise between efficiency and envelope growth.

Each PETS will ideally extract the same amount of energy from the beam, and the energy of the most decelerated particles, E_{most}, will decrease linearly with the number of PETS passed along the lattice

$$E_{\text{most}}(n) = E_0(1 - \eta_{\text{extr}}\frac{n}{N_{\text{PETS}}}), \tag{5.2}$$

where n is the number of PETS the beam has passed and N_{PETS} the total number of PETS per sector. $E_{\text{most}}(N_{\text{PETS}})$ corresponds to E_{min}. Figure 5.1 shows the energy profile along the drive beam train at the entrance and at the exit of the decelerator, as simulated with PLACET. We note first that the head of the pulse is decelerated very little (the PETS has not yet been loaded). At the end of the decelerator the least decelerated particles are therefore 10 times more energetic than the most decelerated particles, as can be observed from Figure 5.1. We note also that in the steady state regime each bunch have a substantial energy spread as well, with energy ranging from 0.24 GeV to about 1 GeV. In this chapter we work with, the beam energy, here denoted E, since this quantity is more relevant for the beam dynamics studies than the energy loss, U.

Comparing Figure 5.1(b) with the bunch energy loss in the 1 meter PETS simulated in Figure 4.6(b), we note that the asymmetry due to single-bunch wake effects is more pronounced in the short CLIC PETS, due to the smaller N_{fill} (only 10 bunches are needed to fill the 21 cm long decelerator PETS). Because N_{fill} is relatively small, there is a discrepancy of about 3% between the maximum deceleration found from Eq. (4.15) and the PLACET calculation (cf. the discussion in Section 4.2). For the decelerator

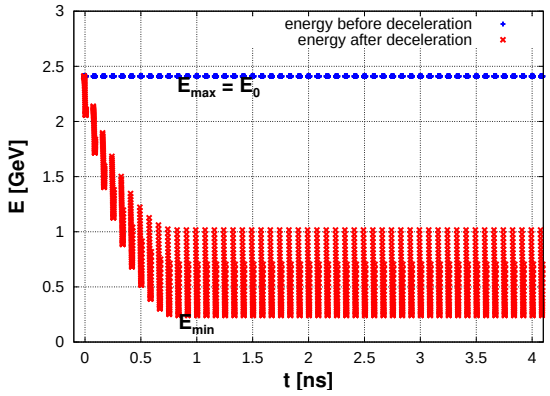

(a) Beam energy profile (first 4 ns)

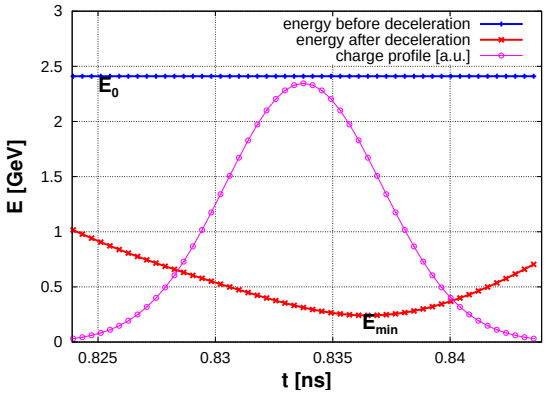

(b) Bunch energy profile (steady state)

Figure 5.1: Decelerator beam energy profiles at injection, in blue (+), and after having passed through an entire sector, in red (x). The Gaussian bunch charge profile is shown, in magenta (o), for clarity. The final energy of the most decelerated particles, E_{min}, is a factor $(1 - \eta_{\text{extr}}) = 0.10$ times the initial energy, E_0. The least decelerated particles lose a negligible amount of energy, and their energy is therefore $E_{\text{max}} = E_0$.

simulations we rely on PLACET calculations in order to ensure an η_{extr} of exactly 90% in the simulations. The asymmetry in the bunch deceleration implies that a relatively smaller part of the total beam energy is extracted with respect to a symmetric bunch deceleration (for a constant η_{extr}), because the peak deceleration is not at the peak charge. In the CLIC drive beam efficiency factor, Eq. (3.2), the corresponding reduction in extraction efficiency is taken into account by the factor η_{dist} (calculated by simulation). In principle the single-bunch effects can be compensated for by frequency detuning, as explained in [99], however, detuning was shown to increase envelope growth due to wake fields (discussed in Section 5.4), and is therefore not part of the CLIC baseline design.

It is important to note that even though the high-energy transient only last for $t_{\text{fill}} \approx 1$ ns, containing less than 0.5% of the train charge, it must be transported through the decelerator equally well as the steady state part. This is because if part of the transient is lost, a new energy transient will build up, potentially leading to continuous losses along the lattice.

5.1.2 Lattice and focusing strategy

To mitigate the effect of the PETS transverse wakes, tight transverse focusing is required along the decelerator. The present baseline design is based on alternating gradient focusing-defocusing (FODO) cells [23], with two quadrupoles installed per CLIC module [38], leading to a FODO cell length of 2.01 m. Between each quadrupole zero, one or two 21 cm long PETS will be installed, depending on how many accelerating structures are installed in the CLIC module. As example, Figure 3.2 shows a CLIC

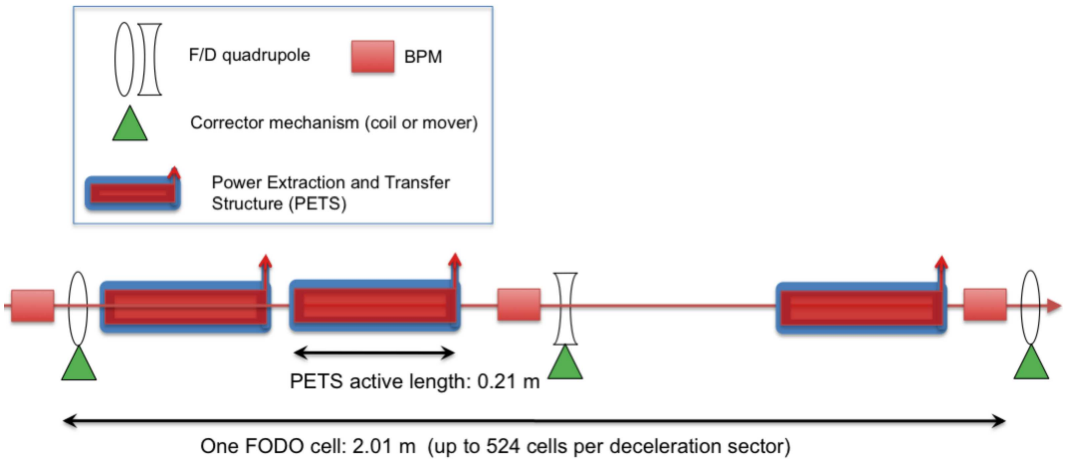

Figure 5.2: Decelerator lattice structure. Transverse focusing is performed by alternating gradient focusing-defocusing (FODO) cells, where the quadrupole gradient decreases along the lattice to keep the phase-advance of the most decelerated particles constant. Between each quadrupole zero, one or two PETS are installed.

module with one PETS in the first half and two PETS in the second half of the drive beam line. As the number of accelerating structures per module vary with the main beam energy, the average number of PETS per module varies as well along the decelerator. Since $\eta_{\text{extr}} = 90\%$ is enforced for every decelerator sector it implies that the sector length varies in order to incorporate the same number of PETS. In the beam dynamics studies the longest decelerator sector, with length $L_{\text{sector}} = 1053$ m (consisting of $N_{\text{FODO}} = 524$ FODO cells) is normally simulated. We often conveniently refer to this sector as "the decelerator".

The decelerator focusing strategy, suggested in [97], is to scale the quadrupoles so that the most decelerated particles experience a constant normalised quadrupole strength $k_{E_{\text{min}}}(n) = k_0$ along the lattice (the corresponding FODO cell phase-advance is $\phi_{\text{FODO}} = 92.5°$). From Eq. (5.2) and the relation $k \propto g/E$ where g is the quadrupole gradient, we see that the least decelerated particles necessarily experience a gradually weaker focusing given by

$$k_{E_0}(n) = k_0(1 - \eta_{\text{extr}}\frac{n}{N_{PETS}}). \tag{5.3}$$

This focusing strategy implies that the gradient of two adjacent quadrupoles should ideally be adjusted in steps of down to 50 mT/m, depending on how many PETS are installed between the two (one, two or zero). Studies have shown, however, that a more coarse gradient tapering might be acceptable, as discussed further in the decelerator quadrupole specification [95], included in Appendix C. Another important implication of the focusing is a relatively tight energy acceptance at the decelerator injection; particles injected with energy ∼3% lower than the nominal, or less, will be lost due to unstable focusing to the end of the lattice, as further discussed in [93].

5.2 Framework for the transverse dynamics studies

5.2.1 Betatron motion

We will adopt a Courant-Snyder like formalism [100] in order to describe the transverse motion of particles in the decelerator. For motion along a linear lattice, only part of the framework in [100] is needed. We here develop the relevant quantities for the decelerator, following [23]. In the decelerator both transverse planes have equal beam dynamics, and the coupling between the planes is very small. When analysing transverse motion we will use the symbol y to describe the transverse position of particles, however, the analyses are equally applicable to the x-plane. In the linear approximation transverse motion of particles is governed by the homogenous Hill's equation

$$y'' + K(s)y(s) = 0, \tag{5.4}$$

where $K(s)$ is the focusing function along the lattice. Eq. (5.4) can be reformulated by seeking a solution of the form

$$y(s) = \sqrt{2J\beta(s)}\cos(\phi(s) + \phi_0), \tag{5.5}$$

yielding the constraints

$$\phi(s) = \int_0^s \frac{d\sigma}{\beta(\sigma)} \tag{5.6}$$

and

$$\frac{1}{2}\beta(s)\beta'' - \frac{1}{4}\beta'^2 + K(s)\beta^2(s) = 1. \tag{5.7}$$

Beta function

From Eq. (5.5) we see that the function $\beta(s)$, which evolves according to Eq. (5.7), quantifies the focusing properties of a beam line lattice. $\beta(s)$ is typically referred to as the betatron amplitude function or, as we will adopt, the "beta function".

Particle action

The particle action, J, defined in Eq. (5.5) is equal to 2π times the area of the transverse phase-space of the state-vector $[y\ y']^T$ describing the particle motion (alternatively, we could have used the Courant-Snyder invariant, $\epsilon = 2J$, to quantify the phase-space area). When a particle undergoes betatron oscillations, with the beta function evolving according to Eq. (5.7), J is an invariant of the motion. J can be calculated from Eq. (5.5) and expressed as [23]

$$2J = \gamma(s)y^2(s) + 2\alpha(s)y(s)y'(s) + \beta(s)y'^2(s) \tag{5.8}$$

where we, as customary, have defined the Courant-Snyder parameters

$$\alpha(s) \equiv -\frac{1}{2}\beta'(s) \tag{5.9}$$

and

$$\gamma(s) \equiv \frac{1+\alpha^2(s)}{\beta(s)}. \tag{5.10}$$

Initial phase-space

The drive beam will be injected into the decelerator FODO lattice with a phase-space assumed to be matched to the periodic solution of the start of the FODO lattice. The drive beam will quickly develop a large energy spread as it is decelerated (Figure 5.1) and we therefore opt to leave the beam phase-space picture after injection, as will be further explained in the next paragraphs.

Dispersive effects

In principle one could define dispersion functions by Taylor expansion of $y(s, E_a + \Delta E)$ around a sufficiently high energy. However, for our purposes we see no particular usefulness of such an approach. First, a large expansion order would be needed to give useful results, second, we are equally interested in particles of all energies. Instead, we will consider the beta function to vary with the particle energy, $\beta(s) = \beta(s, E(s))$. In our framework we thus interpret the beta function as a quantity linked to the individual particles. The rationale of this approach will be clear when we define metrics and criteria for the beam dynamic studies in Section 5.2.

Tune

The betatron phase, ϕ, will advance with different pace for particles of different energies according to Eq. (5.6) where $\beta(s) \to \beta(s, E(s))$. In analogy with circular machines we define the *tune* as the number of betatron oscillations along the entire lattice. In order to avoid confusion with the symbols for the PETS quality factors, we adopt in this thesis the American symbol for the tune: ν. The tune will vary with the final particle energy, E_{final}, according to

$$\nu(E_{\text{final}}) = \frac{1}{2\pi}\int_0^{L_{\text{sector}}} \frac{ds}{\beta(s, E(s))}. \tag{5.11}$$

The most decelerated particles have a tune of $\nu(E_{\text{min}}) = N_{\text{FODO}}\phi_{\text{FODO}}/2\pi = 135$, while the least decelerated particles have a tune of $\nu(E_0) = 70$. In the decelerator there is thus a huge intrinsic "tune spread". The tunes are given here up to the nearest integer, because unlike in rings, we are not particularly concerned with integer parts of the tune.

Smooth approximation

We will in some cases use a smooth approximate model of the betatron motion where the focusing function is averaged over the lattice. The equation of motion is then a simple harmonic oscillator

$$y'' + \frac{1}{\langle\beta\rangle^2} y(s) = 0 \tag{5.12}$$

with

$$\langle\beta\rangle = \frac{L_{\mathrm{FODO}}}{\phi_{\mathrm{FODO}}}, \tag{5.13}$$

which defines the average beta function. Eq. (5.13) is defined so that the phase-advance in the smooth approximation is equal to the phase-advance of real betatron motion for the same cell length.

5.2.2 Physics included in the simulations

The transverse beam size will grow along the decelerator due to a number of physical effects. The decelerator beam is an ultra-relativistic electron beam, to first order travelling in a straight line (the only bending fields in the decelerator lattice arise from quadrupole offsets and correction). The physics considered to be dominant for transverse beam growth in the decelerator are the transverse wake fields in the PETS (see Section 5.4), machine imperfections (see Section 5.5) and adiabatic undamping, present also for a perfect machine (see Section 5.3). The main tool for the beam dynamics studies has been the tracking code PLACET [73]. PLACET incorporates a PETS element which takes into account the PETS energy extraction, adiabatic undamping, rf-kicks and transverse dipole wakes. PLACET also includes an advanced framework for study of machine imperfections, where all machine components can be given arbitrary misalignment. PLACET is to date the only code that can realistically simulate PETS elements, and therefore also the CLIC decelerator. Space-charge and ion effects are not included in the PLACET simulations. These effects will be briefly discussed in Section 5.8. As there are no bending magnet elements in the line, synchrotron radiation effects, both coherent and incoherent, are expected to be very limited.

5.2.3 Modelling of the drive beam in PLACET

The PLACET drive beam is modelled as a train of bunches, where each bunch is sliced longitudinally (we use the terms ”train of bunches” and ”pulse” interchangeably in this text). For each slice a number of macro particles with different centroid motion, different energy and different second order moments to represent the transverse particle distribution, are tracked. The longitudinal charge-distribution is static (the particles do not change relative z-position during the tracking). Figure 5.3 illustrates the PLACET drive beam model. More details about the simulation models can be found in the PLACET manual [101].

In this work, 51 slices per bunch have been used for the simulations, ensuring convergence of single-bunch wake effects. A single macro particle per slice is used. The number of bunches simulated varies according to the subject under study (the simulation times increases by about the square of the number of bunches, so the full train length of 240 ns is usually not simulated), but at least 2 ns of the beam is always simulated in order to cover transient effects arising from the PETS beam loading, shown in Figure 5.1(a). For the dipole wake studies leading to e.g. the PETS design reported in [67], trains of lengths up to 100 ns were simulated in order to study in full eventual envelope growth along the beam. Gaussian longitudinal bunch charge distributions have been used, and the simulated beam intensity profile is rectangular (all simulated bunches are equally spaced, at 12 GHz, and contain the same charge).

5.2.4 Metrics for beam envelope growth

It is vital that all parts of the large energy-spread beam are transported in a robust manner through the entire decelerator. Since each simulated macro particle represents a chunk of the beam with a certain energy we will require that *each* simulated macro particle stay within specific limits all along the lattice. As metric for the overall beam envelope growth we define the quantity

$$r \equiv \max \sqrt{(|x_i| + 3\sigma_{x,i})^2 + (|y_i| + 3\sigma_{y,i})^2}, \tag{5.14}$$

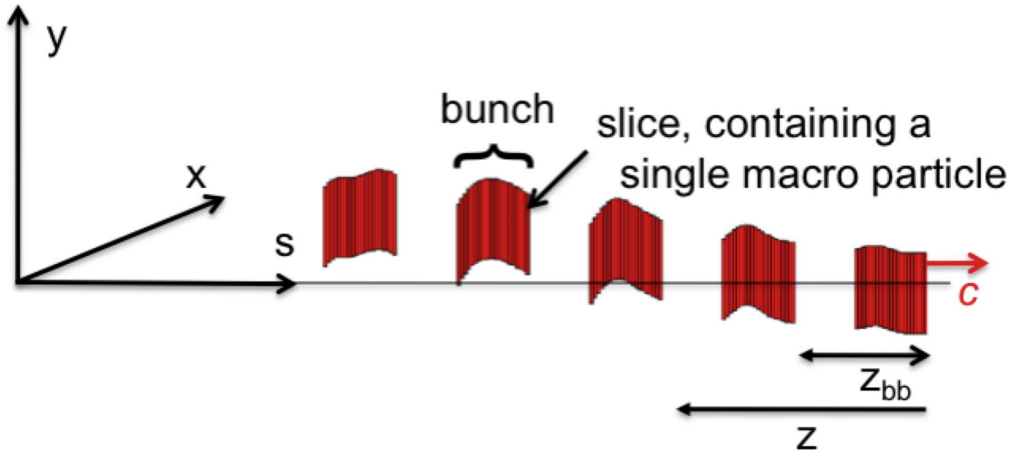

Figure 5.3: PLACET drive beam model. Each train consists of a number of bunches, and each bunch consists of a number of slices. Each slice contains one or more macro particles with different centroid motion, different energy and different second order moments to represent the transverse particle distribution. All macro particles travels along the s-axis with the speed of light, and the distance between slices, measured along the z-axis, is constant along along the decelerator. The direction of the z-axis in the figure follows the PLACET convention.

where the maximum is found by scanning over the macro particles, indexed with i. r is thus driven by the macro particle for which the combined position of the centroid motion (given by x and y) plus 3 sigmas of its transverse distribution (given by σ_x and σ_x) is the largest. r is furthermore calculated to the peak value along the lattice. Normally the peak value will be towards the end of the lattice, where the effects of imperfections and wakes have accumulated, and where the particles are least energetic. In this work, when we speak about the beam envelope, we mean the worst-case 3σ envelope defined by Eq. (5.14), if not stated otherwise.

Simulation criterion

As simulation criterion when analysing the results of realistic simulations (in Section 5.6) we require that r be within half the available aperture, $a_0 = 11.5$ mm, in order to ensure minimum-loss transport,

$$r < \frac{1}{2} a_0. \tag{5.15}$$

The factor half provides margin for unmodelled effects like higher order multipole wakes (cf. the discussion in Section 4.3). Figure 5.4 illustrates a case where the simulation criterion r is fulfilled; the 3σ ellipses for all macro particles are within the half of the aperture (in this illustration, the beam is located in the middle of a quadrupole).

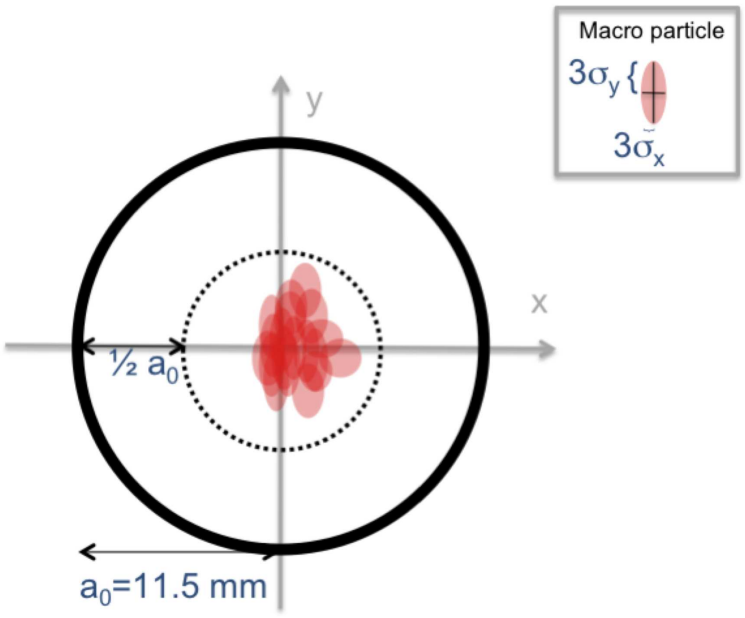

Figure 5.4: Illustration of the simulation criterion. The 3σ ellipses for all macro particles must be contained within half the beam pipe aperture along the entire lattice.

Envelope of the beam centroid

Dipole kicks due to wake fields or machine imperfections affect the macro particle centroid motion, while the individual emittances of the transverse distributions are preserved. When studying the effect of wake fields and imperfections it is therefore of interest to quantify the envelope of transverse motion of the centroid of the simulated macro particles, without incorporating the size and adiabatic undamping of the transverse distributions. Simulations studies in this work are performed in a single plane, unless otherwise stated, and when studying kicks we sometimes use as metric the *envelope of the centroid motion of the beam* in one plane

$$y_c \equiv \max y_i, \tag{5.16}$$

instead of r defined in Eq. (5.14). The part of the beam with the largest transverse offset of the centroid will drive the value of y_c.

Envelope of individual macro particles

It is of interest to compare the envelope of individual macro particle centroids, in order to identify which part of the beam drives envelope. Because the decelerated beam consists of particles with large energy differences, the action alone does not give sufficient information; the particle beta function, β must be taken in account. We define the envelope of the motion of macro particle n as

$$y_{n,c} = \sqrt{2J_{\max}\beta_F}, \tag{5.17}$$

where the action, $J_{\max}$ and β_F are the peak action and beta function experiences by the macro particle along the lattice. The maximum beta function is found close to the F-quadrupole towards the end of lattice, cf. Section 5.3.2 (with "F-quadrupole" we mean, in this work, a quadrupole which focuses in the plane under study).

Implications of the envelope definitions

A few comments regarding our metrics are in place here. First, by adopting metrics based on the *beam envelope*, we choose to not consider the beam emittance. It should be noted that some of the standard formalism and well known formulae dealing with growth of the beam emittance are in general not applicable to the beam envelope. In particular, the decoherence of transverse particle motion due to the spread in energy and phase-advance is not a concern. There is for example no need for chromatic corrections in the decelerator (as shown in Section 5.4 the decoherent particle motion due to the energy spread is in fact rather helpful in the decelerator). Second, our definition of the beam envelope is designed for simulation studies, and is not directly translatable to beam diagnostics observables. E.g. in case only a small fraction of the beam is driven to high amplitudes, the envelope, r, could reach many millimetres at the same time as the

beam centroid as read by a BPM would give readings close to zero. Third, one particular use of the centroid envelopes defined in Eqs. (5.16) and (5.17) is their applicability in calculating wake growth factors, introduced in Section 5.4.

5.3 Beam envelope growth in a perfect machine

The beam envelope, r, will grow significantly even for a perfectly aligned machine and a perfectly injected ideal beam. It is instructive to estimate the growth for the extreme cases, the least and the most decelerated particles.

5.3.1 Most decelerated particles

The most decelerated particles will see a constant FODO phase-advance. However, the deceleration of these particles leads to adiabatic undamping of the $[y\ y']^T$ phase-space. This is exactly the opposite process of adiabatic damping under acceleration, discussed in e.g. [72]. The undamping will increase the average particle action by a factor

$$\frac{J(E_{\min})}{J_0} = \frac{\gamma_0}{\gamma_f} = \frac{1}{1-\eta_{\text{extr}}} = 10, \tag{5.18}$$

where $J(E_{\min})$ is the action of a particle having experienced maximum deceleration at the end of the decelerator and J_0 is the action of this particle at the entrance of the decelerator. γ_0 and γ_f are the particle initial and final Lorentz factors, respectively.

5.3.2 Least decelerated particles

The particles at the head of the train, on the other hand, will experience negligible deceleration, and in the absence of kicks their action is invariant along the lattice. However, they will see a gradually weaker normalised quadrupole strength, according to Eq. (5.3), leading to a gradually larger beta function, and smaller phase-advance per FODO cell. The maximum beta function is given by the solution to the envelope equation, Eq. (5.7), with the beta at the entrance, β_{F0} as initial value. The solution to Eq. (5.7) can be calculated by evolving the beta function according to [23]

$$\mathbf{B}_{n+1} = \mathbf{M}_n^{n+1}\mathbf{B}_n(\mathbf{M}_n^{n+1})^T, \tag{5.19}$$

where $\mathbf{B}$ is a matrix composed of the Courant-Snyder parameters, $b_{11} = \beta$, $b_{21} = b_{12} = -\alpha$ and $b_{22} = \gamma$, defined in Eqs. (5.7), (5.9) and (5.10), and $\mathbf{M}$ are lattice transfer matrices [23] describing sections of the lattice where the focusing function in Eq. (5.4) is constant, $K(s) = K$. It should be noted that along all the lattice, and for all particles energies, the beta function found by applying Eq. (5.19) is within 1% of the beta function found by calculating the period solution of the FODO lattice with the quadrupole

strength k corresponding to the particle energy. The calculation of the periodic solution [23] is much less involved, and therefore very practical when estimating beam dynamics quantities for the decelerator. The near equivalence of the two calculations also implies that α is very small in the middle of all quadrupoles, and to good approximation the maximum beta function is found in the middle of the F-quadrupoles for all particle energies. We use this approximation throughout this thesis by calculating the maximum beta function at the middle of F-quadrupoles. The maximum beta function for the least decelerated particles, $\beta_F(E_0)$, calculated by either method yields

$$\frac{\beta_F(E_0)}{\beta_{F0}} = 4.4, \tag{5.20}$$

where β_{F0} is the beta function in the middle of the first F-quadrupole after decelerator injection.

Figure 5.5(a) illustrates trajectories along a perfect machine, for an on-axis beam, for two particles injected at a distance $3\sigma_y$ from the centre axis. The particle in blue is at the head of the pulse and has almost constant energy along the lattice. The particle in red is situated as to feel maximum deceleration, but is in return focused with a constant phase-advance along the lattice (here set to exactly $\phi_{\mathrm{FODO}} = 90°$ for the purpose of illustration). Figure 5.5(a) shows, as is clear also from Eqs. (5.17), (5.18) and (5.20), that the low energy particles drive the envelope in the case of a perfect machine and on-axis incoming beam. In phase-space, the ellipse of macro particles will vary in size (as they are undamped) and shape (as their beta function increase), as illustrated in Figure 5.5(b) which shows the simulated phase-space after a perfectly injected drive beam has traversed a perfectly aligned decelerator sector.

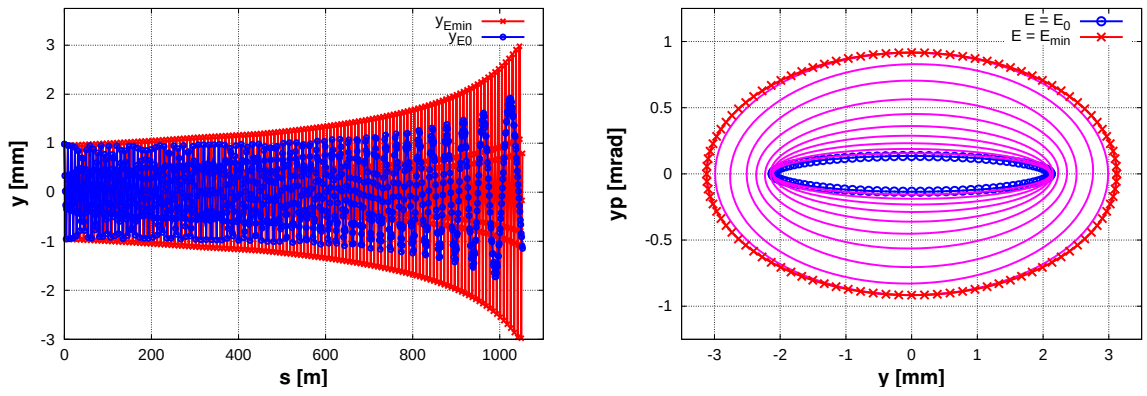

(a) Trajectories along a perfect machine

(b) Phase-space at the end of a perfect machine

Figure 5.5: The drive beam in a perfect machine with perfect injection. (a) The trajectory along the decelerator of a least deceleration particle (in blue, o) and a most decelerated particle (in red, x), injected at a distance $3\sigma_y$ from the centre axis. (b) The macro particle phase-space ellipses (a few slices selected) from a least deceleration particle (in blue, o) to a most decelerated particle (in red, x). The most decelerated particles have the larger action by a factor 10, while the least decelerated particles have a larger beta function by a factor 4.4.

5.4 Beam envelope growth due to transverse wakes

In Section 4.3 the PETS transverse wakes were discussed. As seen from Eq. (4.19) the transverse dipole wake force and the resulting kick on a witness particle inside the PETS are proportional to the centroid offset of the charge generating the wake, with respect to the PETS centre axis. The drive beam might be offset for many reasons, including non-perfect injection, component misalignments and beam jitter. The decelerator PETS must be designed so that the beam envelope is contained for all these scenarios, which has proven to be challenging task [67]. In this section we describe the effects of the dipole wake on the beam, starting from an analytical model for coherent point-like bunch trains, and continuing with analysis of realistic decelerator simulations. At the end of the section we summarise the PETS beam dynamics and rf design cycle, leading to the 12 GHz CLIC baseline PETS. A perfectly aligned machine is assumed throughout this section. The envelope growth due to machine imperfections will be studied in Section 5.5.

5.4.1 Analytical multi-bunch calculations

We start the wake analysis by developing some notions of the effect of the wake fields assuming that the bunch train is modelled as point-like particles. As discussed in Chapter 4, every particle travelling through the PETS will generate a wake field, affecting trailing particles. We denote here the particle generating the wake field the *driving* particle, and the particle witnessing this wake field the *driven* particle.

Modelling the particle motion in the smooth approximation, Eq. (5.12), and assuming equal betatron frequency for both particles it is well known, see e.g. [72], that the driven particle will develop a resonantly driven oscillation, 90° out of phase with the oscillation of the driving particle. The driven oscillation term depends linearly on the distance L travelled,

$$\Upsilon \propto L,$$

where Υ is the *growth factor* of the oscillation amplitude. Ref. [72] also extends the analysis, assuming the smooth approximation, to the cases of continuous acceleration and n-particle models where it is assumed that each particle affects directly only the first trailing bunch (and indirectly the subsequent bunches). To illustrate the concept of resonant growth, Figure 5.6 shows the simulated trajectory of the two first bunches of a point-like bunch train injected with an initial offset in a machine with strong focusing and a very large dipole wake. The first bunch undergoes betatron oscillations, while the second is driven resonantly, leading to a linear increase of the betatron amplitude along the lattice.

The decelerator transverse impedance includes high-Q modes (as seen from the spikes in Figure 4.7), which are not well described by models which ignore directs effects after the first trailing particle. We will here follow the framework developed in [102], which allows for analysis of amplitude growth in cases where each particle directly affects all

trailing particles (thus a full N-particle model), and which takes into account varying lattice and beam parameters. The direct amplification of the oscillation, of particle j due to a driving particle k, caused by a set of localised impedances, can be calculated as a sum [102], which adapted to the decelerator can be written

$$a_{jk} = i \sum_{n=1}^{N_{\mathrm{PETS}}} \frac{L_{\mathrm{PETS}} \Sigma_{l=1}^{9} W'_{T,l}(z_k - z_j)\beta^*(s_n) q_k e}{2E_j(s_n)}, \tag{5.21}$$

where N_{PETS} is the number of PETS in the sector, s_n is the location in the middle of each PETS, $\beta^*(s_n)$ the beta function at locations s_n, E_j the energy of the driven particle at locations s_n, q_k the charge of the driving particle and e the unit charge. $W'_{T,l}$ are the nine dipole wake functions constituting the PETS transverse impedance given by Eq. (4.18), with parameters given in Table A.5, and $z_k - z_j$ the distance between the two particles. The elements a_{jk} thus define a matrix $\mathbf{a}$ where the elements are the *direct* effect of the k'th bunch on the j'th bunch. The a_{jk} are complex because the driven motion is 90° out of phase with the driving oscillations.

Particle k affects particle j directly according to a_{jk}, but also indirectly by amplifying the amplitude of particles in between the two. Ref. [102] elegantly takes the indirect effects into account by modelling the motion as an infinite power of infinitesimal steps yielding

$$\lim_{m\to\infty} (1 + \frac{\mathbf{a}}{m})^m = e^{\mathbf{a}} = \Sigma_{k=0}^{\infty} \frac{\mathbf{a}^k}{k!} = \Sigma_{k=0}^{N-1} \frac{\mathbf{a}^k}{k!} \equiv \mathbf{A}, \tag{5.22}$$

defining the matrix $\mathbf{A}$, which relates the final offset of all N bunches in the train, $\mathbf{y}_f$,

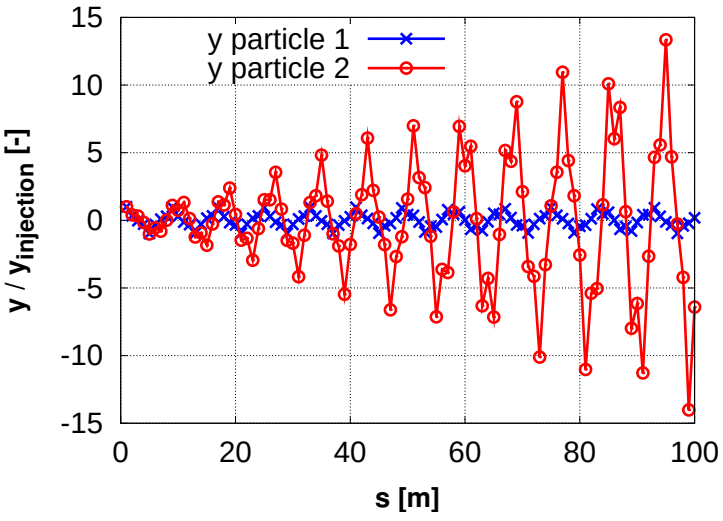

Figure 5.6: Illustration of the effect of the transverse dipole wake: two point-like bunches are injected into a machine where very large dipole wakes are exited. The first particle in the train (in blue, x) undergoes nominal betatron motion, while the second particle (in red, o) is driven resonantly by the dipole wake, leading to a linear increase of the betatron amplitude along the lattice.

to their initial offsets, $\mathbf{y}_i$, as

$$\mathbf{y}_f = \mathbf{A}\mathbf{y}_i, \tag{5.23}$$

taking both direct and indirect effects into account. Equations (5.21), (5.22) and (5.23) are, however, limited to describing growth factors in the cases where particles drive each other resonantly, i.e. if all particles have the same energy and the focusing strength is static in time.

Growth factors

There exist different definitions of wake "growth factors" in literature. We define the growth factor of bunch n, Υ_n, as the amplification of the bunch transverse oscillation amplitude, due to the dipole wake, at the end of the decelerator sector. We use the suffix "ana" for analytically calculated growth factors and "sim" for simulated growth factors. In this section we will limit the discussion of growth to cases where bunch trains are injected into the decelerator with an initial offset, constant along the train. For example, the analytically calculated growth factor of the second bunch is then given by

$$\Upsilon_{2,\mathrm{ana}} = |1 + a_{21}|\,,$$

where a_{21} is defined in Eq. (5.21). The maximum growth factor along a bunch train is $\Upsilon_{\mathrm{beam}} = \max(\mathbf{y}_f)/\max(\mathbf{y}_i)$, and the analytically calculated growth along the envelope can be evaluated as

$$\Upsilon_{\mathrm{beam,ana}} = \frac{\max(\mathbf{y}_f)}{\max(\mathbf{y}_i)} = \max(||\mathrm{A}\mathbf{1}||), \tag{5.24}$$

where $\mathbf{1}$ is a row vector of ones. With our definitions, the corresponding growth factors found by *simulation* are *equivalent* to

$$\Upsilon_{\mathrm{n,sim}} = y_{n,c}/y_{n,c,wo}$$

and

$$\Upsilon_{\mathrm{beam,sim}} = y_c/y_{c,wo}$$

where y_c and $y_{n,c}$ are the metrics defined in (5.16) and Eqs. (5.17) respectively, and the subscript *wo* indicates simulations performed without the effect of the transverse wakes. For the growth factors calculations in this section we assume a decelerator sector with four CLIC baseline PETS installed per FODO cell.

5.4.2 Growth factors along coherent bunch trains

We will use Eq. (5.23) to calculate growth factors for trains injected with an initial offset, for the special cases of all bunches experiencing minimum deceleration, or all bunches experiencing maximum deceleration. Even though unphysical, these cases will give useful insight in the wake growth mechanisms. In the next section, the results will be compared with realistic simulation studies including the effect of the energy transient.

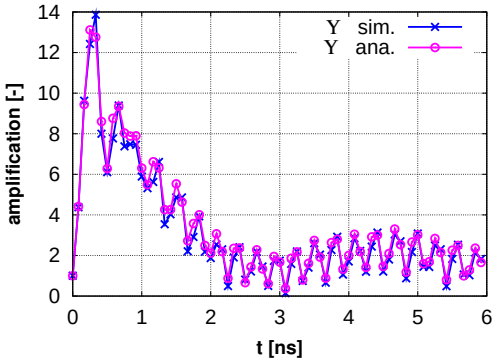

(a) Train of least decelerated bunches

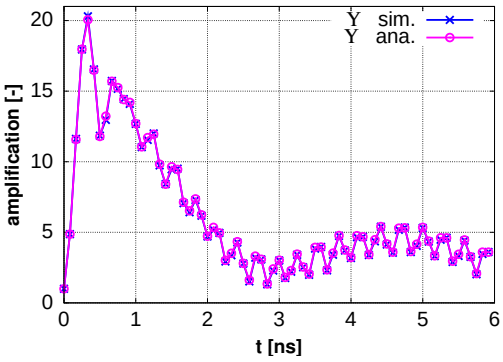

(b) Train of most decelerated bunches

Figure 5.7: Growth factors, at the end of the lattice, along trains with point-like bunches. (a) A train of bunches corresponding to the least decelerated bunches ($E = E_0$ and gradually weaker focusing). (b) A train of bunches corresponding to the most decelerated bunches (constant focusing and gradually lower energy). Simulated growth factors in blue (x) and calculated using Eq. (5.23) in magenta (o).

Least decelerated particles

The least decelerated particles at the head of a train will see a continuously increasing beta function along the lattice. Depending on the PETS group velocity, the energy difference of the first bunches could be small, as will be further discussed in the next section. We assume here a train of point-like bunches of constant energy $E = E_0$, seeing a gradually weaker focusing according to Eq. (5.3). Applying Eq. (5.21) with increasing $\beta^*(s)$ along the lattice yields a severe growth of $\Upsilon_{\text{beam,ana}} = 13$.

Simulating the same scenario ($E = E_0$, no deceleration but decreasing focusing along the lattice) yields almost identical results. There is a small discrepancy due to a small beating of the least decelerated particles (cf. discussion following Eq. (5.19)), which is not taken into account in Eq. (5.21). Figure 5.7(a) shows the growth factor for each bunch along the train, for both the calculated and the simulated case.

The trajectories shown in Figure 5.6 correspond to the scenario simulated in Figure 5.7(a), but with the dipole wake amplitude artificially magnified by a factor 50 to provoke a clear growth of the second particle during the first 100 meters for illustrational purposes. In other words; if the wake amplitude in Figure 5.6 were 50 times smaller, the amplitude of the second particle would have grown by a factor about four at the end of the decelerator, corresponding to the growth factor for the second bunch in Figure 5.7(a).

Most decelerated particles

We next assume a train of point-like bunches injected with an energy $E = E_0$ where all bunches experience maximum deceleration along the lattice (thus neglecting the

transient). In Eq. (5.21) the energy varies according to Eq. (5.2). The increase of the coefficients a_{jk}, with respect to a case of constant energy, E_0, can be written as the integral factor

$$\frac{1}{L_{\text{sector}}}\int_0^{L_{\text{sector}}} ds \frac{1}{\gamma(s)} = \frac{1}{\gamma_{\text{min}} - \gamma_0} \ln \frac{\gamma_{\text{min}}}{\gamma_0},$$

where γ_0 and γ_{min} are the Lorentz factors at the start and at the end of the lattice respectively, and L_{sector} is the sector length. The resulting beam growth factor is $\Upsilon_{\text{beam,ana}} = 20$. Figure 5.7(b) shows the growth factor for each bunch along the train, for both the calculated and the simulated case. We note that there is near perfect agreement between the analytical calculation and the simulation (no artificial fudge factors were introduced).

Figures 5.7(a) and 5.7(b) both indicate a characteristic feature of the dipole wake amplification: a transient growth at the head of the train, decaying towards one far enough into the train, for a finite Q. This comes from the fact that the driven oscillation is 90° out of phase with the driving particle. In Figures 5.7(a) and 5.7(b) we observe as well longer range effects along the train, due to the high-Q PETS modes. For the decelerator studies, where the envelope requirement is defined the same for all particles, it does not matter where the peak amplification occurs; it must in any case be suppressed.

5.4.3 Decoherence due to the PETS group velocity

In general, energy spread in the beam mitigates the envelope growth due to transverse wakes, because the decoherence of the transverse phase-space reduces the beam dipole moment driving the wake, and because the resonance condition for linear growth is not fulfilled anymore. The growth factors depend on the level of decoherence of the particle motion, and for systems which include decoherence we will quantify the growth factors by simulations only.

For the PETS studies it is instructive to discuss separately the decoherence effects in the transient. We emphasise this point because it has lead to direct constraints on the type of PETS considered for CLIC, as will be seen. In the decelerator, decoherent motion of the bunch centroids will automatically be ensured in the transient part of the beam, because of the bunch-to-bunch energy difference due to PETS beam loading, which can be observed in Figure 5.1(a). The PETS power production, Eq. (4.13), is proportional to the ratio R'/Q upon the fundamental mode group velocity v_g, $P \propto \frac{R'/Q}{v_g}$. A degree of freedom when considering PETS design for a given power requirement is thus to vary R'/Q and v_g, keeping their ratio approximatively constant (only approximatively, because bunching effects must be taken into account, cf. Section 4.2). Indeed, alternative PETS designs with lower group velocity and correspondingly higher R'/Q were proposed [75], and analysed in the framework of this thesis.

According to Eq. (4.8) the PETS fill time is inversely proportional to the group velocity. According to Eq. (4.14) the energy difference between the first bunches in the beam,

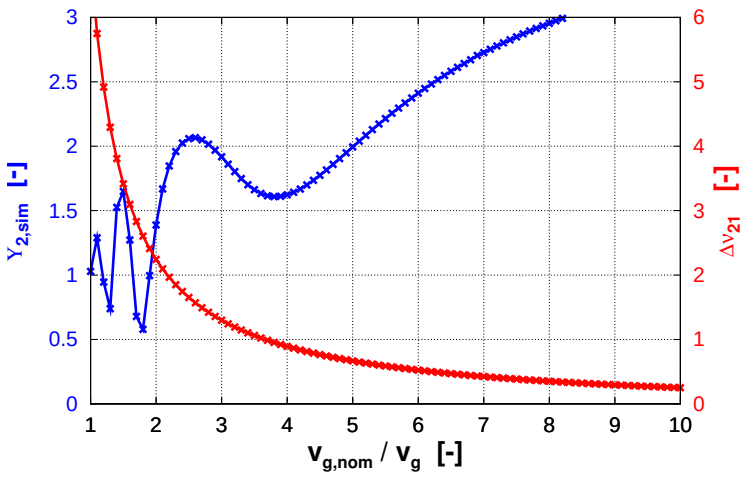

Figure 5.8: Tune difference of bunch 2 with respect to bunch 1 (red) and beam growth factor (blue) as function of PETS fundamental mode group velocity.

ΔE_{21}, is then to first order proportional to the group velocity,

$$\Delta E_{21} \propto v_g.$$

Lower energy difference implies less decoherence of the betatron motion. It is therefore of interest to quantify the decoherence as function of energy difference between subsequent bunches, and furthermore the effect of the decoherence on the growth factors. Starting from the baseline PETS design we scan v_g keeping $\frac{R'/Q}{v_g}$ constant. As growth metric, the simulated growth factor for the second bunch $\Upsilon_{2,\mathrm{sim}}$ is used (growth at the end of lattice). As decoherence metric, the difference in tune between bunch one and two is used $\Delta\nu_{12} \equiv \nu_2 - \nu_1$. Figure 5.8 presents the growth factor and the tune difference for a range of group velocities. For group velocities much lower than nominal $v_{g,\mathrm{nom}}$, a large growth factor is observed. As the group velocity increases a local minimum is observed at $\Delta\nu_{21} \approx 1$. We remind that the decelerator focusing is scaled to follow the most decelerated particles, and the motion of the first bunches is not harmonic; a picture corresponding of decoherence of simple harmonic motion is therefore not to be expected (typical motion of a least decelerated particle is depicted in blue in Figure 5.5(a)). The trend, however, is clear; larger decoherence gives less growth of the second bunch. Figure 5.9(a) shows the multi-bunch growth factors along the train, $\Upsilon_{\mathrm{n,sim}}$, for the baseline PETS. The energy profile along the train is overlaid for clarity. The decoherence is in this case sufficient to suppress the growth in the transient. The characteristic peak growth, however, is now shifted into the steady state part of the train. In comparison, Figure 5.9(b) shows the multi-bunch growth factors for a "slow PETS" with a fundamental mode group velocity $v_g = (1/2.8)v_{g,\mathrm{nom}}$ (approximately 16% of the speed of light). For this PETS we do observe a significant growth in the transient, the decoherence is not sufficient to suppress the growth in this case.

5.4.4 The effects of long bunches

In the previous sections we have simulated point-like bunches, while the decelerator nominal bunch length is specified to $\sigma_z = 1$ mm [38]. By including the full bunch length in the simulations two effects relevant to the envelope growth arise:

1. Decoherence due to the large energy spread within a bunch that develops along the lattice, shown in Figure 5.1(b). This effect mitigates the envelope growth.
2. Single-bunch wake effects; the wake function of Eq. (4.18) acts equally within the individual bunches as from bunch to bunch. This effect aggravates the envelope growth.

For the baseline structure, the PETS induced relative energy spread after deceleration, illustrated in Figure 5.1, is calculated to $\sigma_{E_{\text{first}}}/\langle E_{\text{first}}\rangle = 5\%$ within the first bunch and

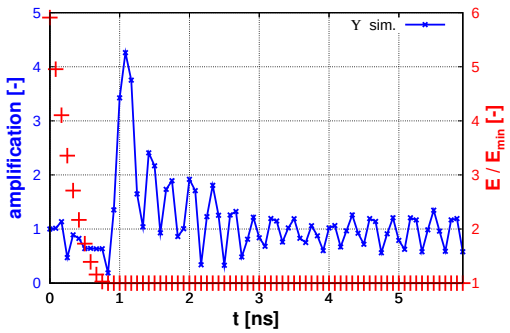

(a) Point-like bunches, baseline PETS

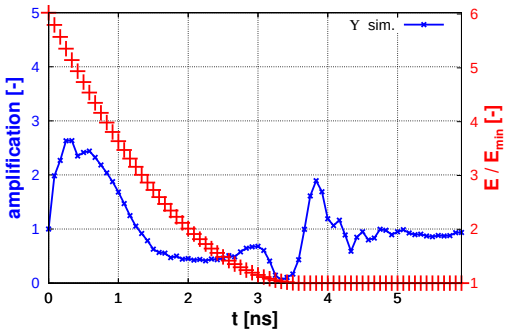

(b) Point-like bunches, slow PETS

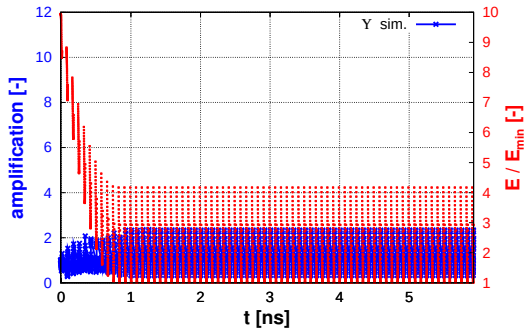

(c) $\sigma_z = 1$ mm, baseline PETS

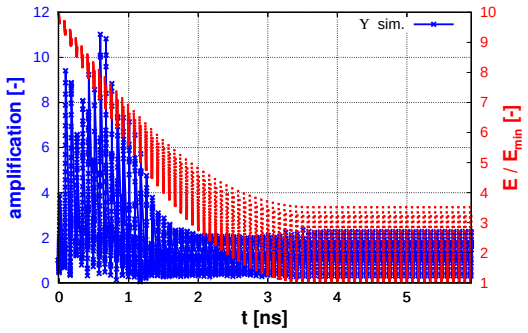

(d) $\sigma_z = 1$ mm, slow PETS

Figure 5.9: Growth factors (blue) and energy profile (red) along the train, at the end of the lattice, for both point-like bunches and realistic bunches. The CLIC baseline PETS is presented in (a) and (c), and the alternative "slow" PETS design in (b) and (d). For the slow PETS neither the decoherence of first bunches nor the intra-bunch energy spread is enough to prevent an unacceptable envelope growth in the transient. The centroid motion of the point-like pulse and the realistic pulse centroid shown in Figure 5.10 correspond to the beams in (a) and (c) respectively.

$\sigma_{E_{\text{final}}}/\langle E_{\text{final}}\rangle = 37\%$ within a steady state bunch, where $\langle E\rangle$ denotes the bunch mean energy and σ_E the rms spread. For the slow PETS, however, the energy spread within the first bunch is $\sigma_{E_{\text{first}}}/\langle E_{\text{first}}\rangle = 1\%$ only, while $\sigma_{E_{\text{final}}}/\langle E_{\text{final}}\rangle = 27\%$ within a steady-start bunch. For both types of structure the energy spread in the steady state part is sufficient to significantly decohere the beam transverse motion after a few hundred meters. This is illustrated in Figure 5.10 where the centroid signal of the entire pulse is plotted (corresponding to the simulated BPM readings), for the two cases of a point-like bunch train and a train with $\sigma_z = 1$ mm. The figure illustrates the baseline PETS, but the features are the same for the slow PETS. The centroid of the point-like pulse is increasing along the lattice, while the centroid of the realistic pulse is reduced by an order of magnitude after passing through a few hundred PETS (a couple of hundred meters along the lattice, depending on the exact length of the given decelerator sector), due to decoherence in the transverse phase-space.

The effect on the growth factors of introducing the nominal bunch length of $\sigma_z = 1$ mm, is presented in Figures 5.9(c) and 5.9(d), which correspond to Figures 5.9(a) and 5.9(b) respectively. For the baseline PETS we no longer observe the characteristic peak growth due to the multi-bunch effects; it has been suppressed due to decoherence caused by the intra-bunch energy spread. The single-bunch effects, though, have magnified the growth factors (up to a factor of about two) for part of the steady state part. In comparison, for the slow PETS, we notice a significant growth in the transient part of the beam. In fact, the multi-bunch effects seen in Figure 5.9(b) have been aggravated by single-bunch effects, and the amplification for some macro particles is more than a factor 10. In the

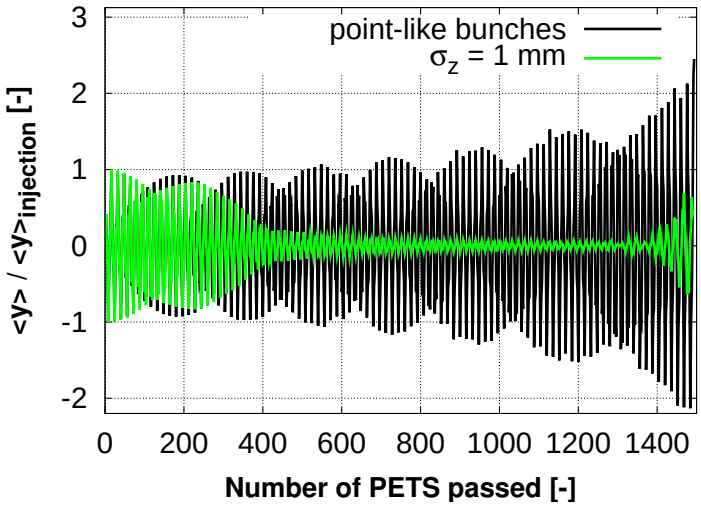

Figure 5.10: Decoherence of transverse motion due to energy spread. The centroid signal of the whole pulse is plotted along the lattice (as function of the number of PETS passed), for the two cases of a point-like bunch train and a train with $\sigma_z = 1$ mm, assuming the baseline PETS design. For the point-like train (in black) the pulse centroid is increasing along the lattice, while the centroid of the realistic pulse (in green) is reduced by an order of magnitude after passing through a few hundred PETS, due to coherence in the transverse phase-space.

steady state part the energy spread is comparable to the baseline PETS, and Υ is of the same order, but the amplification in the transient is nonetheless unacceptable.

In these simulations only the PETS induced energy spread is taken into account. Intrinsic energy spread at the entrance of the decelerator mitigates the problem somewhat, but for robust PETS design we recommend a design with sufficient decoherence to suppress growth in the transient. A rough estimation based on Figure 5.9(a) would imply a decoherence of $\nu_{21} \gtrsim 2$, thus giving a lower limit of the PETS group velocity to about $v_g \gtrsim 0.25c$ assuming the PETS input constraints in [38]. In any case the discussion in this section suggests the importance of a thorough beam dynamics study before eventual new PETS designs are approved.

This discussion has also shown that both multi-bunch and single-bunch effects must be taken into account when studying the envelope growth in the decelerator; it is the interplay between the two that leads to the large growth factors in Figure 5.9(d). New codes simulating PETS should therefore aim to include both effects.

5.4.5 Summary: PETS beam dynamics and rf design cycle

We have seen examples of how the design of a power extraction and transfer structure for the decelerator carefully must take into account the effect of transverse wakes, both multi-bunch and single-bunch effects, as well as the effect of the group velocity. The PETS design therefore requires combined efforts from beam dynamics and rf expertise. The thesis work included responsibility for beam dynamics analysis of a large number of potential PETS designs, evaluating stability and envelope growth for each. Eventually, a convergence on the current CLIC 12 GHz PETS baseline design was reached, presented in [67] and included in Appendix B.

A given PETS rf design yields a set of dipole modes, which must not lead to unacceptable envelope growth of the transverse motion of the injected beam. Injection errors might lead to constant offsets along the train (as discussed in the previous sections), and the incoming beam might also contain transverse jitter. In both cases the growth must be contained. Each PETS design was therefore studied [103], as minimum, by investigating both beams injected with constant offset and beams with jitter of frequencies in the range from a few GHz to a few tens of GHz (covering the full spectrum of the dipole mode frequencies). In addition, tolerances on amplitude, Q-factors and frequency values were investigated [103]. The design cycle continued until an acceptable PETS design was found, where neither the injection offset, nor beam jitter at any frequency, were amplified more than a factor of two. Figure 5.11 illustrates the PETS design cycle, resulting in the CLIC 12 GHz baseline PETS.

As illustration of the performance of the baseline PETS, Figure 5.12(a) shows the growth factors, $\Upsilon_{\mathrm{beam,sim}}$ for beams injected with transverse jitter where the jitter frequencies correspond to each of the dipole mode frequencies. The scan over the mode frequencies has been performed for the nominal Q-values, as well as cases where the Q-factor for all modes is assumed to be a factor two and three higher than the nominal best-estimate

value (the mode Q-value is considered to be the most difficult to estimate with precision [75]). 20 ns long bunch trains are simulated here. From Figure 5.12(a) we observe that no frequency leads to a growth factor along the beam of more than two, assuming nominal Q-values. When taking into account the transverse distribution of each macro particle, the amplification of centroids is found to be less significant, because the macro particle with the largest centroid envelope might not have felt the largest undamping. Figure 5.12(b) shows the full beam envelope, r, along the decelerator lattice, where the incoming beam contains jitter of total magnitude of one rms beam size, distributed equally among the nine mode frequencies. For nominal Q-values the growth of the beam envelope with respect to the case of no transverse wakes is almost negligible. However, for Q-values a factor two higher than the nominal unacceptably high growth occurs, showing that the PETS design margin on the estimated Q-values is less than a factor two.

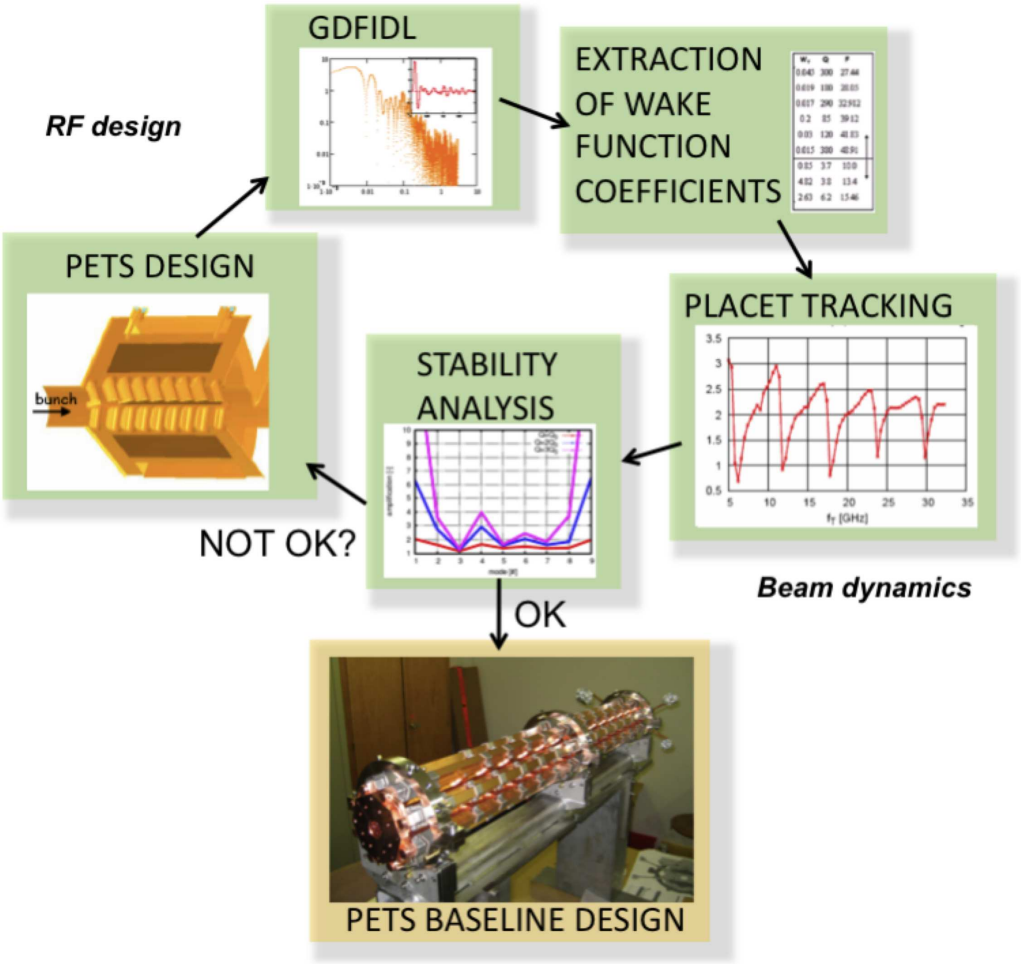

Figure 5.11: The CLIC PETS beam dynamics and rf design cycle.

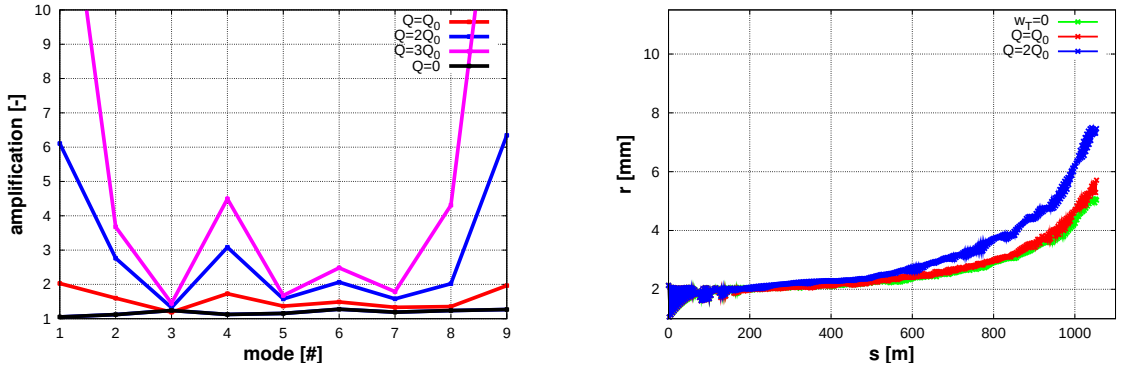

(a) Dipole mode amplification

(b) Envelope growth along the lattice

Figure 5.12: Illustration of the effect of the dipole wake in the CLIC 12 GHz baseline PETS. (a) Beam envelope growth with beam jittered at each mode frequency, for nominal Q-values, and all Q-values scaled by a a factor two and three. (b) beam envelope along the lattice, for nominal Q-values, and all Q-values scaled by a factor two. The nominal Q-values, as estimated from the rf design, lead to a small, but acceptable envelope growth. However, if all Q-values are scaled to a factor two times the nominal, the envelope growth is unacceptably large.

5.5 Beam envelope growth due to machine imperfections

The assumption of a perfectly aligned machine is not realistic; machine components will only be aligned with finite accuracy. In this section we study the effects of component misalignment on the beam envelope, as well as orbit correction schemes to mitigate their effect. The effects of transverse wakes are not included in the simulation studies presented in this section, while in Section 5.6 the results of realistic simulations taking into account the effect of both transverse wakes and misalignment are presented. We shall see that even if very good BPM precision and accuracy in the μm-range are assumed, while we require our beam to stay within the mm-range, standard 1-to-1 correction might not ensure satisfactory drive beam transport in the decelerator. We therefore develop a novel correction scheme for the decelerator based on dispersion-free steering, exploiting the PETS beam loading. The main results of this section were presented in [92], included in Appendix B.

5.5.1 Alignment and tolerances

All lattice components are susceptible to misalignment, and in this thesis we consider PETS, BPMs and quadrupoles misalignment; both tilt and offsets with respect to a laser-straight line. With the novel pre-alignment scheme developed for CLIC, it is expected that components can be aligned with an accuracy of $\sim$ 10 μm [57]. Tolerance limits for the tilt and offsets of the various decelerator components have been studied in [103], based on the following requirement:

- the beam centroid envelope, y_c defined in Eq. (5.16), shall not increase by more than 1 mm due to the effect of a single type of misalignment

The study was performed by tilting or scattering components, according to a Gaussian distribution, around a laser-straight line. It was found that the alignment tolerances were relatively relaxed for rms tilt angles for both PETS and quadrupoles ($\sigma_{\text{tilt}} \sim 1$ mrad) as well as PETS rms offset ($\sigma_{\text{PETS}} \sim 100$ μm). However, the corresponding tolerance on the quadrupole rms offsets was found to be in the order of a few μm, an order of magnitude smaller than what is foreseen to be achievable by the pre-alignment. The quadrupole offsets are therefore the main driver of the beam envelope in the case of an uncorrected machine.

5.5.2 Uncorrected machine

A standard 1-to-1 correction scheme (described in the next section) will to a large extent mitigate the beam envelope growth due to quadrupole kicks. However, in order to get a notion of the magnitude of envelope growth due to imperfections, it is instructive to study the details of an uncorrected machine as well.

We assume a machine where the quadrupoles are scattered randomly, Gaussian distributed with σ_{quad}, around a straight line. In general, we assume a value of $\sigma_{\text{quad}} = 20$ μm rms for an uncorrected machine. We assume further that the machine is otherwise perfectly aligned, and that the beam enters on axis. When a particle passes through an offset quadrupole it will receive a kick. Since we assume a linear decelerator lattice, and thus linear betatron motion, the resulting amplitude of the oscillation can be found by summing the kicks along the lattice. We will estimate the average increase in the particle envelope for the most decelerated particles, due to quadrupole offsets alone. Using thin-lens approximation and assuming uncorrelated quadrupole offset, we can calculate the 2D average envelope of the most decelerated particles, $\langle r_c \rangle_{\text{Emin}}$ as (derivation included in Appendix E)

$$\langle r_c \rangle_{\text{Emin}} \approx 2\sqrt{N} \frac{\sigma_{\text{quad}}}{\cos(\phi_{\text{FODO}}/2)} \sqrt{\frac{(1 - \frac{1}{2}\eta_{\text{extr}})}{(1 - \eta_{\text{extr}})}}, \tag{5.25}$$

where N is the number of quadrupoles in the lattice, σ_{quad} the rms quadrupole offset, ϕ_{FODO} the FODO phase-advance and η_{extr} the energy extraction efficiency, defined in Eq. (5.1). For the decelerator baseline parameters, given in Table A.3, Eq. (5.25) yields $\langle r_c \rangle_{\text{Emin}} = 4.4$ mm. If the quadrupole offsets were assumed to be arranged so that kicks build up coherently (worst case) the envelope would be proportional to N instead of $\sqrt{N}$.

The decelerator transports particles with a large range of energies. For a given machine, with a given pattern of quadrupole misalignment, particles of some energies will sample the misalignment with a certain degree of coherence, yielding an envelope for particles of energies that might be significantly larger than calculated in Eq. (5.25). We illustrate this discussion in Figure 5.13(a) which shows PLACET simulations for the envelope of the lowest energy particle, averaged over 1000 machines in red; Eq. (5.25) calculated

along the lattice in black; Eq. (5.25) with $\sqrt{N} \rightarrow N$ for the coherent worst case in magenta; and the centroid envelope for particles of all energies for a single typical machine in blue). In the latter case, some coherence has been picked up by parts of the beam.

To further illustrate how the various particles energies in the beam drive the envelope, we do the following "simulation experiment": for the same simulated quadrupole misalignment we send in beams with average beam intensity varying from 0.1% of the nominal up to nominal. Since the energy extraction and PETS energy spread are proportional to the beam intensity, the beam with lower intensity will contain a smaller energy spectrum, and thus lower probability of sampling coherence in the quadrupole misalignment. Figure 5.13(b) shows the centroid envelope (for all particles) as function of average intensity, for one given machine (the same machine simulated in blue in Figure 5.13(a)). Starting from a centroid envelope smaller than 2 mm, new envelope plateaux are suddenly reached when the minimum energy reaches an energy level where the particles sample the quadrupole misalignment with a significant level of coherence.

5.5.3 1-to-1 correction

The growth of the centroid envelope due to quadrupole kicks, might be strongly mitigated by steering the beam into the BPM centres. If a corrector is available for each BPM one can steer the beam into the centre of each BPM (1-to-1 correction). If fewer correctors than BPMs are available one can follow different approaches, e.g. MICADO [104]

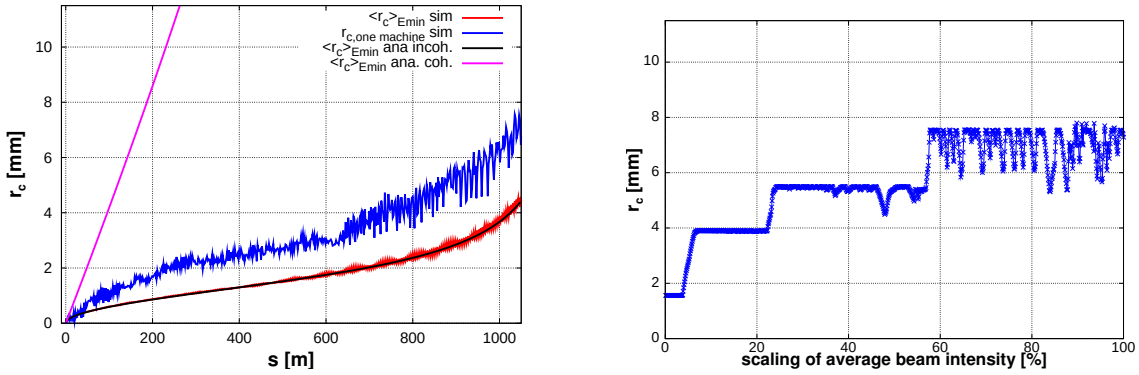

(a) Envelopes along the lattice

(b) Envelope as function of beam intensity

Figure 5.13: Beam envelope growth due to quadrupole misalignment. (a) average 2D centroid envelope along the lattice for the most decelerated particles; simulated (red) and calculated using Eq. (5.25) (black); envelope assuming coherent (worst case) addition of random kicks (magenta); centroid envelope for particles of all energies for one typical machine (blue). (b) centroid envelope one typical machine, at the end of the lattice, as function of average beam intensity. Increased beam intensity corresponds to increased deceleration and energy spread, and particles of different energies arise to drive the envelope as the intensity is increased.

or least-squares solutions to optimise the performance (few-to-few correction).

It is fruitful to describe the correction in a response matrix framework. The corrector-to-BPM response matrix, $\mathbf{R}$, describes the effect of each corrector change on each BPM reading. The matrix elements R_{ij} define the incremental BPM reading i, y_i, produced by an incremental change in corrector j, θ_j

$$R_{ij} = \frac{\partial y_i}{\partial \theta_j}.$$

1-to-1 correction can be then performed by sending a pulse, store the BPM readings as $\mathbf{y}$ and apply corrections according to

$$\Delta\boldsymbol{\theta} = -\mathbf{R}^{\dagger}\mathbf{y}, \tag{5.26}$$

where $\Delta\boldsymbol{\theta}$ is the vector of corrector adjustments and $\mathbf{R}^{\dagger}$ the pseudo-inverse of $\mathbf{R}$ [105]. Subsequent pulses will then yield zero BPM readings within the BPM precision, assuming a linear system, one corrector per BPM and an $\mathbf{R}$ that is a perfect model of the system to be corrected (for non-linear systems, or if imperfect system models are used, the correction might still converge to yield zero BPM readings by applying Eq. (5.26) iteratively).

Particle trajectories along a 1-to-1 corrected decelerator

In the decelerator baseline one corrector per BPM is assumed, as illustrated in Figure 5.2, and the lattice model is linear. The correctors assumed in the thesis work are quadrupole movers with 1 μm resolution. After performing 1-to-1 correction in the decelerator, applying Eq. (5.26), each BPM reading is close to the BPM resolution, specified to 2 μm [96] (the corrector steps add a few μm to the effective resolution) implying that the beam centroid is centred to the ideal machine axis to within the BPM accuracy, specified to a 20 μm [96]. The residual quadrupole kicks will, however, generate dispersion. This spurious dispersion combined with the large energy spread lead to dispersive trajectories that might reach the order of several mm with respect to beam centroid. Thus, even though the beam centroid is well contained, the beam envelope is not. This effect is illustrated in Figure 5.14(c), showing the trajectory of a least decelerated and most decelerated particle along a 1-to-1 steered machine. A most decelerated particle has final energy, $E_{\mathrm{min}} = 0.24$ GeV, which is relatively close to the final centroid energy, $\langle E_{\mathrm{final}} \rangle = 0.38$ GeV, and is less affected by the spurious dispersion than a least decelerated particle. Figures 5.14(a) and Figure 5.14(b) show the trajectories for the same particles tracked through a perfect machine and an uncorrected machine, respectively. In Section 5.6 results of 1-to-1 correction simulations for a large number of realistic machines are presented, but first a more sophisticated correction scheme will be discussed.

5.5.4 Dispersion-free steering

The idea of the correction scheme "dispersion-free steering" (DFS) is to reduce the energy dependence of the centroid trajectories [106]. In dispersion-free steering, the measured orbit of the nominal beam, denoted $\mathbf{y_0}$, is compared to the measured orbit of a "test-beam", denoted $\mathbf{y_1}$, in which the particles see a stronger or weaker optics than in the nominal beam, and thus follow dispersive orbits. By adjusting the correctors to minimise the difference between the nominal and test-beam orbits, $\Sigma(y_{1,i}-y_{0,i})^2$, the harmful components of the quadrupole misalignment can be compensated for. The different optics for the test-beam can in principle be achieved either by adjusting the lattice magnet strengths or by using test pulses with energy different from the nominal; in both cases the absolute beam optics will change. From operational and performance points of view, however, it is preferred not to change the machine lattice when performing correction, and using test-pulses with different energies is therefore preferred. In practice, minimising only the difference trajectory generally lead to unstable solutions in presence of noise, for example finite BPM resolution. Instead, we minimise a weighted sum of the

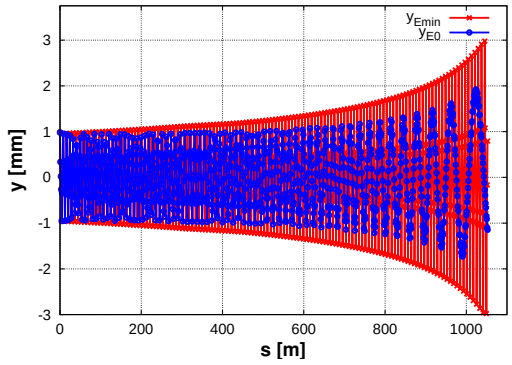

(a) Perfectly aligned machine (3σ particles)

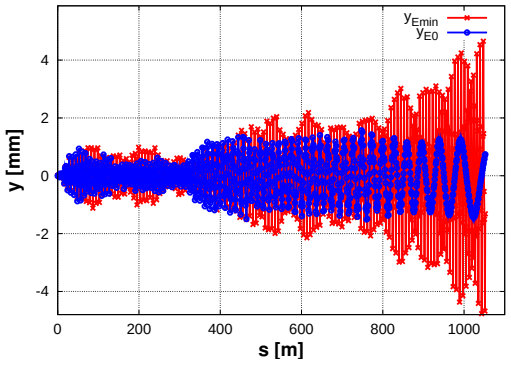

(b) Uncorrected machine (NC)

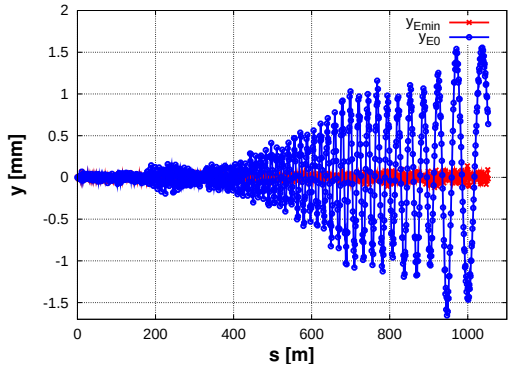

(c) 1-to-1 corrected machine (1-to-1)

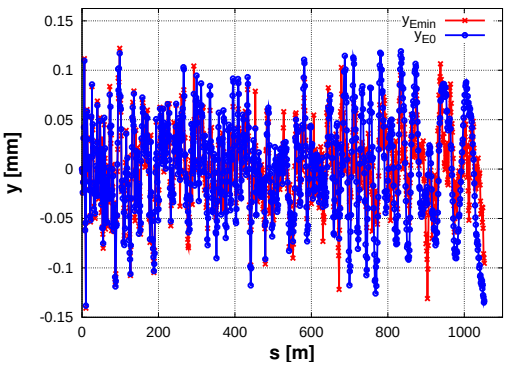

(d) Dispersion-free steered machine (DFS)

Figure 5.14: The trajectory along the decelerator of a least deceleration particle (in blue, o) and a most decelerated particle (in red, x), for the cases of a perfectly aligned machine (a), an uncorrected machine (b), a 1-to-1 corrected machine (c) and a dispersion-free steered machine (d).

difference trajectory and the zero orbit with respect to the centre line [107]

$$\chi^2 = w_0^2 \Sigma y_{0,i}^2 + w_1^2 \Sigma (y_{1,i} - y_{0,i})^2. \tag{5.27}$$

where w_0 is the relative weighting of the zero orbit and w_1 the relative weighting of the difference orbit. The least squares solution with respect to the correctors is found by solving the resulting matrix equations:

$$\begin{aligned} \frac{\partial \chi^2}{\partial \boldsymbol{\theta}} = \frac{\partial}{\partial \boldsymbol{\theta}} \Big\{ & w_0^2 (\mathbf{y}_0 + \mathbf{R}_0 \Delta\boldsymbol{\theta})^T (\mathbf{y}_0 + \mathbf{R}_0 \Delta\boldsymbol{\theta}) \\ + w_1^2 \big((\mathbf{y}_1 - \mathbf{y}_0) + (\mathbf{R}_0 - \mathbf{R}_1)\Delta\boldsymbol{\theta}\big)^T & \big((\mathbf{y}_1 - \mathbf{y}_0) + (\mathbf{R}_0 - \mathbf{R}_1)\Delta\boldsymbol{\theta}\big) \Big\} = 0 \end{aligned}$$

$$\Downarrow$$

$$\begin{bmatrix} w_0 \mathbf{y}_0 \\ w_1(\mathbf{y}_1 - \mathbf{y}_0) \end{bmatrix} = - \begin{bmatrix} w_0 \mathbf{R}_0 \\ w_1(\mathbf{R}_1 - \mathbf{R}_0) \end{bmatrix} \Delta\boldsymbol{\theta}$$

$$\Downarrow$$

$$\Delta\boldsymbol{\theta} = - \begin{bmatrix} w_0 \mathbf{R}_0 \\ w_1(\mathbf{R}_1 - \mathbf{R}_0) \end{bmatrix}^{\dagger} \begin{bmatrix} w_0 \mathbf{y}_0 \\ w_1(\mathbf{y_1} - \mathbf{y}_0) \end{bmatrix}. \tag{5.28}$$

where $\mathbf{R}_0$ is the response-matrix seen by the nominal beam and $\mathbf{R}_1$ the response-matrix seen by the test beam. Comparing Eq. (5.28) to Eq. (5.26) illustrates well the similarities of dispersion-free steering and 1-to-1 correction.

5.5.5 Decelerator implementation of dispersion-free steering

In the decelerator, we suggest to take advantage of the PETS beam loading (discussed in Section 4.2) to generate test-beams for the dispersion-free steering. The steady state energy loss along the decelerator is to first order proportional to the average beam intensity, as can be seen from Eqs. (4.11) and (4.15), and a test-pulse can therefore be implemented by varying the beam intensity. Exploiting the beam loading is also a natural choice for decelerator correction; what we want to mitigate is indeed the effect of the energy spread resulting from the beam loading, so when we minimise the test-beam dispersive trajectories resulting from beam loading, we would expect to see a clear reduction of the spread of dispersive trajectories within the nominal beam as well.

The question of how to vary the drive beam intensity must now be addressed. We suggest to exploit the delayed switching technique [7], already developed for CLIC main beam loading compensation [53]: by delaying the switching in the sub-harmonic buncher before the drive beam linac (see Figure 3.4), empty rf bunches will be inserted in part of the bunch train. Because the half-trains do not interleave perfectly at the exit of the delay loop, the average beam intensity will vary along the drive beam pulse. This method, illustrated in Figure 5.15, thus allows for energy variation along single pulses, requiring but a single machine operation: change of the switching delay. Dispersion-free steering for the decelerator could therefore in principle be applied within a single

pulse, assuming sufficient BPM bandwidth (cf. the BPM specifications [96], included in Appendix C). For the dispersion-free steering simulations in this work, a test-beam with 6 GHz bunch frequency has been used. The resulting average steady state energy is about twice that of the nominal beam, an energy difference comparable to the energy spread due to beam loading, which dispersive effects we seek to minimise. Test-beams with 8 or 9 GHz average bunch frequency (every third or fourth bunch removed) show very similar performance. For all test-beams the bunch charge is unchanged from the nominal. Figure 5.16(a) shows the steady state energy of the nominal beam and the test beam.

Eq. (5.28) requests for a relative weight of the difference orbit with respect to the zero orbit. This weight should be in the order of $w_1^2/w_0^2 = \sigma_{\text{acc}}^2/\sigma_{\text{res}}^2$, since poor BPM accuracy, σ_{acc}, suggests a relatively lower w_0 while poor BPM resolution, σ_{res}, suggests relatively

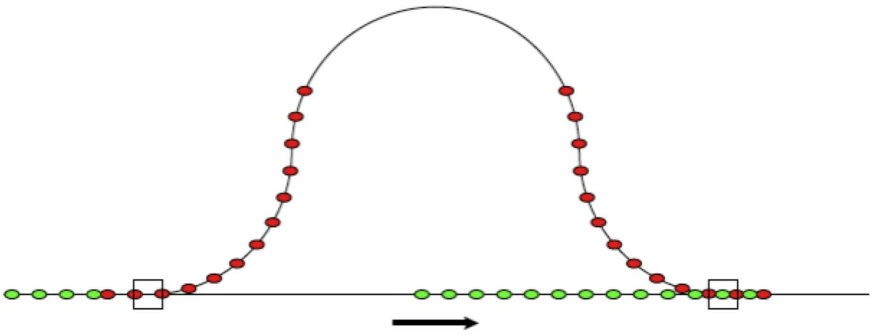

(a) Delay loop nominal operation

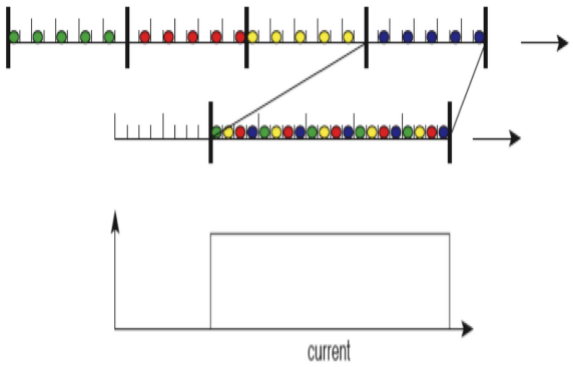

(b) Nominal switching

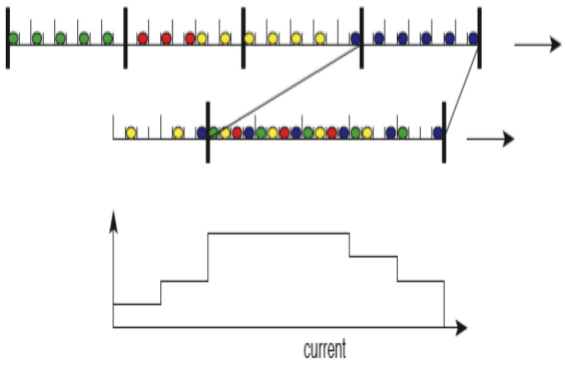

(c) Delayed switching

Figure 5.15: Test beam generation using delayed switching of the phase coding used to select the bunches to be kicked into the delay loop. By delaying the switching in the sub-harmonic buncher of the drive beam accelerator, the average beam intensity can be varied within a single pulse. (a) Principle of the CLIC delay loop, illustrating nominal switching. (b) Part of a combined bunch train, and the corresponding beam intensity, with nominal switching. (c) Part of a combined bunch train, and the corresponding beam intensity, when switching was delayed. Pictures courtesy of the CLIC study [7, 53].

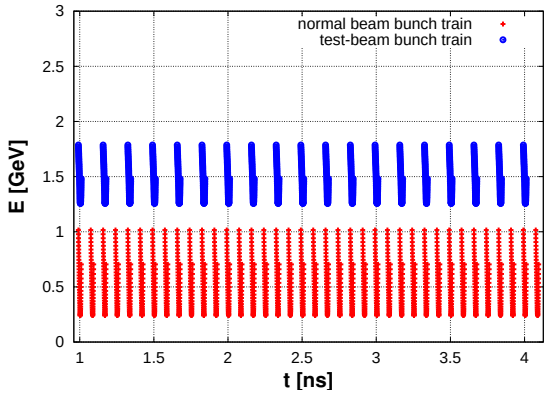

(a) DFS test beam energy profile

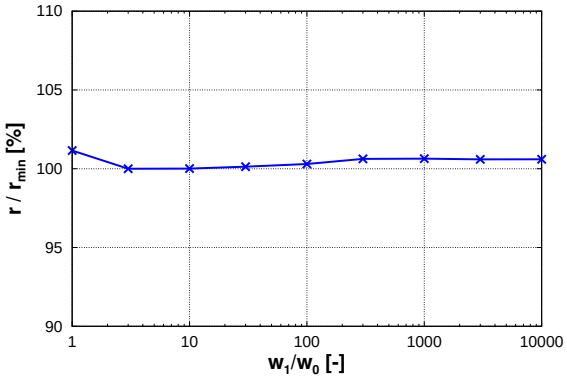

(b) DFS performance weight dependence

Figure 5.16: (a) Steady state energy of the 12 GHz nominal beam and the 6 GHz test beam used for DFS. The resulting mean energy of the test beam is about twice that of the main beam, ensuring a highly dispersive orbit. (b) DFS performance as function of the relative weighting of the zero difference orbit and the zero orbit. Over a range of four orders of magnitude the performance of the algorithm depends only very weakly on the relative weighting.

lower w_1. Optimal weighting is found by simulation (a weight can in addition be given to the resulting corrector amplitude, resulting in additional terms in Eq. (5.28)). For the decelerator the performance of the algorithm depends only weakly on deviations from the optimum weighting; varying w_1/w_0 by four orders of magnitude, $w_1/w_0 \in (1...10'000)$, leads to a relative difference in r of only a few percent, as shown in Figure 5.16(b). An important implication of this is that the choice of weights is robust to parameter changes when doing decelerator beam dynamic studies. It is for instance not strictly necessary to continuously re-optimise the weights when e.g. changing BPM parameters by a small factor. All studies in this work have been performed with the relative weight set to $w_1/w_0 = 100$.

5.5.6 Correction binning

The orbit correction will in practise be performed in ”bins” where one bin consists of a fraction of the lattice. E.g. a pulse is shot, the BPMs are read, and the first 50 BPM signals of the sector are corrected. Then a new pulse is fired and the next 50 BPM signals are corrected, and so on.

An interesting question related to the number of bins, is how large difference is tolerated between the model used for correction and the corresponding real machine, in order to converge to an adequate correction. For the decelerator it is of special interest to look at the beam intensity, since the betatron motion depends strongly on the intensity. If the difference between the model tune and the machine tune is a significant fraction of an integer, within a single bin, the correction is not expected to perform well. The drive beam intensity can be measured and controlled only with limited precision, and we

therefore present results of a simulation study quantifying the tolerance on the intensity error accepted in the model, as function of the size of the bins used for correction, for dispersion-free steering. Figure 5.17(a) summarises the result of the study. The error in the model beam intensity is assumed static during the correction. 50% overlap of the bins has been applied. Using in the range 20 to 40 correctors per bin, model intensity errors from -1.5% up to 0.5% (-1.5 A to 0.5 A) yield an increase of less than 10% of the overall beam envelope with respect to the minimum envelope found for no error, which is deemed acceptable. Both too many and too few bins lead to worse results, and the correction breaks down completely if less than ~ 10 correctors per bin are used. A knowledge of the beam intensity to this level is considered to be feasible; control of the drive beam intensity must in any case be controlled to better than percent level due to requirements on power production and phase tolerances [38]. We therefore do not consider these model error tolerance levels to be a show-stopper for the deceleration correction. Figure 5.17(b) highlights the special case of a perfect model, where there is no error in the intensity estimate, corresponding to the vertical line at 100% in Figure 5.17(a). For this case, varying the number of bins used has a very small effect; the relative difference in r is only a few percent whether all the sector is corrected in a single bin, or using say a hundred bins.

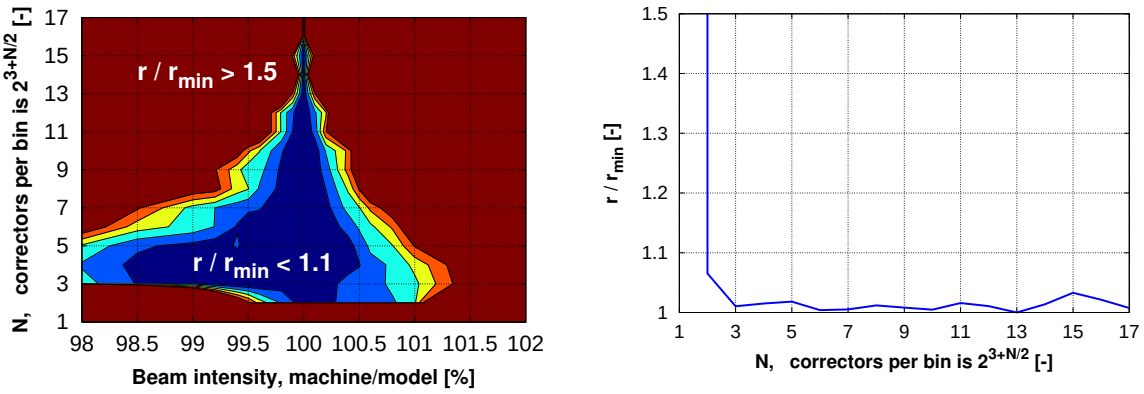

(a) $r/r_{\min}$ versus intensity error and binning

(b) $r/r_{\min}$ for zero intensity error

Figure 5.17: (a) DFS performance as function of the error in the model beam intensity (horizontal axis) and bin length in number of correctors (vertical axis). 50% overlap of the bins has been applied. The darkest blue region indicates an increase in the beam envelope, r, of less than 10% with respect to the minimum $r_{\min}$ (found for no beam intensity error). The bound is increased by 10% per region shown in the figure. As long as the binning is small enough, a model intensity error of up to 0.5% (0.5 A) does not affect correction performance significantly. (b) The special case of perfect model intensity (corresponding to the vertical line at 100% in (a)). For this case varying the number of bins used has a very small effect on the beam envelope.

Particle trajectories along a dispersion-free steered decelerator

Figure 5.14(d) shows the lowest and highest energy particle, for one machine, after DFS steering. Both the lowest energy and the highest energy particles are now confined, unlike the situation after 1-to-1 correction shown in Figure 5.14(c). In Section 5.6 results of dispersion-free steering simulations for a large number of realistic machines are presented, and compared to 1-to-1 correction.

Experimental tests of the dispersion-free steering for the decelerator

The peculiarities of the decelerator dispersion-free steering scheme imply a need for proof-of-principle in a representative test-environment. The ideal test-bench will be the CTF3 Test Beam Line, cf. Chapter 6, which is currently under construction with completion foreseen in 2011-2012. Awaiting the completion of TBL, experiments with dispersion-free steering in the fully loaded CTF3 linac have been performed, further discussed in Section 5.10.

5.6 Results of realistic simulations

In order to quantify the combined effect of the adiabatic undamping (Section 5.3), transverse wakes (Section 5.4) and the different correction schemes (Section 5.5), 500 machines were simulated with all effects included, including realistic values for all types of machine imperfections [103] (values given in Table A.3). The maximum envelopes r along the lattice were calculated for the cases of no correction, 1-to-1 correction and dispersion-free steering. The model used for correction describes the machine perfectly, however, the simulated BPMs have limited resolution and accuracy. The correction is performed in a single bin. As shown in Figure 5.17(b) when using a perfect model, the simulation results do not depend strongly on the number of bins used. Simulations are performed in one plane, but the results are scaled in order to represent the two-dimensional beam envelope, r.

Figure 5.18 presents the simulation results. For the uncorrected case (NC) we observe a rapid growth of the beam envelope, originating mainly from quadrupole misalignment. For the 1-to-1 corrected case (1-to-1) the effect of quadrupole misalignment is strongly mitigated, however, there remains still a significant envelope growth with respect to the minimum envelope growth resulting from the adiabatic undamping (r_{ad}), reaching about half of the aperture. In comparison, after the dispersion-free steered (DFS) the envelope growth is now barely above the minimal growth, implying that the decelerator dispersion-free steering scheme, proposed in the framework of this thesis, has very effectively suppressed dispersive trajectories along the decelerator.

Another comment is here worthwhile: there are 48 decelerator sectors, and each one of them must perform to specification (Eq. (5.15)), in order to ensure nominal CLIC performance. If we require that a reasonable 99.9% of all randomly misaligned CLIC

machines must perform to specification, this translates to a required confidence for each decelerator sector of 99.998% . It is not feasible to simulate enough machines to show such confidence levels directly; instead we inspect the tails of the histogram of all envelopes of the simulated machines. A choice of component tolerance levels yielding significant distribution tails should be avoided. We here use this approach in order to give a rough estimate of the BPM resolution specified. Figure 5.18(b) shows the histogram over the envelope of all 500 machines, for various BPM resolutions used for the dispersion-free steering. For resolutions of a few μm, the tails of the distributions have a relatively sharp fall off, while for higher resolutions the size of the tails increases. This suggests that the BPM resolution should be kept to within a few μm if one wants a very large number of simulated random machines to stay within the specifications.

5.7 Summary of decelerator specifications

Ultimately, one of the main goals of an in-depth modelling and simulation of the CLIC drive beam decelerator is to understand the physics well enough to provide clear specifications for the machine components, a vital input to CLIC technical studies and cost studies. The decelerator studies performed in the framework of this thesis have lead to two sets of specifications, one for the decelerator magnets and one for the decelerator

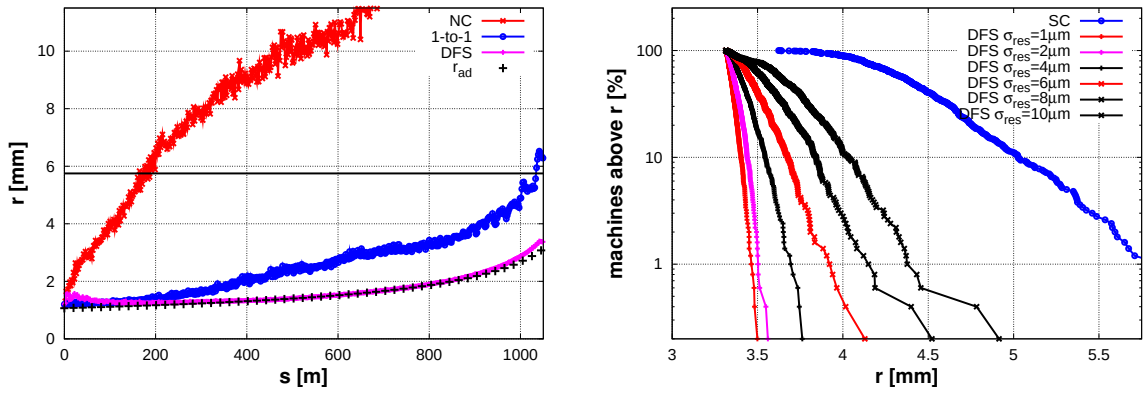

(a) Trajectories along realistic machines

(b) Beam envelopes for 500 machines

Figure 5.18: Results of realistic simulations of 500 machines including transverse dipole wakes and machine imperfections, assuming a quadrupole rms misalignment of $\sigma_{\text{quad}} = 20$ μm and a BPM accuracy of $\sigma_{\text{acc}} = 20$ μm. (a) The beam envelope along the decelerator lattice (the worst machine) in the cases of no correction (red x), 1-to-1 correction (blue o) and dispersion-free steering (magenta +). The minimum achievable envelope due to adiabatic undamping alone is plotted in black. A BPM resolution of $\sigma_{\text{res}} = 2$ μm is assumed in this plot. We observe that the dispersion-free steering has taken out almost all dispersive particle motion, in all parts of the beam. (b) Histogram over the envelope of all 500 machines, for various BPM resolutions used for the dispersion-free steering.

BPMs.

The sheer quantity of magnets and instruments foreseen for the decelerator ($\sim$ 100'000) implies that it is worth investing significant simulation efforts in order to establish the specifications with as high precision as possible.

5.7.1 Quadrupole specifications

The specification for the decelerator quadrupole magnets [95] suggests magnet gradient design accuracy of 1×10^{-3} rms and a power supply accuracy of 5×10^{-4}. As seen from Eq. (5.3) all quadrupole magnets should ideally have different absolute strength in order to follow the energy of the most decelerated particles. Ref. [95] discusses how a limited number of power supplies can be arranged while still giving adequate focusing properties. For further details we refer to the quadrupole specification [95], included in Appendix C.

5.7.2 BPM specifications

The performance of 1-to-1 correction and dispersion-free steering depends on the BPM accuracy and resolution. The beam envelope after performing 1-to-1 correction depends linearly on the BPM accuracy. The envelope after dispersion-free steering does not depend significantly on the BPM accuracy. However, the beam envelope size after performing dispersion-free steering depends linearly on the BPM resolution, when this error source becomes dominant. These considerations suggest a BPM accuracy of $\sim \sigma_{\text{acc}} = 20$ μm and a BPM resolution of $\sim \sigma_{\text{res}} = 2$ μm [96] (in correspondence with Figure 5.18). For further technical and operational details we refer to the BPM specification [96], included in Appendix C, which discusses specific issues including decelerator tune-up and the total number of BPMs needed.

5.8 Discussion of physics not included in the simulations

Neither space-charge nor ion effects are included in the PLACET simulations leading to the results presented in this thesis. An in-depth study of these physical phenomena would be outside the scope of the thesis, but for completeness we perform in this section a rough analytical estimation of their effects, based on already existing formulae.

5.8.1 Space-charge

We will in this section estimate transverse space-charge effects in the decelerator. Only direct space-charge effects will be considered, and we follow the approach in [108]. The

space-charge estimates could also have been performed using envelope equations, following e.g. [72], but we prefer not to introduce this framework for the space-charge estimates alone.

The smooth approximation of betatron motion, Eq. (5.12), will be used, and the effect of transverse space-charge is included by adding a space-charge term, K_{SC}, to the quadrupole strong focusing term, $K_\beta = 1/\langle\beta\rangle^2$, yielding

$$y'' + (K_\beta + K_{\mathrm{SC}})y(s) = 0. \tag{5.29}$$

We will here do a direct comparison of the space-charge effects with the strong focusing; if the space-charge term is of the same order as the strong focusing term, the beam would be space-charge dominated and the validity of our analyses questionable. In the extreme case, if $K_{\mathrm{SC}} > -K_\beta$ the motion would even be unstable.

The maximum transverse space-charge force in free space, F_y, for a round beam with transverse Gaussian distribution, assuming a bunched beam with Gaussian longitudinal charge-profile, with maximum beam intensity $\hat{I}$ is given by [108]

$$F_y(y) = \frac{e\hat{I}}{2\pi\varepsilon_0\beta c\gamma^2}\frac{1}{y}(1 - e^{-\frac{1}{2}(\frac{y}{\sigma_y})^2}), \tag{5.30}$$

where e is the unit charge, ε_0 the permittivity of free space, β the normalised particle velocity, γ the particle Lorentz factor, y the vertical distance from the transverse centre of the beam, and σ_y the vertical rms size (the analysis applies equally to the horizontal plane). For particles close to the transverse centre of the beam, the vertical force is to first order given by

$$F_y(y) \approx \frac{e\hat{I}}{4\pi\varepsilon_0\beta c\gamma^2}\frac{y}{\sigma_y^2}. \tag{5.31}$$

Using that $F_y = \beta^2 E_e \gamma y''$, where E_e is the electron rest energy, we deduce for this case the space-charge term in Eq. (5.29) as

$$y''_{SC} = \frac{e\hat{I}}{4\pi\varepsilon_0 E_e\beta^3 c\gamma^3}\frac{y}{\sigma_y^2} \equiv -K_{\mathrm{SC}}\, y.$$

We will calculate the space-charge defocusing first for the most decelerated particles, towards the end of the lattice. For a transverse Gaussian charge distribution the peak current is calculated as

$$\hat{I} = \frac{z_{bb}}{\sqrt{2\pi}\sigma_z} I,$$

and substituting values from Table A.3 we get $\hat{I} = 1.0\times10^3$ A, $\gamma = E_{\mathrm{min}}/E_e = 4.7\times10^2$, $\beta \approx 1$ and $\sigma_y \sim 1$ mm, we get $K_{\mathrm{SC}} = -5.6\times10^{-4}$ m^{-2}. Furthermore, $K_\beta = 1/\langle\beta\rangle^2 = 0.64$ m^{-2}, yielding

$$\frac{K_{\mathrm{SC}}}{K_\beta} = -9\times10^{-4}.$$

The magnitude of the direct space-charge defocusing is therefore less than 0.1% of the magnitude strong focusing for the most decelerated particles. For the *least* decelerated

particles, the focusing term K_β will decrease by a factor 1/10 towards the end of the lattice, but K_{SC} is about a factor 10 smaller than what we estimated for the most decelerated particles due to the higher energy. The space-charge effects will thus be of the same order for all drive beam particles. The worst-case approximation in Eq. (5.31) is valid for particles close to the centre of the transverse Gaussian distribution. From Eq. (5.30) we see that K_{SC} will decrease towards the bunch transverse edges (K_{SC} will also decrease in the longitudinal direction from the bunch centre), and the space-charge will therefore induce an addition *spread* in betatron tune. However, this spread is also very small compared to the PETS induced tune spread (varying form about 70 to 135), and will therefore not qualitatively change the drive beam physics. Moreover, the space-charge effects calculated here are always defocusing, and can therefore only increase the phase-advance. This implies that the calculation of the focusing strength needed to follow the most decelerated particles, cf. Section 5.1, should not be affected by the space-charge defocusing, even by a a very small value. We conclude that the effects of the transverse direct space-charge are negligible for the decelerator.

5.8.2 Ion effects

The drive beam electrons will ionise residual gas in their path. The electrons of the ionised gas are repelled while the positively charged ions can be trapped inside the beam. In general this might lead to betatron detuning and instabilities. Ion effects for the CLIC drive beam in the long transfer lines [54] upstream of the decelerator, see Figure 3.3, have already been studied using analytical expressions. The rise-time of the fast-ion instability, denoted τ_e, is inversely proportional to the pressure level in the beam pipe, and we here apply the expressions to perform a rough estimate of the required vacuum level, by calculating the pressure that leads to a single rise time along a decelerator sector.

The ion density will grow linearly with the passing of the bunch train, and the ions can be trapped in the potential of the electron beam if their atomic number A is larger than [54]

$$A_{\mathrm{trap}} = \frac{16 Q_i r_p N z_{\mathrm{bb}}}{3\pi^2(\sigma_x + \sigma_y)\sigma_y}, \tag{5.32}$$

where Q_i is the ion charge in units of elementary charge, r_p the classical proton radius, N the bunch population, z_{bb} the bunch to bunch distance and $\sigma_y = \sigma_x$ the transverse beam rms size (negligible ion motion is assumed in Eq. (5.32)). Substituting the decelerator baseline parameters from Table A.3 and assuming single ionisation, $Q_i = 1$, and carbon monoxide, with $A = 28$, as the dominant residual gas, we get

$$A \gg A_{\mathrm{trap}}$$

, indicating that the decelerator train will indeed trap ions.

The rise-time of the fast-ion instability can be estimated using the following formula [109]

$$\frac{1}{\tau_e} = \frac{p\sigma_{\mathrm{ion}}}{kT} \frac{N n r_e c}{\sqrt{18}(\sqrt{\epsilon_{Nx}\epsilon_{Ny}} + \epsilon_{Ny})a} \frac{1}{\sqrt{Q_i}}, \tag{5.33}$$

where p is the pressure, k the Boltzmann constant, T the temperature, σ_{ion} the cross section for ion production (about 2×10^{-22} m^{-2} for carbon monoxide [54]), N the bunch population, n the number of bunches, r_e the classical electron radius, a a frequency factor where $a \approx 0.1$ for a FODO-lattice [109], $\epsilon_{Nx} = \epsilon_{Ny}$ the initial normalised emittances and c the speed of light. The pressure level yielding much less than one fast-ion rise time, during the time the beam needs to pass through a decelerator sector of length L_{sector}, is found by requiring

$$\frac{L_{\text{sector}}}{\tau_e(p)c} \ll 1. \tag{5.34}$$

Combining Eqs. (5.33) and (5.34), and substituting the decelerator parameters in Table A.3, we estimate the required pressure level to

$$p \ll \frac{kT\sqrt{18}(\sqrt{\epsilon_{Nx}\epsilon_{Ny}} + \epsilon_{Ny})a\sqrt{Q_i}}{Nnr_e\sigma_{\text{ion}}L_{\text{sector}}} = 40 \text{ nTorr}. \tag{5.35}$$

The pressure level found is thus considerably less constraining than what was found for the transfer lines [54] (mainly due to the 1 km length of the decelerator sector, with respect to the long transfer length of 21 km). In return, the decelerator vacuum must be attained in an environment filled with power extraction and transfer structures, which will be more challenging.

It should be noted that Eq. (5.33) is an order of magnitude estimate. Also, in Eq. (5.33) the large energy spread of the decelerator drive beam is not taken into account, and it is possible that the decoherent motion of the electrons will lead to a slower rise-time and thus a less severe vacuum requirement. In order to provide more precise estimations for the required decelerator vacuum level, an extension to PLACET that will calculate the Fast-Ion effect during tracking, taking into account the real beam phase-space is foreseen [110].

5.9 Failure modes

A number of failure modes for the drive beam decelerator were studied in the framework of the thesis, and the results are reported in [93], paper included in Appendix B. An important result, highlighting again the interplay between beam dynamics studies and structure rf design, was an estimation of the maximum transverse voltage tolerated during a PETS breakdown, based on the criterion that y_c should be less than 1 m after an eventual breakdown. Figure 5.19 [93] presents the results, showing an analytical estimate [93] in blue and simulation results in red. The actual transverse voltages during breakdown of the 12 GHz CLIC PETS will be a subject of study in the Two-beam Test Stand [68] presented in Section 4.5.

Another study showed that if two or more quadrupoles fail simultaneously more than 10% of the pulse will be lost. With the very high drive beam intensity, losses of this level are of great concern. Machine protection issues have not been part of the thesis, but it is clear that this is an important future subject of study for the decelerator.

5.10 Orbit correction experiments in the CTF3 linac

We have seen in Section 5.5 that the drive beam decelerator requires sophisticated orbit correction in order to ensure robust transport through the entire lattice. In the framework of the thesis, experimental tests of the correction schemes envisaged for the decelerator were performed in the CTF3 linear accelerator. The linac operates with full beam-loading [63], implying that the accelerating voltage depends strongly on the electron current. This renders the linac a particularly good test-bench for the decelerator (where the voltage is purely due to beam loading). Figure 5.20(a) shows the structure of the CTF3 linac, and Figure 5.20(b) shows a photo of a linac girder, with the two SICA type [61] accelerating structures "Florella" and "Sylvie". The corrections were performed over a section of eleven girders, with energy varying from about 20 MeV at the entrance of the corrected lattice section, to about 120 MeV at the end. Both measured response matrices and modelled response matrices were used as basis for the correction (the energy of the fully loaded linac therefore had to be estimated with good precision).

The results of the experiments are reported in [94], paper included in Appendix B. A particularly important and relevant result was the demonstration of dispersion-free steering in the linac, and we highlight this result here: to clearly distinguish the performance of the different correction schemes, large BPM misalignments of up to 6 mm were simulated (by artificially adding this value to the BPM readings). The resulting orbits and dispersion after 1-to-1 correction and dispersion-free steering are shown in Figure 5.21. The 1-to-1 correction [94] steers the beam into the simulated centre of the

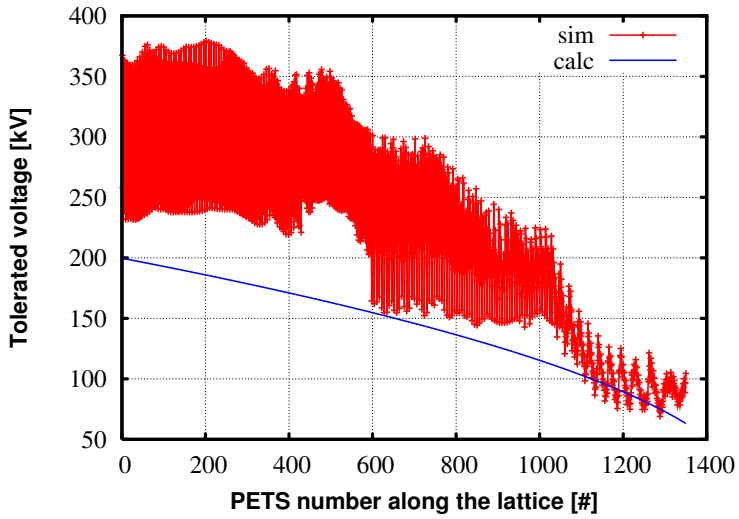

Figure 5.19: The maximum PETS transverse voltage tolerated during breakdown, along the lattice. An analytical estimate [93] in blue and simulation results in red. The tolerated transverse voltage decreases towards the end of the lattice, due to the lower rigidity of the most decelerated particles.

BPMs, thus inducing a large orbit bump generating significant dispersion. Dispersion-free steering, on the other hand, seeks to minimise the difference of dispersive trajectories, see Eq. (5.27). The resulting orbit shows indeed a salient feature of dispersion-free steering; unlike 1-to-1 correction, the dispersion-free steering is mostly oblivious to the (simulated) BPM misalignments. As seen from Figure 5.21 a trajectory close to the real centre orbit is found by the dispersion free steering, resulting in a reduction of the dispersion by a factor three.

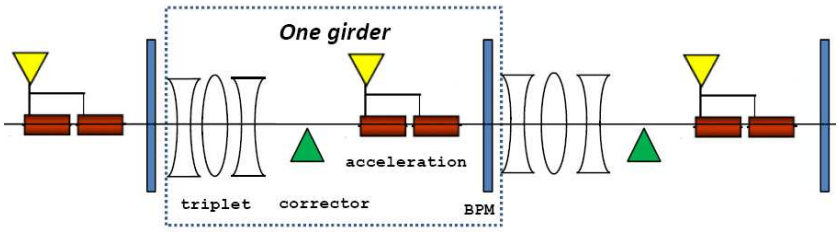

(a) CTF3 linac lattice structure

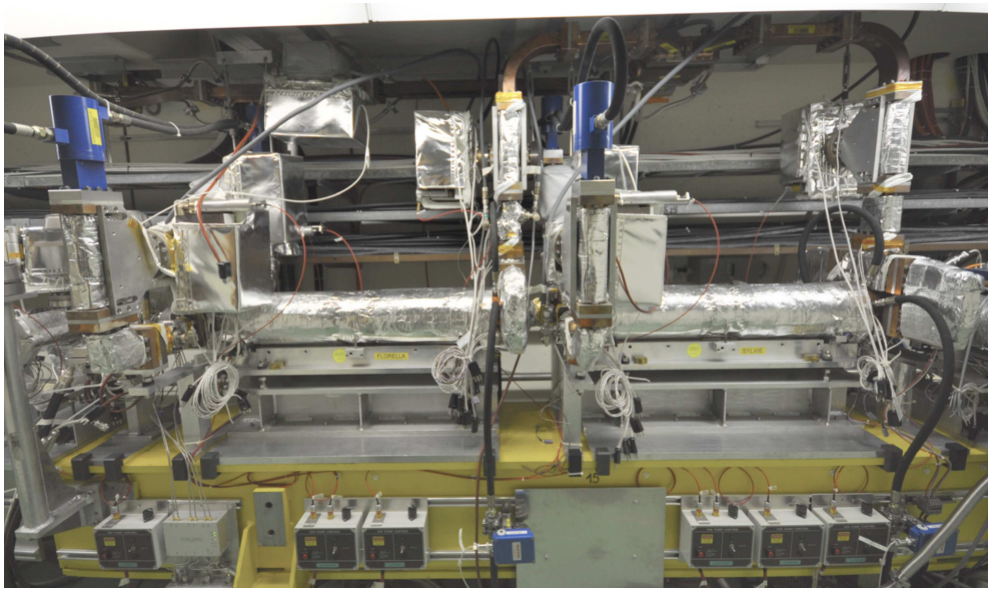

(b) CTF3 linac girder

Figure 5.20: The CTF3 linac. (a) Sketch of the lattice as considered for the steering experiments. (b) Photo of a CTF3 linac girder with two SICA accelerating structures.

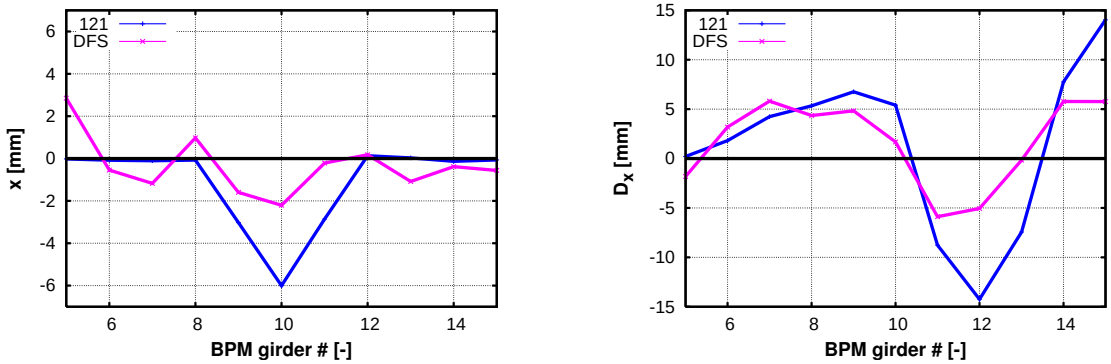

(a) Orbit after correction

(b) Dispersion after correction

Figure 5.21: Resulting orbits (a) and dispersion (b) after 1-to-1 correction (blue) and dispersion-free steering (magenta). The dispersion-free steering mostly ignores the simulated BPM misalignments, finds an orbit close to the centre and reduces the dispersion by a factor three with respect to the 1-to-1 correction.

6. The Test Beam Line

The main purpose of the Test Beam Line (TBL) [111,112] is to provide a realistic demonstration of the CLIC decelerator. The TBL will be installed in the CLIC Experimental Area (CLEX), see Figure 3.6, and will consist of a beam line with 16 cells, each containing a quadrupole mounted on a precision mover, a BPM and a PETS, as illustrated in Figure 6.1. According to the present schedule, 8 PETS should be installed in 2010, and the TBL installation should be completed by 2011-2012. In this chapter we present a study of the beam dynamics in the TBL, emphasising the similarities and differences between the CLIC decelerator and the TBL.

6.1 TBL baseline parameters

The TBL baseline PETS has a length of $L_{\mathrm{PETS}} = 0.8$ m, with all other characteristics equal to the TBTS PETS and the PETS proposed for CLIC (parameters in Table A.4). The PETS length is chosen so that the nominal CLIC PETS power of 135 MW [38] can be produced in CLEX. We define here as nominal TBL parameters a CLEX drive

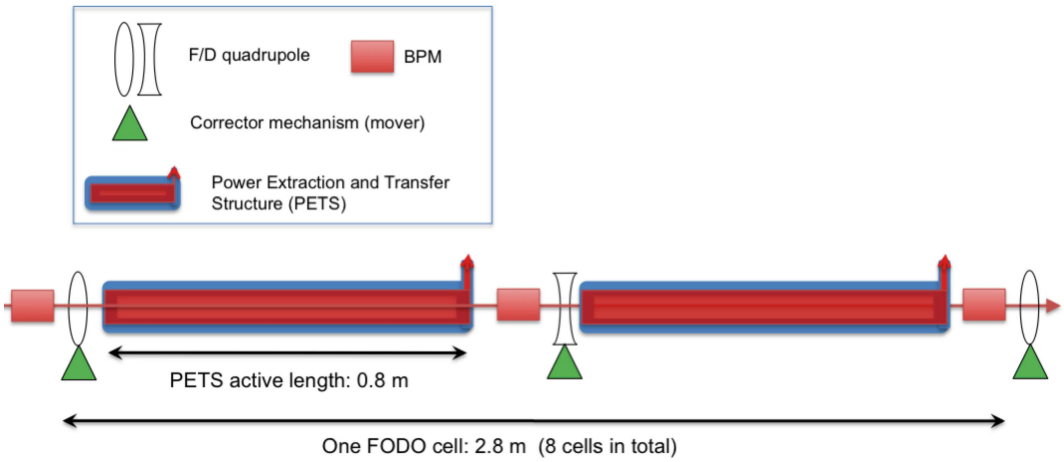

Figure 6.1: TBL lattice structure. The TBL lattice consists of 8 FODO cells, with one 0.8 m PETS installed per quadrupole, in total 16 PETS. The figure should be compared with Figure 5.2 showing the decelerator lattice structure.

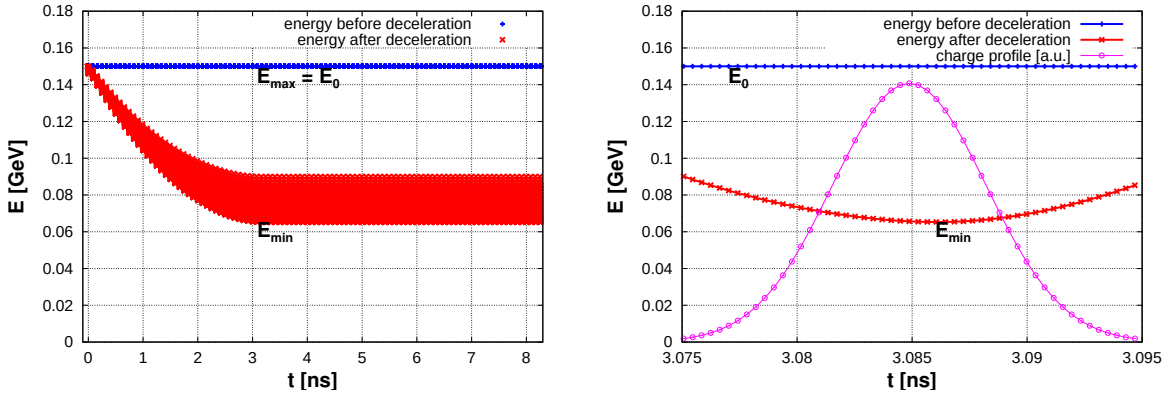

(a) Beam energy profile (first 8 ns)

(b) Bunch energy profile (steady state)

Figure 6.2: CLEX beam energy profiles before entering the TBL, in blue (+), and after having passed through the entire TBL, in red (x). The Gaussian bunch charge profile is shown, in magenta (o), for clarity. The figure should be compared with Figure 5.1 showing the decelerator energy profile.

beam initial energy of $E_0 = 150$ MeV and a CLEX beam intensity of $I_{\text{nom}} = 28$ A. Assuming nominal parameters each PETS will produce a steady state power, according to Eq. (4.13), of

$$P = 139 \text{ MW},$$

slightly more than the 135 MW required for CLIC. According to Eq. (4.15), the maximum energy loss per PETS is

$$\hat{U} = 5.2 \text{ MV}.$$

After passing through $N_{\text{nom}} = 16$ PETS, the minimum residual beam energy will be

$$E_{\text{min}} = E_0 - e\hat{U}N_{\text{nom}} = 67 \text{ MeV}.$$

and the resulting energy extraction efficiency, defined in Eq. (5.1), is

$$\eta_{\text{extr}} = 55 \text{ \%}.$$

According to Eq. (4.8), the fill-time of the TBL PETS is

$$t_{\text{fill}} = 3 \text{ ns},$$

a factor three longer than for the decelerator, due to the longer PETS length in the TBL. Figure 6.2 shows the simulated energy profile after deceleration in the TBL with nominal parameters. Comparing with the CLIC decelerator final energy profile in Figure 5.1, it is seen that the features of the profiles are very similar for TBL and for CLIC, with the difference, however, of longer fill-time and lower η_{extr} for the TBL.

We remind that $\hat{U}$ and η_{extr} correspond to the minimum energy particles, while e.g. a BPM in a spectrometer line would rather measure the mean deceleration, given by Eq. (4.17), $\langle U \rangle = F(\lambda)\hat{U}$.

6.2 TBL energy extraction and beam envelope in a perfect machine

In order to provide a realistic demonstration of the decelerator, it is important that a significant percentage of the beam energy is extracted in the TBL. The normalised emittance in CLEX is estimated to be in the same order as in the decelerator, $\epsilon_N = 150$ μm in both planes, but due to low final energy in the TBL compared with CLIC, the beam envelope, r, as defined in Eq. (5.14), is significantly larger after deceleration in the TBL than after deceleration in the CLIC decelerator. The PETS design, on the other hand, is the same as for CLIC, with the same half-aperture $a_0 = 11.5$ mm. In TBL the incoming beam will, even for a perfect machine and injection, fill up almost half of the aperture

$$r_{\text{incoming}} = 3\sqrt{(\beta_F + \beta_D)\epsilon_N/\gamma_0} = 5.1 \text{ mm},$$

where β_F and β_D are the matched beta functions in the middle of the first TBL quadrupole, and γ_0 the initial Lorentz factor. With 16 PETS and $I = 28$ A, the final beam envelope in a perfect machine is

$$r = 3\sqrt{(\beta_F + \beta_D)\epsilon_N/\gamma_{\text{Emin}}} = 7.6 \text{ mm},$$

where γ_{Emin} is the Lorentz factor of the most decelerated particles. r reaches thus two thirds of the available aperture for a perfect machine and injection. In comparison, in the decelerator the beam envelope, assuming perfect machine and injection, is $r = 3.3$ mm. An ideal demonstration of the deceleration would imply raising η_{extr} from 55% to 90%, and lowering r for a perfect machine from 7.5 mm to 3.3 mm. We will present some calculations of the values for η_{extr} and r available with CLEX. An initial beam energy range from 50 MeV to 200 MeV is considered in order to provide numbers for eventual CTF3 upgrades as well.

Up to the present, CTF3 is far from operating with the nominal beam intensity in CLEX [65]. The quantities η_{extr} and r depend on the incoming beam energy, the beam intensity and the number of PETS installed. For a perfect machine and injection, scaling either the number of PETS or the beam intensity yields the same effect on η_{extr} and r. It is therefore useful to parameterize reduced deceleration by a factor

$$\eta_{\text{red}} = \frac{N}{N_{\text{nom}}}\frac{I}{I_{\text{nom}}}$$

where $\eta_{\text{red}} = 1$ corresponds to nominal TBL parameters ($N_{\text{nom}} = 16$ and $I_{\text{nom}} = 28$ A). Figure 6.3 shows r and η_{extr} after deceleration with different values of η_{red}, assuming perfect machine and injection. From Figure 6.3(a) it is seen that in order to achieve a high fraction of energy extraction at all, it is vital that either the beam intensity in CLEX reaches the nominal value, or alternatively that one or more PETS are equipped with recirculation as in the TBTS [69], or with rf priming (rf coupled into the PETS from an external source).

Even with recirculation or rf priming, η_{extr} will be limited by the CLEX initial energy, due to beam envelope limitations, see Figure 6.3(b). Sending a low energy beam into CLEX would in principle lead to a high δ_{expr}, but the beam might be lost before the end of the TBL. In order to demonstrate high power extraction efficiency, and at the same time keep losses low, the CLEX initial energy should be as high as possible. This is illustrated in Figure 6.4 which shows the energy extraction efficiency, η_{extr}, as function of E_0 for a given maximum beam envelope (the beam envelope, r, is allowed to reach 1/2, 2/3 and 1/1 of the vacuum chamber aperture, respectively). In this graph no limits on the deceleration are assumed (PETS operation with field recirculation or priming is assumed where necessary). We see that if the beam envelope should stay within half the available aperture, which is the requirement for CLIC, η_{extr} would be limited to 25 %, regardless of the available beam intensity, if we assume the nominal CLEX energy of $E_0 = 150$ MeV.

Finally, it should be noted that operating the TBL with recirculation or priming to achieve the nominal deceleration, with beam intensity smaller than the nominal, will typically result in less severe transverse wakes than for nominal operation. Because the transverse wake is one of the most important effects to study, the TBL would be a less good demonstration if it is not run with the nominal beam intensity. In the remaining sections we will uniquely discuss TBL operation with nominal parameters.

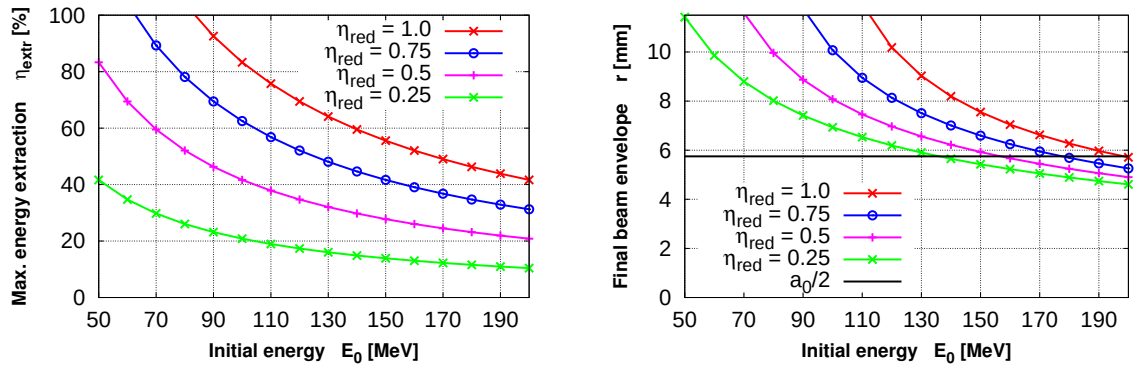

(a) Energy extraction efficiency

(b) Beam envelope

Figure 6.3: The energy extraction efficiency (a) and beam envelope r (b) after deceleration in the TBL, in a perfect machine with perfect injection. Each line represents a different deceleration reduction factor, $\eta_{\text{red}} = (N/N_{\text{nom}})(I/I_{\text{nom}})$, where η_{red} corresponds to the nominal TBL parameters. An energy range from 50-200 MeV is considered in order to provide numbers for eventual CTF3 upgrades.

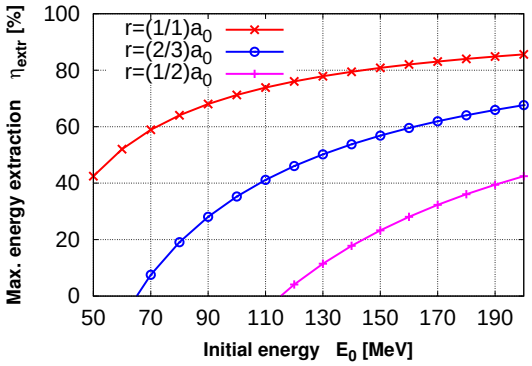

Figure 6.4: The maximum attainable energy extraction efficiency, in a perfect machine with perfect injection, as function of the CLEX beam energy, for fixed beam envelope, r. No limitations on the CLEX beam intensity are applied here (PETS operation with field recirculation or priming is assumed where necessary).

6.3 TBL transverse wakes

In this section nominal TBL parameters are assumed. In particular, it is assumed that the PETS damping slots are filled with dielectric material, providing strong dipole mode damping [67], corresponding to the wake parameters in Table A.5.

Analogous to the analysis in Section 5.4 we simulate the envelope growth for trains injected with a static offset; both point-like TBL bunch trains and trains with full bunch lengths. Figure 6.5(a) shows the wake growth factors, $\Upsilon_{\mathrm{n,sim}} = y_c/y_{c,wo}$, along a train with point-like bunches, after having passed through the TBL. We observe that the wake growth factor is very small; a maximum amplification of around 10%. For the decelerator on the other hand, Figure 5.9(a) shows a significant growth, reaching a factor 4. Figure 6.5(c) shows the amplification for a train with long bunches (σ_z = 1 mm). In this case a small fraction of the bunch charge shows indeed wake growth factors above two, however, the bunch centroid motion is not amplified significantly, because the bulk of the charge has very small growth. Similar results are obtained when scaling the Q-factors or the wake amplitudes by a factor of 2; neither scaling yields significant amplification of the beam centroid motion. In order to provoke a significant growth factor for point-like bunches, the wake amplitude had to be increased by a factor three with respect to the nominal. For illustration, this (hopefully) unrealistic case is presented in Figures 6.5(b) and 6.5(d), where we observe a growth reaching a factor three in the transient.

One of the main diagnostic tools in the TBL will be the BPMs. Figure 6.6(a) shows the simulated BPM position signal, integrated over a pulse train of 140 ns, injected at a constant offset, for the cases of no transverse wakes, nominal transverse wakes and wake amplitude three times the nominal. The difference between no wakes and the nominal wake is not very large, as expected due to the small amplification of the beam centroid (Figure 6.5(b)). Neither for a wake amplitude three times the nominal is the

amplification of the BPM reading significantly increased. For this latter case, however, the effect of the wake has significantly changed the phase-advance of the beam centroid. This indicates that phase-advance measurements might be an interesting observable of wake effects in the TBL. The wake effects are somewhat more pronounced when considering beams with incoming jitter, for worst-case jitter frequencies. Figure 6.6(b) shows the amplification of a beam injected with transverse jitter with jitter frequency at the dipole mode frequency of 13.4 GHz . The nominal PETS wake amplifies the jitter by a factor of about two. In order to artificially induce and measure beam jitter at specific frequencies, Ref. [111] suggests to use resonant kickers and BPMs, however, this equipment is presently not a part of the baseline TBL design.

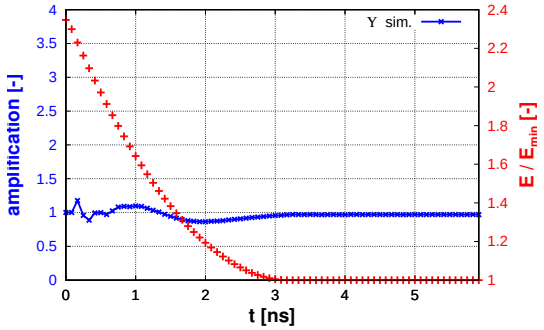

(a) Point-like bunches, nominal wake amplitude

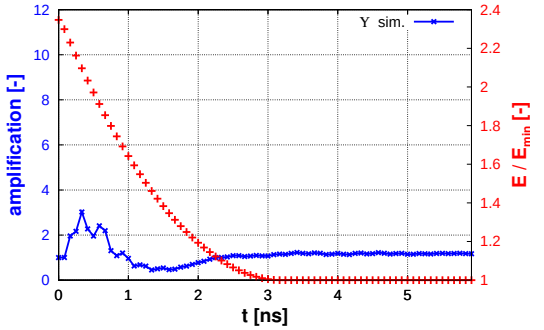

(b) Point-like bunches, three times wake amplitude

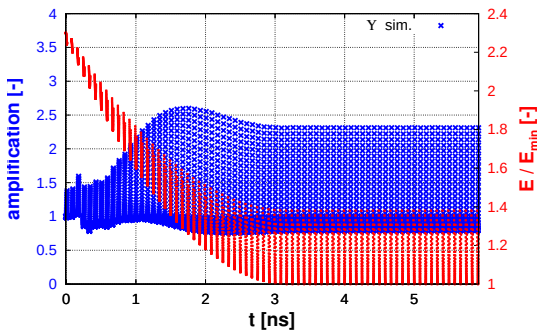

(c) $\sigma_z = 1$ mm, nominal wake amplitude

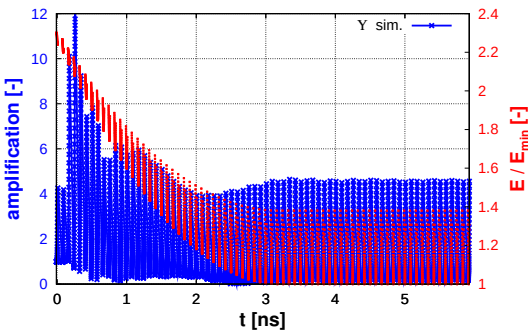

(d) $\sigma_z = 1$ mm, three times wake amplitude

Figure 6.5: Wake growth factors for TBL bunch trains, injected with a static offset. (a) and (c) show the wake growth factors for nominal parameters, for point-like bunches and full-length bunches respectively. The multi-bunch effects for point-like bunches are negligible. (a) and (c) should be compared with Figures 5.9(a) and 5.9(c), which show the simulations for nominal decelerator parameters. (b) and (d) show the growth factors for a wake amplitude three times the nominal, for point-like bunches and full-length bunches respectively. For this case a significant amplification is observed, especially in the high-energy transient.

6.4 TBL orbit correction

In this section nominal TBL parameters are assumed. Figure 6.7 presents results of orbit correction simulations, analogous to the results presented for the decelerator in Figure 5.18. The quadrupole initial rms offset is $\sigma_{\text{quad}} = 100$ μm (a reasonable estimate for CTF3), and 100 machines are simulated. The results show that some losses are expected for an uncorrected machine, and that 1-to-1 steering brings the envelope close to that of a perfect machine. The dispersion-free steering performs as well as the 1-to-1 steering towards the end of the lattice. (dispersion-free steering performs less well in the first cells, however, this does not matter as long as the overall envelope growth along the lattice is contained).

The decelerator dispersion-free steering scheme, discussed in section 5.5.5, was based on using delayed-switching in the sub-harmonic buncher to create a longer train with a beam intensity that varies in step functions along the trail, see Figure 5.15. Due to the PETS beam loading, the mean energy loss in the test-beam is about half of that of the nominal beam, resulting in a highly dispersive trajectory. The principle is elegant, however, a similar correction scheme has to our knowledge not been applied previously, and it is therefore of high interest to demonstrate this scheme. Even though DFS is not *required* as alignment technique for the TBL, the TBL can still act as a valuable *test-bed* for the decelerator scheme. Analogous to what is proposed for the decelerator, the

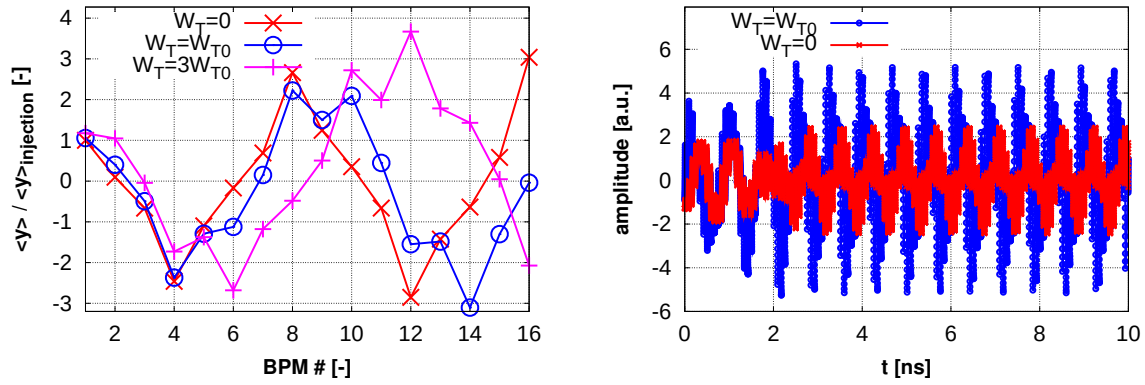

(a) BPM readings (constant injection offset)

(b) Amplification of beam jitter

Figure 6.6: Potential TBL wake observables. (a) Simulated BPM readings along the TBL a train injected with constant offset, for cases without any transverse wake (red x), nominal transverse wake (blue o) and wake amplitude three times the nominal (magenta +). In no cases a significant amplification of the beam centroid is observed along the TBL. For a wake amplitude three times the nominal, a significant change in the centroid phase-advance is observed. (b) Amplification of a beam injected with transverse jitter on a dipole mode frequency, for cases without any transverse wake (red x), nominal transverse wake (blue o). The nominal PETS wake amplifies the jitter by a factor of about two, potentially observable on a BPM sensitive to the jitter frequency.

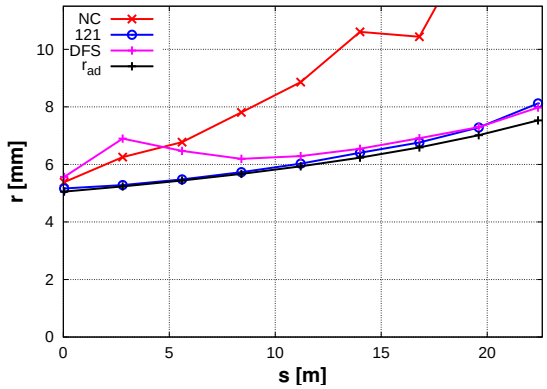

Figure 6.7: The beam envelope along the TBL lattice in the cases of no correction (red x), 1-to-1 correction (blue o) and dispersion-free steering (magenta +). The minimum achievable envelope due to adiabatic undamping alone is also plotted for comparison (black +). The 1-to-1 steering is sufficient to correct the machine very close to the minimum envelope, however, the dispersion-free steering is performing equally well. The figure should be compared with Figure 5.18 showing the decelerator orbit correction performance.

delay-loop in CTF3 (shown in Figure 3.5) can generate bunch trains with every second bunch removed in part of the train. The TBL beam loading will lead to a dispersive orbit (in the simulation in Figure 6.7 a test-beam with every second bunch missing has been used). This technique of test-beam generation is precisely the same as for the CLIC decelerator, as described in Section 5.5.4.

The performance of the DFS in the TBL can be further investigated by simulating large TBL BPM misalignments, analogous to the experiments performed for the CTF3 linac, as described in Section 5.10.

6.5 TBL as a demonstration of the decelerator

We end the discussion on the TBL with some general considerations concerning TBL as a demonstration of the decelerator.

A key demonstration in the TBL is production of 12 GHz rf power in a stable manner. The power production should be uniform both along the TBL and along the pulse train. Furthermore, it must be verified with high precision that the energy extracted from the beam corresponds to the 12 GHz rf power. The Two-beam Test Stand, discussed in Section 4.5, can perform precise correspondence measurements for a single PETS, so the emphasise of the TBL should be to verify the power producing along the lattice, and compare the total power production with the total energy extracted. Specialised spectrometer dumps are being developed in order to accommodate precision energy measurements during the various stages of TBL installation (1 PETS, 8 PETS and 16 PETS) [113].

The direct effect of the transverse wakes seems to be limited in the TBL, assuming the damping of the dipole modes is as good as promised by rf simulations. Because the transverse wake effects are less severe in TBL than in the CLIC decelerator, small or negligible observed wake effects in the TBL would not prove the feasibility of the CLIC decelerator. If, on the other hand, if significant amplification of the beam centroid or unexplainable losses *are* observed, it might mean that the transverse wakes are significantly larger than predicted. Furthermore, if no effect is seen, it should be considered removing the damping material from the PETS in order to aggravate the wake effects. During commissioning, however, we do recommend to start with damped PETS and only remove damping material when stable beam transport has been proven.

The incoming beam intensity should be as high as possible, preferably the nominal value of 28 A, in order to perform a realistic demonstration of energy extraction and to maximise the effect of the transverse wakes. The bunch length should also be as short as possible, since e.g. the power produced by 2 mm bunches is about 20 % smaller than the power produced by 1 mm bunches.

The TBL will act as a test-facility for PETS, but also for other vital parts of the decelerator components. For the beam-based alignment, high-precision quadrupole movers have been developed [114], and will be used to test the 1-to-1 steering and the DFS. The performance of the TBL BPMs [115] with the highly decohered TBL beam will also be quantified.

The full TBL beam-line will be installed before all PETS are installed, and there might therefore be opportunities to perform other experiments relevant to the decelerator, not including the PETS, e.g. a verification of the fast-ion instability, discussed in Section 5.8.2, by controlled variation of the TBL vacuum level (proposed by [116]).

Because of the low final energy, and the subsequently large beam envelope even for a perfect machine ($r = 7.5$ mm for a perfect machine), it will be challenging but in principle possible, to achieve a low-loss transport through the TBL. If the transport can be achieved using orbit correction, with a test-beam generated by delayed-switching, it will be a significant statement of feasibility of the proposed correction scheme for the CLIC drive beam decelerator.

Some considerations on the TBL beam diagnostics

In the TBL simulations the injected beam has a flat, ideal energy profile $E(z) = E_0$, and regular bunch spacing and charge profile. In CLEX this will not be the case, and therefore a complete characteristics of the incoming beam is important in order to disentangle the beam dynamics in the TBL. In particular, the emittance, the energy and charge profile along the pulse, the position and angle along the pulse, as well as the bunch length should be measured with good precision.

In Chapter 5 we studied the performance of the CLIC decelerator in terms of Eq. (5.14), r: the PETS and machine design must result in an r contained along the entire decelerator. In the TBL BPMs we do not observe r directly, and cases might occur where

r is very large, while the BPM readings remain very small. On the other hand, a large r could be observable on screens with sufficient sensitivity, or eventually in loss monitors along the TBL lattice. It is therefore of high importance to install both transverse screens and loss monitors with sufficient sensitivity in the TBL. Ideally, the sensitivity should correspond to a fraction of the CLEX bunch charge, however, this target is probably not feasible with the available technology, and the exact specification of the TBL instrumentation is still under study.

In Figures 6.5(b) and 6.5(d) the amplification is mainly in the transient part of the beam, within the first 3 ns. The CTF3 beam has additional transient effects due to e.g. the linac beam loading, however, the transient part of the beam will in general follow a different beam dynamics from the steady state part. For the decelerator, loss-minimisation in the transient is as important as in the steady state part, and it is therefore of importance that at least part of the TBL beam diagnostics tools achieve time resolutions in the order of 1 ns, in order to resolve beam dynamics effects in the transient (e.g. the spectrometer readout and/or a dedicated fast BPM).

7. Conclusions and Outlooks

This thesis has focused on the heart of the two-beam scheme proposed for the Multi-TeV electron-positron collider, CLIC: the rf power production and the corresponding deceleration of the drive beam.

The power extraction and transfer structure, the PETS, has been thoroughly presented with the aim of providing the physics base to understand the beam dynamics in the CLIC decelerator. A simple model of PETS field recirculation has been developed as well, in order to reflect the test set-up for the first 12 GHz PETS tests with beam in the Two-beam Test Stand. The theoretical framework developed has been used to reconstruct measurements of PETS rf power, phase and beam energy loss, and good agreement between reconstruction and measurements has been found.

The decelerator, consisting of up to 1 km long sectors filled with almost 1500 PETS each, has been simulated in detail. The next step of decelerator experiments, the Test Beam Line, has been studied, indicating that some, but not all, key concepts of the decelerator can be studied in this facility. It must be stressed that for the Test Beam Line studies, it is of high importance to reach the nominal beam intensity foreseen for CLEX. Even with the completion of the Test Beam Line, feasibility studies for the decelerator must to a large degree be based on theory and simulation, and in the framework of this thesis a methodology has been built up in order to study key decelerator beam dynamics feasibility issues.

By simulation we have investigated beam envelope growth in the decelerator due to the transverse dipole wake. Mitigation of the wake effects has been one of the major constraints on the PETS design, and with the current design the effect of wakes seems to be adequately contained. However, the margin is not large; simulation studies have revealed that for example failure to achieve the design Q-values by a factor two leads to unacceptable envelope growth along the beam. Furthermore, the simulations have shown that robust suppression of the dipole wake depends strongly on the PETS group velocity, even if the ratio between impedance and group velocity stays constant, since the impedance must sufficiently decohere the motion at the head of the drive beam. Simulations studies have also revealed that due to the particularly large energy spread in the drive beam under deceleration, a standard 1-to-1 correction where the beam centroid is steered into the centre of the BPMs, might not be sufficient to minimise beam losses, even if excellent component pre-alignment of 20 micrometers is assumed. Instead a correction scheme based on dispersion-free steering is proposed. We have shown that a

test beam generated by bunch gymnastics using delayed switching, taking advantage of the PETS beam loading, is well suited to take out the dispersion. Because there are 48 decelerator sectors, we require a very high level of confidence that each sector performs to specification in order to reach a high level of confidence for the CLIC machine. This requirement leads to relatively tight tolerance limits for the decelerator BPM resolution and accuracy. In short, the simulations show that with the present PETS design and proposed orbit-correction scheme, the drive beam should be transported along the entire decelerator with only a minimal envelope growth due to imperfections or wake effects. Some simulation issues remain still to be addressed though, e.g. inclusion of the beam-loading ramp for the 12 GHz CLIC which will affect the transient part of the beam, and the inclusion of other physics, including ion effects and space-charge in the PLACET simulations.

There is still room for future optimisation of the decelerator lattice. The fact that the decelerator has by far the largest number of both lattice magnets and beam position monitors of all CLIC sub-systems calls for further integrated rf and beam dynamics studies with aim of reducing these numbers. In the extreme case: if the dipole wakes were completely suppressed, it is possible that the number of both lattice magnets and instrumentation items could be reduced by a factor two. An even broader optimisation scope could be imagined: the maximum energy extraction of drive beam particles is currently specified to 90%, as a compromise between efficiency and envelope growth. If one allows for lower extraction efficiency, the beam envelope growth might be reduced and tolerances might become looser, however, at the same time the overall efficiency of the CLIC machine will decrease. Contrariwise, extracting more energy from the drive beam increases efficiency, but might lead to tighter component tolerances. This optimisation scope would therefore be more involved, possibly including cost studies. However, we recommend it to be looked into at least before the completion of a technical design for CLIC.

On the medium term, though, we consider that the vital next steps for the decelerator studies are thorough benchmarking of the decelerator and PETS simulation studies against experiments. The first PETS beam tests, presented in this thesis, show that we are on a good path to understanding the physics details. Further tests planned for the short and medium term include precise studies of the dipole wake, as well as power production versus energy extraction in the Two-beam Test Stand, as well as the important demonstration of beam transport where a large fraction of the energy is extracted along the lattice, to be performed in the Test Beam Line. The fact that the final CLIC machine will include 42 km of decelerator lattice with more than 70'000 PETS, suggests that the details of power production, energy extraction, beam envelope growth and instrumentation issues should be understood to a very good level of detail from the planned experiments.

The overall goal to which we hope this thesis has contributed, is to show full feasibility of CLIC by the time the first LHC results are ready. In this case, the international particle physics community will have access to a proven Multi-TeV lepton collider concept, ready to be implemented in order to further unfold the discoveries made by the LHC.

Bibliography

[1] H. Murayama, "The origin of neutrino mass," Physics World, May, 2002.

[2] P. Watkins, *Story of the W and Z.* Cambridge University Press, 1986.

[3] G. Arnison, A. Astbury *et al.*, "Experimental observation of isolated large transverse energy electrons with associated missing energy at s**(1/2) = 540-GeV," *Phys. Lett.* B122, p. 103, 1983.

[4] G. Arnison, A. Astbury *et al.*, "Experimental observation of lepton pairs of invariant mass around 95-GeV/c**2 at the CERN SPS collider," *Phys. Lett.* B126, p. 398, 1983.

[5] J. Rees, in *Handbook of Accelerator Physics and Engineering*, 3rd ed. World Scientific Publishing Co. Pte. Ltd, 2006, sec. 1.6.3, p. 11.

[6] ILC Global Design Effort and World Wide Study, "International Linear Collider Reference Design Report," 2007.

[7] The CLIC Study Team, "A 3 TeV e+e- Linear Collider Based on CLIC Technology," 2000.

[8] W. Schnell, "A Two-Stage RF Linear Collider using a Superconducting Drive Linac," CERN CLIC Note 13, 1986.

[9] The CLIC-CTF3 collaboration. [Online]: http://clic-meeting.web.cern.ch/clic-meeting/CTF3_Coordination_Mtg/Table_MoU.htm

[10] The CERN Council Strategy Group. [Online]: http://council-strategygroup.web.cern.ch/

[11] S. Glashow, *Nucl. Phys.* 22, p. 579, 1961.

[12] S. Weinberg, *Phys. Rev. Lett.* 19, p. 1264, 1967.

[13] A. Salam, *in Elementary Particle Theory, p. 367*, N. Svartholm, Ed. Stockholm: Almqvist and Wiksell, 1968.

[14] F. Mandl and G. Shaw, *Quantum Field Theory.* John Wiley & Sons, Ltd., 1993.

[15] C. Amsler, M. Doser *et al.*, "2008 Review of Particle Physics," *Phys. Lett.* B667, no. 1, p. 473, 2008.

[16] The ATLAS Collaboration, "ATLAS Detector and Physics Performance - Technical Design Report, Vol. II," 1999.

[17] The TESLA collaboration, "TESLA Technical Design Report," 2001.

[18] M. Battaglia, A. De Roeck, J. Ellis, and D. Schulte (Eds.), "Physics at the CLIC Multi-TeV Linear Collider," 2004.

[19] A. De Roeck and J. Ellis, in *Briefing Book for the Zeuthen Workshop, v.2*, 2006, p. 2.1.05.

[20] LHC/LC Study Group: G. Weiglein, T. Barklow *et al.*, "Physics Interplay of the LHC and the ILC," *arXiv:hep-ph*, no. 0410364v1, 2004.

[21] M. T. Dova, P. Garcia-Abia, and W. Lohmann, "Determination of the Higgs boson spin with a linear e+e- collider," *arXiv:hep-ph*, no. 0302113, 2003.

[22] R. Assmann, "LEP Operation and Performance with Electron-Positron Collisions at 209 GeV," CERN-SL-2001-003 DI, 2001, Chamonix.

[23] K. Wille, *The Physics of Particle Accelerators*. OXFORD University Press, 2000.

[24] T. Sen and J. Norem, "Very large lepton collider in the Very Large Hadron Collider tunnel," *Phys. Rev. ST AB*, vol. 5, p. 1, 2002.

[25] The NLC Collaboration, "2001 Report on the Next Linear Collider," 2001.

[26] R. P. Johnson, "Ionization Cooling and Muon Colliders," in *Proceedings of the 11th biennial European Particle Accelerator Conference, EPAC'08*, 2008, p. 2917.

[27] G. A. Loew, in *Handbook of Accelerator Physics and Engineering*, 3rd ed. World Scientific Publishing Co. Pte. Ltd, 2006, sec. 1.6.11, p. 31.

[28] D. Proch, in *Handbook of Accelerator Physics and Engineering*, 3rd ed. World Scientific Publishing Co. Pte. Ltd, 2006, sec. 7.3.10, p. 576.

[29] Final International Technology Recommendation Panel Report. [Online]: http://www.fnal.gov/directorate/icfa/ITRP_Report_Final.pdf

[30] A.Yamamoto, "Global R&D Effort for the ILC Linac Technology," in *Proceedings of the 11th biennial European Particle Accelerator Conference, EPAC'08*, 2008, p. 12.

[31] G. A. Loew and J. W. Wang, in *Handbook of Accelerator Physics and Engineering*, 3rd ed. World Scientific Publishing Co. Pte. Ltd, 2006, sec. 6.12, p. 428.

[32] S. Döbert, C. Adolphsen *et al.*, "High Gradient Performance of NLC/GLC X-Band Accelerating Structures," in *Proceedings of the 21st IEEE Particle Accelerator Conference, PAC'05*, 2005, p. 372.

[33] O. S. Bruening, P. Collier, P. Lebrun, S. Myers, R. Ostojic, J. Poole, and P. Proudlock (Eds.), "LHC Design Report, v.1," 2004.

[34] D. Schulte, "Luminosity Limitations at the Multi-TeV Linear Collider Energy Frontier," in *Proceedings of the 8th biennial European Particle Accelerator Conference, EPAC'02*, 2002, p. 59.

[35] D. Schulte, "Main Linac Emittance Growth and Luminosity in Future Linear Colliders," in *Proceedings of the 20th IEEE Particle Accelerator Conference, PAC'03*,

2003, p. 2727.

[36] M. A. Furman, in *Handbook of Accelerator Physics and Engineering*, 3rd ed. World Scientific Publishing Co. Pte. Ltd, 2006, sec. 2.5.11, p. 148.

[37] F. Zimmermann, in *Handbook of Accelerator Physics and Engineering*, 3rd ed. World Scientific Publishing Co. Pte. Ltd, 2006, sec. 2.5.10, p. 144.

[38] H. H. Braun, F. Tecker (Ed.) *et al.*, "CLIC 2008 Parameters," CERN CLIC Note 764, 2008.

[39] W. D. Kilpatrick, "Criterion for Vacuum Sparking Designed to Include Both rf and dc," *Rev. Sci. Instrum.*, vol. 28, no. 10, p. 824, 1957.

[40] H. H. Braun, F. Tecker (Ed.) *et al.*, "Updated CLIC Parameters 2005," CERN CLIC Note 627, 2005.

[41] W. Wuensch, "CLIC Accelerating Struture Development," in *Proceedings of the 11th biennial European Particle Accelerator Conference, EPAC'08*, 2008, p. 2922.

[42] A. Grudiev, D. Schulte, and W. Wuensch, "Optimum Frequency and Gradient for the CLIC Main Linac," in *Proceedings of the 10th biennial European Particle Accelerator Conference, EPAC'06*, 2006, p. 1867.

[43] A. Grudiev, H. H. Braun, D. Schulte, and W. Wuensch, "Optimum Frequency and Gradient for the CLIC Main Linac Accelerating Structure," in *Proceedings of the XXIV Linear Accelerator Conference, LINAC'08*, 2008, p. 527.

[44] A. Grudiev and W. Wuensch, "Design of an X-band Accelerating Structure for the CLIC Main Linac," in *Proceedings of the XXIV Linear Accelerator Conference, LINAC'08*, 2008, p. 933.

[45] C. Adolphsen, G. Bowden *et al.*, "Results from the CLIC X-Band Structure Test Program at NLCTA," in *Proceedings of the 23rd IEEE Particle Accelerator Conference, PAC'09*, 2009.

[46] Y. Papaphilippou, private communication.

[47] Y. Papaphilippou, H. Braun, and M. Korostelev, "Parameter Scan for the CLIC Damping Rings," in *Proceedings of the 11th biennial European Particle Accelerator Conference, EPAC'08*, 2008, p. 679.

[48] S. Redaelli, R. Assmann, W. Coosemans, G. Guignard, D. Schulte, I. Wilson, and F. Zimmermann, "CLIC Magnet Stabilization Studies," in *Proceedings of the XXII Linear Accelerator Conference, LINAC'04*, 2004, p. 483.

[49] R. Tomás, H. H. Braun, M. Jørgensen, and D. Schulte, "Optimizing the CLIC Beam Delivery System," in *Proceedings of the 11th biennial European Particle Accelerator Conference, EPAC'08*, 2008, p. 631.

[50] Z. D. Farkas, in *Handbook of Accelerator Physics and Engineering*, 3rd ed. World Scientific Publishing Co. Pte. Ltd, 2006, sec. 6.7.1, p. 407.

[51] A. M. Sessler, "The FEL as a Power Source for a High Gradient Accelerating

Structure," in *AIP Conf. Proc.*, vol. 91, 1982, p. 154.

[52] H. H. Braun, R. Corsini (Ed.) *et al.*, "The CLIC RF Power Source - A Novel Scheme of Two-Beam Acceleration for Electron-Positron Linear Colliders," 1999.

[53] D. Schulte, "Beam Loading Compensation in the Main Linac of CLIC," in *Proceedings of LINAC 2000*, 2000, p. 41.

[54] J. Jeanneret, E. Adli, A. Latina, G. Rumolo, D. Schulte, and R. Tomás, "Beam Dynamic Issues in the CLIC Long Transfer Line," in *Proceedings of the 11th biennial European Particle Accelerator Conference, EPAC'08*, 2008, p. 3017.

[55] R. Corsini, private communication.

[56] K. Thompson and K. Yokoya, in *Handbook of Accelerator Physics and Engineering*, 3rd ed. World Scientific Publishing Co. Pte. Ltd, 2006, sec. 2.5.1, p. 120.

[57] H. M. Durand and T. Touzé, "The Active Prealignment of the CLIC Components," in *Proceedings of the 9th International Workshop on Accelerator Alignment*, 2006, WE006.

[58] A. Andersson and J. P. H. Sladen, "RF-based Electron Beam Timing Measurement with sub-10fs Resolution," CERN CLIC Note 734, 2008.

[59] 4th CLIC Advisory Committee (CLIC-ACE). [Online]: http://indico.cern.ch/conferenceDisplay.py?confId=58072

[60] G. Geschonke and A. Ghigo (Eds.), "CTF3 Design Report," CERN CTF3 Note 047, 2002.

[61] E. Jensen, "CTF3 Drive Beam Accelerating Structures," in *Proceedings of the XXI Linear Accelerator Conference, LINAC'02*, 2002, p. 34.

[62] H. Braun, R. Corsini, L. Groening, F. Zhou, A. Kabel, T. Raubenheimer, R. Li, and T. Limberg, "Coherent Synchrotron Radiation Measurements in the CLIC Test Facility (CTF II)," in *Proceedings of the XX Linear Accelerator Conference, LINAC'00*, 2000, p. 726.

[63] R. Corsini, H. Braun *et al.*, "First Full Beam Loading Operation with the CTF3 Linac," in *Proceedings of the 9th biennial European Particle Accelerator Conference, EPAC'04*, 2004, p. 39.

[64] H. Shaker, E. Adli, R. Corsini, A. E. Dabrowski, A. Latina, T. Lefevre, P. K. Skowronski, F. Tecker, and P. Urschutz, "Status of Longitudinal Beam Dynamics Studies in CTF3," in *Proceedings of the XXIV Linear Accelerator Conference, LINAC'08*, 2008, p. 278.

[65] S. Bettoni, E. Adli, R. Corsini, A. E. Dabrowski, S. Döbert, D. Manglunki, P. Skowronski, and F. Tecker, "Achievements in CTF3 and Commissioning Status," in *Proceedings of the 23rd IEEE Particle Accelerator Conference, PAC'09*, 2009, FR1RAC04, to be published.

[66] CLIC evolution from 500 GeV to 3 TeV. [Online]: http://clic-meeting.web.cern.ch/clic-meeting/clic500-3000.html

[67] I. Syratchev, D. Schulte, E. Adli, and M. Taborelli, "High RF Power Production for CLIC," in *Proceedings of the 22nd IEEE Particle Accelerator Conference, PAC'07*, 2007, p. 2194.

[68] R. Ruber, V. Ziemann *et al.*, "The CTF3 Two-beam Test Stand Installation and Experimental Program," in *Proceedings of the 11th biennial European Particle Accelerator Conference, EPAC'08*, 2008, p. 2821.

[69] E. Adli, R. Ruber, V. Ziemann, R. Corsini, S. Döbert, A. Dubrovskiy, G. Riddone, D. Schulte, I. Syratchev, and S. Vilalte, "First Beam Tests of the CLIC Power Extraction Structure in the Two-beam Test Stand," in *Proceedings of the 19th European Workshop on Beam Diagnostics and Instrumentation for Particle Accelerators, DIPAC'09*, 2009, MOPD29, to be published.

[70] Y. H. Chin, "ABCI," CERN SL/92-49 (AP), 1992.

[71] P. B. Wilson, "High Energy Electron Linacs: Applications to Storage Ring RF Systems and Linear Colliders," SLAC-PUB-2884 (Rev.), 1991.

[72] A. W. Chao, *Physics of Collective Beam Instabilities in High-Energy Accelerators*. John Wiley & Sons, Inc., 1993.

[73] D. Schulte, "PLACET: A Program to Simulate Drive Beams," in *Proceedings of the 7th biennial European Particle Accelerator Conference, EPAC'00*, 2000, p. 1402.

[74] A. Millich and L. Thorndahl, "Loss factor Dependence on Group Velocity in Disk-Loaded Travelling-Wave Structures," CERN CLIC Note 366, 1999.

[75] I. Syratchev, private communication.

[76] Ansoft Corporation HFSS. [Online]: http://www.ansoft.com/products/hf/hfss/

[77] W. Bruns, "GdfidL: A Finite Difference Program with Reduced Memory and CPU Usage," in *Proceedings of the 17th IEEE Particle Accelerator Conference, PAC'97*, 1997, p. 2651.

[78] I. Syratchev and W. Bruns, "Time Domain Simulations of the CLIC PETS (Power Extraction and Transfer Structure) with GdfidL," in *Proceedings of the 19th IEEE Particle Accelerator Conference, PAC'01*, 2001, p. 3780.

[79] A. Millich, A. Riche, and D. Schulte, "Beam Stability in the Drive-Beam Decelerator of CLIC Using Structures of High-Order Symmetry," in *Proceedings of the 18th IEEE Particle Accelerator Conference, PAC'99*, 1999, p. 1863.

[80] R. Jones, V. Dolgashev, K. Bane, and E. Lin, "Wakefield Band Partitioning in Linac Structures," SLAC-PUB-9467, 2003.

[81] E. Adli, D. Schulte, and I. Syratchev, "Beam Dynamics of the CLIC Decelerator," in *Proceedings of the 44th ICFA Workshop on X-Band RF Structures and Beam Dynamics*, 2008.

[82] E. Adli, "Analysis of the first 12 GHz PETS tests with beam using a constant parameter recirculation model," CERN CTF3 Note 096, 2009.

[83] I. Syratchev, G. Riddone, and S. Tantawi, "CLIC RF High Power Production Testing Program," in *Proceedings of the 11th biennial European Particle Accelerator Conference, EPAC'08*, 2008, p. 1909.

[84] R. Ruber and V. Ziemann, "An Analytical Model for PETS Recirculation," CERN CTF3 Note 092, 2009.

[85] V. Ziemann, "Data Analysis for PETS Recirculation," CERN CTF3 Note 094, 2009.

[86] E. Adli, "Techniques for estimations of beam energy loss in the Two-beam Test Stand PETS, applied to the first 12 GHz PETS tests with beam," CERN CTF3 Note 097, 2009.

[87] T. Ekelöf, M. Johnson, V. Ziemann, H. Braun, S. Döbert, G. Geschonke, J. Sladen, and W. Wuensch, "The Two-beam Test Stand in CTF3," in *Proceedings of the 10th biennial European Particle Accelerator Conference, EPAC'06*, 2006, p. 2445.

[88] R. Tomás for the CLIC/CTF3 collaboration, "CLIC Project Overview," in *Proceedings of the 23rd IEEE Particle Accelerator Conference, PAC'09*, 2009, FR1RAI01, to be published.

[89] I. Syratchev, E. Adli *et al.*, "High-Power Testing of X-Band CLIC Power Generating Structures," in *Proceedings of the 23rd IEEE Particle Accelerator Conference, PAC'09*, 2009, WE3RAC02, to be published.

[90] M. Johnson, "Beam-based Diagnostics of RF-breakdown in the Two-beam Teststand in CTF3," CERN CLIC Note 710, 2007.

[91] A. Dabrowski, private communication.

[92] E. Adli and D. Schulte, "Beam-Based Alignment for the CLIC Decelerator," in *Proceedings of the 11th biennial European Particle Accelerator Conference, EPAC'08*, 2008, p. 547.

[93] E. Adli, D. Schulte, and I. Syratchev, "A Study of Failure Modes in the CLIC decelerator," in *Proceedings of the 11th biennial European Particle Accelerator Conference, EPAC'08*, 2008, p. 550.

[94] E. Adli, R. Corsini, A. Dabrowski, D. Schulte, S. Shaker, P. Skowronski, F. Tecker, and R. Tomás, "Status of an Automatic Beam Steering for the CLIC Test Facility 3," in *Proceedings of the XXIV Linear Accelerator Conference, LINAC'08*, 2008, p. 422.

[95] E. Adli, "Drive Beam Decelerator magnet specification," CERN Technical Note, 2009.

[96] E. Adli, "Drive Beam Decelerator BPM specification," CERN Technical Note, 2009.

[97] J. A. Riche, "Maximum Energy Transfer Efficiency in CLIC Drive Beam and Proposal for a Method of Focusing, Derived from a very General Discussion on Focusing in Linacs," CERN CLIC Note 266, 1994.

[98] A. Riche and D. Schulte, "The Drive Beam Decelerator of CLIC," in *Proceedings of the XIX Linear Accelerator Conference, LINAC'98*, 1998, p. 118.

[99] D. Schulte, "Stability of the Drive Beam in the Decelerator of CLIC," in *Proceedings of the 8th biennial European Particle Accelerator Conference, EPAC'02*, 2002, p. 497.

[100] E. D. Courant and H. S. Snyder, "Theory of the Alternating-Gradient Synchrotron," *Ann. Phys.*, vol. 3, p. 1, 1958.

[101] The Tracking Code PLACET. [Online]: http://isscvs.cern.ch/cgi-bin/viewcvs-all.cgi/placet-development/doc/placet.pdf?root=placet&view=co/

[102] D. Schulte, "Multi-bunch Calculations in the CLIC Main Linac," in *Proceedings of the 23rd IEEE Particle Accelerator Conference, PAC'09*, 2009.

[103] E. Adli and D. Schulte, "Alignment Tolerances for the CLIC decelerator," CERN CLIC Note 733, 2008.

[104] B. Autin and Y. Marti, "Closed orbit correction of A.G. machines using a small number of magnets," CERN-ISR-MA-73-17, 1973.

[105] W. H. Press, S. A. Teukolsky, W. T. Vetterling, and B. P. Flannery, *Numerical Recipes - The Art of Scientific Computing*, 3rd ed. Cambridge University Press, 2007.

[106] T. Raubenheimer and R. Ruth, "A dispersion-free trajectory correction technique for linear colliders," *Nucl. Instrum. Methods Phys. Res.*, vol. A302, p. 191, 1991.

[107] D. Schulte, A. Latina, and P. Eliasson, "Dynamic Effects During Beam-Based Alignment," in *Proceedings of PAC 2007*, 2007, p. 2847.

[108] K. Schindl, "Space charge," in *CERN Accelerator School: Basic Course on General Accelerator Physics*, 2000, p. 285.

[109] T. Raubenheimer and D. Schulte, "Fast Beam-ion Instability in CLIC," Unpublished.

[110] G. Rumolo, private communication.

[111] D. Schulte and I. Syratchev, "Considerations on the Design of the Decelerator of the CLIC Test Facility (CTF3)," in *Proceedings of the 21st IEEE Particle Accelerator Conference, PAC'05*, 2005, p. 1177.

[112] S. Döbert, G. Rumolo, D. Schulte, I. V. Syratchev, and D. Carrillo, "Progress on the CTF3 Test Beam Line," in *Proceedings of the 10th biennial European Particle Accelerator Conference, EPAC'06*, 2006, p. 783.

[113] M. Olvegaard, A. Dabrowski, T. Lefevre, S. Döbert, and E. Adli, "Time Resolved Spectrometry on the Test Beam Line at CTF3," in *Proceedings of the 19th European Workshop on Beam Diagnostics and Instrumentation for Particle Accelerators, DIPAC'09*, 2009, TUPB40, to be published.

[114] F. Toral, C. Burgos *et al.*, "Design, Manufacturing and Tests of a Micrometer Pre-

cision Mover for CTF3 Quadrupoles," in *Proceedings of the 11th biennial European Particle Accelerator Conference, EPAC'08*, 2008, p. 1517.

[115] J. Garcia-Garrigos, A. Faus-Golfe, and J. Civera-Navarrete, "Design and Construction of an Inductive Pick-Up for Beam Position Monitoring in the Test Beam Line of the CTF3," in *Proceedings of the 11th biennial European Particle Accelerator Conference, EPAC'08*, 2008, p. 1110.

[116] H. H. Braun, private communication.

A. Symbol and Parameter Tables

A.1 List of abbreviations

Abbreviation	**Meaning**
CERN	The European laboratory for particle physics
CLEX	CLIC Experimental Area
CLIC	Compact Linear Collider
CTF3	CLIC Test Facility 3
DFS	Dispersion-Free Steering
FODO	Focusing Defocusing
GLC	Global Linear Collider
LEP	Large Electron Positron Collider
LHC	Large Hadron Collider
ILC	International Linear Collider
NLC	Next Linear Collider
PETS	Power Extraction and Transfer Structure
PLACET	The particle tracking code PLACET (org.: Program for Linear Accelerator Correction Efficiency Tests)
TBL	Test Beam Line
TBTS	Two-beam Test Stand

Table A.1: List of abbreviations

A.2 Key parameters in Chapter 4

PETS parameters	**Symbol**	**Value**	**Unit**
PETS (TBTS) fund. mode frequency	f_{rf}	12.00	GHz
PETS (TBTS) fund. mode impedance	R'/Q	2'222	linac-Ω/m
PETS (TBTS) fund. mode group velocity	β_g	46	% of c
PETS (TBTS) length	L_{PETS}	1.0	m
PETS (TBTS) fill-time	t_{fill}	3.9	ns
PETS (TBTS) ohmic losses reduction factor	$\eta_{\Omega,\mathrm{PETS}}$	0.98	-
Beam parameters	**Symbol**	**Value**	**Unit**
Average beam intensity	I		A
Bunch frequency	f_{bunch}	12.00	GHz
Bunch to bunch distance	z_{bb}	25.0	mm
Bunch length	σ_z	-	mm
Bunch form factor	$F(\lambda(\sigma_z))$	-	%
PETS power production	P		MW
Calculated quantities without recirculation	**Symbol**	**Value**	**Unit**
Fundamental mode field at PETS end	E_{beam}		V/m
PETS output power	P		W
PETS peak voltage	$\hat{U}$		V
PETS mean voltage	$\langle U \rangle$		V
Recirculation parameters	**Symbol**	**Value**	**Unit**
Recirculation fitted phase	ϕ	18	deg
Recirculation fitted total round-trip field gain	g	75	%
Fitted constant factor for reconstructed field	k	78	%
Round-trip ohmic losses reduction factor	$\eta_{\Omega,\mathrm{circ}}$		-
Calculated quantities with recirculation	**Symbol**	**Value**	**Unit**
Fundamental mode field at PETS end	$\tilde{E}_M$		V/m
Field phase with respect to beam generated field	θ		deg
PETS output power	P_M		W
PETS peak voltage	$\hat{U}_M$		V
PETS mean voltage	$\langle U_M \rangle$		V

Table A.2: Symbol and parameter table for Chapter 4

A.3 Key parameters in Chapter 5

PETS parameters	**Symbol**	**Value**	**Unit**
PETS (CLIC 2008) fund. mode frequency	f_{rf}	12.00	GHz
PETS (CLIC 2008) fund. mode impedance	R'/Q	2'294	linac-Ω/m
PETS (CLIC 2008) fund. mode group velocity	β_g	45	% of c
PETS (CLIC 2008) length	L_{PETS}	0.21	m
PETS (CLIC 2008) fill-time	t_{fill}	0.9	ns
PETS (CLIC 2008) half-aperture	a_0	11.5	mm
Lattice parameters	**Symbol**	**Value**	**Unit**
Decelerator sector length (longest sector)	L	1053	m
Number of PETS per sector	N_{PETS}	1492	-
Quadrupole active length	L_{quad}	0.15	m
Lattice FODO cell length	L_{FODO}	2.01	m
Lattice FODO phase-advance (lattice start)	ϕ_{FODO}	92.5	deg
Lattice maximum beta function (lattice start)	β_F	3.40	m
Lattice average beta function (lattice start)	$\langle\beta\rangle$	1.25	m
Number of FODO cells (longest sector)	N_{FODO}	524	-
Drive beam parameters	**Symbol**	**Value**	**Unit**
Drive beam average beam intensity	I	101	A
Drive beam initial energy	E_0	2.4	GeV
Drive beam energy extraction efficiency	η_{extr}	90	%
Drive beam minimal final particle energy	E_{min}	0.24	GeV
Drive beam train length	t_{train}	244	ns
Drive beam bunch frequency	f_{bunch}	12.00	GHz
Drive beam bunch to bunch distance	z_{bb}	25.0	mm
Drive beam bunch length	σ_z	1	mm
Drive beam bunch form factor	$F(\lambda(\sigma_z))$	96.9	%
Drive beam initial norm. emittance	$\epsilon_{\mathrm{Nx,Ny}}$	150	μm
CLIC PETS power production	P	135	MW
Imperfections	**Symbol**	**Value**	**Unit**
Quadrupole offsets	σ_{quad}	20	μm rms
BPM accuracy (mech. + elec.)	σ_{acc}	20	μm rms
BPM resolution	σ_{res}	2	μm rms
PETS	σ_{PETS}	100	μm rms
Pitch/roll	$\sigma_{\theta,\phi}$	1	mrad rms

Table A.3: Symbol and parameter table for Chapter 5

A.4 Key parameters in Chapter 6

PETS parameters	**Symbol**	**Value**	**Unit**
PETS (TBL) fund. mode frequency	f_{rf}	12.00	GHz
PETS (TBL) fund. mode impedance	R'/Q	2'222	linac-Ω/m
PETS (TBL) fund. mode group velocity	β_g	46	% of c
PETS (TBL) length	L_{PETS}	0.8	m
PETS (TBL) fill-time	t_{fill}	3.1	ns
PETS (TBL) half-aperture	a_0	11.5	mm
Lattice parameters	**Symbol**	**Value**	**Unit**
TBL length	L	24	m
Number of PETS in the TBL	N_{PETS}	16	-
Quadrupole active length	L_{quad}	0.15	m
Lattice FODO cell length	L_{FODO}	2.80	m
Lattice FODO phase-advance (lattice start)	ϕ_{FODO}	90.2	deg
Lattice maximum beta function (lattice start)	β_F	4.72	m
Lattice average beta function (lattice start)	$\langle\beta\rangle$	1.77	m
Number of FODO cells	N_{FODO}	8	-
CLEX beam parameters	**Symbol**	**Value**	**Unit**
CLEX beam average beam intensity	I	28	A
CLEX beam initial energy	E_0	150	MeV
CLEX beam energy extraction efficiency	η_{extr}	55	%
CLEX beam minimal final particle energy	E_{min}	67	MeV
CLEX beam train length	t_{train}	140	ns
CLEX beam bunch frequency	f_{bunch}	12.00	GHz
CLEX beam bunch to bunch distance	z_{bb}	25.0	mm
CLEX beam bunch length	σ_z	1	mm
CLEX beam bunch form factor	$F(\lambda(\sigma_z))$	96.9	%
CLEX beam initial norm. emittance	$\epsilon_{\mathrm{Nx,Ny}}$	150	μm
TBL PETS power production	P	139	MW
Imperfections	**Symbol**	**Value**	**Unit**
Quadrupole offsets	σ_{quad}	100	μm rms
BPM accuracy (mech. + elec.)	σ_{acc}	100	μm rms
BPM resolution	σ_{res}	2	μm rms
PETS	σ_{PETS}	100	μm rms
Pitch/roll	$\sigma_{\theta,\phi}$	1	mrad rms

Table A.4: Symbol and parameter table for Chapter 6

A.5 Transverse dipole modes for PETS with damping material

The following table presentes the parameters of the nine wake functions fitted to best represent the transverse impedance calculated with GdfidL, assuming dielectric damping material in the slots. These parameters have been used for all the beam dynamics simulations in Chapters 5 and 6.

Mode number	$2k'_T = W'_T(0)$ [V/pC/m/m]	Q_T [-]	f_T [GHz]	β_T [-]
1	45	300	27.44	0
2	19	180	28.05	0
3	17	290	32.9	0
4	200	85	39.12	0
5	30	120	41.8	0
6	15	380	48.9	0
7	850	3.7	10.0	0
8	4'820	3.8	13.4	0
9	2'630	6.2	15.46	0

Table A.5: Dipole mode parameters for the damped 12 GHz PETS

B. Collection of Publications

B.1 High RF Power Production for CLIC

This paper presents the design of the 12 GHz CLIC power extraction and transfer structure (PETS). The PETS design process must take into account a number of constraints, including critical constraints on the allowed magnitude and shape of the PETS transverse impedance. These constraints are driven by beam dynamics studies.

The candidate was responsible for analysing a number of potential PETS designs, investigating the decelerator performance and beam stability for each, and working in loop with the RF-design expert (Igor Syratchev) until an acceptable PETS design was found. The resulting PETS design is now the CLIC base line design.

The text in this paper was written mainly by Igor Syratchev, however the beam dynamics analyses performed by the candidate was a vital part of the design procedure leading to the paper. Daniel Schulte, as CLIC Beam Physics study leader, introduced the challenges related to the beam dynamics studies.

HIGH RF POWER PRODUCTION FOR CLIC

I. Syratchev, D. Schulte, E. Adli, M. Taborelli, CERN, Geneva, Switzerland.

Abstract

The CLIC Power Extraction and Transfer Structure (PETS) is a passive microwave device in which bunches of the drive beam interact with the impedance of the periodically loaded waveguide and excite preferentially the synchronous mode. The RF power produced (several hundred MW) is collected at the downstream end of the structure by means of the Power Extractor and delivered to the main linac structure. The PETS geometry is a result of multiple compromises between beam stability and main linac RF power needs. Another requirement is to provide local RF power termination in case of accelerating structure failure (ON/OFF capability). Surface electric and magnetic fields, power extraction method, HOM damping, ON/OFF capability and fabrication technology were all evaluated to provide a reliable design.

INTRODUCTION

The CLIC PETS is one of the key components in the CLIC two-beam acceleration scheme [1]. In general, the decelerating module, consisting of PETS, quadrupoles and high power RF networks, must not be longer than the accelerating structure it drives, to ensure maximum effective gradient. The PETS should deal with high current electron beams (~100 A) and thus should provide extremely stable beam transportation for a few hundred meters. In the presence of deceleration, the final energy spread in a drive beam of ~90% is needed in order to achieve high efficiency of the RF power production; therefore, strong FODO lattice and strong damping of any deflecting HOM in the PETS are required to prevent significant beam losses [2].

The basic CLIC parameters were drastically changed recently [3, 4]. The major modifications concerned the operating frequency and the accelerating gradient in the main linac. Both the operating frequency and the accelerating gradient were reduced. The new operating frequency of 12 GHz (cf. 30 GHz) and the accelerating gradient of 100 MV/m (cf. 150 MV/m) were adopted after a thorough study.

These modifications required a complete revision of the whole CLIC scheme. In this paper, the new X-band version of the CLIC RF power generating structure is presented.

RF POWER GENERATION IN PETS

The new layout of the CLIC module is shown in Fig.1. In this layout, the single PETS should produce RF power for two accelerating structures. The length of the module is driven by the physical length of the accelerating structure. The module, in itself, consists of the two focusing quadruples and four PETS connected to the eight accelerating structures. The new CLIC decelerator sector parameters are listed in Table 1.

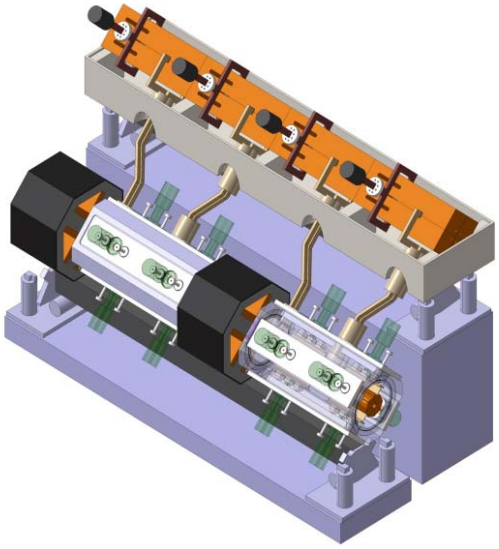

Figure 1: The CLIC module layout

Table 1: The X-band CLIC decelerator parameters

Number of sectors/linac	26
Sector length, m	810
Number of PETS/sector	1376
Drive beam energy, GeV	2.4
Drive beam current, A	93.3

The RF power generated by the bunched beam in a constant impedance periodic structure in general can be expressed as:

$$P = I^2 L^2 F_b{}^2 \omega_0 \frac{R/Q}{V_g 4} \quad (1),$$

where I is the beam current, L – the active length of the structure, F_b – the single bunch form factor, ω_0 – the bunch frequency, R/Q – the impedance per meter length, Q - the quality factor and V_g – the group velocity. At a given frequency and with fixed RF power and beam current, the only free parameters are the structure length and structure aperture. In our case, the PETS active length is limited by the module layout and thus the structure aperture absolute upper limit is well defined (impedance ~ $1/a^2$). The lower limit for the structure aperture is governed by the RF constraints [5]. In a simple way it can be written as: $a_{PETS} \geq a_{as} \times n_{as}$, where a_{as} is the input aperture of the accelerating structure and n_s is the number of accelerating structures fed by the single PETS. In addition, the choice of the aperture defines the power extraction strategy, which in turn, can influence the active

length. As a result of multiple compromises the PETS aperture with a/λ=0.46 was chosen, see Table 2.

Table 1: The X-band CLIC PETS parameters

Aperture, mm	23
Phase advance/cell, degrees	90
R/Q, Ohm/m	2290
$\beta=V_g/c$	0.453
Q-factor	7200
Active length, m	0.231 (37 cells)
RF pulse length, ns	290
RF power, MW	138

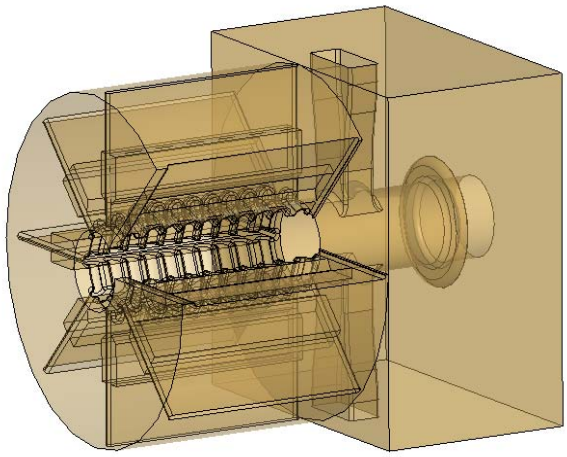

Figure 2: The CLIC PETS general view

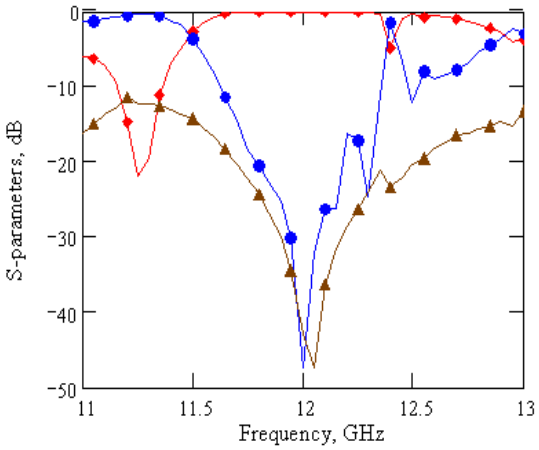

Figure 3: The PETS S-parameters, diamonds - transmission, circles - reflection and triangles - isolation.

In its final configuration, PETS comprises eight octants separated by the damping slots. Each of the slots is equipped with HOM damping loads. This arrangement follows the need to provide strong damping of the transverse modes. In periodic structures with high group velocities, the frequency of a dangerous transverse mode is rather close to the operating one. The only way to damp it is to use its symmetry properties. To do this, only longitudinal slots can be used. These slots also naturally provide high vacuum conductivity for the structure pumping. The upstream end of the PETS is equipped with a special matching cell and the output coupler [6], see Fig. 2. The simulated efficiency of the power extraction from PETS is above 99%, see S-parameters simulated with HFSS [7] in Fig.3.

Throughout the PETS design, special care was taken to reduce the surface field concentration in the presence of the damping slots. This was done using special profiling of the iris, see Fig. 4. Compared to the structure with the circular symmetry, a field enhancement of only 20% was achieved. The maximum surface electric field for the nominal RF power is 48 MV/m.

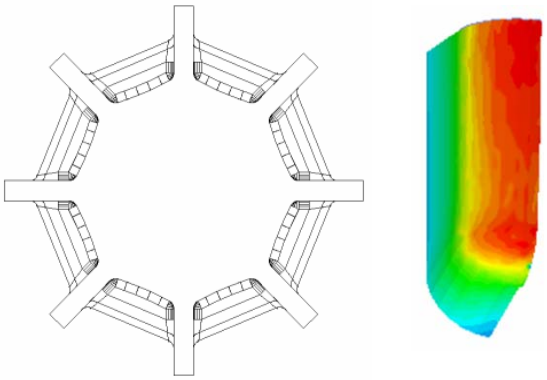

Figure 4: The PETS cross-section and electric field plot on the iris tip (one quarter of the iris is shown).

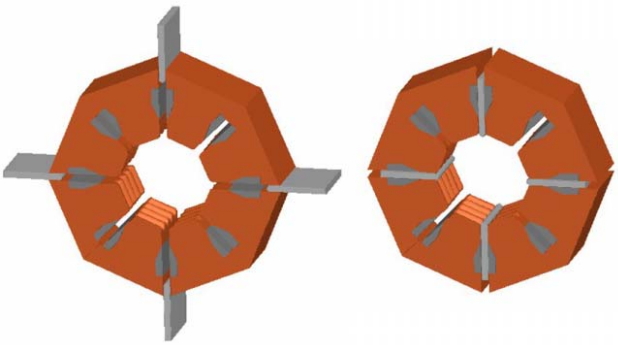

Figure 5: PETS ON (left) and OFF (right) configurations with detuning wedges.

During machine operation, it will be necessary to locally turn the RF power production OFF when either PETS or an accelerating structure fails due to breakdown. The net RF power generated by the beam at the end of the constant impedance structure will be zero if the structure synchronous frequency is detuned by amount $\pm\beta c/(1-\beta)L$, where $\beta - V_g/c$ and L - length of the structure, see [8] for more details. We have found that such a strong detuning can be achieved by inserting four thin wedges through four of the eight damping slots, see Fig. 5. The wedge geometry and the final wedge position are optimised in such a way that at any intermediate wedge position, there is no electrical field enhancement in the gap between the wedge and the wall; thus, the device can operate as a variable attenuator.

HOM DAMPING AND BEAM STABILITY

In the case of a structure with a high group velocity ($\beta=V_g/c$) and finite length (L), the expression for the wake potential [9] should be evaluated:

$$W(z) = 2q \times K \sin\left(\frac{\omega z}{c}\right) e^{-\frac{\omega z}{2Q(1-\beta)c}} \times \left\{1 - \frac{\beta z}{L(1-\beta)}\right\}$$

$$W(z) = 0, \quad z > L\frac{1-\beta}{\beta} \qquad (2),$$

here we have included the catch-up parameter for damping and drain out from the structure of the finite length. Following (2), the best scenario to provide the fast decay of the wakefields is to reduce the Q-factor and to increase the group velocity as much as possible.

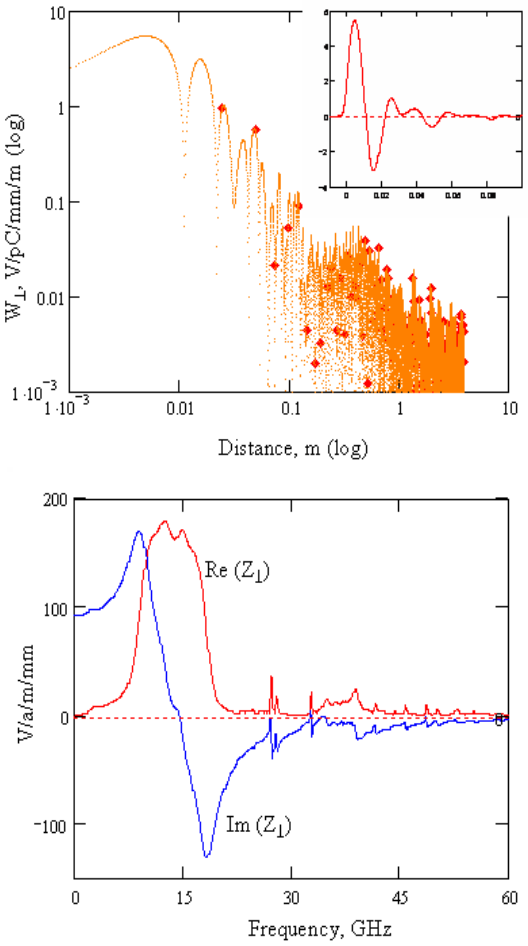

Figure 6: The transverse wake potential (upper plot) and impedance (lower plot) simulated with GDFIDL for the complete PETS geometry.

In the presence of the longitudinal slots, the transverse mode field pattern is dramatically distorted so that a considerable amount of the energy is now stored in the slots. The new, TEM-like nature of the mode significantly increases the group velocity, in our case from 0.42c to almost 0.7c. With introduction of the lossy dielectric material close to the slot opening, the situation improves further. The proper choice of the load configuration with respect to the material properties makes it possible to couple the slot mode to a number of the heavily loaded modes in dielectric. This gives a tool to construct the broad wakefields impedance. The transverse wakepotential simulations in a complete PETS geometry were done with GDFIDL [10], see Fig. 6. The computer code PLACET [11] was then used to analyze the beam dynamic along the decelerator in the presence of strong deceleration and calculated wakefields. The results of the simulation (see Fig. 7) clearly indicate that the suppression of the transverse wakefields obtained, is strong enough to guarantee the beam transportation without losses.

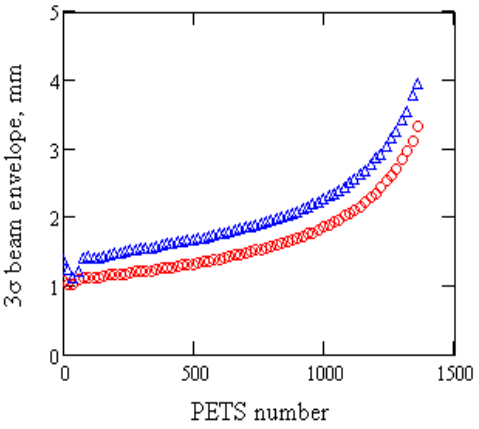

Figure 7: Evolution of the 3σ beam envelope along the decelerator sector; circles – without wakefields, triangles – with wakefields included.

REFERENCES

[1] H.H. Braun et al., Updated CLIC parameters 2005, CLIC-Note-627 - Geneva, CERN, 12 May 2006.
[2] D. Schulte, Stability of the drive beam in the decelerator of CLIC, CLIC-Note-528 – Geneva, CERN, 25 Jul 2002.
[3] R. Corsini, Results on CLIC Proof of Principle from CTF3, this Conference.
[4} CLIC DRAFT PARAMETER LIST 2007. http://cern.ch/clic-meeting/clictable2007.html
[5] W. Wuensch, Progress in Understanding the High-Gradient Limitations of Accelerating Structures, CLIC-Note-706 - Geneva, CERN, 08 Mar 2007.
[6] I. Syratchev, Mode Launcher as an Alternative Approach to the Cavity-Based RF Coupler of Periodic Structures, CLIC-Note-503 – Geneva, CERN, 17 Jan 2002.
[7] Ansoft Corporation - HFSS. http://www.ansoft.com/
[8] I. Syratchev, 30 GHz High Power Production for CLIC, 7th Workshop on High Energy Density and High Power RF, Kalamata, Greece, 13-17 June 2005.
[9] P.B. Wilson, Introduction to Wakefields and Wake Potentials, SLAC-PUB-4547, 1989
[10] The GdfidL Electromagnetic Field simulator. http://www.gdfidl.de/
[11] D. Schulte et al. Simulation Package based on PLACET, Proceedings of the 2001 Particle Accelerator Conference, Chicago, pp. 3033-3035.

B.2 First Beam Tests of the CLIC Power Extraction Structure in the Two-beam Test Stand

This paper presents the firsts tests of the 12 GHz CLIC power extraction and transfer structure (PETS) with an electron drive beam. The structure tested corresponds to the design reported in the paper "HIGH RF POWER PRODUCTION FOR CLIC", also included in this thesis.

The experiments were performed using the Two-beam Test Stand (TBTS) test-facility, for which Roger Ruber is project manager. The candidate's work includes responsibility for the data acquisition and TBTS operation co-ordination during the 2008 run as well as the analysis of the data logged during the 2008 run.

The text in this paper was written mainly by the candidate and Roger Ruber. The candidate wrote the sections "Recirculation", "Reconstruction" and "Energy loss measurements". Roger Ruber wrote the sections "Introduction" and "The Two-beam Test Stand". The remainder was written together. The candidate produced all of the plots and the figure in the paper.

FIRST BEAM TESTS OF THE CLIC POWER EXTRACTION STRUCTURE IN THE TWO-BEAM TEST STAND*

E. Adli†, University of Oslo, Norway and CERN, Geneva, Switzerland
R.J.M.Y. Ruber, V. Ziemann, Uppsala University, Sweden
R. Corsini, S. Doebert, A. Dubrovskiy, G. Riddone, D. Schulte,
I. Syratchev, CERN, Geneva, Switzerland
S. Vilalte, IN2P3-LAPP, Annecy-le-Vieux, France

Abstract

The two-beam acceleration scheme foreseen for CLIC and the associated radio-frequency (RF) components will be tested in the Two-beam Test Stand (TBTS) at CTF3, CERN. Of special interest is the performance of the power extraction structures (PETS) and the acceleration structures as well as the stability of the beams in the respective structures. After the recent completion of the TBTS, the first 12 GHz PETS has been tested with beam, using so-called recirculation of the RF power inside the PETS. The TBTS allows precise measurement of beam parameters before and after the PETS as well as RF power and phase. Measurements of transverse kick, energy loss and RF power with recirculation are discussed and compared with estimations, including first measurements of pulse shortening probably due to RF breakdown.

INTRODUCTION

The Two-beam Test Stand (TBTS) is a unique and versatile facility devised to test key components of the two-beam acceleration concept that is the basis of the CLIC project [1]. Worldwide it is the only facility where CLIC type power production (PETS) and accelerating structures can be tested with beam. The TBTS is part of the CTF3 complex at CERN [2] that creates a high power drive beam which is then decelerated in order to generate the RF power needed to accelerate a second, probe, beam which is provided by a another linac. The drive beam has a time structure suitable for power generation at all harmonics of 1.5 GHz but is optimised for the nominal CLIC frequency of 12 GHz. It can reach beam intensities up to 30 A, pulse lengths up to 1500 ns and beam energies up to 150 MeV. The probe beam can reach beam intensities up to 0.9 A, pulse lengths up to 150 ns and beam energies up to 170 MeV.

Commissioning of the TBTS drive beam line started last year. As the available drive beam current will be some four times lower than in the CLIC design, the installed PETS has a modified design. It has increased length to 1 m from 0.215 m and is equipped with external RF recirculation [3]: the PETS operates as an amplifier feedback ring driven by the drive beam power. Up to 30 MW of 12 GHz RF power has been produced from a 5 A beam.

* Work supported by the Swedish Research Council, the Knut and Alice Wallenberg Foundation, the Research Council of Norway and the Commission of the European Communities under the 6th Framework Programme Structuring the European Research Area, contract number RIDS-011899.

† Erik.Adli@cern.ch

THE TWO-BEAM TEST STAND

The TBTS consists of two parallel beam lines for the drive and probe beam and a two meter long test area in each. The layout of the two beam lines is almost identical [4]. The experiments described in this report are performed on the drive beam line. The layout of the line with PETS installation is shown in Figure 1.

Two quadrupole triplets are used to vary and optimise the beam size inside the PETS and on an OTR screen following a spectrometer dipole in order to maximise the energy resolution. Moreover, four steering magnets are available to adjust the orbit inside the PETS with a closed bump. Five inductive BPMs [5] are installed for intensity and position measurements. Their bandwidth allows to observe the position within a bunch train and this is used to determine kicks and energy loss of the beam during normal operation and when a RF breakdown occurs inside the PETS. The achievable resolution to determine the kicks is in the order of a few micro radians and 4×10^{-4} for the energy [6].

The PETS RF recirculation loop contains a variable splitter to control the amount of power in the loop and a phase shifter to tune the loop's length. The RF power and phase are measured through directional couplers connected to 12 GHz diodes and I&Q demodulators.

RECIRCULATION

In the recirculator a fraction of the field g (product of the splitter ratio κ and the round-trip ohmic losses) is coupled

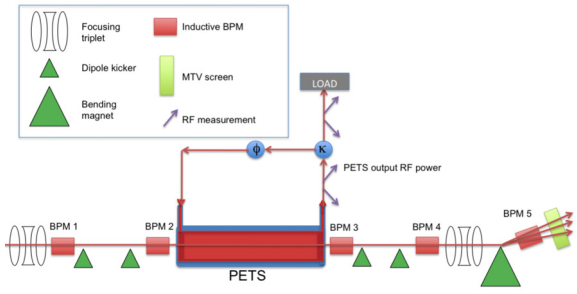

Figure 1: Sketch of the Two-beam Test Stand's drive beam line (not to scale).

back into the PETS with an eventual phase-shift ϕ with respect to the beam generated field [7–9]. For a rectangular pulse, neglecting system bandwidth limitations, and keeping all parameters constant one can calculate the peak electric field at the PETS output after M full recirculation cycles, E_M, as [9]

$$E_M = E_{beam} \sum_{m=0}^{M} g e^{j\phi} \qquad (1)$$

where E_{beam} is the peak electric output field generated by the beam before the recirculation starts to act. Using the same assumptions the beam energy loss, $\langle U_M \rangle$, can be calculated as [10]

$$\langle U_M \rangle = \Re(E_M) LF(\lambda) - \frac{1}{2} E_{beam} LF(\lambda) \qquad (2)$$

where L is the structure length and $F(\lambda)$ the form factor.

RECONSTRUCTION

Extending Eq. (1) to arbitrary beam pulse intensities, while keeping other parameters constant, we use BPM intensity measurements to reconstruct the PETS output peak field, E, the phase of the total field with respect to the beam generated field, θ, and the output power, P. The relative field phase was measured using I and Q demodulator channels on the signal from the PETS output RF window, indicated in Figure 1.

For the 2008 run the recirculator parameters g and ϕ were unknown, and as part of the reconstruction process these parameter had to be identified. A continuous series of 200 logged pulses were used to fit the unknown parameters by comparing the power and phase reconstruction with the RF measurements yielding $g = 0.75$, ϕ = -18 deg [9]. No precise bunch length measurements were available for the run, and an overall scaling factor had therefore to be fitted as well.

The rms difference of the measured and reconstructed power pulses lies within 10% for 75% of the pulses in the series used for the fit. Figures 2 and 3 show examples of reconstructed and measured power and phase.

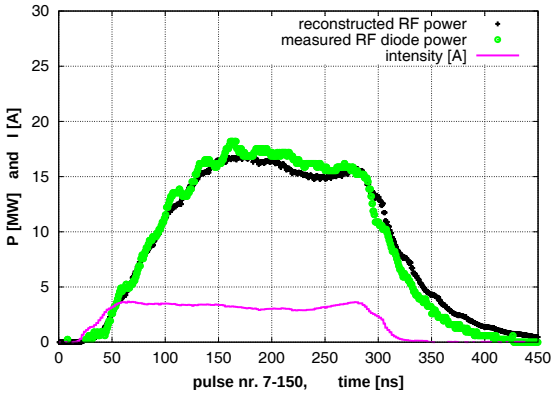

Figure 2: Reconstructed RF power from intensity measurements in black (+), measured RF power in green (o), BPM intensity in magenta (-), for a nominal pulse.

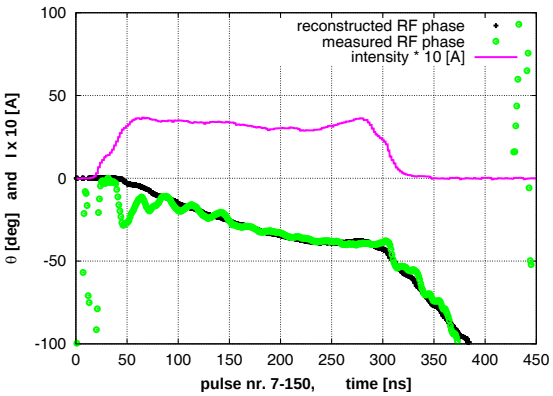

Figure 3: Reconstructed relative field phase from intensity measurements in black (+), measured relative field phase in green (o), BPM intensity in magenta (-), for a nominal pulse.

The beam intensity was gradually increased during the 2008 run, and in specific time intervals the measured RF power pulse was significantly shorter than the power reconstructed from the intensity measurements for a given pulse, as shown in Figure 4. The dynamics of such pulses can be modelled by varying the recirculation gain and phase [8] during the pulse, or, alternatively, by varying the bunch arrival phase [11]. This work is ongoing and the instrumentation of the TBTS proves to be very useful for the understanding of the dynamics of the PETS. The analysis software will be incorporated in the on-line analysis software and will serve as an indicator for breakdown, such that interesting pulses can be automatically stored for further post-processing at a later time.

ENERGY LOSS MEASUREMENTS

The PETS transfers part of the drive beam energy into RF power. In [10] three different approaches for estimating of corresponding beam energy loss are presented. First, we can determine the energy loss from the BPM in the spectrometer [6]. Second, the loss can be deduced from the power measurements in addition to the intensity measure-

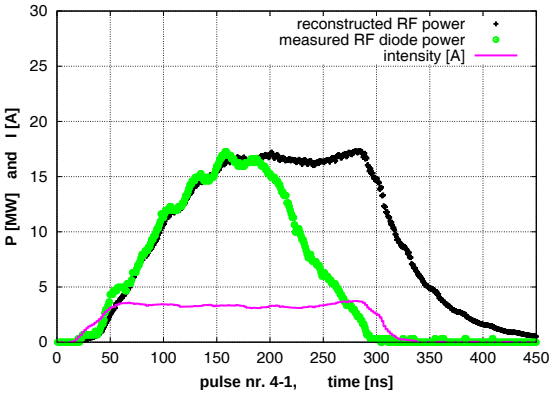

Figure 4: Reconstructed RF power from intensity measurements in black (+), measured RF power in green (o), BPM intensity in magneta (-), for a shortened pulse.

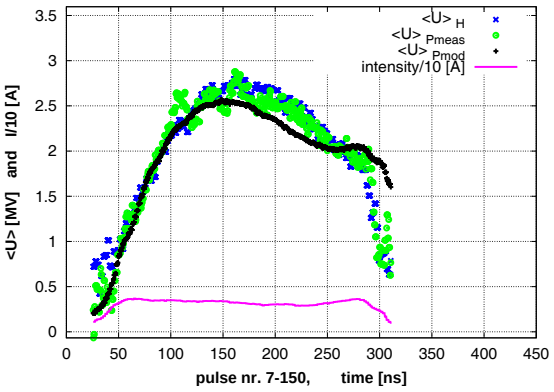

Figure 5: Energy loss estimates based on spectrometer measurements, $\langle U \rangle_H$, in blue (x), PETS power combined with BPM intensity measurements $\langle U \rangle_{P\mathrm{meas}}$, in green (o) and BPM intensity measurements alone, $\langle U \rangle_{P\mathrm{mod}}$, in black (+).

ments. Third, we can can use the intensity measurements alone, combined with Eq. (2). The rms difference between the three estimates lies within 20% for 75% of the pulses in the series used for the fit. Figure 5 shows an example of the mean voltage seen by the beam, along the pulse, estimated using these three approaches.

KICK MEASUREMENTS

For the design of a future two-beam accelerator and its stability it is also important to know if the beam receives any kick on its way through the PETS. Any such kick can be determined using the horizontal and vertical BPM measurements. For simplicity in the commissioning phase we assume here that such a kick would originate in the longitudinal centre of the PETS. From simulations we expect that the kick due to transverse dipole wakes in the PETS should be less than 100 μrad if the incoming beam offset is 1 mm parallel along the PETS centre line. Due to mechanical and electrical BPM offsets, not yet precisely identified, it was not possible to resolve the absolute angle and kick measurements accurately at this stage of operation. We therefore consider only relative changes along the pulse.

Figure 6 shows the estimated vertical offset (y), angle (yp) and kick in the middle of the PETS, for the pulse presented in Figure 4. During the time period that corresponds with the build up of the RF field in the PETS and the external RF power, the kick angle changes with approximately 0.5 mrad. From 250 ns on the kick angle changes with more than 1 mrad in the opposite direction. This could possibly indicate a relation between the beam kick and the field inside the PETS when pulse shortening is observed, and will be studied further during the next run. The horizontal measurements of the same pulse do not show a significant change in kick angle.

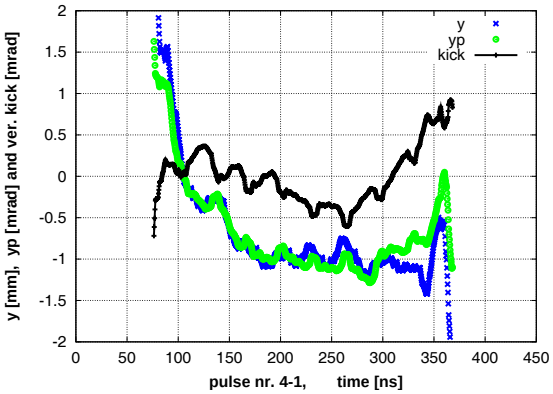

Figure 6: Estimated beam centroid offset, y, in blue (y), beam angle in the PETS, yp, in green (o) and kick angle, in black (+). All quantities are estimated in the middle of the PETS.

CONCLUSIONS

The first beam tests of a PETS in the TBTS have proven the extensive possibilities to correlate beam and RF measurements. Using a simple constant parameter model, a good agreement has been reached between estimations and measurements of the RF power production and beam energy loss. Being in the commissioning phase, work is ongoing to improve the quality of the modelling and measurements and extend their scope. The first results presented here demonstrate already that the TBTS is an excellent tool for studying the PETS dynamics.

REFERENCES

[1] G. Guignard (ed.), "A 3TeV e^+e^- Linear Collider based on CLIC Technology", CERN, Geneva (2000) CERN 2000-008.

[2] G. Geschonke and A. Ghigo (eds.), "CTF3 Design Report", *CERN CTF3 Note 047* (2002)

[3] I. Syratchev et al., "CLIC RF High Power Production Testing Program", EPAC'08 (2008) WEOBG01

[4] R.J.M.Y. Ruber et al., "The CTF3 Two-beam Test-stand Installation and Experimental Program", EPAC'08 (2008) WEPP139

[5] M. Gasior, "An Inductive Pick-up for Beam Position and Current Measurements", DIPAC'03, May 2003, Mainz, p.53, http://bel.gsi.de/dipac2003

[6] M. Johnson, "Beam-based Diagnostics of RF-breakdown in the Two-beam Test-stand in CTF3", *CERN CLIC Note 710* (2007)

[7] R. Ruber and V. Ziemann, "An Analytical Model for PETS Recirculation", *CERN CTF3 Note 092* (2009)

[8] V. Ziemann, "Data Analysis for PETS Recirculation", *CERN CTF3 Note 094* (2009)

[9] E. Adli, "Analysis of the first 12 GHz PETS tests with beam using a constant parameter recirculation model", *CERN CTF3 Note 096* (2009)

[10] E. Adli, "Techniques for the estimations of beam energy loss in the TBTS PETS, applied to the first 12 GHz PETS tests with beam", *CERN CTF3 Note 097* (2009)

[11] Igor Syratchev and Erk Jensen, private communication

B.3 Beam Dynamics of the CLIC Decelerator

This paper presents an overview of the beam dynamics challenges in the CLIC decelerator, as well as how they plan to be addressed. The test-facilities for decelerator beam dynamics experiments are also presented.

The results in this paper are based on simulation and theoretical studies. The candidate produced all the simulation results and the analysis in the paper. The candidate provided the plots and figures, and wrote the text in this paper. Daniel Schulte and Igor Syratchev acted as consulting experts in the fields of beam physics and radio frequency engineering respectively.

Beam Dynamics of the CLIC Decelerator*

E. Adli†, D. Schulte and I. Syratchev, CERN, Geneva, Switzerland

Abstract

The CLIC Drive Beam decelerator will extract X-band RF-power from a 100 A Drive Beam. The focussing and alignment systems must ensure transport of particles of all energies through the decelerator sectors, ensuring minimal losses. This paper summarizes the current status of the beam dynamics studies, including the effect of wake fields, the focusing strategy, the alignment strategy and resulting tolerances.

INTRODUCTION

The CLIC Drive Beam Decelerator is responsible for producing the RF-power for the main linacs accelerating structures, operating at an X-band frequency of 11.9942 GHz.

The RF-power will be generated by a 100 A electron Drive Bream being decelerated by a number of high-impedance Power Extraction and Transfer Structures (PETS). In order to ensure a stable and uniform power production it is very important that the Drive Beam is transported with a minimum of losses.

This paper is a review of the the current status of beam dynamic studies of the CLIC decelerator, using CLIC 2008 baseline design parameters [1] (some listed in Table 1).

Table 1: Decelerator lattice and beam parameters.

Decelerator parameters	Symbol	Value	Unit
Maximum sector length	L	1053	m
FODO cell length	L_{FODO}	2.01	m
Initial energy	E	2.4	GeV
Initial average current	I_0	101	A
Final max. energy spread	S	90.0	%
Frequency	f_L	12.00	GHz

LATTICE LAYOUT

Each decelerator sector consists of a FODO lattice, with up to two PETS inserted between each quadrupole, as shown in Figure 1. We require the maximum extracted energy to be the same for each sector. Because the fill pattern of accelerator structure varies, the length of the decelerator sector also varies. As baseline we simulate the longest sector (about 1050 m).

SIMULATION METHODS AND METRICS

The beam dynamics simulations have been performed with the tracking code PLACET [2], and more detail about the simulation set-up can be found in [3].

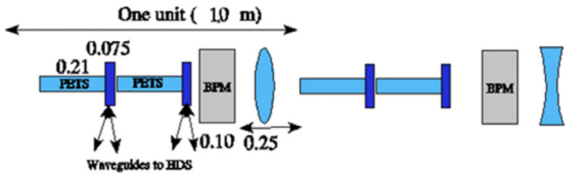

Figure 1: Decelerator lattice

As simulation criterion for minimum-loss transport we require the entire 3-sigma beam envelope, denoted r, defined as $r \equiv \max \sqrt{(|x_i| + 3\sigma_{x,i})^2 + (|y_i| + 3\sigma_{y,i})^2}$, to be within half the available aperture, $a_0 = 11.5$mm, in order to have a margin for unmodelled effects like higher order wake fields.

FOCUSING STRATEGY

The decelerator focusing strategy is to keep the phase-advance per cell constant at $\mu_{FODO} \approx 90^\circ$ for the *lowest* energy particles. For a perfect beam and machine, higher energy particles will then be contained in the envelope of the lowest energy particles.

In the baseline design the required quadrupole gradient starts at 81 T/m (field of 0.9 T close to the poles) at the beginning of the lattice, changing in steps of down to 0.05 T/m (corresponding to deceleration due to one PETS) along the decelerator lattice. For the current baseline neither tune-up nor orbit correction strategies require that the lattice magnet strength be re-scaled. Therefore, permanent magnets might be an option for the lattice. However, the current and energy acceptance is only a few percent [3], meaning that a permanent magnet solution will not be flexible wrt. small changes in drive-beam "working-point".

For cost reasons it is of interest to see if we can accept a coarser quadrupole strength granularity. Preliminary studies with a stair-case decrease in field strength show, however, that even a $\sim$1% quadrupole strength granularity leads to an $\sim$10% increase in the beam envelope.

PETS TRANSVERSE WAKES

The PETS dipole wake can at worst significantly distort the drive beam and cause heavy losses. Part of the PETS design process was therefore to bring the effect of the dipole wake down to an acceptable level. This work was performed as an iterative process, as outlined in Figure 2, where PETS design was improved until the effect of the wakes on the envelope growth was deemed acceptable.

* Work supported by the Research Council of Norway and the Commission of the European Communities under the 6th Framework Programme Structuring the European Research Area, contract number RIDS-011899.

† Erik.Adli@cern.ch, University of Oslo and CERN

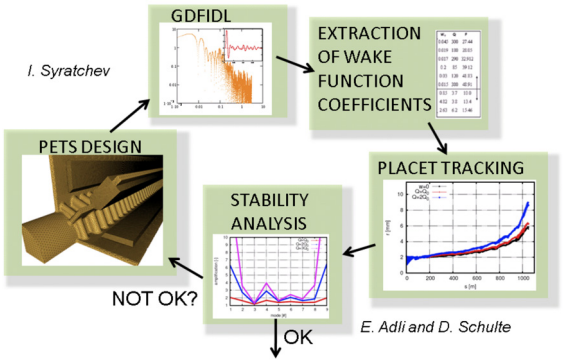

Figure 2: PETS dipole wake optimization

A variety of tracking simulations, taking into account misalignments, energy spread, adiabatic undamping, as well as beam jitter and offset, were performed in order to investigate the envelope growth and eventual instabilities driven by the transverse modes. The outcome of this study - a PETS design were the dipole wake amplification is deemed sufficienty damped - was a set of nine dipole modes, used as baseline for further the baseline beam dynamics studies[4]. Figure 3 shows the amplification of each dipole mode when driven by beam jitter at the mode frequency, for different Q-values. We see that for nominal Q-values, as predicted by the current PETS design, the amplification of a single mode is at worst a factor two.

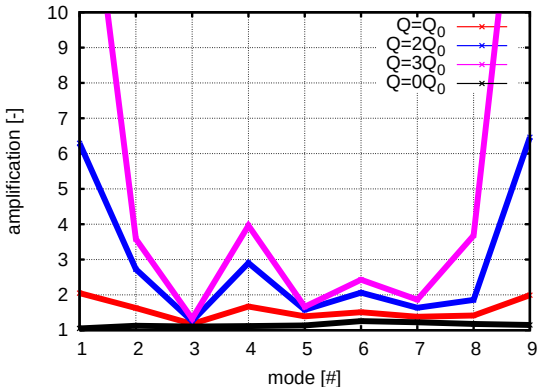

Figure 3: Amplification of PETS dipole modes

The dipole modes are used to simulate both multi-bunch effects and single-bunch effects. A comparison with the K. Bane formula [6] for the short-range wake shows that extracted wake functions indeed corresponds very well with up to 4 σ_z, as shown in Figure 4 (even though the PETS is outside the usual area of usage for this formula). In Figure 3 the $Q = Q_0$ graph corresponds to single-bunch effects only, and we see that the effect single-bunch effects are quite negligible.

Finally, we note that even if the current PETS design shows acceptable beam dynamics performance for nominal Q-values, we note that a scaling of the Q-factors by two leads to unacceptable increase in beam envelope (due to high-Q modes that don't die out, but grow along the beam).

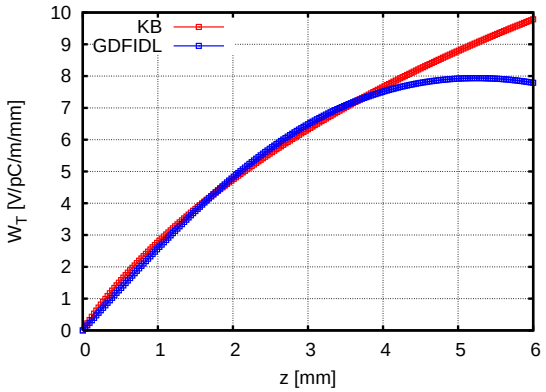

Figure 4: Single-bunch wake compared to K. Bane formula

BEAM BASED ORBIT CORRECTION

The effect of quadrupole kicks

In order to underline the need for beam based orbit correction we first discuss in some details the drivers of the beam envelope. We have observed the previous section that the beam envelope amplification due to transverse wake fields is suppressed due to the PETS design. The driver of the beam envelope is now quadrupole kicks due to quadrupole misalignments. We estimate that static alignment of the machine at best can give a resulting rms offset of $\sigma_{quad} \approx 20$ μm. We can calculate the statistical average of a particle having a FODO phase-advance of μ_{FODO} by summing kicks, yielding an average centroid offset of :

$$< r > \approx 2\frac{\sigma_{quad}}{\cos(\mu_{FODO}/2)}\sqrt{2N_{FODO}}\sqrt{\frac{(1-\frac{1}{2}S)}{1-S}}$$

yielding 4 mm for the lowest energy particle. This corresponds to incoherent build-up of the kicks. However, for a given machine some particles will sample the quadrupoles with some coherence, and thus build up kicks faster. This is illustrated in Figure 5 (transverse wakes are not included in these simulations).

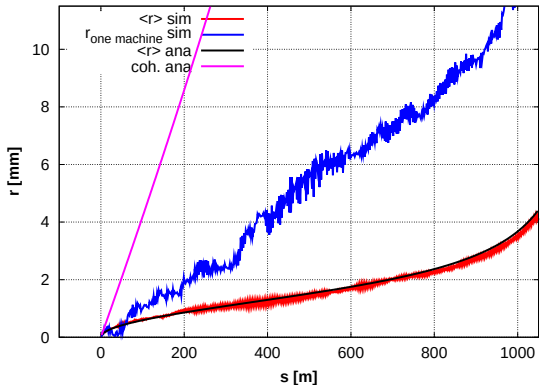

Figure 5: The effect of quadrupole kicks

In the case above it is the lowest energy particles sam-

ples the quadrupole with some coherence and drives the envelope, but this will change from one random machine to another. In fact, because the transient head of the drive beam pulse includes particles of a larger energy range, it is probable that the transient will drive the beam envelope.

Steering strategies

In [5] it is shown that after simple 1-to-1 steering the bean envelope growth is still significant, but that Dispersion-Free Steering can efficiently suppress the beam envelope growth due to quadrupole kicks, assuming the BPM resolution is about 2 μm. Details about these steering schemes can also be found. Figure 6 show the envelopes without correction, after 1-to-1 correction and after Dispersion-Free Steering. [7] describes tests of steering algorithms for the decelerator in the CLIC Test Facility 3.

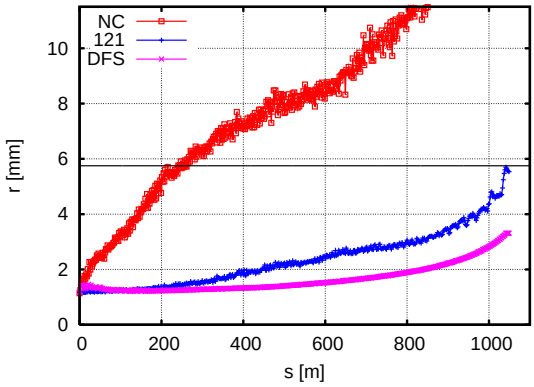

Figure 6: Beam envelopes after steering

DECELERATOR CTF3 TEST-BENCHES

Test Beam Line (TBL)

The main test-bench for the CLIC Decelerator will be the Test Beam Line (TBL), due for completion towards the end of 2010. In the TBL it is foreseen to decelerate a combined CTF3 beam, of up to 30A and 150 MeV, extracting ca. 60% of the total energy, using 16 PETS of 0.8 m.

Simulations predict that the beam envelope amplification due to transverse wakes is slightly larger in the TBL than in the decelerator. Large over-estimations in Q-factors in the PETS design should therefore be observable in the TBL, e.g. in the form of losses due to high-Q modes leading to instabilities.

Because of it small numbers of quadrupoles in the TBL (16) versus the decelerator ($>$ 1000) we do not expect advanced beam-based alignment to be necessary. However, simulations show that Dispersion-Free Steering will still be at least *as effective* as 1-to-1, and the TBL could therefore be a potential test-bed for the Dispersion-Free Steering techniques suggested for the decelerator.

Finally, the TBL final energy will be a factor four lower than for CLIC, and the beam envelope for a perfect machine and beam (resulting from adiabatic undamping alone) is predicted to be almost 8 mm - more than 2/3 of the PETS aperture - potentially leading to strong higher-order mode excitation (we remind that for the CLIC Decelerator we aim to keep the beam within 1/2 of the PETS aperture along the whole lattice). A 3-sigma transport through the TBL therefore looks like a difficult task, but if we come close to achieving it, it will be a great step towards proving feasibility of the CLIC decelerator

Two-Beam Test Stand

Starting operation this year the Two-Beam Test Stand (TBTS) will decelerate the beam through a single PETS of 1 m, using recirculation of the extracted field to increase power production and deceleration for a given beam current. In addition to proving RF-power extraction and transfer, the TBTS will provide the first tests for the decelerator scheme, allowing e.g to correlate simulations measurements of beam current, power production and measured deceleration in a dispersive region.

CONCLUSIONS

In order to ensure minimum-loss beam transport in a robust way through the CLIC Decelerator, the following items have been studied and optimized :

- Tightly focusing FODO lattice with smooth decrease of quadrupole gradient
- Optimization of the PETS design in order to minimize dangerous modes of the transverse wakes
- Advanced beam-based orbit correction to transport particles of all energies

Simulations show that the a beam-envelope very close to minimum can be achieved with the current design. Test-facilities are underway to prove the feasibility of the above items.

ACKNOWLEDGEMENTS

Helpful discussions with S. Doebert, R. Zennaro and V. Ziemann are gratefully acknowledged.

REFERENCES

[1] CLIC parameters 2008, F. Tecker ed., *CERN CLIC-Note 764* (2008)

[2] https://savannah.cern.ch/projects/placet

[3] E. Adli et al., A Study of Failure Modes in the CLIC decelerator, *Proceeding of EPAC 2008* (2008)

[4] I.Syratchev et al., High RF Power Production for CLIC, *CERN CLIC-Note 720* and *PAC 2007* (2007)

[5] E. Adli and D. Schulte, Beam-Based Alignment for the CLIC Decelerator, *Proceeding of EPAC 2008* (2008)

[6] K. Bane, Short-range dipole wake elds in accelerating structures for the NLC, SLAC-PUB-9663 (2003)

[7] E. Adli et al., Status of an Automatic Beam Steering for the CLIC Test Facility 3, *Proceeding of Linac 2008* (2008)

B.4 Beam-Based Alignment for the CLIC Decelerator

This paper presents a study of the challenges of transporting the 100 ampere electron drive beam through the decelerator. Solutions are suggested, including the use of dispersion-free steering in order to take out dispersive errors due to the large energy spread.

The results in this paper are based on simulation and theoretical studies. The candidate produced all the simulation results and the analysis in the paper. The candidate provided the plots and figures, and wrote the text in this paper. Daniel Schulte provided ideas and suggestions, as expert in the field of beam physics.

BEAM-BASED ALIGNMENT FOR THE CLIC DECELERATOR*

E. Adli†, D. Schulte, CERN, Geneva, Switzerland

Abstract

The CLIC Drive Beam decelerator requires the beam to be transported with very small losses. Beam-based alignment is necessary in order to achieve this, and various beam-based alignment schemes have been tested for the decelerator lattice. The decelerator beam has an energy spread of up to 90%, which impacts the performance of the alignment schemes. We have shown that Dispersion-Free-Steering works well for the decelerator lattice. However, because of the transverse focusing approach, modifications of the normal DFS schemes must be applied. Tune-up scenarios for the CLIC decelerator using beam-based alignment are also discussed.

INTRODUCTION

The purpose of the CLIC decelerator is to produce the correct RF power for the main beam, timely and uniformly along the decelerator, while achieving a high power extraction efficiency. Uniform power production implies that the electron drive beam must be transported to the end with very small losses. The transverse motion will be perturbed by quadrupole misalignment as well as wake field deflections.

RF-power is produced by Power Extraction and Transfer Structures (PETS) (more than 1300 for each decelerator sector). The PETS fundamental mode is tuned to the frequency of the bunch train (12.0 GHz), and the field builds up resonantly. This field drains out of PETS with a finite group velocity of β_g=0.46, implying steady-state deceleration after a transient of $\lceil (\frac{l_{PETS}}{z_{bb}})\frac{(1-\beta_g)}{\beta_g} \rceil$ = 11 bunches (z_{bb} is the bunch distance and l_{PETS} the PETS length). Each steady-state bunch will have a substantial energy spread, due to the finite bunch size. Figure 1 shows the energy profile at the end of the decelerator. This paper focuses on transverse beam dynamics. Some complementary topics, including detuning and longitudinal stability, have been discussed in [1].

We start by summarizing the alignment tolerances needed to mitigate the effect of transverse wakes and to provide a starting point for beam-based alignment. We then discuss beam envelope growth and alignment schemes to reduce it. We will see that the large energy spread provides a challenge, suggesting the need for advanced alignment schemes. Input parameters for this study are based on [2], slightly adapted in order to achieve a maximum energy spread at the end of the lattice of $S \equiv (E_0 - E_{min})/E_0 = 90\%$ (reference for the decelerator studies). Details about the parameters and the simulation method are presented in the accompanying paper [3].

* Work supported by the Research Council of Norway and the Commission of the European Communities under the 6th Framework Programme Structuring the European Research Area, contract number RIDS-011899.

† Erik.Adli@cern.ch, University of Oslo and CERN

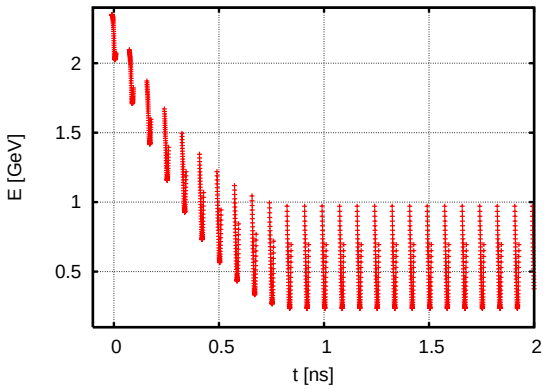

Figure 1: Energy profile after deceleration (start of pulse)

ALIGNMENT TOLERANCES

A study has been performed in order to find the alignment tolerances resulting from beam dynamics requirements [4]. It was required that a single type of misalignment should result in a maximum increase in the beam centroid envelope of 1 mm. For the quadrupoles the resulting misalignment tolerance is not feasible with planned static alignment, and the tolerances given below represents the expected residual error. The tolerances are shown in Table 1, and are used for the simulations in this paper. BPM resolution is further discussed below; initially a value of 2 μm is used.

Table 1: Alignment tolerances

Misalignment	Symbol	Value	Unit
PETS misalignment	σ_{PETS}	100	μm
Quadrupole misalignment	σ_{quad}	20	μm
BPM misalignment	σ_{BPM}	20	μm
BPM resolution	σ_{res}	2	μm
Pitch/roll misalignments	$\sigma_{\theta,\phi}$	1	mrad

BEAM ENVELOPE GROWTH

Simulation Criterion

As simulation criterion for minimum-loss transport we require the entire 3-sigma beam envelope, defined as $r \equiv \max \sqrt{(|x_i| + 3\sigma_{x,i})^2 + (|y_i| + 3\sigma_{y,i})^2}$, to be within half the available aperture, a_0, to have a margin for unmodelled effects of higher order wake fields. There will be $\sim$ 50 decelerator sectors, and we require 99% confidence that all sectors simultaneously adhere to this criterion. This implies that 99.98% of random instances of a single sector

must fulfill $r < \frac{1}{2}a_0 = 5.75$mm. It is not feasable to simulate enough machines to do a direct verification of this. Instead, 500 machines are simulated and the tail of the resulting beam envelope distributions will be inspected.

Sources of Envelope Growth

The beam envelope will grow due to the following effects :

- spurious dispersion induced by quadrupole offsets
- adiabatic undamping due to deceleration by the PETS
- transverse kicks due to the PETS dipole wake and RF

The beam is modelled as bunches consisting of slices in z with variable energy and with second order moments to represent the transverse particle distribution of each slice. We first note that since we are interested in the envelope, and not the emittance, the relative orientation of the distribution phase-advances (decided by the lattice chromaticity) is irrelevant for our study. The beam envelope will be determined by the motion of the slice centroids, plus the adiabatic undamping of the distributions. The latter will grow by a factor $\sqrt{\gamma_i/\gamma_f}$, leading to a maximum envelope for a perfect beam going through a perfect machine of $r_{ad} = \sqrt{3^2\sigma_x^2 + 3^2\sigma_y^2} \approx 3\sqrt{2L_{cell}\varepsilon_N/\gamma_f} = 3.3$ mm ($\mu_{cell} \approx 90^o$ assumed).

In order to discuss other contributions to the envelope growth and the choices of steering algorithms, we imagine a "pencil beam" consisting of centroids only. We denote the maximum centroid offset as r_c. Typical residual misalignments of quadrupole and BPMs will be of the order 20 μm rms. For a regular FODO lattice without deceleration we estimate the final rms centroid offset, due to sporious dispersion, by doing an ensemble average over the sum of quadrupole kicks yielding $r_{c,rms} \approx \frac{\sigma_{quad}}{\cos(\mu_{cell}/2)} 2\sqrt{2N_{cell}}$ =1.8 mm. The PETS will induce additional growth due to adiabatic undamping, RF-kicks and transverse wakes. Including all effects in the simulations we find $r_{c,rms} = 11$mm, where the dipole wake causes an amplification of approximately 20% (PETS design / misalignment tolerances are such that the effect of dipole wakes shall not be dominant [4]). Figure 2 shows the uncorrected total envelope (NC), maximum of 500 machines. We note that it largely exceeds our criterion, implying a need for steering.

STEERING

1-to-1 Correction (SC)

We consider first a simple 1-to-1 correction scheme, where the total beam centroid is steered into the centre of each BPM. Quadrupole movers are assumed as correctors in this study. In Figure 2 we observe the resulting envelope. We see that although the envelope is now much smaller, we still have a significant residual envelope. A particular problem is that the 1-to-1 correction steers the steady-state part of the beam, while the particles constituting the transient high-energy head will move on highly dispersive trajectories, and might drive the envelope. Closer inspection reveals that it is indeed the transient part that drives the envelope. After 1-to-1 correction the beam envelope is slightly larger than our criterion (even for a limited number of machines). This leads us to the study of Dispersion-Free steering, in order to reduce the dispersive error.

Dispersive-free Steering (DFS)

The idea of Dispersion-free steering is to reduce the energy dependence of the centroid trajectories [6]. BPM reading i is related to a corrector kick j via the response matrix element, $b_i = R_{ij}(p)c_j$. For the decelerator, $R_{ij}(p)$ and therefore also b_i, are highly non-linear in the momentun p. However, we assume linear optics, so b_i is linear in c_j. With perfect knowledge of our system, and perfect measurement, we could in principle use correctors to zero the difference between two arbitrary energy centroid trajectories, $y_0(s), y_1(s)$. For several reasons this solution is not attainable in practice; our models are not perfect and the precision of our BPMs is finite, leading to an unstable solution. The difference orbit is therefore weighted against the central orbit, resulting in the following metric to be minimized: $\chi^2 = w_0\Sigma y_{0,i}^2 + w_1\Sigma(y_{1,i} - y_{0,i})^2$ where the relative weighting should be in the order $w_1/w_0 = \sigma_{BPM}^2/\sigma_{res}^2$. Optimal weighting wrt. to r was found by simulation.

We must also ensure that ineffective corrector modes are not applied, because this would lead to large corrector offsets. By doing an SVD-analysis of the resulting matrix, we find indeed that $\sigma_{max}/\sigma_{min} \sim 10^7$. In this study we only include corrector modes with $\sigma_{max}/\sigma \sim 10^3$ or higher, yielding $\sigma_{quad,corrected} < 2\sigma_{quad}$.

Decelerator Challenges: Test-beam

One particular challenge for the decelerator is to find a suitable test-beam for difference-trajectory minimization; a higher energy beam will not be available, a lower energy beam will not be stable with the nominal optics [4]. We solve this by taking advantage of the PETS: since $\Delta E_{PETS} \propto I$, a test-beam with an energy difference increasing linearly wrt. to the nominal beam can be produced by reducing the current. The energy spread of the nominal beam increases linearly as well, therefore we do not get large dispersive errors at the start of the lattice. A practical manner to reduce the current is to use the combiner rings or delayed switching [5] to generate a bunch train with empty buckets. For these simulations we use a test-beam where every 3^{rd} bucket is missing. The net result has been shown to be similar to simply reducing the bunch charge (less practical in the real machine).

Our suggestion for dispersion-free steering has the advantages that the quadrupole strength is kept constant (avoids potential problems with change of quadrupole center with strength), and that the main beam and the test-beam could be combined in one pulse (avoids potential problem with relative offsets of the two beams).

RESULTS

Figure 2 shows the 3-sigma envelope for the cases of no correction (NC), simple 1-to-1 correction (SC) and dispersion-free steering (DFS) with BPM resolution of 2μm. Recalling the minimum achievable performance of $r_{ad} = 3.3$ mm, we conclude that the dispersion-free steering has very effectively suppressed the dispersive errors.

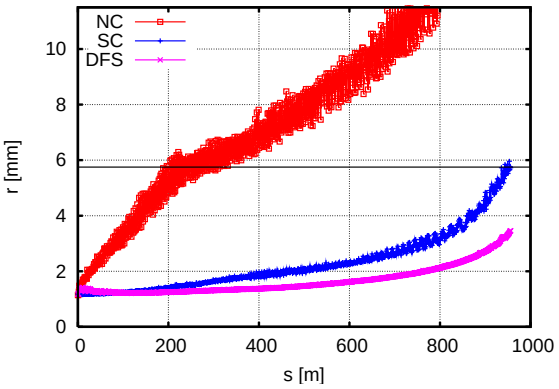

Figure 2: Beam envelope with no correction, simple correction and dispersion-free steering (maximum of 500 machines)

Dependence on BPM Resolution for DFS

For the dispersive -free steering, the maximum envelope depends linearly with σ_{res} when this error contribution becomes dominant ($> 6\mu$m in our case) . Table 2 shows the envelope versus resolution (maximum of all machines).

Table 2: Dependence on BPM resolution.

$\sigma_{\mathbf{res}}[\mu\mathbf{m}]$	1.0	2.0	4.0	6.0	8.0	10.0
r [mm]	3.4	3.5	3.6	3.7	3.9	4.2

Tail distributions versus CLIC target

Figure 3 shows the accumulated distribution of the envelopes for all machines, for the SC case, as well as DFS cases with BPM resolutions ranging from 1μm to 10μm. For a BPM resolution of 1 μm or 2 μm the tails have sharp fall off, while for higher resolutions tail sizes start to increase. Although the data available do not give a precise limit for the BPM resolution required, we do suggest a resolution of $\sigma_{res} = 2.0\mu$m. Requiring more precise BPMs will not improve the performance noticeably, and this choice also indicated good confidence wrt. to our simulation criterion for the entire CLIC.

OPERATIONAL ASPECTS AND TUNE-UP

Transport through an uncorrected machine will lead to losses, on average found to be in the order of several %. For initial alignment we propose to reduce the envelope

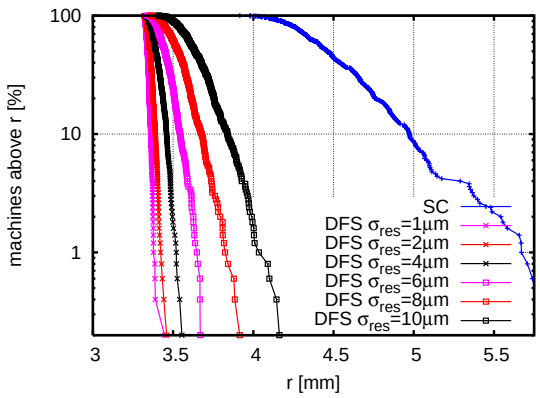

Figure 3: Histogram over all simulated machines

by inserting empty buckets between bunches (yielding less average current, adiabatic undamping and dipole wakes). With a few empty buckets between bunches, simulations show very small average losses. 1-to-1 steering, then DFS can then be performed, and the number of empty buckets can be gradually reduced until nominal beam is reached. This method would require BPMs to be sensitive down to a fraction of the nominal current. Finally, we note that to be robust against current/energy differences between response and real machine, corrections should be performed in bins.

CONCLUSIONS

We have shown that the CLIC decelerator needs beam based alignment in order to achieve small losses during operation, and that dispersion-free steering is an excellent candiate. An appropriate test-beam with empty buckets can be generated using combiner rings or delayed switching. For initial alignment one can use reduced current test-beams, and then increase the current to nominal. We estimate a BPM resolution of $\sigma_{res} = 2.0$ μm to be adequate.

ACKNOWLEDGEMENTS

Helpful discussions with A. Latina, J.B. Jeanneret, H. H. Braun and S. Stapnes are gratefully acknowledged.

REFERENCES

[1] D. Schulte, Stability of the Drive Beam in the Decelerator of CLIC, *CERN CLIC-Note 528* (2002)

[2] CLIC parameters 2008, F. Tecker ed., to be issued., *CERN CLIC-Note* (2008)

[3] E. Adli et al., A Study of Failure Modes in the CLIC decelerator, MOPP002, these proc.

[4] E. Adli and D. Schulte, Alignment Tolerances for the CLIC decelerator, *CERN CLIC-Note 733* (2008)

[5] D. Schulte, Beam Loading Compensation in the Main Linac of CLIC, *Proceeding of LINAC 2000* (2000)

[6] T.O. Raubenheimer and R.D. Ruth, A dispersion-free trajectory correction technique for linear colliders, NIM A302 (1991) 191-208

B.5 A Study of Failure Modes in the CLIC decelerator

This paper presents a study of various failure modes for the drive beam decelerator. The very high current, combined with the special characteristics power extraction and transfer structures, lead to challenges that are particular to this machine.

The results in this paper are based on simulation and theoretical studies. The candidate produced all the simulation results and the analysis in the paper. The candidate provided the plots and figures, and wrote the text in this paper. Daniel Schulte and Igor Syratchev acted as consulting experts in the fields of beam physics and radio frequency engineering respectively.

A STUDY OF FAILURE MODES IN THE CLIC DECELERATOR*

E. Adli†, D. Schulte, I. Syratchev, CERN, Geneva, Switzerland

Abstract

The CLIC Drive Beam decelerator is responsible for producing the RF power for the main linacs, using Power Extraction and Transfer Structures (PETS). To provide uniform power production, the beam must be transported with very small losses. In this paper failure modes for the operation of the decelerator are investigated, and the impact on beam stability and loss levels is presented. Quadrupole failure, PETS inhibition and PETS RF break down scenarios are being considered.

INTRODUCTION

The CLIC decelerator transports a very high-intensity electron beam where the deceleration induces up to 90% energy spread at the end of the lattice. A tightly focusing FODO lattice ensures transport of particles in the entire energy range and mitigation of the transverse wake fields induced by the PETS. Quadrupole failure leads to blow-up of the beta function as well as effective kicks with respect to a steered trajectory. A mechanism to inhibit the PETS in case of structure break down is planned. The PETS inhibition will change the wake modes, and thus affect the trajectory. In this paper the effect on the beam stability and beam losses for a number of quadrupole/PETS failure and operational scenarios has been quantified by simulation.

METHOD

The input parameters for this study, slightly adapted in order to achieve a maximum energy spread of S=0.90, are based on [1] and [2] and are summarized in Table 1.

Table 1: Decelerator lattice and beam parameters.

Parameters	Symbol	Value	Unit
Beam parameters			
Decelerator sector length	L	960	m
Bunch separation	$z_{\rm bb}$	25	mm
Bunch rms length	σ_z	1.0	mm
Bunches per train	n	2900	-
Initial average current	I_0	94.7	A
Initial energy	E_0	2.35	GeV
Final max. energy spread	S	90.0	-
Initial norm. emit.	$\epsilon_{\rm n\,x,y}$	150	μm rad
PETS parameters			
Frequency	f_L	12.00	GHz
Impedance [linac conv.]	R'/Q	2.22	kΩ/m
Group velocity	β_g	0.46	-
PETS half-aperture	a_0	11.5	mm
Lattice parameters			
FODO cell length	$L_{\rm cell}$	2.0	m
FODO phase-advance	$\mu_{\rm cell}$	92	deg
Average beta function	β	1.9	m
Quadrupole misalignment	$\sigma_{\rm quad}$	20	μm
BPM misalignment	$\sigma_{\rm BPM}$	20	μm
BPM resolution	$\sigma_{\rm res}$	2	μm
PETS misalignment	$\sigma_{\rm PETS}$	100	μm
Pitch/roll misalignments	$\sigma_{\theta,\phi}$	1	mrad

There are 24 CLIC decelerator sectors along each linac, differing in length depending on the number of empty PETS slots in the FODO cells, which again depends on the main linac design. For this study a decelerator of 960 m is considered (70% of all possible slots are filled with PETS).

Simulations have been performed using the simulation code PLACET [3]. The PLACET PETS model includes both long and short range wakes. The monopole mode decelerates the beam, and the set of dipole modes kicks the beam transversally. Each mode is defined with amplitude, frequency, damping factor and group velocity, based on field simulations of the PETS [4]. Nominal PETS parameters are used for the simulations. Higher order modes are not taken into account. The beam is modeled as slices in z with varying energy and with second order moments to represent the transverse particle distribution of each slice. Simulating the real pulse length of 240 ns is too CPU intensive. Because of the high Q-factors enough bunches to incorporate most of the wake effect must be simulated (50 used), and to ensure convergence of the single-bunch effects enough slices per bunch must be used (51 used). The real length is mimicked by weighting the last simulated bunch appropriately in the BPMs. For loss studies the beam transverse size was simulated by transversally distributing 11 zero-emittance macro particles for each slice, simulating one dimension with losses taken at $a = a_0/\sqrt{2}$. It was verified that the loss levels were approximately the same for longer simulated beams. The loss levels calculated in this study is our best estimate, but should be taken rather as order of magnitude calculations than precise number.

For some of the studies in this papers losses are calculated, while for others it is of interest to see the relative change of the beam envelope. As standard metric, the 3-σ beam envelope defined as $r = \max \sqrt{(|x_i| + 3\sigma_{x,i})^2 + (|y_i| + 3\sigma_{y,i})^2}$ (maximum along the lattice) is used.

The Drive Beam envelope will increase due to adiabatic undamping as well as dipole kicks due to component misalignment. The need for and use of steering algorithms have been shown in [2], and for the simulations of failure modes we look at results for the cases of uncorrected ma-

* Work supported by the Research Council of Norway and the Commission of the European Communities under the 6th Framework Programme Structuring the European Research Area, contract number RIDS-011899.

† Erik.Adli@cern.ch, University of Oslo and CERN

chines (NC), machines corrected using simple 1-to-1 steering (SC) and dispersion-free steered machine (DFS). For each of these steering approaches we average the results over a number of random machines.

LATTICE FOCUSING

The quadrupoles will be scaled such that the lowest energy particles have a constant phase-advance per cell ($\mu_{cell} \approx 90^o$). For a perfect machine, higher energy particles will then be contained in the envelope [5]; the maximum envelope of the lowest energy slice is $(\gamma_i/\gamma_f \varepsilon\hat{\beta})^{1/2} = (10\varepsilon\hat{\beta})^{1/2}$, while for the highest energy it is $(\varepsilon\hat{\beta}_{max})^{1/2} \approx (4.6\varepsilon\hat{\beta})^{1/2}$. We note that as a consequence of the focusing strategy, the FODO stability limit is surpassed at the lattice end if the initial beam energy is too low by a factor $E_{unstable}/E_0 < (1-S)(\frac{\sin(\mu/2)}{\sin(180^0/2)}) + S \approx 0.97$. Because the deceleration scales with current, there is a similar limit for the current: $I_{unstable}/I_0 > \frac{1}{S} - (\frac{1}{S} - 1)\frac{\sin(\phi_0/2)}{\sin(180^0/2)} \approx 1.03$.

Because the quadrupole strength decays linearly along the lattice, a possibility is to put families of quadrupoles in series to limit the number of power supplies. The impact of this will be analyzed below.

QUADRUPOLE FAILURES

We first investigate the effect of random quadrupole failures (failure implies here k=0). Total losses over machines where N random quadrupoles have failed are calculated (averaged over 10 machines) . We note that failure of a quadrupole results in up to 25-fold magnification of the beta function for the lowest energy particles. Figure 1 shows the percentage of the beam lost for 0 to 5 quadrupole faults. For an uncorrected machine, several percent of the beam is lost even with one quadrupole failure, while for a corrected machine one quadrupole failure leads to sub-percent loss level. Study of loss maps (not included here) shows that for single quad failure, the average losses take place uniquely at the last part of the machine, as expected by the envelope growth. The effect of failure when F or D quadrupoles fail in pairs is shown in Figure 2. Here even corrected machines suffer from 10% loss levels for a single failure.

QUADRUPOLE POWER RIPPLE

In order to get an estimate of the power supply precision needed, the effect of power ripple is simulated by putting random noise on the quadrupole strength and average over a 100 machines. Figure 3 shows the envelope growth compared to the same machines with no ripple. Ripple up to 10^{-3} is accepted without significant envelope increase . If power supplies are connected in series, the ripple will be correlated. For completeness Figure 4 shows the extreme case where all F's are scaled together and all D's are scaled together. The ripple is now negligible, as expected.

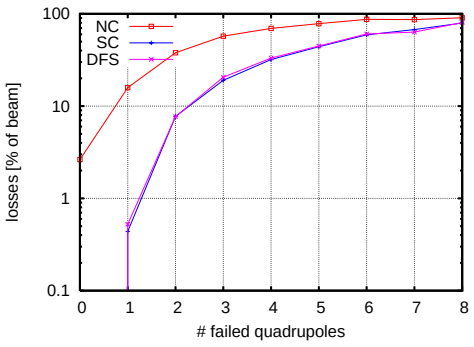

Figure 1: Independent quadrupole failure

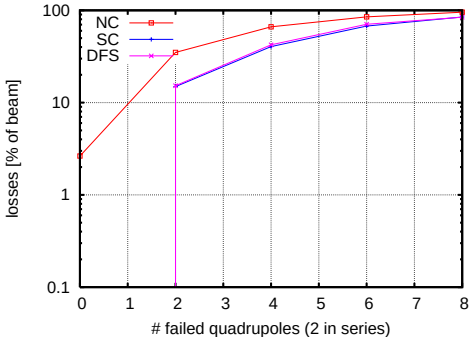

Figure 2: Quadrupole series failure

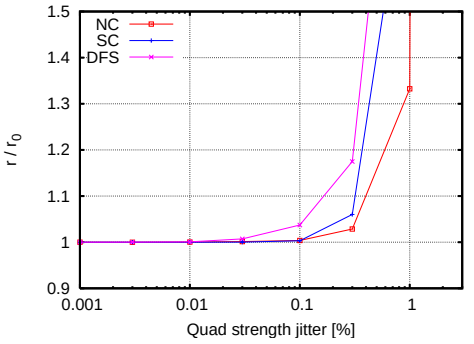

Figure 3: The effect of quadrupole jitter

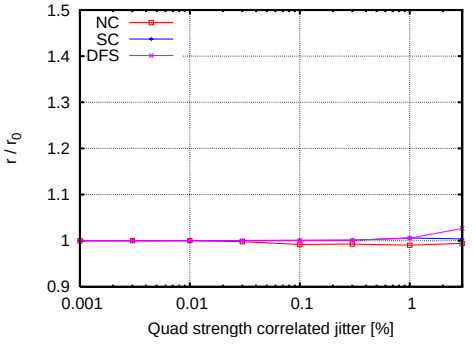

Figure 4: The effect of quadrupole jitter - all quads of one family in series

PETS

The Effect of PETS Inhibition

The lattice contains up to two PETS between each quadrupole, where each PETS extracts $\sim$ 0.1% of the beam energy. During machine operation it will be necessary to inhibit PETS power production in case of structure breakdown. One mechanism being considered is detuning wedges, described in [4]. The wedges occupy four out of the eight transverse damping slots. A worst-case estimate of how the transverse modes are affected is therefore to double all the transverse Q-factors. In the simulations a PETS is inhibited by setting R'/Q to 0 while doubling Q_T. Inhibiting a PETS affects the beam as follows:

- the lack of deceleration leads to higher minimum beam energy and thus less adiabatic undamping and less energy spread
- dipole wake kicks increase; for a steered trajectory the change of kicks will in addition spoil the steering
- the coherence of the beam energy will increase, and thus also the coherent build up of tranverse wakes

For all the points above we expect the effect to be small for few PETS. However, it is of interest to know how the machine performs with a large number of PETS inhibited. Figure 5 shows the relative change in beam envelope when a number of PETS are inhibited at random positions (averaged over 100 machines). For a dispersions-free steered machine there is indeed a slight decrease of the beam envelope whenever less than 2/3 of the PETS are inhibited. However, for all steering scenarios we observe envelope growth when the major part of the PETS is inhibited.

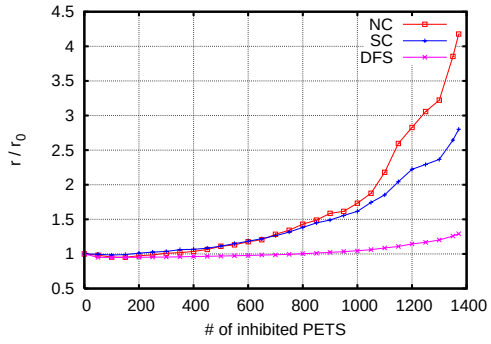

Figure 5: The effect of PETS inhibition

PETS Break Down Voltage

An RF break down will induce transverse voltage in the PETS, with an amplitude depending on many factors, including PETS design. In this section we estimate the maximum acceptable PETS transverse voltage by finding the voltage needed to kick an initial unperturbed beam in a perfect machine so that the maximum centroid envelope along the lattice is 1 mm. An analytical estimate is found as $U = \Delta y' \times E = \frac{r}{A\hat{\beta}} / \sqrt{\frac{E_i}{E_f}} \times E_i = \frac{r}{A\hat{\beta}} \sqrt{E_i E_f}$, where E_i is the energy at the kick location, $\frac{E_i}{E_f}$ the effect of adiabatic undamping, $\hat{\beta}$ the beta function at the kick locations (worst case assumed, $\beta = \hat{\beta}$). A is an estimate for the transverse wake amplification, set to $A = 1.2$ based on previous experience. Figure 6 shows the estimate as well as simulation results (PETS are located at points of varing beta function, and there are varying patterns of empty "slots"). We conclude that, with our criterion of maximum 1 mm centroid motion, there is an acceptance of about 200 kV at the start of the lattice, decreasing towards 50 kV towards the end of the lattice.

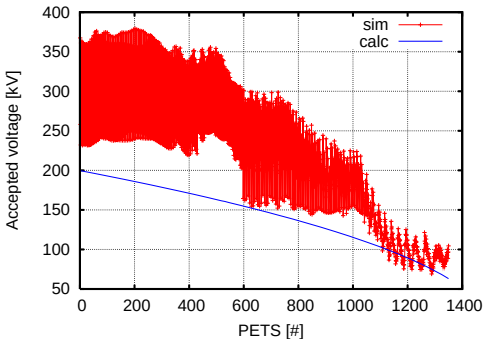

Figure 6: Maximum accepted PETS break down voltage

CONCLUSIONS

A properly steered machine behaves better than an uncorrected one also wrt. failure modes. For a steered machine we conclude: more than two simultaneous quadrupole failures leads to unacceptable loss levels. Quadrupole power supply jitter is acceptable up to 10^{-3}. Inhibiting up to 1/3 of the PETS is not severe for beam stability (up to 2/3 for a dispersion-free steered machine). PETS break down voltage up to 50-200 kV is acceptable for beam stability, depending on PETS position.

ACKNOWLEDGEMENTS

Helpful discussions with A. Latina, J.B. Jeanneret, H.H. Braun and S. Stapnes are gratefully acknowledged.

REFERENCES

[1] CLIC parameters 2008, F. Tecker ed., to be issued., *CERN CLIC-Note* (2008)

[2] E. Adli and D. Schulte, Beam-Based Alignment for the CLIC Decelerator, MOPP001, these proc.

[3] D. Schulte et al. *CERN/PS 2001-028* (AE) and *PAC 2001* (2001)

[4] I.Syratchev et al., High RF Power Production for CLIC, *CERN CLIC Note 720* and *PAC 2007* (2007)

[5] The CLIC RF Power Source, H. H. Braun and R. Corsini (eds.), *CERN Yellow Report 99-06* (1999)

B.6 Status of an Automatic Beam Steering for the CLIC Test Facility 3

This paper presents experimental results concerning steering of the electron beam in the CLIC Test Facility 3 (CTF3) linear accelerator. In particular the alignment algorithms studied in the paper "Beam-Based Alignment for the CLIC Decelerator" also included in this thesis, were investigated, and the algorithms were proven to work well.

The results in this paper are based on experiments with the CTF3 machine as well as analysis and simulation studies. The CTF3 operation team, under supervision of Roberto Corsini, provided invaluable assistance in explaining the physics of the machine and in explaining how to interface to the control system in order to command and acquire data from the machine. The operation team also provided help and expertise in the machine operation during the experiment runs. Daniel Schulte provided ideas and suggestions, as expert in the field of beam physics.

The candidate was responsible for the implementation of the steering algorithms, the data acquisition as well as operation of the CTF3 machine during dedicated test-runs. The candidate wrote the text, analysed the data and provided the plots for the paper.

STATUS OF AN AUTOMATIC BEAM STEERING FOR THE CLIC TEST FACILITY 3*

E. Adli†, R. Corsini, A. Dabrowski, D. Schulte, S.H. Shaker,
P. Skowronski, F. Tecker, R. Tomas, CERN, Geneva, Switzerland

Abstract

An automatic beam steering application for CTF 3 is being designed in order to automatize operation of the machine, as well as providing a test-bed for advanced steering algorithms for CLIC. Beam-based correction including dispersion free steering have been investigated. An approach based on a PLACET on-line model has been tested. This paper gives an overview of the current status and the achieved results of the CTF3 automatic steering.

INTRODUCTION

The Compact LInear Collider (CLIC) study has shown that advanced beam-based correction will be needed to reach nominal performance of several parts of the collider [1], [2]. The CLIC Test Facility 3 (CTF3) has been constructed at CERN in order to demonstrate feasibility of several key concepts of CLIC [3]. New areas are added to CTF3 for each new phase, making operation more complicated, and it is therefore of significant interest to ease the operation of this machine. The purpose of the work described here is thus two-fold:

- test of correction algorithms devised for CLIC on a real machine
- aid operation of CTF3 by automating beam steering (currently performed by hand)

CORRECTION APPROACHES

The correction algorithms investigated here are "all-to-all" (A2A) and dispersion-free steering (DFS) [4]. In this paper we use "correction" and "steering" interchangeably. Both algorithms can be implemented using response matrices. Their effect when applied to a defined lattice segment is ideally:

- A2A: steers the beam to get BPM zero-readings, by simply inverting the response matrix of the nominal machine optics
- DFS: minimizes the difference of dispersive trajectories, using responses corresponding to optics with different $\Delta p/p$; weighted against A2A

Matrix inversion for both candidates is performed in the Least-Squares sense, using SVD. Smoothing can be introduced by taking out corrector modes corresponding to small singular values, effectively smoothing out noise effects. Furthermore, defect BPMs and/or correctors can be taken easily into account by zeroing rows and/or columns of the response matrix. A2A and DFS then find the global solution within the defined lattice segment (this is why we say "all-to-all" rather than "1-to-1").

For quick and effective correction computer model generated responses are needed. With model-based steering, one can perform all-to-all steering for a lattice segment in few tens of seconds. In comparison, to obtain machine responses in CTF3 takes from 1/4 h to 1/2 h per optics, per plane, totaling to hours if one wants to do dispersion-free steering. On the other hand, model-based steering require a good correspondence model/machine, and obtaining the needed model accuracy might be challenging.

TEST-CASE: THE CTF3 LINAC

The CTF3 linac, characterized by operation with full beam-loading [5], was chosen as "test-lattice", because of higher applicability wrt. [1], [2]. We apply correction on a straight part of the linac, with regular lattice structure consisting of 11 girders ("nr. 5" to "nr. 15"), where each girder supports a quadrupole triplet, one corrector coil, and one BPM, as shown in Figure 1. For girders 5,6,7,11,12,13 and 15 there are in addition two accelerating structures, fed by one klystron, located between the corrector and the BPM.

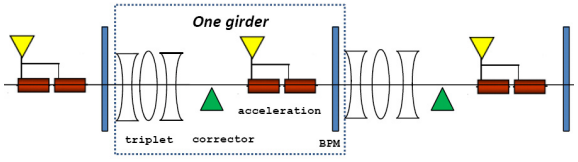

Figure 1: Structure of the CTF3 linac (not to scale).

Dispersion and Emittance Growth

Dispersion measurement and DFS were in this work performed by scaling magnet currents. We therefore consider only dispersion building up from the start of the test-lattice (we do not consider, and cannot mitigate, upstream dispersion). There are no powered dipoles in the test-lattice, so the dispersion comes mainly from parasitic dispersion due to quadrupole offsets (we also get a small contribution from the correctors, dispersion due to incoming beam offset/angle and due to transverse wakes). We note that our 11 cell lattice accomodates little more than a single betatron-oscillation, and we therefore expect dispersion to be small, even for the uncorrected case (no resonant build-up possible). The CTF3 component alignment tolerance is 100 μm

* Work supported by the Research Council of Norway and the Commission of the European Communities under the 6th Framework Programme 'Structuring the European Research Area', contract number RIDS-011899.
† Erik.Adli@cern.ch, University of Oslo and CERN

rms. PLACET simulations estimate the resulting dispersion growth to 5 mm (rms of 100 seeds). By simulation we estimate emittance growth without correction, assuming a bunch-length of 1.6 mm and an initial normalized emittance of 100 μm, to be in the order of percent, and an ultimate test of DFS would be to compare emittance growth before and after correction.

MODEL IDENTIFICATION

A linac model implemented in PLACET was to be used for the model-based correction. It was decided to verify and eventually improve the model before using it for steering. An attempt to use "LOCO-type" global identification [6] was initiated (not applied to the linac before), and a new identification code was written in Octave for this purpose. Improvement of the model with this method turned out to be difficult because of the triplet cells (see below) combined with imprecise response measurement (the same response point was found to vary up to 10% rms, due to beam jitter, different working points, hysteresis etc).

Triplet Cells

The linac focusing is done with quadrupoles in triplets, powered 2+1 or 1+1+1, with a single BPM and corrector per triplet cell (see Figure 1). The similarity of difference orbit when changing either of the outer quadrupoles, as well as almost opposite orbit of the middle quad, leads to near degeneracies which becomes difficult to resolve with imprecise data. Quantitatively we see this by error propagation through the covariance matrix $(\frac{\partial E}{\partial K}^T \frac{\partial E}{\partial K})^{-1}$ [7]; inputting the imprecision of the response points, the standard uncertainty of the parameter estimates is for many of the quadrupoles of the same order as the parameter itself, even when disregarding the first few triplet cells (the least constrained ones). As comparison, with quadrupole currents frozen, the uncertainty of the corrector gains is $\sim 1\%$. The phase-difference between model and machine was shown to be reasonable small by direct SVD analysis, and it was therefore decided to go on with quadrupole parameters frozen. The trustworthiness of individual corrector gain identification with quadrupoles frozen is not clear, and therefore the only parameters fitted before correction was global scaling + the ratio of the calibration factor of the two different corrector types in the test-lattice.

Requirement for Model-machine Correspondence

After identification we still have a certain mismatch between model and machine. We want to estimate, by simulation, the error accepted on the model parameters while still achieving adequate correction. To study this, A2A was applied to a perturbed model using ideal model responses. Each quadrupole strength was randomly scaled by an rms value of $\sigma_{\Delta k}$ %. The maximum resulting BPM readings after 5 iterations of A2A, averaged over 100 machines, are shown in Table 1. For strength rms error of up to 12%, A2A still converges to BPM readings $< 100\mu$m (Perfect BPMs were assumed for these simulations).

Table 1: Correction Convergence with Model Discrepancy

$\sigma_{\mathbf{\Delta k}}[\%]$	4	6	8	10	12	14	16	20
y [mm]	0	0	0.02	0.04	0.1	0.3	0.7	3.6

CORRECTION RESULTS

All-to-all

Using machine responses both planes were corrected to within 0.15 mm rms in two iterations (this illustrates some imprecision in the machine responses and/or machine jitter). Then, correction was performed using responses calculated from the PLACET model. The calculation of the responses takes less than 5 seconds. Both planes did converge, but needed up to to four iterations before reaching the convergence criterion, showing that the model of the linac is not perfect but good enough for steering. Each iteration takes from 10 to 20 seconds, depending on whether a corrector has to switch polarity or not.

Non-functioning correctors or BPMs can be taken into account by first identifying them (e.g manually or from machine responses). A device is disregarded by the algorithm by simply setting the corresponding row or column to zero. One corrector was very unreliable during this work (DVD1420), and was turned off and the corresponding column set to 0. The resulting system is under-actuated (10 correctors and 11 BPMs), and instead of trying to achieve zero BPM readings A2A finds the least-square solution. The result after model-based A2A correction, with one defect corrector in the vertical, is show in Figure 2. The oscillatory pattern in the vertical corresponds to the uncorrectable BPM mode, belonging to the zero singular value which is due to the defect corrector. Dispersion after A2A steering was measured to less than 5 mm (error margin of about 0.5 mm). This is comparable to dispersion measured after manual correction of the machine. We conclude that model-based all-to-all correction seems to work well, is reasonably fast, and robust wrt. corrector or BPM defects.

Dispersion Free Steering

Since A2A correction gives a very small residual dispersion (showing reasonably small misalignments), we do not expect to improve this result, given the beam jitter and limited BPM resolution of 10 μm. As test-case we instead *simulate* misalignment of 3-6 mm for a few BPMs. A2A will now steer the beam into the simulated centre, creating a position bump in the real trajectory. The red line of Figure 3 shows the position bump (the plot shows *real* BPM readings, as opposed to the readings with *simulated* misalignments that the correction algorithm sees). This bump increases the local dispersion by a factor 3, up to 15 mm, as shown in red in Figure 4.

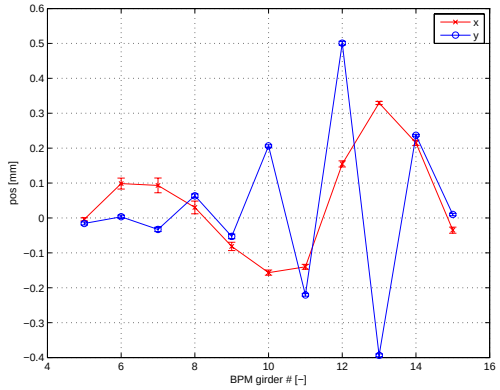

Figure 2: Model-based A2A (BPM readings for both planes).

One of the salient features of dispersion-free steering is that absolute BPM position readings are mostly disregarded, and instead difference readings are used to minimize the difference of dispersive trajectories. We therefore expect a successful DFS to find an orbit with smaller dispersion than A2A, while being mostly oblivious to the simulated BPM misalignment. However, the performance of the DFS depends on the precision with which the difference orbit can be obtained. We had dispersion of ~ 10 mm and a dispersion measurement precision of ~ 0.5 mm for $\Delta p/p = 10\%$, with present machine conditions. It was therefore not straightforward to find a good solution for DFS, but after substantial trials with different weighting wrt. the zero-reading (w_1/w_0=10 used), different SVD-cuts (70% used) and different $\Delta p/p$ (0.2 used), solutions were found that clearly indicates how the dispersion and position bump is reduced, shown in blue in Figure 3 and 4. The BPM readings including the simulated misalignments (seen by our correction algorithms) would show a large bump after the DFS, giving operators indications of large BPM misalignment. Finally, we note that applying DFS without simulated BPM misalignment gave similar performance as with these misalignments.

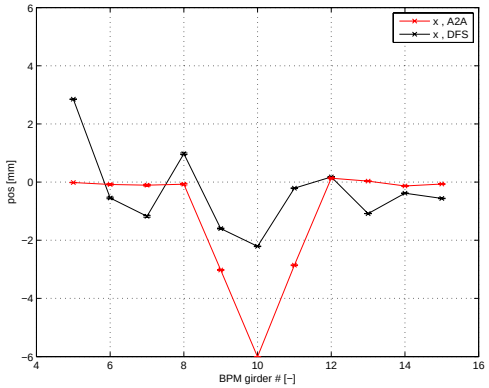

Figure 3: DFS versus A2A (*real* BPM readings after correction).

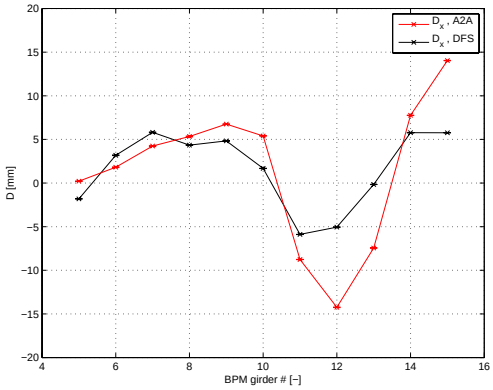

Figure 4: DFS versus A2A (dispersion after correction).

The initial large offset after DFS is due to incoming beam offset/angle (reproduceable in simulations). Machine-based responses were used for the dispersion-free steering. The results show that when dispersion is significant after A2A correction, for instance due to large BPM misalignment, DFS can provide a solution with lower dispersion and at the same time indicating the source of the problem. However, as correction algorithm for CTF3, DFS does not give a clear advantage over A2A.

CONCLUSIONS

The triplet structure impeded further model improvement. Model-based A2A has been applied successfully in a robust way to the CTF3 linac. DFS performance was superior to A2A in a test-case with artificially large BPM misalignment. However, for nominal linac operation we recommend A2A because of its faster execution.

ACKNOWLEDGEMENTS

Helpful discussions with A. Latina, K. Fuchsberger, S. Stapnes and V. Ziemann are gratefully acknowledged.

REFERENCES

[1] D. Schulte, Different Options for Dispersion Free Steering in the CLIC Main Linac, *Proceeding of PAC 2005* (2005)

[2] E. Adli and D. Schulte, Beam-Based Alignment for the CLIC Decelerator, *Proceeding of EPAC 2008* (2008)

[3] I. Wilson for the CLIC Study Team, CLIC Accelerated R&D, CLIC-Note 620 (2005)

[4] T.O. Raubenheimer and R.D. Ruth, A dispersion-free trajectory correction technique for linear colliders, **NIM** A302 (1991) 191-208

[5] R. Corsini et al., First Full Beam Loading Operation with the CTF3 Linac, *Proceeding of EPAC 2004* (2004)

[6] J. Safranek, Experimental Determination of Storage Ring Optics using Orbit Response Measurements, **NIM** A388 (1997) 27-36

[7] W.H. Press et al., Numerical Recipes, 3rd Edition, Cambridge University Press (2007)

C. Collection of Specifications

C.1 Drive Beam Decelerator Magnet Specification

This specification concerns the around 42'000 quadrupole magnets foreseen for the CLIC decelerator. Due to the high number, the required magnet design accuracy and power supply stability specified have a significant impact on the CLIC cost estimates.

The magnet specifications are driven by beam dynamics performance. A vital part of the thesis was therefore to develop a beam dynamics simulation framework where tolerances for all components, including magnet parameters, could be studied in detail. An important topic discussed in this specification, related to CLIC cost estimates, is the impact of a non-smooth tapering of the quadrupole gradient along the lattice.

The specification was written entirely by the candidate, with input from the Beam Physics study leader Daniel Schulte. The specification is marked "draft" because as the CLIC project evolves, the specification is expected to evolve as well.

Draft Drive Beam Decelerator Magnet Specification

E. Adli (University of Oslo and CERN)

July 13, 2009

Contents

1 Introduction

In the Drive Beam Decelerator the beam is focused and guided by quadrupoles in a FODO configuration, where each CLIC module incorporates one F and one D quadrupole.

Each Decelerator is divided into 24 sectors. Each sector is of varying length, with the same number of PETS per sector (ensuring the same energy extraction in each sector), but with a different number of quadrupoles. The longest sector is about 1050 m, the shortest about 840 m, with an average length of about 880 m. The half-cell length is 1.005 m, and the total number of quadrupoles needed for both Decelerators is about 42000.

1.1 Focusing principle

As the beam passes through a Decelerator sector, energy will be extracted by the 1491 PETS, and an energy spread will develop. The baseline is to have a maximum of $S = 90\%$ extracted at the end of the lattice.

The quadrupoles will be scaled such that the lowest energy particles have a constant phase-advance per cell ($\mu_{cell} \approx 90^o$). The beam loses the same amount of energy per PETS, so the ideal quadrupole gradient is linear with the number of PETS, see Figure 1.

We note that as a consequence of the focusing strategy, the FODO stability limit is surpassed at the lattice end if the initial beam energy is too low by a factor $E_{unstable}/E_0 < (1-S)(\frac{\sin(\mu/2)}{\sin(180^0/2)}) + S \approx 0.97$. Because the deceleration scales with the current, there is a similar limit for the current: $I_{unstable}/I_0 > \frac{1}{S} - (\frac{1}{S} - 1)\frac{\sin(\phi_0/2)}{\sin(180^0/2)} \approx 1.03$.

1.2 Beam-based correction

The Decelerator requires beam-based correction [1]. For this purpose either quadrupoles on movers or dipole corrector coils, in both the horizontal and the vertical plane, must be used. For movers we estimate a maximum displacement of $\pm$1mm in each plane to be sufficient for normal operation as well as tune-up. The corresponding maximum corrector integrated field required is 12 mT m. Whether movers or corrector coils are to be used is still to be decided (cost issued needs to be addressed).

2 Specifications

2.1 Active length

The quadrupole active length is specified to l =0.15 m.

2.2 Gap size

The inner radius of the vacuum chamber is specified to 11.5 mm. In addition the thickness of the vacuum chamber walls must be foreseen. If movers are to be used, space to move the quadrupoles in order to correct the orbit [1] must be foreseen. We estimate a total of 2 mm extra gap in each plane to be enough. If corrector coils are to be used enough space to accommodate the coils in the quadrupole design must be foreseen, the resulting gap parameters will depend on the design of the corrector coils.

Thus, the required quadrupole gap size should be in the case of

- movers: 23 mm + vacuum chamber walls thickness × 2 + 2 mm
- coils: 23 mm + vacuum chamber walls thickness × 2 + space needed for corrector coil integration

2.3 Gradient

At the start of the lattice a quadrupole gradient of $\hat{G}$ = 81.2 T/m is required. For each PETS the beam sees, the gradient shall ideally decrease in steps of 0.0489 T/m per PETS (from zero to two PETS will be installed between each quadrupole). The resulting gradient for the last quadrupole is $\check{G} = (1 - S)\hat{G} = 8.12$ T/m,

2.4 Magnet design accuracy

Magnet imperfections affect both the beam focusing and the beam steering, but the effect of the latter is removed by beam-based correction. The effect of gradient imperfections on the drive beam envelope has been investigated by simulation [2]. It was found that a relative integrated gradient error up to 1×10^{-3} rms can be accepted in the current baseline design. This corresponds to a maximum uniform-distribution tolerance of $\sqrt{3} \times 10^{-3}$.

2.5 Power supply accuracy

Power supply ripple affects both the beam focusing and the beam steering, also after steering (dynamic error source). An rms ripple of $5 \cdot 10^{-4}$ can be accepted in the current

baseline design.

Table 1 summarizes the specifications for an ideal focusing.

Quadrupole parameters			
Active length	l	0.15	m
Gap (pole to pole)	g	See Section 2.2	mm
Max. gradient	$\hat{G}$	81.2	T/m
Max. energy extraction	S	90	%
Min. gradient	$\check{G} = (1 - S)\hat{G}$	8.12	T/m
Min. gradient step	ΔG	0.0489	T/m
Magnet design accuracy rms	$\sigma(Gl)/(Gl)$	1×10^{-3}	-
Resulting magnet design tolerance	$\Delta(Gl)/(Gl)$	$\sqrt{3} \times 10^{-3}$	-
Power supply accuracy rms	$\sigma(I)/I$	5×10^{-4}	-
Total nb. of quads	N_{tot}	$\sim$42000	-

Table 1: Ideal decelerator quadrupole specification

3 Implementation issues and optimization

3.1 Powered magnets

In order to provide a gradient varying with the granularity as specified in Section 2 one would require an individual power supply for each quadrupole (or, in the case of permanent magnets, more than 1000 different types, see Section 3.2).

As a strategy to reduce the number of power supplies (PS), we suggest to use a number of quadrupole types, N_T, and let one PS power a string of quadrupoles of different types. In order to keep the relative gradient error small, the quadrupole types will be adjusted to perfectly match the N_T at the smallest energy intervals. Within each string the current, as well as the number of quadrupoles, will be adjusted in order to keep the average slope of the gradient equal to the ideal. The absolute gradient error within each string will increase towards the start of the lattice, however, the relative error will be of the same order along the lattice. Figure 2 illustrates the steps in the absolute gradient, due to the string approach, towards the end of the lattice.

For a given N_T, a given number power supplies, N_P, will be needed per sector. Note that N_P is much smaller than the total number of gradients needed divided by N_T. Figure 5 shows the product $N_P N_T$. If one attributes a cost to adding another PS and a cost to introducing an additional type one can find an optimum N_T by minimizing $c_P N_P + c_T N_T$.

As an example, we define $N_T = 50$ types (minimum if $c_P \approx 10 c_T$), yielding a total of $N_P = 9$ power supplies per sector, each powering from about 50 to about 300 magnets (number will vary slightly from sector to sector). The resulting relative error in the normalized strength is within 0.4%, as shown in Figure 3. The error due to the steps is correlated, so the effect is not as strong as independent errors of the same magnitude.

Simulations show that the beam envelope growth is noticable with respect to the ideal focusing. The effect is most noticeable in the case of a dispersion-free corrected machine. Figure 4 shows the beam envelope for a number of corrected machines with both ideal gradient and gradient with steps corresponding to $N_T = 50$. The envelope increase is significant (from 6% to 12% increase) with respect to ideal focusing, but with the present baseline setup it is considered small enough to be acceptable, especially in light of the potential savings in the number of power supplies (from ∼40000 to ∼400). However, further study of the effect of such steps should be studied in more detail if the baseline design changes significantly.

In order to refine further the exact number of quadrupole types and power supplies, a cost study would be required to estimate c_P and c_T. However, we believe that the results we have got for $N_T = 50$ will be similar for a range of values of c_P/c_T.

3.1.1 Effect of magnet failure

When discussing a reduction of the number of power supplies, it should be noted that a failure of several quadrupoles in series will affect the beam more severely than one single quadrupole. However, in [2] it was shown that already when two or more quadrupoles in series fails, the beam losses will be more than ∼10%, so that using few rather than many power supplies might not significantly mitigate this problem, unless individual power supplies are used.

We summarize the example configuration with $N_T = 50$ in Table 2 (other numbers stay as in Table 1.

Powered magnets			
Number of different quadrupole types	N_T	50	-
Number of power supplies per sector	N_P	∼9	-
Number of power supplies in total	N_{Ptot}	∼432	-
Resulting max. relative error of normalized strength due to steps	k/k_0	0.4	%

Table 2: Example specification with reduced number of power supplies

3.2 Permanent magnets

Permanent magnets could in principle be considered for the decelerator. However, as discussed in Section 1.1 the focusing properties of the lattice is very sensistive to changes of the initial current. For instance with 3% more current than the nominal design value the focusing of the beam will become unstable towards the end of the lattice if the quadrupole strength is not adjusted correspondingly. Conversely, with low current test beams, normalized gradients will vary substantially if absolute gradients are fixed. Initial tune-up and operation and later diagnostic work of the line may then be made unduly difficult. This may therefore imply that permanent magnets might be unsuitable for the decelerator. All these points must be clarified before permanent magnets are to be considered for the decelerator.

However, if permanent magnets are to be considered, the number of different types can be estimated from Figure 5 (some further optimization can possibly be performed by studying each individual sector in detail), yielding a minimum of about 400 different magnet types (the total number of about 42000 magnets will of course still remain the same).

We summarize the permanent magnets characteristics in Table 3.

Permanent magnets			
Number of types	N_T	$\sim$400	-
Maximum relative error of normalized strength	k/k_0	0.4	%
Magnet design accuracy rms	$\sigma(Gl)/(Gl)$	1×10^{-3}	-
Resulting magnet design tolerance	$\Delta(Gl)/(Gl)$	$\sqrt{3} \times 10^{-3}$	-

Table 3: Example specification with permanent magnets

References

[1] E. Adli and D. Schulte, Beam-Based Alignment for the CLIC Decelerator, *Proceeding of EPAC 2008* (2008)

[2] E. Adli et al., A Study of Failure Modes in the CLIC decelerator, *Proceeding of EPAC 2008* (2008)

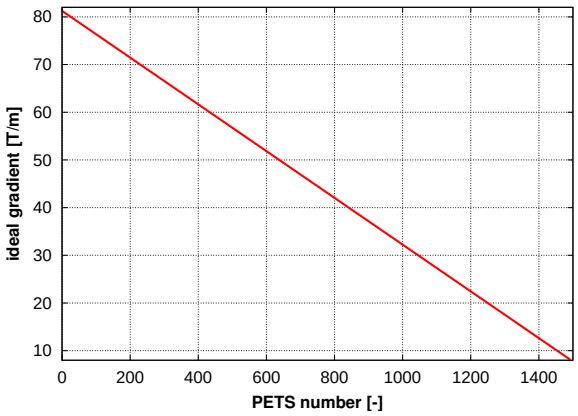

Figure 1: Ideal quadrupole gradient

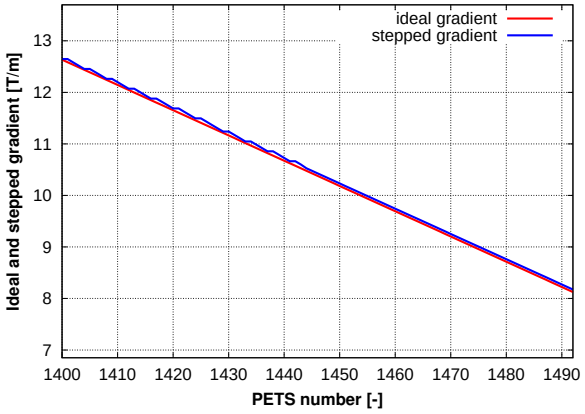

Figure 2: Stepped gradient versus ideal gradient towards the end of the lattice ($N_T = 50$)

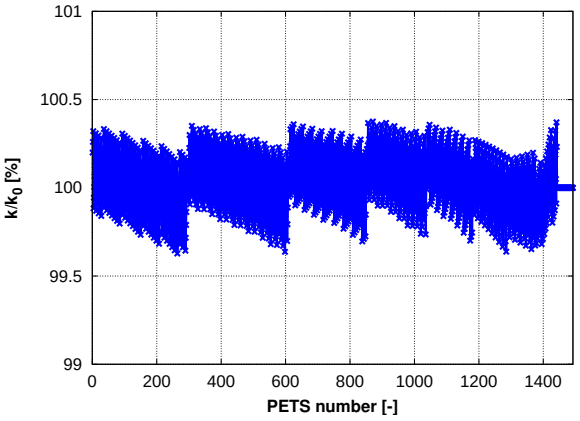

Figure 3: Relative error in normalized strength due to stepped focusing ($N_T = 50$)

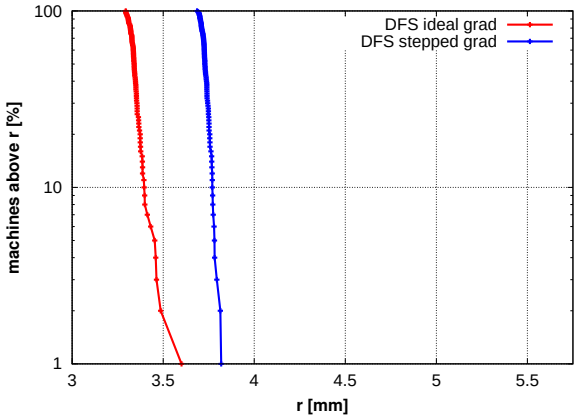

Figure 4: Envelope for ideal and stepped focusing ($N_T = 50$)

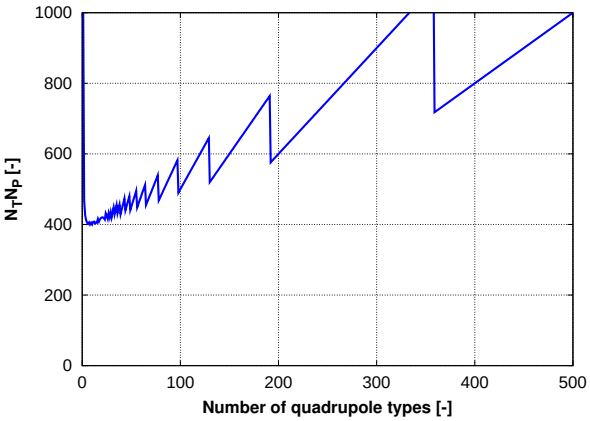

Figure 5: Number of quadrupole types times number of power supplies ($N_T = 50$)

C.2 Drive Beam Decelerator BPM Specification

This specification concerns the around 42'000 beam position monitors (BPMs) foreseen for the CLIC decelerator. Due to the high number, the required BPM accuracy and resolution specified have a significant impact on the CLIC cost estimates.

The BPM specifications are driven by the performance of the beam-based correction schemes. A vital part of the thesis was therefore to first develop suitable beam-based correction schemes and then investigate their performance as function of BPM parameters. An important topic discussed in this specification, related to CLIC cost estimates, is the effect on the correction scheme performance when a reduced number of BPMs is used.

The specification was written entirely by the candidate, with input from the Beam Physics study leader Daniel Schulte and in discussion with physicists from CERN beam instrumentation group. The specification is marked "draft" because as the CLIC project evolves, the specification is expected to evolve as well.

Draft Drive beam decelerator BPM functional specification

E. Adli (University of Oslo and CERN)

July 31, 2009

Contents

1 Scope

This specification covers the Beam Position Measurement System (BPM System) for the CLIC Drive Beam decelerator. Considerations on the BPM spatial accuracy, spatial resolution and time resolution will be given. Relevant beam dynamics issues impacting the specifications given will be briefly discussed. Arguments for the number of BPM specified will be given.

This is the first version of the specification, and machine protection issues have not been studied at this time. This document should therefore be considered a working draft, as future studies taking into account additional items might lead to modifications of the specifications given here.

2 Description of the decelerator lattice

CLIC has 48 decelerator sectors. Each sector is between 840 m and 1050 m long, consisting of up to 524 CLIC modules. Each CLIC module incorporates two quadrupoles (F and D) and up to four PETS. Figure 1 shows the CLIC machine, where a single decelerator sector is highlighted in red. Figure 2 shows a single CLIC module. The 48 decelerator sector lattices are independent, and the beam dynamics studies leading to the specifications in this document are based on studies of a single sector. We will for simplicity refer to this decelerator sector as the "the decelerator".

The CLIC Drive Beam decelerator requires the beam to be transported with very small losses. Beam-based correction is necessary in order to achieve this, and the BPM specifications are driven by the correction schemes. More details about the decelerator beam dynamics is found in [1].

In the current base line one BPM and one corrector per quadrupole are foreseen. The corrector will either be quadrupole vertical and horizontal movers, or horizontal and vertical corrector coils. For the simulations in this document quadrupole movers are simulated. The number of BPMs and correctors needed for correction will be addressed further in Section 4.6. Figure 3 shows the drive beam decelerator lattice corresponding to one CLIC module, as simulated for the BPM specification studies. The decelerator optics is the same in both planes, and the BPM specifications given will therefore apply to both planes.

All figures are collected at the back of the document.

3 Description of the beam observable

3.1 Production beam

The production drive beam consists of pulses consisting of 2922 bunches, spaced equally with a bunch frequency of 12 GHz (83 ps). Each bunch is assumed to have a Gaussian longitudinal charge profile with a 1 mm rms length. The average train current is 101 A, yielding a bunch charge of 8.4 nC. The drive beam requirements come from the drive beam power production requirements. The 12 GHz bunch frequency is a result of combining bunches from the 0.5 GHz drive beam accelerator by a factor 24, using the delay loop and the two combiner rings. The pulses arrive at the machine repetition rate of 50 Hz. [2].

3.2 Pilot beam

To tune-up the machine it is foreseen to start with a much less intensive beam. The current strategy is to start the tune-up with a uncombined beam. The bunch frequency of this beam will be 0.5 GHz, while the bunch charge and the average bunch length is foreseen to be the same as for the production beam. The pilot beam will thus have an average current of 4.2 A. The train length of the pilot beam is not yet decided upon; it will depend on among other things machine protection issues. The repetition rate of the pilot beam can be lower than for the production beam, typically low enough to allow for manual analysis between each shot. The pilot beam will be used to perform initial beam based correction; both 1-to-1 correction and dispersion-free steering (DFS).

3.3 Intermediate beams and tune-up considerations

The PETS beam loading implies that a large difference in the average current leads to a large difference in the beam average energy along the decelerator. A machine that has been corrected using the 0.5 GHz pilot beam will not perform well when sending through the 12 GHz production beam. It is foreseen that the tune-up correction shall be performed in steps of increasing average current (going e.g. from a bunch frequency of 0.5 GHz to 2 GHz, 4 GHz, 6 GHz etc). The exact number of different current plateaux needed is to be studied further, but we suggest to allow for resolvability of any average current between the pilot beam and the production beam.

The beam types foreseen are summarised in Table 1.

Beam type	Particle	Bunch charge [nC]	# of bunches	Bunch spacing [GHz]	σ_z [μm]
Production	e^-	8.4	2922	12	1000
Intermed.	e^-	8.4	$\leq$2922	0.5 - 12	1000
Pilot	e^-	8.4	<2922	0.5	1000

Table 1: Drive Beam decelerator beam types

4 Beam-based correction and resulting BPM constraints

4.1 Beam envelope growth

4.1.1 Lattice focusing

The decelerator focusing strategy is to keep the FODO phase-advance per cell constant a $\mu_{FODO} \approx 90°$ for the *lowest* energy particles. Details about the decelerator transverse focusing strategy can be found in [3].

4.1.2 Metrics and correction criterion

As criterion for minimum-loss transport we require the entire 3σ beam envelope, denoted r, defined as $r \equiv \max \sqrt{(|x_i| + 3\sigma_{x,i})^2 + (|y_i| + 3\sigma_{y,i})^2}$, to be within half the available aperture, $a_0/2 = 5.75$ mm, in order to have a margin for unmodelled effects like higher order wake fields. In this document we will with "beam envelope" refer to the 3-sigma envelope as defined here.

All 48 decelerator sectors should fulfil the above criterion. As baseline we simulate 100 machines and give the maximum beam envelope along the lattice of these 100 machines.

4.1.3 Envelope growth for a perfectly aligned machine

Due to adiabatic undamping the beam envelope will be amplified substantially even for a perfectly aligned machine with an ideal beam entering the machine at zero offset and angle. The most decelerated particles will have a final energy of only 10% of the least decelerated particles [2]. The focusing strategy ensures that higher energy particles will be contained in the envelope of the lower energy particles. With respect to the 3σ envelope of the incoming beam, the 3σ envelope of the lowest energy particle will at worst be amplified by a factor [1]

$$\frac{r_{\check{E}}}{r_0} = \sqrt{\frac{\gamma_f}{\gamma_0}} = \sqrt{1/(1-S)} = 3.2$$

while the 3σ envelope of the highest energy particle will at worst be be amplified by a factor of

$$\frac{r_{\hat{E}}}{r_0} = \sqrt{\frac{\hat{\beta}_{max}}{\beta_{max,0}}} = 2.1$$

Figure 4 illustrates the amplification of transverse envelope along a perfect machine for two particles starting at an offset from the axis. The particle in blue is at the head of the pulse and keeps almost constant energy along the lattice. The particle in red is situated so that it feels maximum deceleration, but is in return focused with a constant phase-advance, $\mu_{FODO} = 90°$, along the lattice.

4.1.4 Envelope growth for an uncorrected machine

For a machine with realistic misalignments the beam envelope will grow due to the effects of quadrupole misalignments and transverse wake kicks, in addition to the adiabatic undamping. The beam envelope amplification due to transverse wake fields is to a large extent suppressed due to the PETS design. The driver of the beam envelope is, for most scenarios, kicks due to quadrupole misalignments.

As a starting point for simulations we assume that static alignment of the machine at best can give a resulting rms offset of $\sigma_{quad} \approx 20$ μm. We can calculate the statistical average centroid position due to quadrupole kicks, of a particle having a FODO phase-advance of μ_{FODO} by summing kicks, yielding an average centroid offset of [1] :

$$< r > \approx 2\frac{\sigma_{quad}}{\cos(\mu_{FODO}/2)}\sqrt{2N_{FODO}}\sqrt{\frac{(1-\frac{1}{2}S)}{1-S}}$$

yielding about 4 mm for the lowest energy particle. This corresponds to incoherent build-up of the kicks. However, for a given machine some particles will sample the quadrupoles with some coherence, and thus build up kicks faster.

Figure 5 shows the uncorrected envelope (NC) along the decelerator (worst of 100 machines). We observe that the uncorrected beam envelope quickly grows above our criterion of $\frac{1}{2}a_0 = 5.75$ mm.

Figure 6 shows the lowest and highest energy particle for one uncorrected machine. We see that in this case the lowest energy particle has a higher amplitude; however this is not always the case, as it depends on the quadrupole misalignment pattern. In any case the transverse orbit amplitudes are too large, and must be corrected.

4.2 1-to-1 correction

The most straight-forward correction strategy is to use correctors to steer the beam centroid into the centre of each BPM. However, the beam will not pass through the exact

center of the quadrupoles. Dispersion due to quadrupole kicks will therefore build up. The 1-to-1 steering will therefore effectively confine the transverse amplitude of particles with energy close to the centroid energy, while particle with large energy deviation will follow trajectories with large dispersive errors and lead to beam envelope growth.

Figure 5 shows the 1-to-1 corrected envelope (SC) along the decelerator (worst of 100 machines). We see that this envelope also approaches closely the limit $\frac{1}{2}a_0 = 5.75$ mm. We want to be confident that all 48 decelerator sectors are within this limit, and the significant envelope growth after to 1-to-1 correction, with respect to a perfect machine, is therefore unacceptable. Figure 7 shows the lowest and highest energy particle, for one machine, after 1-to-1 steering. We see clearly how the lowest energy particle is confined with respect to Figure 6, while the highest energy particle trajectory has large dispersive errors and has not improved significantly with respect to Figure 6.

These simulations have been performed assuming a quadrupole misalignment of $\sigma_{quad} = 20$ μm, a BPM accuracy of $\sigma_{acc} = 20$ μm and a BPM resolution of $\sigma_{res} = 2$ μm.

4.3 Dispersion-free steering

The idea of dispersion-free steering (DFS) is to reduce the energy dependence of the centroid trajectories, and is therefore a seemingly ideal choice for decelerator correction. The dispersion-free steering is planned to be implemented by varying the average drive beam current in a pulse with delayed switching. The current difference will convert into an energy difference due to the PETS beam loading [4].

Figure 5 shows the DFS corrected envelope (worst of 100 machines). We see that this envelope growth is now barely above the minimal envelope growth, marked in black, meaning that the DFS has very effectively suppressed the dispersive errors. Figure 8 shows the lowest and highest energy particle, for one machine, after DFS steering, showing how both lowest energy and highest energy particles are confined with respect to Figure 6.

These simulations have been performed assuming a quadrupole misalignment of $\sigma_{quad} = 20$ μm, a BPM accuracy of $\sigma_{acc} = 20$ μm and a BPM resolution of $\sigma_{res} = 2$ μm.

4.4 Correction binning

The correction algorithms, both the 1-to-1 and the DFS will be performed in bins, where one bin consists of a fraction of the lattice. E.g.: a pulse is shot, the BPMs are read, and the first 100 meters of the decelerator sector are corrected. Then a new pulse is fired, the BPMs are read, and the second 100 meters are corrected and so on. In some cases it might also be advantageous to have some overlap between the bins (e.g. half the bin size). If the response matrix used for correction is close enough to the real machine, decelerator simulations shows that the number of bins used does not influence much the

final envelope growth. The optimal number of bins to be used for a machine depends on a number of factors and will have to be studied further.

In the studies leading to this specification a single bin (all the machine is corrected at once) has been used for simplicity.

4.5 Correction dependence on BPM parameters

4.5.1 Dependence on BPM accuracy (mechanical + electronic)

The beam envelope growth after performing 1-to-1 correction depends linearly on the BPM accuracy, as seen in Figure 9. The growth after dispersion-free steering does not depend significantly on the BPM accuracy (but instead on the BPM resolution, cf. next section). This means that if the BPM accuracy is larger than the $\sigma_{acc} = 22$ μm it might be difficult to get the beam through when doing 1-to-1 steering, and subsequently it might also be difficult to perform the dispersion-free steering. ($\sigma_{acc} = 20$ μm is simulated in Figure 5, and we can afford to increase by about 10% before hitting the half-aperture limit, thus the number $\sigma_{acc} = 22$ μm).

4.5.2 Dependence on BPM resolution (differential measurements)

The beam envelope growth after performing dispersion-free steering depends linearly on the BPM resolution, when this error source becomes dominant, as seen in Figure 10. The growth after 1-to-1 correction is a result of the BPM resolution adding in quadrature to the BPM accuracy to give the effective accuracy for the 1-to-1 correction.

From Figure 10 we observe that if $\sigma_{res} > 2\mu$m the finite resolution results in significantly increase in the beam envelope. In order to reach optimal performance for the dispersion-free steering we therefore suggest a BPM resolution of $\sigma_{res} = 2\mu$m.

4.6 Number of BPMs required

In Figure 5 simulations have performed with BPMs and correctors installed for each quadrupole.

We saw in Section 4.2 that after 1-to-1 correction there will still be beam envelope growth due to the dispersion induced by the quadrupole kicks. If BPMs and correctors are installed for every N quadrupole instead, the beam centroid will have a larger transverse offset close to the quadrupoles where no BPM is installed in their vicinity. The resulting dispersion due to quadrupole kicks, and also the total beam envelope, will therefore increase with respect to having BPMs and correctors for each quadrupole.

Figure 11 illustrates this effect for scenarios with every N=1, 2, 3 and 4 quadrupoles equipped with BPM and correctors. For illustration purposes these simulations have been performed for perfect BPMs, and for one machine only. The points in magenta, $< y >$, is the beam centroid in y as read by "virtual" monitors, not used for correction, which are installed for each quadrupole (as opposed the real BPMs installed for every Nth quadrupole). The line in blue, r_c, is the growth of the centroid beam envelope along the lattice due to the dispersion induced by the quadrupole kicks. Both the centroid displacement, $< y >$, and the centroid beam envelope growth, r_c, increase as more and more BPMs are taken away, as expected. For N=4 $< y >$ increases without bounds because there is now around one betatron oscillation between each BPM.

4.6.1 Reduction of BPM number combined with 20 μm quadrupole pre-alignment

Figure 12 shows the resulting total envelope for $\sigma_{quad} = 20$ μm. We note that equipping every second quadrupole with BPMs instead of every quadrupole (the baseline) does only give a slightly worse performance: 15% larger envelope in the case of 1-to-1 and less than 10% in the case of DFS.

4.6.2 Reduction of BPM number combined with large quadrupole pre-alignment

However, reducing the number of BPMs makes the envelope growth after steering sensitive to the misalignment of the quadrupole. Figure 12 shows the resulting total envelope for $\sigma_{quad} = 100$ μm (marked with x), overlaid on the results for $\sigma_{quad} = 20$ μm (marked with o). It is important to note than even perfect BPMs would not improve 1-to-1 steering results significantly for the case of $\sigma_{quad} = 100$ μm.

This implies that if one does not install one BPM and corrector for each quadrupole the correction performance will depend strongly on the quadrupole pre-alignment.

5 Time resolution

The production pulse length is $t_p = 240$ ns. The dispersion-free steering is foreseen to be performed by the delayed switching technique [4], generating energy variations along the pulse. We therefore require the BPMs to be able to resolve a fraction of one pulse. We consider it adequate if the BPM readings can be resolved for each $t_{resolve} = 60$ ns fraction of the pulse.

6 Other operational considerations

It should be remembered that the BPMs will be distributed in 48 independent beam lines (the 48 decelerator sectors). The specified time resolution of $t_{resolve} = 60$ ns is only required during orbit correction operations. If the decelerator sectors are corrected one by one, only a fraction of the BPMs (maximum $\sim$1/40) would have to be read out simultaneously with this time resolution.

For normal operation one would need all BPMs to be read-out simultaneously. Read out corresponding to the repetition rate of 50 Hz would probably be adequate, but this has to be studied further, including machine protection studies.

7 Summary of requirements

If the quadrupole pre-alignment is assumed to be larger than $\sigma_{quad} > 20$ μm, we recommend installing BPMs and correctors for each quadrupole. The preliminary BPM specifications are then listed in Table 2.

If one can assume a quadrupole pre-alignment of $\sigma_{quad} \leq 20$ μm one can probably relax the number of BPMs and correctors by a factor 2 (one BPM installed per F-quadrupole, or per D-quadrupole). As seen from Figure 12 the BPM accuracy should be slightly tighter ($\sigma_{acc} = 20$ μm) in order to give the same performance for 1-to-1 correction. Apart from that the specifications stay the same. The preliminary BPM specifications for this case are listed in Table 3.

Quantity	Symbol	Value	Unit
# of quadrupoles per BPMs	N	1	-
Total number of BPMS	N_{tot}	42000	-
Production beam			
BPM accuracy	σ_{acc}	22	μm
BPM resolution	σ_{res}	2	μm
Time resolution	$t_{resolve}$	60	ns
Pilot beam			
BPM accuracy	σ_{acc}	22	μm
BPM resolution	σ_{res}	4	μm
Time resolution	$t_{resolve}$	60	ns

Table 2: Specification set 1

Quantity	Symbol	Value	Unit
# of quadrupoles per BPMs	N	2	-
Total number of BPMS	N_{tot}	21000	
Production beam			
BPM accuracy	σ_{acc}	20	μm
BPM resolution	σ_{res}	2	μm
Time resolution	$t_{resolve}$	60	ns
Pilot beam			
BPM accuracy	σ_{acc}	20	μm
BPM resolution	σ_{res}	4	μm
Time resolution	$t_{resolve}$	60	ns

Table 3: Specification set 2, assuming $\sigma_{quad} \leq 20$

References

[1] E. Adli, D. Schulte and I. Syratchev, Beam Dynamics of the CLIC Decelerator, *Proceeding of the 44th ICFA Advanced Beam Dynamics Workshop* (2008)

[2] CLIC parameters 2008, F. Tecker ed., *CERN CLIC Note 764* (2008)

[3] E. Adli, Drive Beam Decelerator magnet specification, CERN Technical Note (2009) https://edms.cern.ch/document/992790/1

[4] E. Adli and D. Schulte, Beam-Based Alignment for the CLIC Decelerator, *Proceeding of EPAC 2008* (2008)

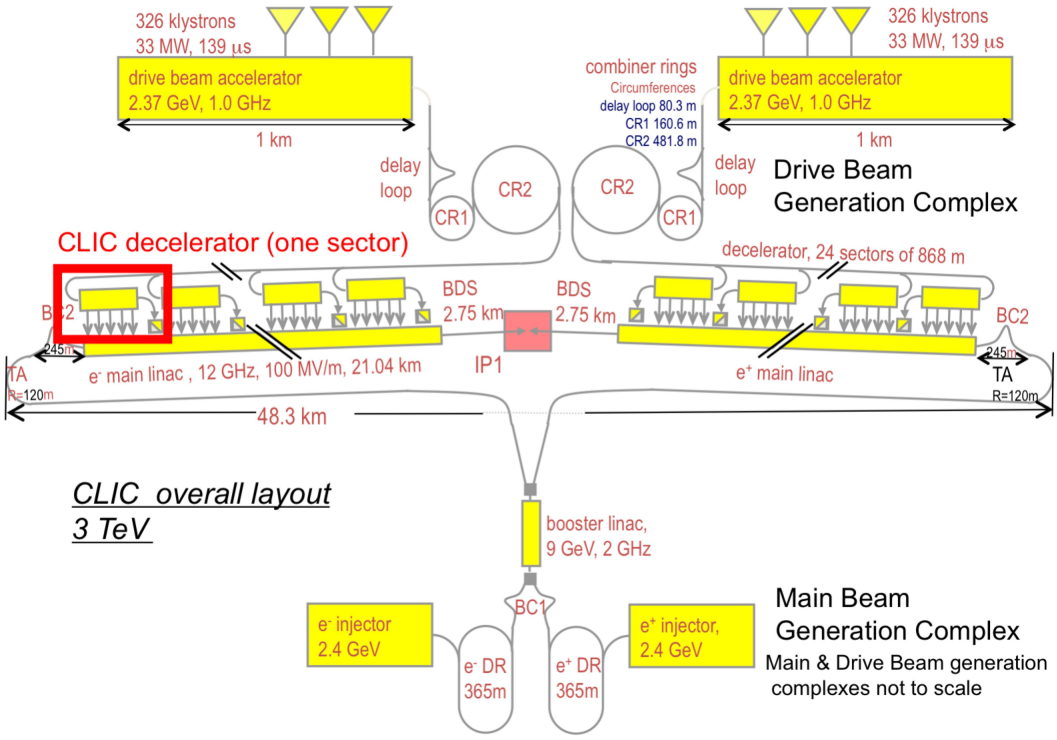

Figure 1: The 12 GHz CLIC machine with one decelerator sector outlined in red.

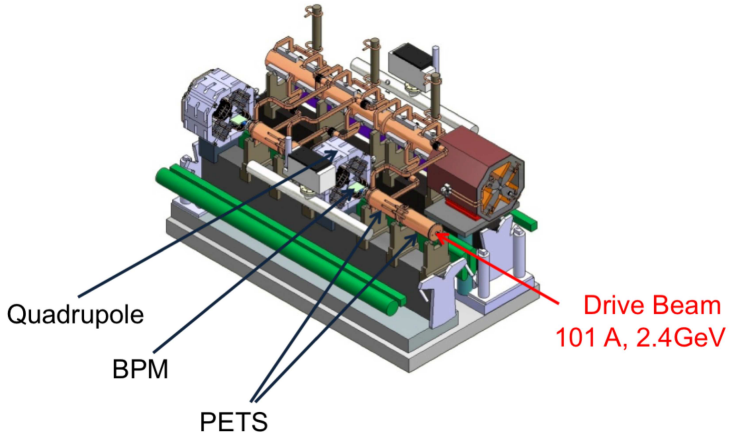

Figure 2: A single CLIC module with the components relevant for the BPM specification study indicated.

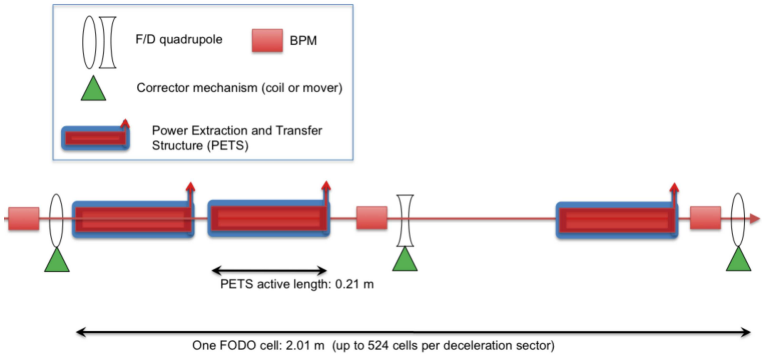

Figure 3: Simulation layout of the CLIC module.

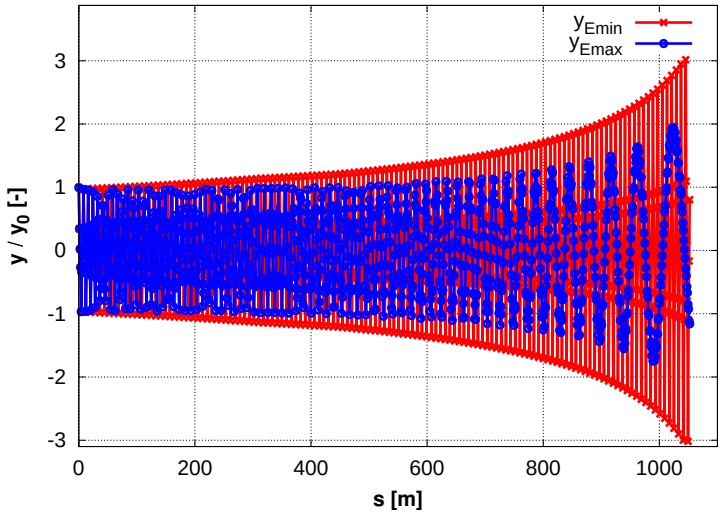

Figure 4: Amplification of particle transverse envelopes along a perfectly aligned decelerator. The particle in blue is at the head of the pulse and feels almost no deceleration. The particle in red is situated so that it feels maximum deceleration.

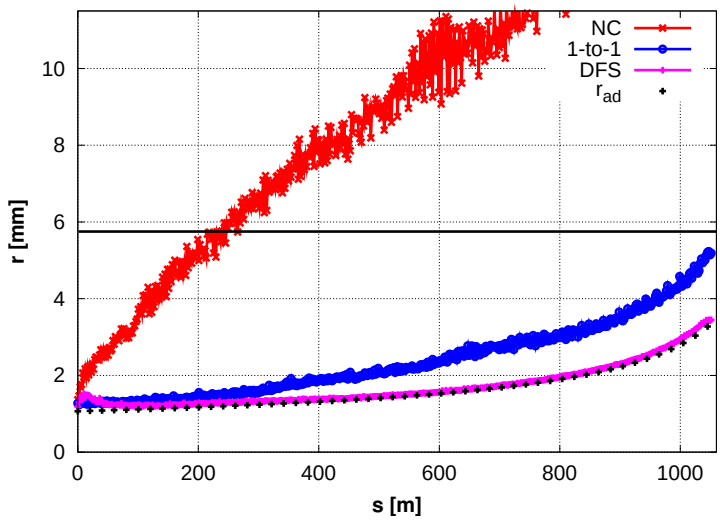

Figure 5: The 3σ beam envelope (worst of 100 machines) along the decelerator lattice in the cases of no correction (red), 1-to-1 correction (blue) and dispersion-free steering (magenta). The minimum achievable envelope due to adiabatic undamping alone is plotted in black. We observe that the dispersion-free steering has taken out almost all residual particle movement, in all parts of the beam.

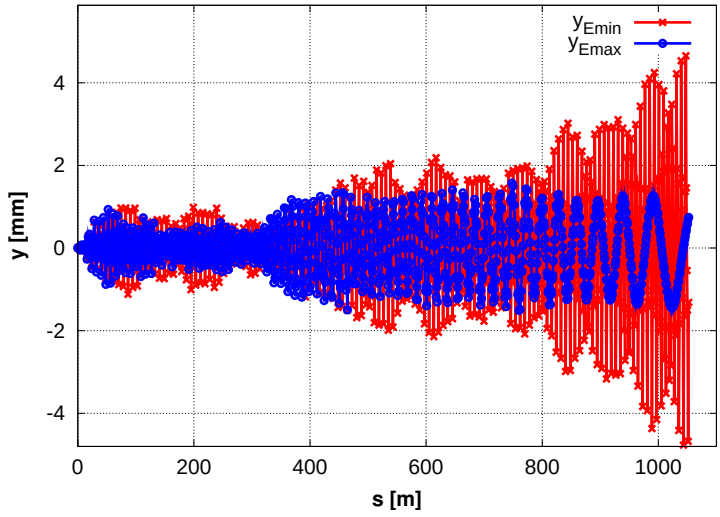

Figure 6: Example of the least decelerated macro particle (in blue) and the most decelerate macro particle (in red) along an uncorrected machine (NC).

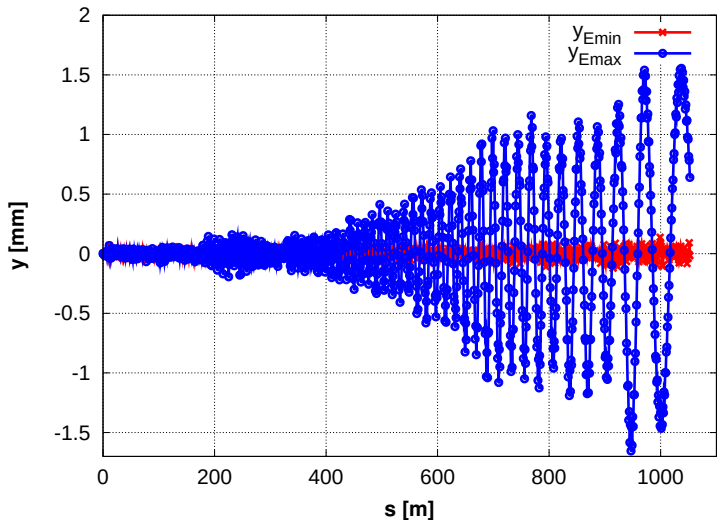

Figure 7: Example of the least decelerated macro particle (in blue) and the most decelerate macro particle (in red) along a 1-to-1 steered machine (1-to-1).

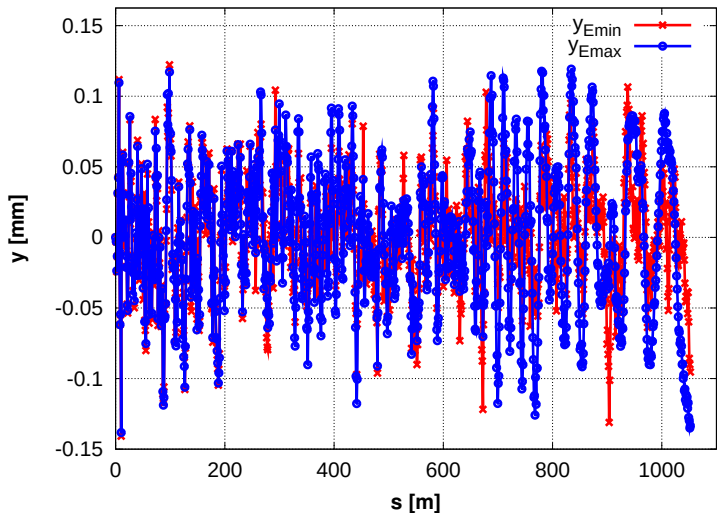

Figure 8: Example of the least decelerated macro particle (in blue) and the most decelerate macro particle (in red) along a dispersion-free steered machine (DFS).

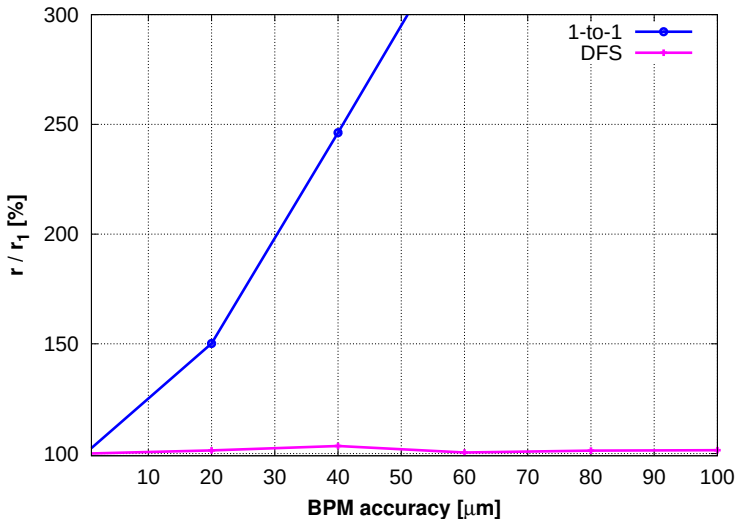

Figure 9: Dependence of 1-to-1 correction and dispersion-free steering on the BPM accuracy.

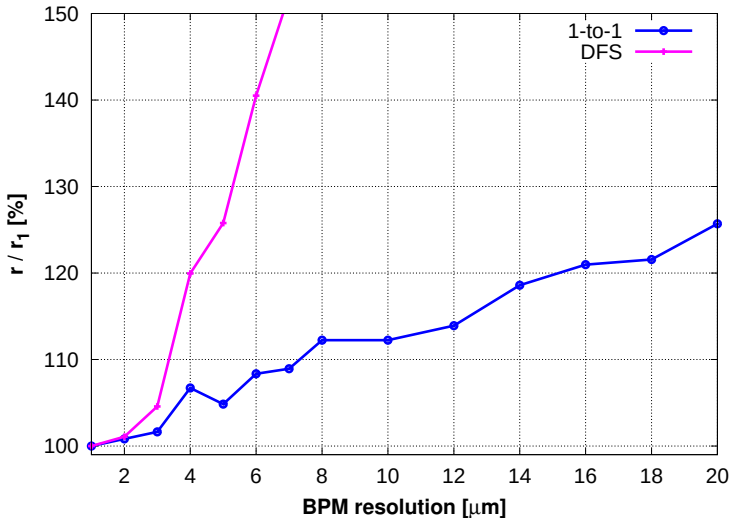

Figure 10: Dependence of 1-to-1 correction and dispersion-free steering on the BPM resolution.

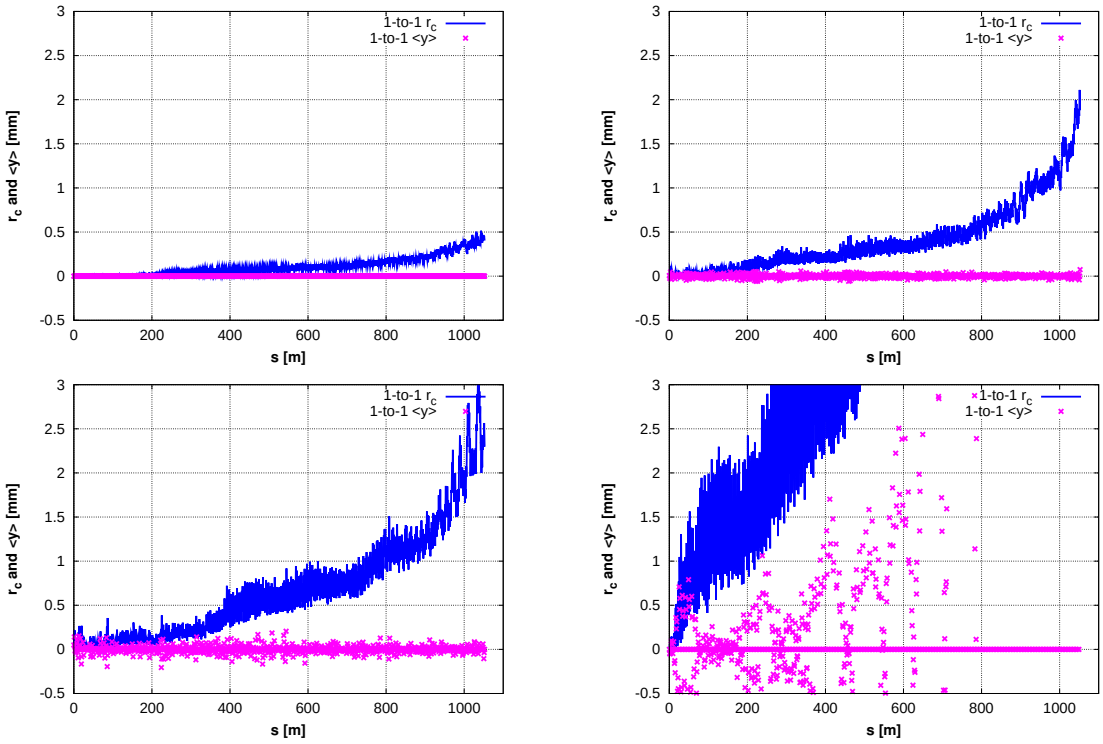

Figure 11: 1-to-1 correction simulations where every N=1, 2, 3 and 4 quadrupoles are equipped with BPM and correctors; simulations performed for perfect BPMs and for one machine. In magenta, $< y >$, the beam centroid in y as read by "virtual" monitors installed for each quadrupole (as opposed the real BPMs used for correction installed for every Nth quadrupole). In blue, r_c, the growth of the centroid beam envelope along the lattice due to the dispersion induced by the quadrupole kicks.

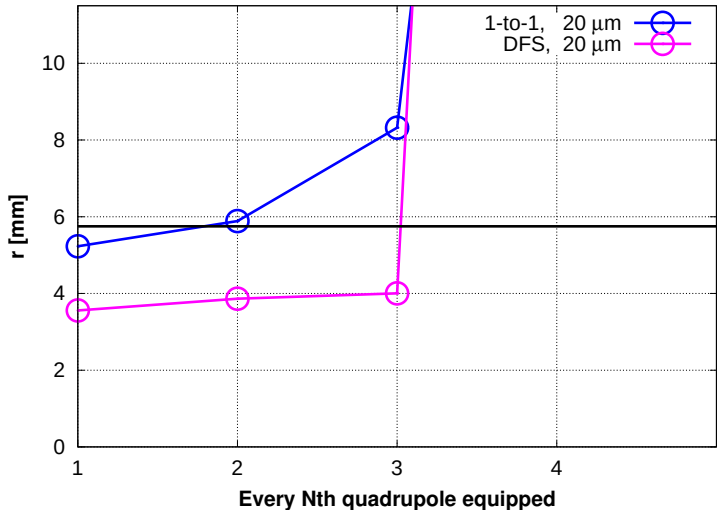

Figure 12: The effect on the total beam envelope of having BPMs and correctors installed for every Nth quadrupole. $\sigma_{quad} = 20$ μm.

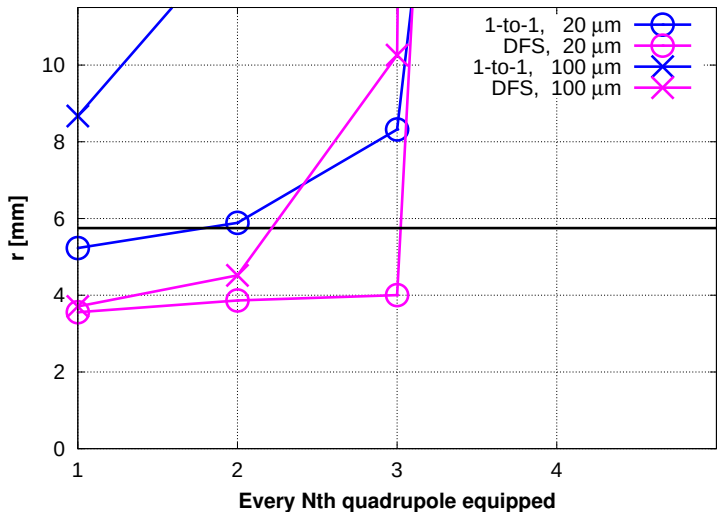

Figure 13: The effect on the total beam envelope of having BPMs and correctors installed for every Nth quadrupole. $\sigma_{quad} = 20$ μm and $\sigma_{quad} = 100$ μm.

D. Energy Loss Calculations

In Eqs. (4.31) and (4.36) we derived expressions for the mean energy loss based on two different starting points: considering the field in the phase with the beam, or considering the power leaving the system. For completeness we will now show that these two expressions are indeed equal, in our model, for pulses with constant beam intensity, I. We start by developing Eq. (4.36). Using

$$P_M = \frac{\mathrm{Abs}(\tilde{E}_M)^2}{(R'/Q)\omega_{RF}} v_g$$

we get

$$\langle U_M \rangle_{POW} = \frac{1}{I\eta_{\Omega,PETS}} \frac{v_g}{(R'/Q)\omega_{RF}} (\mathrm{Abs}\Big\{\tilde{E}_M\Big\}^2 - g^2 \mathrm{Abs}\Big\{\tilde{E}_{M-1}\Big\}^2).$$

By further substituting

$$\tilde{E}_M = E_{\mathrm{beam}} \sum_{m=0}^{M} (g\exp(j\phi))^m \equiv E_{\mathrm{beam}} \frac{1-(g\exp(j\phi))^{M+1}}{1-g\exp(j\phi)}$$

and

$$E_{\mathrm{beam}} = \frac{1}{2}(R'/Q)\omega_{RF}\frac{L}{v_g} I F(\lambda)\eta_{\Omega,PETS}$$

we get

$$\langle U_M \rangle_{POW} = \frac{1}{2} E_{\mathrm{beam}} L F(\lambda) (\mathrm{Abs}\Big\{\frac{1-(g\exp(j\phi))^{M+1}}{1-g\exp(j\phi)}\Big\}^2 - g^2 \mathrm{Abs}\Big\{\frac{1-(g\exp(j\phi))^{M}}{1-g\exp(j\phi)}\Big\}^2). \tag{D.1}$$

We develop Eq. (4.31) in a similar manner

$$\langle U_M \rangle = \Re(\tilde{E}_M) L F(\lambda) - \frac{1}{2} E_{\mathrm{beam}} L F(\lambda)$$

yielding

$$\langle U_M \rangle = \frac{1}{2} E_{\mathrm{beam}} L F(\lambda) (2\Re\Big\{\frac{1-(g\exp(j\phi))^{M+1}}{1-g\exp(j\phi)}\Big\} - 1). \tag{D.2}$$

Furthermore, for any complex number $q = g\exp(j\phi) \neq 1$ the algebraic equivalence

$$2\Re\Big\{\frac{1-q^{M+1}}{1-q}\Big\} - 1 \equiv \mathrm{Abs}\Big\{\frac{1-q^{M+1}}{1-q}\Big\}^2 - \mathrm{Abs}(q)^2 \mathrm{Abs}\Big\{\frac{1-q^{M}}{1-q}\Big\}^2$$

is trivially shown on the real axis. By the Identity Theorem of Complex Analysis, the equivalence then holds in the entire complex plane. We have thus shown that Eq. (D.1) is equal to Eq. (D.2), $\langle U_M \rangle_{POW} \equiv \langle U_M \rangle$, and that the two ways of calculating the beam energy loss are equivalent.

E. The Effect of Quadrupole Kicks

In this appendix we estimate the effect of quadrupole kicks on the most decelerated particles. We assume a linear decelerator lattice and linear betatron motion. The quadrupole induced kicks then add linearly as well. We furthermore assume the thin-lens approximation for the quadrupoles [23]. In general the effect of a kick θ_j, at location s_j, on the amplitude y_i, at location i, is given by

$$y_i = R_{ij}\theta_j$$

with transfer element $R_{ij} = \sqrt{\beta_i\beta_j}\sin\psi_{ij}$, $\psi_{ij} = \psi(j) - \psi(i)$ [23].

We are concerned with the maximum amplitude y_F in a focusing quadrupole with $\beta = \beta_F$ towards the end of the lattice. The dipole kick due to a quadrupole with focal length f_j, offset at a distance ξ_j from the centre line, is given by $\theta_j = \frac{\xi_j}{f_j}$. The random quadrupole offset is described by the random variable $\xi \sim N(0, \sigma_{\text{quad}})$. We will calculate the effect of kicks on the lowest energy particles in the drive beam. These particles see a constant FODO phase-advance ϕ_{FODO} throughout the entire decelerator lattice, implying constant focal length $f_j = f$. However, the resulting amplitude induced by the kick will grow by a factor $\sqrt{\frac{\gamma_j}{\gamma_f}}$ due to the adiabatic undamping, where γ_j and γ_f is the Lorentz factor at the location of the kick and at the end of the lattice, respectively. The resulting amplitude from the sum of kicks along the decelerator can then be calculated as

$$y_F = \Sigma_{j=1}^{N} R_{Fi}(\xi_j/f)\sqrt{\frac{\gamma_j}{\gamma_f}} = \frac{1}{f}\sqrt{\frac{\beta_F}{\gamma_f}}\Sigma_{j=1}^{N}\xi_j\sqrt{\gamma_j\beta_j}\sin\psi_{Fj}.$$

We calculate the mean of the square of the amplitude, $\langle y_F^2\rangle$

$$\langle y_F^2\rangle = \frac{1}{f^2}\frac{\beta_F}{\gamma_f}\Sigma_{j=1}^{N}\Sigma_{k=1}^{N}\langle\xi_j\xi_k\rangle\sqrt{\gamma_j\beta_j}\sqrt{\gamma_k\beta_k}\sin\psi_{Fj}\sin\psi_{Fk}.$$

Assuming independent quadrupole offsets the cross-terms become zero. Substituting $\langle\xi_j\xi_k\rangle = 0$ and $\langle\xi_j\rangle = \sigma_{\text{quad}}$ we get

$$\langle y_F^2 \rangle = (\frac{\sigma_{\rm quad}}{f})^2 \frac{\beta_F}{\gamma_f} \Sigma_{j=1}^N \gamma_j \beta_j \sin^2 \psi_{Fj}. \tag{E.1}$$

The adiabatic undamping term, γ_j, varies slowly with respect to the oscillating term. The sum term, disregarding the adiabatic term, can be averaged to

$$\Sigma_{j=1}^N \beta_j \sin^2 \psi_{Fj} \approx \frac{(\beta_F + \beta_D)}{2} \frac{N}{2} \tag{E.2}$$

using that half of the kicks are applied in focusing quadrupoles where $\beta = \beta_F$ and half in defocusing quadrupoles where $\beta = \beta_D$.

We write the adiabatic term γ_j in terms of the decelerator design parameter $\eta_{\rm extr}$. The energy decreases linearly from E_0 at the entrance of the lattice to a level $E_0(1 - \eta_{\rm extr})$ at the sector end at $s = L_{sector}$, yielding at distance s_j a value

$$\gamma_j = \frac{E_0}{E_e}(1 - \eta_{\rm extr} \frac{s_j}{L_{sector}})$$

which integrates to

$$\frac{1}{N} \Sigma_{j=1}^N \gamma_j \approx \frac{E_0}{E_e} \frac{1}{L_{sector}} \int_0^{L_{sector}} (1 - \eta_{\rm extr} \frac{s_j}{L_{sector}}) ds = \frac{E_0}{E_e}(1 - \frac{1}{2}\eta_{\rm extr}). \tag{E.3}$$

Similarly γ_f can be written as

$$\gamma_f = \frac{E_0}{E_e}(1 - \eta_{\rm extr}). \tag{E.4}$$

Inserting Eqs. (E.2), (E.3) and (E.4) into Eq. (E.1) yields

$$\langle y_F^2 \rangle = (\frac{\sigma_{\rm quad}}{f})^2 \beta_F \frac{(\beta_F + \beta_D)}{2} \frac{(1 - \frac{1}{2}\eta_{\rm extr})}{(1 - \eta_{\rm extr})} \frac{N}{2}. \tag{E.5}$$

To calculate the average centroid envelope for the lowest energy particles, $\langle r_c \rangle_{\rm Emin}^2 = \langle x_F^2 \rangle + \langle y_F^2 \rangle$, we use that the drive beam is round, and that the derivation of (E.5) is independent of which plane is considered. Since a quadrupole focusing in vertical is defocusing in the horizontal, $\beta_{y,F} = \beta_{x,D}$ we get

$$\langle x_F^2 \rangle = (\frac{\sigma_{\rm quad}}{f})^2 \beta_D \frac{(\beta_F + \beta_D)}{2} \frac{(1 - \frac{1}{2}\eta_{\rm extr})}{(1 - \eta_{\rm extr})} \frac{N}{2}$$

and

$$\langle r_c \rangle_{\rm Emin}^2 = \frac{N}{4} (\beta_F + \beta_D)^2 (\frac{\sigma_{\rm quad}}{f})^2 \frac{(1 - \frac{1}{2}\eta_{\rm extr})}{(1 - \eta_{\rm extr})}.$$

The average envelope of the lowest energy particles is thus

$$\langle r_c \rangle_{\mathrm{Emin}} = \frac{\sqrt{N}}{2}(\beta_F + \beta_D)(\frac{\sigma_{\mathrm{quad}}}{f})\sqrt{\frac{(1-\frac{1}{2}\eta_{\mathrm{extr}})}{(1-\eta_{\mathrm{extr}})}}.$$

Using thin-lens approximation [23] we can simplify the expression further by writing

$$(\beta_F + \beta_D) = \frac{L_{FODO}}{\sin\phi_{\mathrm{FODO}}}(1 + \frac{L_{FODO}}{4f} + 1 - \frac{L_{FODO}}{4f}) = 2\frac{L_{FODO}}{\sin\phi_{\mathrm{FODO}}}$$
$$= \frac{L_{FODO}}{\sin(\phi_{\mathrm{FODO}}/2)\cos(\phi_{\mathrm{FODO}}/2)} = \frac{4f}{\cos(\phi_{\mathrm{FODO}}/2)},$$

yielding the final result

$$\langle r_c \rangle_{\mathrm{Emin}} = 2\sqrt{N}\frac{\sigma_{\mathrm{quad}}}{\cos(\phi_{\mathrm{FODO}}/2)}\sqrt{\frac{(1-\frac{1}{2}\eta_{\mathrm{extr}})}{(1-\eta_{\mathrm{extr}})}}. \tag{E.6}$$